GRAPHENE SUPPORTED ELECTROCATALYSTS FOR ALKALINE ANION-EXCHANGE MEMBRANE-BASED DIRECT METHANOL FUEL CELL (AAEM-DMFC) APPLICATIONS

NG JEN CHAO

DEPARTMENT OF MECHANICAL ENGINEERING
FACULTY OF ENGINEERING
UNIVERSITY OF MALAYA
KUALA LUMPUR

2019

University of Malaya

GRAPHENE SUPPORTED ELECTROCATALYSTS FOR ALKALINE ANION-EXCHANGE MEMBRANE-BASED DIRECT METHANOL FUEL CELL (AAEM-DMFC) APPLICATIONS

NG JEN CHAO

THESIS SUBMITTED IN FULFILMENT OF THE REQUIREMENTS FOR THE DEGREE OF DOCTOR OF PHILOSOPHY

DEPARTMENT OF MECHANICAL ENGINEERING
FACULTY OF ENGINEERING
UNIVERSITY OF MALAYA
KUALA LUMPUR

2019

University of Malaya

UNIVERSITY OF MALAYA

ORIGINAL LITERARY WORK DECLARATION

Name of Candidate: Ng Jen Chao

Matric No: KHA140074

Name of Degree: Doctor of Philosophy

Title of Project Thesis ("this Work"):

Graphene Supported Electrocatalysts for Alkaline Anion-Exchange Membrane-Based Direct Methanol Fuel Cell (AAEM-DMFC) Applications

Field of Study: Manufacturing Processes

I do solemnly and sincerely declare that:

(1) I am the sole author/writer of this Work;
(2) This Work is original;
(3) Any use of any work in which copyright exists was done by way of fair dealing and for permitted purposes and any excerpt or extract from, or reference to or reproduction of any copyright work has been disclosed expressly and sufficiently and the title of the Work and its authorship have been acknowledged in this Work;
(4) I do not have any actual knowledge nor do I ought reasonably to know that the making of this work constitutes an infringement of any copyright work;
(5) I hereby assign all and every rights in the copyright to this Work to the University of Malaya ("UM"), who henceforth shall be owner of the copyright in this Work and that any reproduction or use in any form or by any means whatsoever is prohibited without the written consent of UM having been first had and obtained;
(6) I am fully aware that if in the course of making this Work I have infringed any copyright whether intentionally or otherwise, I may be subject to legal action or any other action as may be determined by UM.

Candidate's Signature Date:

Subscribed and solemnly declared before,

Witness's Signature Date:

Name:

Designation:

University of Malaya

GRAPHENE SUPPORTED ELECTROCATALYSTS FOR ALKALINE ANION-EXCHANGE MEMBRANE-BASED DIRECT METHANOL FUEL CELL (AAEM-DMFC) APPLICATIONS

ABSTRACT

Fuel cells are potential alternative green energy sources. Alkaline anion-exchange membrane-based direct methanol fuel cell (AAEM-DMFC) emerges as one of the best candidates because of its cheap liquid fuel, low operating temperature, and high efficiency. Nonetheless, AAEM-DMFC has been limited by poor anodic methanol oxidation reaction (MOR). In this regard, catalyst plays an important role by lowering the activation energy of MOR. Palladium (Pd) has recently emerged as potential catalysts owing to its lower cost and abundancy. Pd exhibits superior catalytic activity and stability for the alcohol oxidation in alkaline medium because of its higher tolerance to CO-poisoning. Nevertheless, catalyst nanoparticles (NPs) tend to irreversibly agglomerate, reducing the surface area for the reaction, and thus poor electrochemical performance. Loading catalysts on catalyst supports, especially graphene, is an effective solution to prevent agglomeration. In this study, graphene was produced by reduction of graphene oxide (GO) by microwave reduction method. Our group successfully loaded Pd NPs on the surface of reduced graphene oxide (rGO). This paper started with preliminary studies to optimize the rGO supported Pd (Pd/rGO) from the aspect of: (i) optimum ratio of palladium to graphene and (ii) reduction duration. Results proved that 1:1 and 700 s are the optimum ratio and reduction duration, respectively. On the basis of the preliminary works, the electrocatalytic activity of Pd/rGO was further improved in two main directions: (i) catalyst and (ii) catalyst support (graphene). In the context of catalyst, particle size and distribution of catalyst NPs can influence the catalytic performance. Despite the remarkable performance via the introduction of various reagents, such as surfactants, these reagents tend to cover the catalytic sites and are

University of Malaya

difficult to be completely removed at the end of the synthesis. This work manipulated the Pd particle size and dispersion by (i) adjusting the concentration of precursor mixture solution (palladium chloride + GO) and (ii) modifying the conventional synthesis method. The concentration of the metal precursor mixture has significant effect to the rate of nucleation and growth. Results discovered performance difference as high as 195 % by simply varying the mixture concentration. The second approach was stemmed from the observation on the colour changes of the mixture solution during the conventional synthesis process. The colour changes reflected multi-stages reduction of the nanocomposite which is unfavourable for the synthesis of small size nanoparticles with uniform distribution. A modified method was proposed to discard the synthesis steps that induce multi-stages mild reduction, and induce rapid nucleation and supersaturation that facilitate small size nanoparticles. As to the catalyst support, rGO, its weak interaction with Pd NPs leads to agglomeration. Guanine, a nucleobases found in deoxyribonucleic acid and ribonucleic acid, was introduced to Pd/rGO to overcome the limitation. The guanine adsorbed to rGO via π-π interaction, whereas its amino, imino, and amide groups serve as anchoring sites for Pd ions and nanoparticles and control their synthesis. The guanine was revealed to exhibit catalytic capability, significantly enhancing the MOR of Pd/rGO compared to its counterpart at the absence of guanine.

Keywords: Direct methanol fuel cell, palladium, graphene, guanine, nucleation and growth

University of Malaya

ELEKTROKATALIS DIPAUTKAN KE GRAPHENE UNTUK APLIKASI SELFUEL METANOL TERUS DENGAN MEMBRAN YANG BERASASKAN PERTUKARAN ANION ALKALI (AAEM-DMFC)

ABSTRAK

Selfuel merupakan sumber tenaga hijau alternatif yang berpotensi. Selfuel metanol terus yang berasaskan pertukaran anion alkali (AAEM-DMFC) muncul sebagai salah satu calon terbaik disebabkan air fuelnya yang murah, suhu operasi yang rendah dan kecekapan yang tinggi. Tetapi, prestasi AAEM-DMFC dihadkan oleh pengoksidaan metanol (MOR) yang lemah. Dalam konteks ini, pemangkin yang aktif memainkan peranan yang penting dengan menurunkan tenaga pengaktifan MOR. Paladium (Pd) muncul sebagai pemangkin yang popular disebabkan kos yang lebih rendah dan bekalan yang lebih lumayan. Pd mempunyai aktiviti pemangkin and kestabilan yang memuaskan dalam pengoksidaan alkohol di medium alkali disebabkan toleransinya yang tinggi terhadap keracunan CO. Walau bagaimanapun, nanopartikel (NPs) pemangkin cenderung terhadap aglomerasi, mengurangkan kawasan permukaan untuk tindak balas dan menyebabkan prestasi electrokimia yang lemah. Pemendapan pemangkin pada penyokong pemangkin, terutamanya graphene, didapati berkesan untuk manangani aglomerasi pemangkin. Dalam kajian ini, graphene dihasilkan dengan reduksi graphene oxide (GO) melalui kaedah reduksi oleh gelombang mikro. Kumpulan kami berjaya memautkan NPs Pd pada permukaan GO yang telah direduksikan (rGO). Penyelidakan kami bermula dengan beberapa kajian asas untuk mengoptimumkan pemangkin Pd yang dipautkan pada rGO (Pd/rGO) dari aspek: (i) nisbah optimum Pd terhadap rGO, dan (ii) tempoh reduksi. Keputusan membuktikan nisbah 1:1 dan 700 saat merupakan nisbah dan tempoh reduksi yang optimum. Berdasarkan hasil penemuan kajian asas, aktiviti elektrokatalik Pd/rGO dinaiktarafkan dari dua dimensi tertakluk: (i) pemangkin dan (ii) penyokong pemangkin (graphene). Dalam konteks pemangkin, saiz partikel dan

University of Malaya

pengagihan pemangkin boleh mempengaruhi prestasi pemangkin. Walaupun prestasi pemangkin yang cemerlang telah dicapai melalui penambahan pelbagai reagen, seperti surfaktan, reagen tersebut cenderung untuk menutup tapak pemangkin dan sukar untuk dihapuskan di peringkat akhir sintesis. Kajian ini memanipulasikan saiz partikel and pengagihan pemangkin melalui (i) pelarasan kepekatan larutan campuran prekursor (paladium klorida + GO), dan (ii) mengubahsuaikan kaedah sintesis konvensional. Kepekatan larutan campuran prekursor logam mempunyai kesan yang ketara terhadap kadar nukleasi and pertumbuhan NPs. Kajian kami melaporkan perbezaan prestasi setinggi 195% dengan pengubahan kepekatan campuran. Pendekatan kedua berasal daripada pemerhatian terhadap perubahan warna larutan campuran semasa sintesis konventional. Perubahan warna mewakili reduksi berperingkat yang tidak memanfaatkan produksi nanopartikel yang kecil dan pengagihan yang seragam. Kaedah yang diubahsuaikan dicadangkan untuk mengelakkan langkah sintesis yang menyebabkan reduksi berperingkat, serta menstimulasikan nukleasi yang pantas dan supersaturation yang mendorong sintesis NPs yang kecil. Berkenaan dengan penyokong pemangkin, rGO, interaksinya yang lemah terhadap NPs Pd menyebabkan aglomerasi. Guanine, merupakan nucleobase asid deoksiribonukleik dan asid ribonukleik, ditambahkan ke Pd/rGO untuk memperbaiki interaksi. Guanine tersebut menyerap ke rGO melalui interaksi π-π manakala kumpulan kimianya seperti kumpulan amino, imino dan amide berfungsi sebagai tapak perlabuhan untuk ion dan NPs Pd, dan mengawal sintesis berkenaan. Guanine tersebut juga didapati mempunyai keupayaan pemangkin, meningkatan prestasi Pd/rGO secara ketara berbanding dengan Pd/rGO tanpa kewujudan guanine.

Keywords: Selfuel methanol terus, palladium, graphene, guanine, nukleasi dan pertumbuhan

University of Malaya

ACKNOWLEDGEMENTS

I would like to utilize this opportunity to express my heartfelt of gratitude to my thesis supervisors. Assoc. Prof. Dr. Tan Chou Yong and Assoc. Prof. Dr. Oi Boon Hong @ Ong Boon Hoong are very supportive and generous in sharing their knowledge throughout my entire study. They have been guiding me with utmost care, encouragement, and patience. I am also in immense grateful to Prof. Atsunori Matsuda, Dr. Go Kawamura, and Dr. Tan Wai Kian for their kind assistance and constructive suggestions during my exchange study in Japan.

I am also in deep appreciation to my family members. They are very understanding and always lend me their ear. Their love, support, and encouragement are the main elements that drive me to where I am today.

Furthermore, I would also like to thank all my friends for their help in the laboratory and readiness to share my sorrow and joy. They have never been stingy in sharing information, knowledge, and experience to me.

Last but not least, I am thankful to the faculty and staff for assisting me either in the aspect of experimental-related facilities and service, or document/paper work-related support throughout the study.

This work was supported under the Frontier Research Grant with grant number FG0011-17AFR, Postgraduate Research Grant (PPP) with grant number PG207-2015A and Nippon Sheet Glass Foundation for Materials Science and Engineering (NSG Foundation) with grant number IF014-2017. I would also gratefully acknowledge AUN/SEED-Net, JICA, University of Malaya and the Ministry of Higher Education Malaysia for the financial support.

University of Malaya

TABLE OF CONTENTS

University of Malaya

University of Malaya

University of Malaya

University of Malaya

LIST OF FIGURES

University of Malaya

University of Malaya

University of Malaya

LIST OF TABLES

University of Malaya

LIST OF SYMBOLS AND ABBREVIATIONS

AA	:	Ascorbic acid
AB_2O_4	:	Spinel oxide
ABX_3	:	Perovskite
AAEM	:	Alkaline anion-exchange membrane
Ag	:	Silver
$Ag(OH)_{ads}$	:	Hydroxide ion adsorbed to silver
AOA	:	5-aminoorotic acid
Au	:	Gold
B	:	Boron
BC_3	:	Boron-carbon active sites
β-CDP	:	B-cyclodextrin polymer
BGNs	:	Branched poly(ethylenimine)-functionalized graphene nanosheets
BGR	:	Boron modified graphene
B–N	:	Boron–nitrogen active sites
BNFe–C–G	:	Boron, nitrogen, and iron ternary-doped carbonized graphene oxide
B_xO_y	:	Boron oxide
BPEI	:	Branched poly(ethylenimine)
Br	:	Bromine
Br^-	:	Bromide ion
C	:	Concentration of the solute
C_o	:	Equilibrium concentration or solubility
Ca	:	Calcium

University of Malaya

CA	:	Chronoamperometry
CB	:	Carbon black
C–C	:	Carbon–carbon sigma bond
C=C	:	Carbon–carbon double bond
CCD	:	Charge-coupled-device
CdS	:	Cadmium sulfide
C–H	:	Carbon–hydrogen sigma bond
C_2H_4	:	Ethylene
CH_3OH	:	Methanol
$C_2H_2O_4$	:	Oxalic acid
$C_2H_4O_2\cdot$	:	Acetic acid free radical
$C_2H_5O_2\cdot$	:	Ethylene glycol free radical
Cl	:	Chlorine
ClFG	:	Chlorine–fluorine codoped graphene
ClG	:	Chlorine-doped graphene
$[C_{16}MMIm]Br$	:	1–hexadecyl–2,3–dimethyl imidazolium bromide
C–N	:	Carbon–nitrogen sigma bond
C=N	:	Carbon–nitrogen double bond
CNs	:	Carbon–nitrogen structures
CNSs	:	Carbon nanoscrolls
CNTs	:	Carbon nanotubes
CN_x	:	Nitrogen-rich carbon
Co	:	Cobalt
Co^{2+}	:	Cobalt ion with +2 charge
Co^{3+}	:	Cobalt ion with +3 charge
CO	:	Carbon monoxide

University of Malaya

CO_{ads}	:	Adsorbed carbon monoxide
C–O	:	Carbon–oxygen sigma bond
C=O	:	Carbon–oxygen double bond
$\frac{C}{O}$	:	Ratio of carbon to oxygen
CO_2	:	Carbon dioxide
$CoFe_2O_4$/PANI/rGO	:	Cobalt ferrite/polyaniline composite supported on reduced graphene oxide
Co–N	:	Cobalt–nitrogen sigma bond
Co–NCNT/NrGO	:	Cobalt-embedded nitrogen-doped carbon nanotubes and nitrogen-doped reduced graphene oxide
Co/N–rGO	:	Cobalt loaded on nitrogen-doped reduced graphene oxide
CoO_x	:	Cobalt oxide
Co–O	:	Cobalt–oxygen sigma bond
COO^-	:	Carboxylate ion
CoO_x–Ag/rGO	:	Cobalt oxide incorporated in reduced graphene oxide-supported silver
$CoO_{shell}Co_{core}$/N–rGO	:	Shell-core structural cobalt oxide–cobalt nanoparticles on nitrogen-doped reduced graphene oxide
Co_xP	:	Cobalt phosphide
Co_3O_4/N–rmGO	:	Cobalt oxide loaded on nitrogen-doped reduced graphene oxide
Co_2P@CoNPG	:	Cobalt phosphide particles supported on cobalt, nitrogen, and phosphorus-codoped graphene nanosheets
Co@Pt NPs	:	Cobalt core–platinum shell nanoparticles
$Co_{1-x}S$	:	Cobalt sulfide

University of Malaya

CP	:	Conducting polymer
CrN	:	Chromium nitride
CS_2	:	Carbon disulfide
CTAB	:	Cetyltrimethylammonium bromide
CTAC	:	Cetyltrimethylammonium chloride
Cu	:	Copper
Cu(0)	:	Zero-valent copper
Cu(I)	:	Copper with +1 charge
Cu(III)	:	Copper with +3 charge
Cu(IV)	:	Copper with +4 charge
CuO	:	Copper oxide
CV	:	Cyclic voltammetry
CVD	:	Chemical vapor deposition
ε_d	:	d-band center
DA	:	Dopamine
DMAB	:	Dimethyl amine borane
DMFC	:	Direct methanol fuel cell
DNA	:	Deoxyribonucleic acid
DI	:	Deionized
DPARH	:	Three-dimensional porous heteroatom-doped bio-palladium-gold loaded on reduced graphene oxide
$\bar{e}$	:	Electron
ECSA	:	Electrochemically active surface area
EDX	:	Energy-dispersive X-ray spectroscopy
EG	:	Ethylene glycol
EGOR	:	Ethylene glycol oxidation reaction

University of Malaya

$E_{1/2}$	:	Half-wave potential
E_{onset}	:	Onset potential
EOR	:	Ethanol oxidation reaction
E_{peak}	:	Peak potential
ERGO	:	Electrochemically reduced graphene oxide
F	:	Fluorine
fcc	:	Face-centered cubic
FCO/HrGOs	:	$FeCo_2O_4$ spinel nanoparticles covalently coupled to hollow reduced graphene oxide spheres
Fe	:	Iron
$FeCl_3$	:	Iron (III) chloride
FeC_x	:	Iron alloyed by carbon atoms
FeCo–N–rGO	:	Nitrogen-coordinated iron–cobalt loaded on reduced graphene oxide
Fe@N–G	:	Iron nanofragment embedded into nitrogen-doped graphene-shelled nanocages
$Fe–N_x$	:	Iron nitrogen-containing moieties
$Fe–N_x–C$	:	Iron–nitrogen–carbon active sites
Fe–N–S/rGO	:	Iron, nitrogen, and sulfur-codoped reduced graphene oxide
Fe_3O_4	:	Iron oxide
FePPc/PSS–Gr	:	Iron polyphthalocyanine loaded on poly(sodium-p-styrenesulfonate)-modified graphene
FESEM	:	Field-emission scanning electron microscopy
FeTsPc	:	Tetrasulfophthalocyanine
F–G	:	Fluorine-doped graphene
FMN	:	Flavin mononucleotide

University of Malaya

FTIR	:	Fourier-transform infrared spectroscopy
ΔG^*	:	Critical energy
ΔG_v	:	Change of Gibbs free energy per unit volume of the nucleus
Gas	:	Graphene aerogels
GCE	:	Glassy carbon electrode
g–C_3N_4	:	Graphitic carbon nitride
g–C_3N_4@rGO	:	Graphitic carbon nitride polymer on reduced graphene oxide
GNS-CNT	:	Graphene nanosheet-carbon nanotube hybrid
GO	:	Graphene oxide
G–V(C,N)	:	Graphene-supported vanadium carbonitride
H·	:	Hydrogen free radical
H^+	:	Hydrogen ion
H_2	:	Hydrogen gas
HCl	:	Hydrochloric acid
HCN	:	Hydrogen cyanide
H_2CO_3	:	Carbonic acid
HF	:	Hydrogen fluoride
HO_2^-	:	Hydroperoxide
H_2O	:	Hydrogen oxide
H_2O_2	:	Hydrogen peroxide
HOMO	:	Highest occupied molecular orbital
H_3PO_4	:	Phosphoric acid
HrGOs	:	Hollow reduced graphene oxide
HRTEM	:	High-resolution transmission electron microscopy
H_2PtCl_6	:	Chloroplatinic acid
H_2S	:	Hydrogen sulfide

University of Malaya

H_2SO_4	:	Sulfuric acid
I	:	Iodine
I^-	:	Iodide ion
$\frac{I_D}{I_G}$	:	Intensity ratio of raman D band to G band
$\frac{I_f}{I_b}$	:	Ratio of forward to backward peak current density
I_{peak}	:	Peak current density
k	:	Boltzmann constant
KCl	:	Potassium chloride
$KMnO_4$	:	Potassium permanganate
KNO_3	:	Potassium nitrate
KOH	:	Potassium hydroxide
$LaMnO_3$	:	Lanthanum manganite
LDH	:	Layered double hydroxide
$LiNO_3$	:	Lithium nitrate
LUMO	:	Lowest unoccupied molecular orbital
Mn	:	Manganese
Mn^{2+}	:	Manganese ion with +2 charge
Mn^{3+}	:	Manganese ion with +3 charge
$MnCo_2O_4$/N–rmGO	:	Spinel manganese cobalt oxide loaded onto nitrogen-doped reduced graphene oxide
MnO_x	:	Manganese oxide
MnOOH	:	Manganese oxohydroxide
$M–N_x$	:	Transition metal nitrogen-containing moieties
MO	:	Metal oxide
MOF	:	Metal organic framework

University of Malaya

$M–(OH)_{ads}$	:	Catalyst adsorbed with hydroxide
MOR	:	Methanol oxidation reaction
MoS_2	:	Molybdenum disulfide
MPc	:	Transition metal phthalocyanine
MPN	:	Metal-polymer network
MPPcs	:	Transition metal polyphthalocyanine
MWCNTs	:	Multi-walled carbon nanotubes
N	:	Nitrogen
N_2	:	Nitrogen gas
Na^+	:	Sodium ion
$NaBH_4$	:	Sodium borohydride
Na_2CO_3	:	Sodium carbonate
$NaNO_2$	:	Sodium nitrite
NaOH	:	Sodium hydroxide
Na_2PdCl_4	:	Sodium tetrachloropalladate
N–C	:	Nitrogen–carbon active sites
NCC	:	Nucleation Centers for Clustering
N–Cdots	:	Nitrogen–doped carbon dots
N–Cdots/GO	:	Nitrogen-doped carbon dots decorated graphene oxide
NDs	:	Nanodendrites
NG	:	Nitrogen-doped graphene
N–G	:	Nitrogen-doped graphene
N–Gas	:	Nitrogen-doped graphene aerogels
N–H	:	Nitrogen–hydrogen sigma bond
NH_2	:	Amine groups
NH_3	:	Ammonia

University of Malaya

NH_4OH	:	Ammonium hydroxide
NH_4SCN	:	Ammonium thiocyanate
Ni	:	Nickel
NiFe–LDH/NrGO	:	Nitrogen-doped nickel–iron layered double hydroxide supported on reduced graphene oxide
NiO	:	Nickel oxide
NiOOH	:	Nickel oxide hydroxide
$Ni(OH)_2$	:	Nickel (II) hydroxide
NMP	:	N-methyl-2-pyrrolidone
NPM	:	Non-precious metal
NPs	:	Nanoparticles
N–rGO/ NrGO	:	Nitrogen-doped reduced graphene oxide
NRs	:	Nanorods
NSs	:	Nanosheets
NWs	:	Nanowires
O_2	:	Oxygen gas
OAm	:	Oleylamine
$OH\cdot$	:	Hydroxide free radical
OH^-	:	Hydroxide ion
O–H	:	Oxygen–hydrogen sigma bond
1D	:	One-dimensional
O–O	:	Oxygen–oxygen sigma bond
ORR	:	Oxygen reduction reaction
P	:	Phosphorus
PA–GNs	:	1-pyrenamine-functionalized graphene nanosheets
PANI	:	Polyaniline

University of Malaya

pATP	:	p-aminothiophenol
P–C	:	Phosphorus–carbon sigma bond
Pd	:	Palladium
Pd(II)	:	Palladium ion with +2 charge
Pd(0)	:	Zero-valent palladium
PDA	:	Polydopamine
$Pd(acac)_2$	:	Palladium acetylacetonate
PdAg/rGO	:	Palladium–silver alloy loaded on reduced graphene oxide
Pd/BG	:	Palladium supported on boron oxide incorporated holey graphene sheets
$Pd(C_2H_3O_2)_2$	:	Palladium acetate
$PdCl_2$	:	Palladium chloride
$(PdCl_2–GO)_{BU}$	:	Mixture of graphene oxide and palladium chloride before ultrasonication
$(PdCl_2–GO)_{AU}$	:	Mixture of graphene oxide and palladium chloride after ultrasonication
$(PdCl_2–GO)_{EG}$	:	Mixture of graphene oxide and palladium chloride after addition of ethylene glycol
$(PdCl_2–GO)_{pH}$	:	Mixture of graphene oxide and palladium chloride after pH adjustment
PdCu/flat-lying rGO	:	Flat-lying reduced graphene oxide supported dealloyed palladium–copper nanoparticles
PDDA	:	Poly(diallyldimethylammonium chloride)
Pd–Ni–P	:	Palladium doped with nickel and phosphorus
PdO	:	Palladium oxide
Pd–P	:	Palladium doped with phosphorus

University of Malaya

Pd/Ppy–graphene	:	Palladium loaded on polypyrrole-functionalized graphene
Pd/rGO	:	Palladium loaded on reduced graphene oxide
Pd/rGO(2:1)	:	Palladium loaded on reduced graphene oxide with ratio of palladium to graphene equal to 2:1
Pd/rGO(1:1)	:	Palladium loaded on reduced graphene oxide with ratio of palladium to graphene equal to 1:1
Pd/rGO(0.5:1)	:	Palladium loaded on reduced graphene oxide with ratio of palladium to graphene equal to 0.5:1
Pd/rGO_{500}	:	Palladium loaded on reduced graphene oxide by 500 s of microwave irradiation
Pd/rGO_{700}	:	Palladium loaded on reduced graphene oxide by 700 s of microwave irradiation
Pd/rGO_{900}	:	Palladium loaded on reduced graphene oxide by 900 s of microwave irradiation
Pd/rGO (0.5)	:	Palladium loaded on reduced graphene oxide at concentration of 0.5 mg mL^{-1}
Pd/rGO (1.0)	:	Palladium loaded on reduced graphene oxide at concentration of 1.0 mg mL^{-1}
Pd/rGO (2.0)	:	Palladium loaded on reduced graphene oxide at concentration of 2.0 mg mL^{-1}
Pd/rGO (3.0)	:	Palladium loaded on reduced graphene oxide at concentration of 3.0 mg mL^{-1}
Pd/rGO (4.0)	:	Palladium loaded on reduced graphene oxide at concentration of 4.0 mg mL^{-1}
Pd/rGO_G	:	Reduced graphene oxide supported palladium that functionalized by guanine

University of Malaya

Pd/rGO_M	:	Palladium loaded on reduced graphene oxide by modified synthesis method
Pd/rGO_O	:	Palladium loaded on reduced graphene oxide by original synthesis method
PEM	:	Proton-exchange membrane
PEMFC	:	Pronton exchange membrane fuel cell
P–O	:	Phosphorus–oxygen sigma bond
PPcs	:	Polyphthalocyanines
Pt	:	Platinum
Pt^0	:	Zero-valent platinum
Pt–C	:	Platinum–carbon sigma bond
Pt/C	:	Carbon supported platinum
Pt/C/Gas	:	Hybrid of carbon-supported platinum nanoparticles and three-dimensional graphene aerogel
Pt–CO	:	Platinum adsorbed with carbon monoxide
PtCo/rGO	:	Platinum–cobalt alloy loaded on reduced graphene oxide
Pt_n/gDNA–GO	:	Platinum nanoclusters loaded on genomic deoxyribonucleic acid-graphene oxide
Pt–$Ni(OH)_2$–graphene	:	Platinum–nickel hydroxide–graphene ternary hybrid
Pt–Ni–P	:	Platinum doped with nickel and phosphorus
PtNWs	:	Platinum nanoworms
Pt_2Pd/NPG	:	Platinum–palladium alloy embedded into nitrogen-rich graphene nanopores
PtPd/rGO	:	Platinum–palladium alloy loaded on reduced graphene oxide
PtRu/rGO	:	Platinum–ruthenium alloy loaded on reduced graphene oxide
Pt@SC_6H_4–rGO	:	Platinum nanoparticles on 4-aminothiophenol-modified

University of Malaya

		reduced graphene oxide
Pt/S–rGO	:	Platinum loaded on sulfonic acid-grafted reduced graphene oxide
PVA	:	Polyvinyl alcohol
Pt/TiO_2–FGSs	:	Platinum catalysts supported onto titanium oxide-functionalized graphene nanosheets
PVP	:	Polyvinylpyrrolidone
r*	:	Critical size
rGO	:	Reduced graphene oxide
rGO–Ams	:	Reduced graphene oxide-encapsulated amine-functionalized iron oxide magnetic nanospheres
rGO–CN	:	Combination of rGO and nitrogen-doped carbon nanowires
RGO–OMC	:	Reduced graphene oxide–ordered mesoporous carbon
Rh	:	Rhodium
RNA	:	Ribonucleic acid
Ru	:	Ruthenium
Ru^0	:	Zero-valent ruthenium
RuO_2	:	Ruthenium oxide
Ru–OH	:	Ruthenium adsorbed with hydroxide
ɣ	:	Surface energy per unit area
S	:	Sulfur
S_{ads}	:	Adsorbed sulfur
SC	:	Supercritical
S–C	:	Sulfur–carbon active sites
Se	:	Selenium
SiO_2	:	Silica

University of Malaya

Sn	:	Tin
SnO_2	:	Tin oxide
SO_2	:	Sulfur dioxide
SO_3H–GCB	:	p-phenyl sulfonic acid functionalized graphitic carbon black
S–rGO	:	Sulfonic acid-grafted reduced graphene oxide
$SrTiO_3$	:	Strontium titanate
SSA	:	Specific surface area
T	:	Temperature
TEM	:	Transmission electron microscopy
3D	:	Three-dimensional
TiN	:	Titanium nitride
TiO_2	:	Titanium dioxide
$Ti_{1-x}O_2$	:	Titanium oxide
TMC	:	Transition metal-carbide
TMN	:	Transition metal-nitride
TOP	:	Trioctylphosphine
TOPO	:	n-Tri-octylphosphine oxide
TPB	:	Triple-phase boundary
2D	:	Two-dimensional
UV	:	Ultraviolet
UV-vis	:	Ultraviolet-visible spectroscopy
VG	:	Vertically oriented graphene
WO_3	:	Tungsten trioxide
wt%	:	Weight percentage
XPS	:	X-ray photoelectron spectroscopy
XRD	:	X-ray diffraction

University of Malaya

0D	:	Zero-dimensional
Zn	:	Zinc
Zn^{2+}	:	Zinc ion
ZnO	:	Zinc oxide
ZnO/rGO	:	Zinc oxide loaded on reduced graphene oxide
σ	:	Supersaturation

University of Malaya

LIST OF APPENDICES

University of Malaya

CHAPTER 1: INTRODUCTION

1.1 Background Study

Energy starvation is an impending problem as the gear of time rolls. Fossil fuels which provide about 80 % of world energy are depleting and have caused environmental pollution (Salvi et al., 2013). These problems spark the interests of science communities to look for alternative energy devices among which fuel cells stand up to be the one prominent. Fuel cells have been recognized capable to convert energy efficiently (36-69 %), emit low or even no pollutant, have good fuel availability, and are proficient for both transportation and stationary application (Lee et al., 2006). Owing to the promising characteristics of methanol including high energy density, easy storage and handling, low cost, and wide availability, direct methanol fuel cells emerge as potential candidates for portable devices (Shao, 2013, p. 1). The simple chemical structure of methanol, with only one carbon in its molecule, makes the electrooxidation of methanol simpler than other alcohol. Nonetheless, direct methanol fuel cell (DMFC) is facing incomplete and slow methanol oxidation reaction at anode, resulting to low power density and efficiency (James & Andrew, 2003, p. 142). Methanol crossover from anode to cathode is another pressing problem of DMFC (James & Andrew, 2003). Methanol crossover has a few detrimental effects, that is, (i) it is a waste of fuel, thus reduces the fuel efficiency; (ii) the methanol that reaches the cathode is oxidized (i.e., methanol oxidation reaction (MOR) and oxygen reduction reaction (ORR) occur simultaneously), leading to a mixed potential and reducing the voltage of the fuel cell; and (iii) deactivates the electrocatalytic activity of the catalyst (Kang et al., 2014; Li et al., 2015; Wang et al., 2008). The methanol crossover is especially serious in DMFC with acidic electrolyte membrane, namely, proton-exchange membrane-based DMFC (PEM-DMFC) as shown in Figure 1.1A. On the contrary, alkaline anion-exchange membrane-based DMFC (AAEM-DMFC) (Figure 1.1B) does not have much methanol

University of Malaya

crossover issue because this type of cell conducts hydroxide ions from cathode to anode, in the opposite direction of methanol crossover.

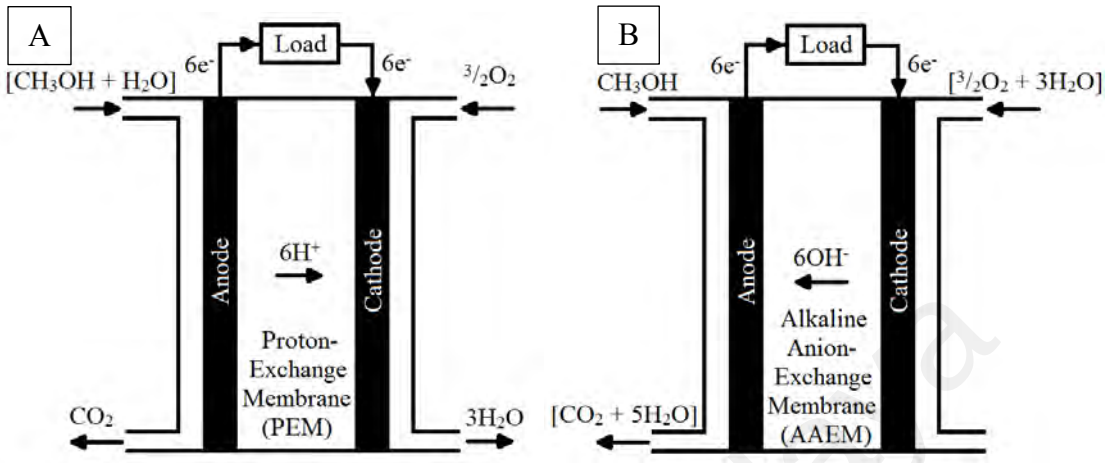

Figure 1.1: Figures showing difference between (A) PEM-DMFC and (B) AAEM-DMFC.

Catalyst is a crucial part in fuel cells to catalyze the anodic and cathodic reaction by lowering the activation energy of the reactions. Active catalyst enables fast and complete methanol oxidation reaction, reducing the chance for the methanol at anode to permeate through the membrane to the cathode. It is estimated that catalysts consume approximately 30-50 % of the fuel cell cost (Bag et al., 2015). The most commonly used catalyst, platinum (Pt), is high in cost, limited available, and easily poisoned by intermediate species, particularly carbon monoxide (CO), which can degrade the efficiency of fuel cells (Lee et al., 2006; Zheng et al., 2014). Alternative cheaper catalysts or combination of different metal catalysts have thus been explored. Palladium (Pd) stands out to be a promising alternative catalyst because of their abundancy (50 times more abundant on earth), cheaper price, similar catalytic performance, and resists better to poisoning of intermediate species (Martins et al., 2014; Wang et al., 2013; Zhang et al., 2014). Catalysts in nanometer scale have been in the spot light for its remarkable catalytic activity at this size range. At this small size (in a couple of nanometers), enormous fraction of the total number of atoms is at the surface, exposing

University of Malaya

for the reaction (Cao, 2004, p. 15). Nevertheless, catalyst nanoparticles (NPs) are thermodynamically unstable or metastable because of their high surface energy at nanosize. Thus, catalyst NPs tend to agglomerate together to reduce the surface energy, resulting in decreased electrochemically active surface area (ECSA) for the catalytic reaction (Cao, 2004, p. 24).

Graphene has been discovered as a potential catalyst support to avoid the agglomeration of catalyst NPs because of its exceptional electronic conductivity (7200 S/cm), chemical stability, and large specific surface area (theoretical value of 2630 m^2 g^{-1}) (Du et al., 2008; Kakaei & Zhiani, 2013; Lin et al., 2014; Martins et al., 2014; Peigney et al., 2001). The nanocatalysts affix on both sides of the graphene layer, greatly maximizing the availability of effective surface areas of catalyst. Nonetheless, graphene tends to restack because of the π-π interactions between adjacent sheets, greatly reducing the surface area for the deposition of the catalysts (Jinglin Zhang et al., 2014). Furthermore, the reactants and products will experience difficulty to reach to and leave from the catalysts that are loaded on graphene for the reaction and after the reaction, respectively. Focusing on the graphene supported/related catalysts, there are a few persisting challenges, such as (i) low catalytic performance which can be reflected by the low current density, (ii) large onset reaction overpotential, and (iii) poor stability (Wu et al., 2014). These limitations are direct consequences of (i) poor intrinsic electrocatalytic activity, (ii) limited electron conductivity, (iii) slow mass transfer of reactants and product molecules, and (iv) low electrocatalytic surface area (Wu et al., 2014). Enormous efforts have already been contributed to tackle these problems, such as alloying with other catalysts (for example, reduced graphene oxide (rGO) supported Pt-Pd alloy (PtPd/rGO), rGO supported Pd-silver (Ag) alloy (PdAg/rGO), and rGO supported Pt-cobalt (Co) alloy (PtCo/rGO)) (Kakaei & Dorraji, 2014; Ojani et al., 2014; Qianet al., 2015). Different structures of electrocatalysts (nanodendrites, core-shell,

University of Malaya

porous, etc.) have also been synthesized (Lv et al., 2014). However, synthesis of electrocatalysts of various structures usually requires the use of stabilizing agent, structure directing agent, and capping agents. These chemical agents might cover their active sites, negatively affecting their catalytic activity (Cai et al., 2014). Introduction of foreign compounds/macromolecules, such as carbon nanotubes (CNTs) and multi-walled carbon nanotubes (MWCNTs), have also been reported and obtained rather satisfactory results (Du et al., 2012; Jie Zhang et al., 2014). Nonetheless, expensive and complex set-ups are needed to synthesize CNTs and MWCNTs. Detailed review on the current efforts that have been dedicated will be reviewed in Chapter 2.

This work aims to develop rGO supported Pd (Pd/rGO) electrocatalysts that are reactive toward MOR via microwave-assisted reduction method. The work started with oxidation of graphite to graphite oxide by improved Hummer's method. The oxidation process enlarged the interlayer distance of graphene layers, weakening the interlayer binding van der Waals forces. The graphite oxides were then exfoliated by ultrasonication to mono- or few-layered graphene oxide (GO). The oxidation process functionalized the graphene layers by carbonyl (C=O) and carboxyl (–COOH) groups at the edges as well as epoxy (C–O) and hydroxyl (C–OH) groups on both sides of the surface. These oxygen-relating groups partially degrading sp^2 configuration to sp^3 carbon, destroying the π–π stacking stability, mechanical, and electrical properties of graphene. As a consequence, the GO behaves like an insulator. To be used as catalyst support, the GO need to be reduced to rGO, eliminating the oxygen-containing groups to recover the unique properties of graphene. Despite not fully recovered, rGO still largely retain the properties of pure graphene. Notably, this paper added Pd ions to the GO and simultaneously reduced by microwave irradiation for 700s at 700W. The obtained final sample is named as Pd/rGO. Microwave method is chosen because of its high energy efficiency, simple and convenient implementation, economical,

University of Malaya

controllable, and high focal volumetric heating. High focal volumetric heating not only accelerates the reduction process in short times, but also avoid thermal gradients and provides a uniform heating (Hu et al., 2007; Solano et al., 2012; Yan et al., 2010).

With these basic setups, optimum synthesis parameters were first defined, including (i) reduction duration and (ii) ratio of Pd to rGO. The optimum reduction duration and ratio were found to be 700 s and 1:1, respectively. On the basis of the discovery of the preliminary works, further advanced works were contributed in the perspective of catalysts and catalyst support (graphene). As mentioned, small catalyst size is favourable for exceptional electrooxidation of methanol. Fine NPs can be achieved by rapid nucleation and slow growth. In this aspect, two approaches were conducted, involving (i) manipulating the concentration of precursor mixture solution (palladium (II) chloride ($PdCl_2$) + GO) and (ii) modifying the conventional synthesis method. It has been claimed that nucleation and growth of catalyst nanoparticles can be influenced by the concentration of the metal precursor solution (Cao, 2004, p. 58). Instead of solely focusing on palladium, the entire mixture of GO and Pd ions should be considered as a whole and adjusted the concentration. Hence, at fixed optimized mass ratio of palladium to graphene and mixture volume, the effect of various precursor mixture concentrations to the MOR activity was investigated. Performance difference as high as 195 % was obtained by altering the mixture concentration. The sample with concentration 1.0 mg mL^{-1} gave the best performance but concentration 2.0 mg mL^{-1} was selected for the consecutive experiments because of the only slight poorer performance but the final amount of sample was twofold higher. During the conventional synthesis process, it was observed that the mixture solution gradually changed in colour. Such phenomenon can be attributed to the multi-stages reduction of the nanocomposite, and can adversely affect the size and distribution of the catalyst nanoparticles. In this regard, a modified method was suggested to remove the synthesis steps with multi-stages mild reduction,

University of Malaya

induce rapid nucleation, and incur high supersaturation which have been revealed advantageous for fine nanoparticles. The rapid nucleation was achieved by removing the steps involving multi-stages gradual reduction, adding in sodium carbonate (Na_2CO_3) that serves to adjust the pH of the mixture solution and acts as second reducing agent, and microwave-irradiating the reducing agents (ethylene glycol (EG) + Na_2CO_3) for 100 s to generate the highly active free radicals before the addition of precursor mixture. At the meantime, high supersaturation was realized by introducing room temperature precursor mixture. In the context of catalyst support, rGO weakly anchored the Pd NPs, leading to agglomeration of Pd NPs. The agglomeration diminished the active surface area for electrooxidation of methanol. As a solution to this issue, guanine, a nucleobases found in ribonucleic acid (RNA) and deoxyribonucleic acid (DNA), was added to Pd/rGO. Guanine adsorbed to rGO by π-π interaction, whereas its functional groups, such as amino, imino, and amide groups, act as anchoring sites of Pd ions as well as nanoparticles, and control their synthesis. Furthermore, the guanine itself was found reactive towards methanol oxidation, acting as second catalyst. The guanine functionalization was found effective to boost the electrochemical performance.

1.2 Problem Statement

DMFCs have been facing poor anodic methanol oxidation reaction, limiting its application. With this regard, active catalysts are essential. The active electrocatalysts catalyze the electrooxidation of methanol by lowering its activation energy. Palladium emerges as a potential catalyst because it possesses advantages in term of abundancy, price, and resistance to the poisoning intermediate species (Martins et al., 2014; Wang et al., 2013; Zhang et al., 2014). Active catalysts can be achieved by small particle size with uniform distribution. Nevertheless, agglomeration of catalyst NPs has been a daunting problem when the catalyst NPs are reduced to nanometer scale. At nanosize,

University of Malaya

the surface energy is high, making the NPs unstable and agglomerate together to reduce the surface energy (Cao, 2004, p. 24).

Loading catalyst NPs on graphene, either pristine graphene or reduced graphene oxide that is reduced from graphene oxide, has been found effective in suppressing the agglomeration. The catalyst NPs loaded on the graphene sheets also help to prevent the restacking of graphene sheets (Sharma et al., 2010). A great number of researches have been contributed to graphene-related/supported catalysts. Small catalyst NPs with uniform dispersion on the surface of graphene have been ventured by controlling the growth of the catalyst NPs via the addition of surfactants or capping agents, such as polyvinyl pyrrolidone (PVP) (Lv et al., 2014), polyvinyl alcohol (PVA) (Yunhe Su et al., 2014), and poly(diallyldimethylammonium chloride) (PDDA) (Yang et al., 2014). These surfactants or capping agents were reported to cause negative effect, covering the active sites of catalysts and difficult to be completely removed at the end of synthesis (Shengchun Yang et al., 2014). Theoretically, concentration of precursor can change the rate of nucleation and growth (Cao, 2004). High concentration favours rapid nucleation and growth. Nevertheless, fast particle growth is unintended as it results in large particle size. Thus, it is worth to consider the graphene and palladium as one whole object and alters the concentration of precursor mixture (GO + $PdCl_2$) to study its effect to the final electrochemical performance.

Synthesis method of graphene-related/supported catalyst NPs is also imperative in determining its catalytic performance. Microwave-assisted synthesis approach has gained immense attention because of its uniform and highly focused local heating (Hu et al., 2007; Solano et al., 2012; Yan et al., 2010). These advantages of microwave irradiation shorten the synthesis time by several orders of magnitude. Conventional microwave-assisted synthesis involves ultrasonication, followed by stirring, pH

University of Malaya

adjustment, and eventually microwave irradiation of precursor mixture (Sharma et al., 2010). During the ultrasonication or stirring stage, EG which serves as solvent and reducing agent was added. The ultrasonication and addition of EG changed the yellow-brown colour of the precursor mixture solution to dark brown. The mixture even turned black during the pH adjustment step. The colour change at different stages can be ascribed to the gradual reduction of some metal ions to metal NPs and GO to rGO. Such multi-stages gradual nucleation of both catalysts and GO led to agglomeration and big catalyst NPs with wide size distribution.

Despite the unique properties of pristine graphene, it does not interact well with the catalyst NPs. Most catalyst NPs are mainly observed at the graphene edge and less in the graphene plane (Ayán-Varela et al., 2017; Shen et al., 2014b). The non-uniform distribution resulted in low catalytic performance. On the contrary, more catalyst NPs can be observed on the rGO plane. The residual oxygen-containing functional groups and defective sites on the rGO plane that were created by reduction process serve as anchoring sites of catalyst NPs (Li et al., 2014). Nonetheless, rGO is inferior to pristine graphene and thus, the rGO supported/related catalyst NPs is not promising. In fact, despite the better distribution of rGO supported/related catalyst NPs, there is still room for improvement. Uniform dispersed catalyst NPs on the surface graphene sheets, either rGO or pristine graphene, were successfully obtained by functionalizing the graphene sheets with various reagents including branched poly(ethylenimine) (BPEI) (Lv et al., 2013), 1-pyrenamine (Li et al., 2013), polydopamine (PDA) (Ye et al., 2014), PDDA (Fan et al., 2015; Zhang et al., 2015), polybenzimidazole (PBI) (Xin et al., 2016), and flavin mononucleotide (FMN) (Ayán-Varela et al., 2017). Some dispersing or capping agents, such as oleylamine (OAm) (Sudong Yang et al., 2014), PVP (Lv et al., 2014; Martins et al., 2014), 1-hexadecyl-2,3-dimethylimidazolium bromide ([C_{16}MMIm]Br) (Lv et al., 2014), and trioctylphosphine (TOP) (Sudong Yang et al., 2014), were also

University of Malaya

investigated. In spite of the positive results, these reagents and agents are not without drawbacks, such as harmful, toxic, expensive or involve complex processing. It is therefore necessary to introduce new environmental friendly low cost reagents to the graphene supported/related catalyst NPs.

1.3 Research Objectives

This research focuses on synthesizing Pd/rGOs that are active toward MOR via microwave-assisted reduction method. The performance of Pd/rGO were investigated by altering the concentration of precursor mixture, modifying the synthesis process, and introduction of guanine. The main objectives are:

i) To investigate the effect of concentration of precursor mixture (GO + $PdCl_2$) towards the catalytic performance.
ii) To induce rapid nucleation by modifying the conventional synthesis method.
iii) To enhance the catalytic activity through the addition of low cost and environmental friendly guanine.

1.4 Scope of Research

The research can be divided into three parts. The first part was the preliminary study to ensure the Pd/rGO can be successfully obtained via the microwave-assisted synthesis method. At the stage, optimum microwave-assisted reduction duration and ratio of rGO to Pd were determined.

The second part was to further improve the optimized Pd/rGO from the prospect of Pd catalysts via the control of rate of nucleation and growth of Pd NPs. The rate of

University of Malaya

nucleation and subsequent growth of Pd NPs were manipulated through (i) altering the concentration of the precursor mixture (GO + $PdCl_2$) and (ii) modifying the synthesis process to induce rapid nucleation.

The final part covered improvement conducted from the direction of catalyst support (rGO). Guanine, a nucleobases found in RNA and DNA, was added to Pd/rGO. The guanine adsorbed to rGO via π–π interaction. The functional groups of guanine, such as amino, imino, and amide groups, act as anchoring sites of Pd ions and NPs and control their synthesis. Notably, the guanine itself also played the role as second catalyst.

On the whole, the main goal of this research is to enhance the catalytic activity of Pd/rGO towards MOR.

1.5 Structure of the Thesis

Chapter 2 provides an incisive overview on the recent literatures of graphene-related/supported electrocatalysts. Owing to the fact that the works conducted by scientists and researchers were specifically focusing on either catalyst NPs or graphene (catalyst support), the literatures will be reviewed in these two perspectives. In term of the catalyst NPs, it will be further discussed in graphene-related/supported precious metal, graphene-related/supported non-precious metal, and metal free catalysts. As to the catalyst support, various approaches in enhancing the capability of graphene to be a promising catalyst support will be presented.

In Chapter 3, the chemicals used throughout the experiment and their respective sources are given. The synthesis procedures are divided into two parts comprising synthesis of GO and preparation of Pd/rGO electrocatalysts. Various characterizations and electrochemical measurements are also illustrated in this chapter.

University of Malaya

Results and discussions are available in Chapter 4. Thorough explanation, theoretical formulas, mathematical calculations, and discussion on the results obtained from the characterizations as well as electrochemical measurements are presented. The chapter begins with the determination of optimum reduction duration and ratio of rGO to Pd. Based on the optimized parameters, further investigation is focused on the effect of concentration of precursor mixtures (GO + $PdCl_2$) to the final electrochemical performance of the samples. A modified synthesis method is also explored. Its feasibility is tested and supported by various characterizations and electrochemical testings. Finally, guanine, which is a nucleobase of DNA and RNA, is introduced to the Pd/rGO nanocomposite to boost the electrooxidation of methanol. Comparative study on the samples with and without guanine is also carried out.

Chapter 5 concludes the entire work based on the findings obtained. Future work plans are provided in Chapter 6. The experimental details and research publications are available in appendices.

In summary, the focus of this research is to improve Pd/rGO electrocatalysts from two perspectives: the catalyst and graphene that plays the role as catalyst support. In the aspect of catalysts, the catalytic performance is highly depending on the particle size and distribution of catalyst. Two approaches were taken, including (i) manipulating the concentration of precursor mixture solution (palladium (II) chloride ($PdCl_2$) + GO) and (ii) modifying the conventional synthesis method. In the context of graphene (catalyst support), guanine was proposed to be coordinated to the surface of graphene. The guanine serves as interlinker to improve the interaction between Pd NPs and graphene, restraining the undesired agglomeration of Pd NPs. The synthesized electrocatalysts are eventually to be applied in AAEM-DMFC.

University of Malaya

CHAPTER 2: LITERATURE REVIEW

2.1 Introduction

Since the first major oil well was drilled in 1859, fossil fuels have been widely used and now provide approximately 80% of energy in the world (Ania et al., 2015; Levitan et al., 2014; Salvi et al., 2013). The extensive consumption of non-renewable fossil fuels has resulted in the scarcity of reserves, pollution, and global warming to an alarming level. Being aware of these impending dangers as reflected by climate change, iceberg melt and collapse, and other natural disasters, scientists have been vigorously searching for alternative renewable energy sources. In this context, fuel cells have shown considerable potential because of its high energy conversion efficiency (i.e., 36% to 39%), little or no pollutant emission, good fuel availability, and suitability for stationary and transportation applications (Lee et al., 2006). The fuel cell, an energy-conversion device, comprises three main compartments, namely, cathode, anode, and separation membrane sandwiched between both electrodes (Choi et al., 2012). The fuel cell directly converts chemical energy into electrical energy via fuel oxidation at the anode and oxygen reduction at the cathode. In fact, fuel cell technology is not sufficiently mature yet. The commercialization of fuel cells still has many obstacles. This review focuses on the technical problems at the electrodes, that is, slow reaction rate. The slow reaction rate results in low current and power.

The reaction rate at both electrodes has a close relationship with the catalysts used. Catalysts account for a large part of the fuel cell cost. Standalone catalyst NPs tend to agglomerate, significantly reducing the surface area for the reactions at electrodes. Thus, immense attention has been focused on the catalysts to improve the catalytic activity and reduce the cost, including (i) alloying of metal catalysts, (ii) reducing the size of catalysts, (iii) manipulating the morphology and shape of electrocatalysts, (iv)

University of Malaya

doping the metal catalysts with nonmetal elements, and (v) loading the catalysts onto catalyst supports.

Loading catalysts onto catalyst supports is the main concern of this review. Loading catalysts onto catalyst supports has been reported to be able to suppress the agglomeration of catalysts effectively, maximize the available surface area of nanocatalysts, and enhance the mass transport of reactants to and from the catalysts. The most frequently investigated supports comprise carbon black (CB) Vulcan XC-72, carbon nanotubes, and carbon nanofibers. Although carbon nanotubes are better than the previously mentioned carbon supports, its application is limited by its high cost. Since the first isolation of single-layer graphene sheets from graphite by Novoselov et al. (2004) using the micro-mechanical stripping method, it has attracted immense attention from scientific communities. The unique properties of graphene, such as high surface area, good electrical conductivity, low manufacturing cost, ease of functionalization, strong affinity toward the nanocatalysts, and strong chemical stability, make it an appealing alternative catalyst support to improve the catalytic activity, stability, and durability of electrocatalysts in fuel cells. Graphene endued with a two-dimensional (2D) layered structure effectively utilizes both surfaces to immobilize the catalysts. The thickness of the 2D layered structure, that is, one atom thick, enables every atom in graphene to be the surface atom. Thus the electrons that are transferred through graphene are sensitive to the adsorbed molecules/catalysts.

A considerable number of studies have been focusing on graphene-supported/related electrocatalysts to improve the electrochemical performance. This review provides an incisive overview of recent works in the direction of catalysts and catalyst support (graphene). Throughout the review, several distinctive synthesis methods will be

University of Malaya

presented in the respective sections. Finally, future challenges and perspectives will be briefly discussed.

2.2 Catalysts

The catalyst is an essential part of fuel cells, which has been estimated to cost approximately 30% to 50% of the fuel cell cost (Bag et al., 2015). Catalysts lower the activation energy, making the reactions at the anode and cathode easier and faster. However, during the fuel cell operation, the electric field can induce damage to the structure of catalyst NPs because of (i) metallic dissolution, (ii) oxidation of NPs with subsequent redeposition onto larger NPs (Ostwald ripening), (iii) coalescence due to the migration and collision of NPs with the surface of the support, (iv) detachment of NPs due to carbon corrosion, and (v) superficial reorganization of NPs. This section reviews recent works on graphene-based electrocatalysts where the contribution is solely focused on catalysts. The electrocatalysts are divided into three categories, namely, precious metal, non-precious metal (NPM), and metal-free (Martins et al., 2014).

2.2.1 Precious Metal Electrocatalysts

Precious metals, such as Pt, Pd, gold (Au), Ag, osmium, iridium, ruthenium (Ru), and rhodium (Rh), are favorable for their remarkable reactivity and pure four-electron pathway toward ORR at cathode. Nevertheless, the long-term stabilities and contaminant tolerances of these precious metals are beyond fixable, significantly limiting their practical use (Sun et al., 2014). Pt-based electrocatalysts are currently used in commercial applications, for example, Pt/Co alloy is the catalyst used in Toyota Mirai because of its high work function capability with a wide range of fuels (Singh & Sharma, 2012; Tan et al., 2017). Nonetheless, Pt NPs face serious limitations, such as high cost, limited reserves, and easy deactivation from the surface adsorption of

University of Malaya

poisonous intermediates or reaction products (Li et al., 2016). The carbonaceous intermediate species cover the surface-active sites by chemical adsorption and gradually decrease their catalytic activity, resulting in sluggish kinetics (Jiang et al., 2014; Lu et al., 2013). Pt catalyzes the corrosion of the carbon support to carbon dioxide (CO_2) at potentials as low as 0.55 V vs. the reversible hydrogen electrode (Tiido et al., 2013).

Pd-based catalysts emerge as a suitable substitute for Pt because of (i) its intrinsic capability comparable or even superior to Pt in alkaline solution because of the similar valence shell electronic configuration and lattice constant (same atomic size and group in the Periodic Table and crystal structure) (Antolini, 2009b; Singh & Sharma, 2012), (ii) it is 200 times more abundant than Pt on earth (Carrera-Cerritos et al., 2014), (iii) it has better resistance to the poisoning effect of intermediate species, and (iv) it is 5 times cheaper than Pt (Ksar et al., 2009; Pinithchaisakula et al., 2017; Yang et al., 2015). According to Seo et al. (2015), Pd catalyst is even more thermodynamically stable than other transition metals, for example, nickel (Ni), copper (Cu), iron (Fe), manganese (Mn), tin (Sn), and Co. Pd is capable of fully reducing oxygen into water with low overpotential and producing hydrogen peroxide (H_2O_2) or peroxy-radicals (Carrera-Cerritos et al., 2014). Pd catalysts outperform Pt catalysts in terms of alcohol oxidation and formic acid oxidation at anode for direct alcohol fuel cell and direct formic acid fuel cell, respectively (Xie et al., 2017). The low 3*d* electron density of Pd makes the adsorption strength of the formate intermediate weak, such that the surface coverage is reduced, benefiting the direct formic acid electrooxidation (Xie et al., 2017). Meanwhile, upon ethanol oxidation at anode of direct ethanol fuel cells, the activity of Pt is higher than that of Pd, resulting in faster production of acetaldehyde and correspondingly faster deactivation. Despite the fact that acetaldehyde can be oxidized to acetate, the rate of acetaldehyde production on Pt might be faster than the rate of subsequent acetaldehyde oxidation, such that aldol condensation would proceed with a

University of Malaya

strong poisoning effect. By contrast, the modestly active Pd achieves more balance between the formation of acetaldehyde and the subsequent oxidation to acetate. Thus, the poisoning effect on Pd is less severe. However, the reasons for the commercial use of Pt instead of Pd can be attributed to the drawbacks of Pd, that is, (i) it is inactive in acidic medium (Kakaei & Dorraji, 2014) and (ii) it is electrochemically unstable at high potentials, such as those occurring in proton exchange membrane fuel cells (PEMFCs) under open circuit voltage and starvation conditions (Carrera-Cerritos et al., 2014).

Compared with Pt and Pd, Ag is more abundant and 1/60th of the price of Pt (Soo et al., 2016). Ag exhibits oxophilic properties, facilitating the formation of $Ag(OH)_{ads}$, thereby promoting the removal of the adsorbed intermediate species at lower potential, exposing the active sites of catalysts, and contributing to better tolerance toward poisoning intermediate species (Xu et al., 2016).

In spite of the fact that different catalysts exhibit different intrinsic properties, and thus different electrochemical performances, the catalytic activities of all catalysts are highly dependent on its (i) morphology, (ii) shape, (iii) size, (iv) particle distribution, and (v) electronic interactions (Pinithchaisakula et al., 2017). Alloying with foreign metal and doping with non-metal elements have also been investigated to enhance the catalytic activity further. Recently conducted efforts will be reviewed in the subsequent subsections.

2.2.1.1 Morphology, size and shape control

The shape of the catalysts defines its electronic structure and crystalline surface. The electronic structure and crystalline surface were reported to have influence to the catalytic properties of catalysts (Na et al., 2015; N. Tian et al., 2007; Zhou et al., 2010). This phenomenon can be well exemplified by an order of magnitude of increase in electrocatalytic activity by controlling the crystal facets of Pt (Tian et al., 2007; Wu et

University of Malaya

al., 2012; Zhou et al., 2010). Owing to the high density of edges, atomic steps, kinks, and dangling bonds, the high-index facets of face-centered cubic (fcc) metals are usually more catalytically active than the common basal facets, such as [111], [100], and [110] (Gong et al., 2015). However, of those catalysts with common basal facets, Carrera-Cerritos et al. (2014) reported that Pd(100) is more active than Pd(110) and Pd(111). More specifically, the activity of Pd(100) is 14 and 3 times larger than that of Pd(111) and Pt(111), respectively. Furthermore, the structure and composition, such as the interatomic distance, number of neighboring metal atoms, band vacancy, and metal content on the surface, can influence the catalytic activity (Kowal et al., 2009; Mazumder et al., 2010).

Various chemical protocols have been explored to achieve partial control of the nanostructures. Generally, the nanostructures can be categorized into zero-dimensional (0D; e.g., spherical NPs), one-dimensional (1D; e.g., nanowires (NWs) and nanotubes), 2D (e.g., nanosheets (NSs)), and three-dimensional (3D; e.g., nanodendrites (NDs), nanoflowers, and multipod) (Du, Lu et al., 2014; Na et al., 2015; Ye et al., 2014).

Sudong Yang et al. (2014) combined OAm and TOP to obtain monodisperse 0D Pd NPs on the surface of rGO. When either of OAm or TOP was used alone, controlling the size and shape of Pd NPs became difficult (Sudong Yang et al., 2014). TOP is a surfactant, which is capped on the surface of metal particles without stopping the growth of particles (Sudong Yang et al., 2014). This finding explains the formation of large and agglomerated particles when TOP is used alone. However, a good size distribution can be obtained at an appropriate amount of TOP. Excessive TOP creates a large steric hindrance, resulting in a random size distribution. Meanwhile, OAm acts as surfactant and middle reducing agent. OAm is imperative in stabilizing colloidal NPs. When added in excess, the strong binding of OAm caused the polydispersion and

University of Malaya

agglomeration of NPs. Therefore, less Pd is exposed for nucleation. Another capping agent and structure director, that is, 5-Aminoorotic acid (AOA), was used by Ju et al. (2016). The functional groups of AOA, such as amino, imino, and carboxyl groups, strongly adsorb onto the metal ions, controlling the morphology of nanomaterials. Upon the formation of the nuclei, AOA preferentially adsorb onto the specific crystal planes and direct the growth of catalysts. Figure 2.1 elucidates that the crystallites agglomerate together to form the nanostructure driven by van der Waals forces and hydrogen bonding. The catalytic activity of the obtained electrocatalysts for the EG oxidation reaction (EGOR) is recorded in Table 2.1.

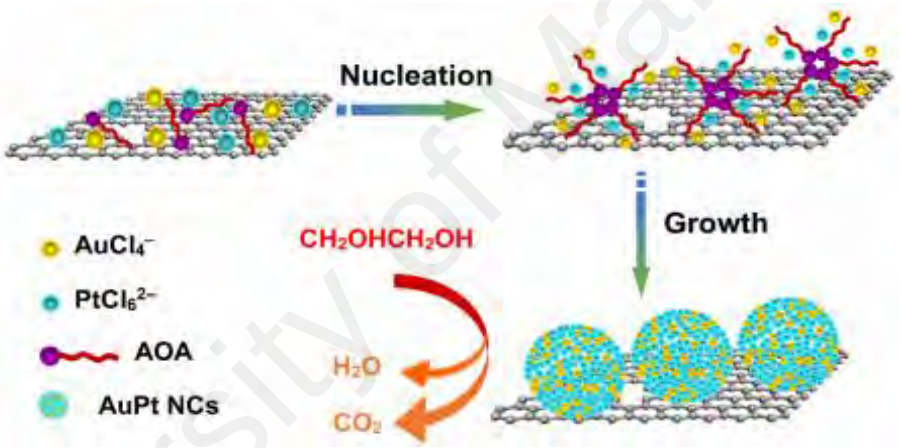

Figure 2.1: Formation mechanism of AuPt nanocrystals (NCs)/RGO and electrocatalytic mechanism of EG.

(Ju et al., 2016)

Du et al. (2014) claimed that the morphology of catalysts changes with the reaction duration. By using the wet chemical approach, their team collected samples after 2 and 5 h of reaction. Spherical NPs were obtained at 2 h, whereas short NWs with the mean length of 10 nm were obtained at 5 h. Beyond 5 h, the length of the NW further increased up to 20–200 nm. Notably, the rate of reduction is another influencing factor. A rapid reduction process would cause agglomeration (Sun et al., 2017). Reddy et al. (2017) reported that reducing agents also have a distinct effect on the size, structure, and morphology of catalysts as well as its distribution density on the surface of catalyst

University of Malaya

supports (Wang et al., 2014). For instance, solid spherical NPs and irregular porous nanospheres with a broad size distribution were obtained using sodium borohydride ($NaBH_4$) and ascorbic acid (AA), respectively (Lv et al., 2014). The significant difference in morphology can be ascribed to the different reaction kinetics of the reducing agents. AA, a weak reducing agent, has a slow nucleation rate, thus resulting in selective growth of a large porous nanostructure. By contrast, strong reductants, such as $NaBH_4$, induce the rapid nucleation and growth of the nuclei into nanospheres to minimize the surface energy. Sudong Yang et al. (2014) demonstrated that the precursors of catalysts can also dominate the growth of Pd. Pd NPs on rGO surface with different morphologies were prepared from three Pd precursors, namely, palladium acetylacetonate ($Pd(acac)_2$), palladium acetate ($Pd(C_2H_3O_2)_2$), and sodium tetrachloropalladate (Na_2PdCl_4). According to their study, $Pd(acac)_2$ yielded the best quality of Pd NPs. By contrast, the two other precursors formed large NPs and nanopod-like Pd clusters. Such an observation can be attributed to the different reaction kinetics of the precursors.

NWs or nanorods (NRs), as 1D nanostructure, have been exhibiting high catalytic activity for various catalysis applications as a result of their anisotropic structure and unique surface properties (Jeena et al., 2016; Koenigsmann & Wong, 2011; Sun et al., 2011). Du et al. (2014) reported a breakthrough synthesis of PtPd NW arrays supported on rGO as shown in Figure 2.2. Utilizing the small lattice mismatch (only 0.77 %) between Pt and Pd, the Pd NPs were first loaded onto rGO as seeds. Upon the chemical reduction of chloroplatinic acid (H_2PtCl_6), Pt NWs projected outward from the Pd seeds on the support surface at random orientations.

University of Malaya

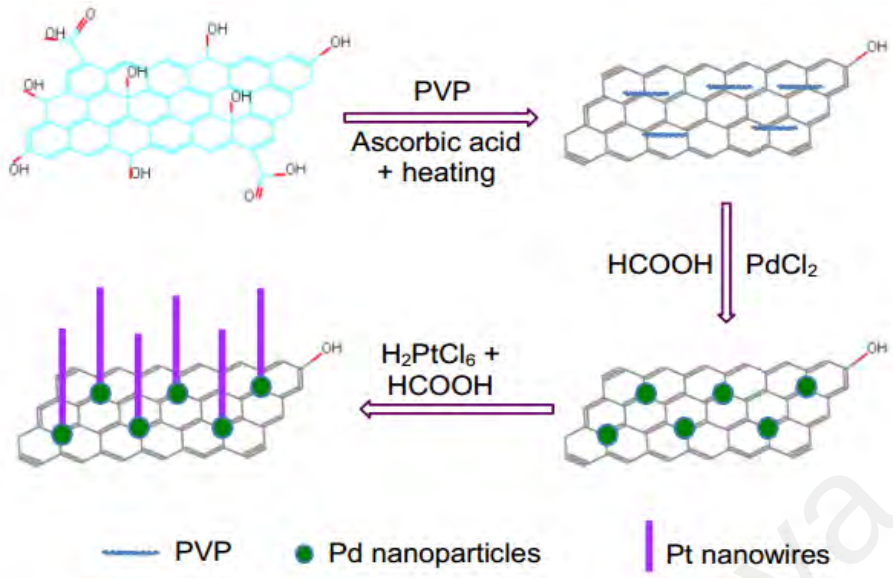

Figure 2.2: Procedure to grow PtPd nanowire arrays on the reduced graphene oxide nanosheets.

(Du et al., 2014)

Shengchun Yang et al. (2014) grew 2D single-crystal Pt nanosheets on rGO in a potassium nitrate-lithium nitrate (KNO_3-$LiNO_3$) eutectic mixture molten salt medium. The molten salt system is highly stable as well as recyclable and has a low vapor pressure under ambient pressure. Shengchun Yang et al. (2014) proposed two conditions to obtain sheet-like structure, that is, (i) Pt NPs need to be constructed to direct the subsequent agglomeration and sintering of the isolated NPs into nanosheets and (ii) GO needs to be used as template because the oxygen-containing functional groups on the GO surface are crucial for the formation of nanosheets. Similar synthesis was conducted using pre-reduced GO instead, but failed to obtain a sheet-like structure. The mass ratio between catalyst precursor and GO plays a significant role in tailoring the size of nanosheets. A high ratio of catalyst precursor leads to a high loading of NPs onto the surface of rGO (Wang et al., 2014; Shengchun Yang et al., 2014). During the synthesis process, NPs grow in the anisotropic direction into nanosheets until all of the NPs are exhausted.

University of Malaya

Owing to the fact that catalytic reactions occur at the surface atoms of NPs, a large fraction of metal in the core of the NP was wasted. As a consequence, several researchers proposed to replace the core with less expensive transition metals (e.g., Cu, Fe, Ni, Co, etc.) (Zhang et al., 2015). The subsurface metals change the interatomic distance of the surface metal catalysts, modifying the electronic interaction, and thus, changing the binding enthalpies. This phenomenon influences the binding of adsorbates to the particle surface, enhancing the rate and selectivity in the catalytic process (Stamenkovic et al., 2007). Synthesis can be conducted by the (Jeena et al., 2016) (i) simultaneous co-reduction of two different metal catalyst precursors, (ii) sequential reduction of one metal over the seed of another metal, and (iii) electroless galvanic replacement method. The last method has gained high popularity as it is simple and efficient. Utilizing the difference in standard reduction potentials between the metals, a thin shell layer of any precious metal catalyst can be formed from a low proportion of precursors by replacing the base metal. Notably, the galvanic replacement time needs to be properly controlled: A long replacement duration increases the amount of the precious metal shell, thus resulting in better reactivity; by contrast, a prolonged duration significantly reduces the real surface area of precious metals (Ojani et al., 2014). Realizing the promising performance of such core–shell structure, several researchers further explored its benefits via the use of alloy core (Aristatil et al., 2015; Na et al., 2015). Jeena et al. (2016) proposed another exceptional Ag-core@Pt-shell NRs on L-tryptophan-functionalized electrochemically reduced graphene oxide (ERGO), as illustrated in Figure 2.3. This brilliant work combined the advantages of 1D and core–shell structures.

University of Malaya

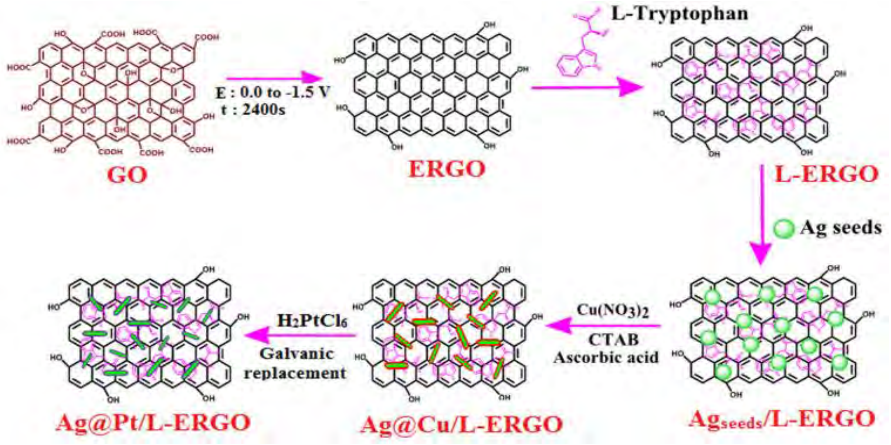

Figure 2.3: Stepwise growth of Ag seed into bimetallic Ag@Pt NRs on L-ERGO nanosheets.

(Jeena et al., 2016)

Dutta et al. (2016) brought the research on 1D and core–shell structures into an entirely new level by fabricating rGO-supported dog-bone-shaped Au NR_{core}-$Pt_{sandwich}$-Pd_{shell} trimetallic NPs via stepwise addition of Pt and Pd sources into the pre-prepared Au NRs. When the sequence of addition of catalyst precursors was changed, that is, injection of $PdCl_4^{2-}$ followed by $PtCl_6^{2-}$, a spongy Au NRs/Pd/Pt core–shell structure was obtained. Despite the spongy nature providing better electrocatalytic activity, the Pt shell easily agglomerated and detached, resulting in poor durability. The discrepancy in morphology can be attributed to the high surface and cohesive forces of Pt, which result in the formation of small isolated Pt NPs at the periphery of the underlying Pd NPs, yielding a roughened outer appearance. In fact, obtaining a homogeneous, unique, and compositionally uniform trimetallic rGO composite is a rather challenging task. The electrostatic attraction plays an essential role in this case and can be managed by different capping agents. Dutta et al. (2016) compared two different capping agents, that is, cetyltrimethylammonium bromide (CTAB) and citrate. Citrate ions are negatively charged. Upon capping of the seed, the seed becomes negatively charged, which generates repulsive force to the precursors of the same nature (either anionic or negatively functionalized) and does not allow surface-mediated smooth growth

University of Malaya

(inhomogeneous NPs). In the meantime, the cetyltrimethyl-ammonium groups of CTAB render the capped seed positively charged, electrostatically attracting the negatively charged precursor ions and allowing its effective decoration on GO with negative functionalities. The special dog-bone shape was in fact driven by the structure-directing agent, CTAB. The bromide and Ag ions block the side facets of the NRs. Thus, the fresh precursor ions preferentially deposit on the end facets with high surface energy and form the unique dog-bone-shaped morphology.

The 3D structured materials have attracted considerable interest in various applications because of its unique properties, including multiphase heterogeneous interfaces, abundant inner voids (porous structure), controllable physical and chemical microenvironment, and branched morphology (Ghosh et al., 2017). These materials also have a high surface area because of its abundant reactive edges, corners, and stepped atoms on their branches, which highly expose the atoms for the reaction, thus fully utilizing their inherent potential and maximizing their catalytic performance (Sahu et al., 2013). Different porous size ranges play different roles to benefit the surface reaction: micropore (< 2nm) holds active sites, mesopore (2–50 nm) is responsible for mass transportation and active surface, and macropore (> 50 nm) behaves just like macroscopic surface (Wang et al., 2017). With the understanding of the effect of reducing agents, as mentioned previously, Lv et al. (2014) synthesized 3D nanoflowers via the combination of structure-directing agent and reductant with appropriate reducing power (sodium nitrite ($NaNO_2$) + PVP). Lv et al. (2014) verified that such a unique structure can hardly be achieved during the (i) absence of $NaNO_2$ and PVP, (ii) insufficient $NaNO_2$ and PVP, and (iii) excess $NaNO_2$. In most cases, surfactants, organic solvents, or capping agents, for instance, liposome, CTAB/cetyltrimethylammonium chloride (CTAC), PVP, oleylamine/oleic acid, Pluronic 123, hexadecylpyridinum chloride, and etc., are applied to stabilize the facets

University of Malaya

of the NPs or induce their anisotropic growth of 3D nanostructures (Lim et al., 2009; Ruan et al., 2013; Wu et al., 2010; Shengchun Yang et al., 2014). Ample research has indicated their importance to obtain high-quality catalysts of different shapes, morphologies, and narrow size ranges. Nonetheless, adverse opinion has been expressed, claiming that the absence of surfactant or capping agent enables the large scale production of NPs with a tailored morphology (Gopalsamy et al., 2017). When the stabilizers and ligands are added, the catalysts will interact with the ligands, possibly inducing irreversible passivation, which may affect its electrochemical performance (Tan et al., 2017). Furthermore, the capping agents, surfactants, and organic solvents will inevitably result in detrimental effects on the environment and health as well as difficulty in completely removing from the final products, which may, as a consequence, prevent the reactants from adsorbing onto the active sites during the catalytic reactions (Shengchun Yang et al., 2014). An easy, green, rapid, and template-free seed-mediated growth method without any surfactant or halide ions (particularly bromide ion (Br^-) and iodide ion (I^-)) was investigated to achieve nanodendrite-structured metal catalysts on graphene, as shown in Figure 2.4, to overcome all of these drawbacks (Cai et al., 2014). With the first-formed Pd as seed, the subsequent rapid reduction of Pt contributed to dendritic growth. The amount of Pd needs to be properly controlled because increased content is unfavorable for dendritic growth. Dealloying was another technique for the rapid and direct generation of nanoporous metals (Yang et al., 2015). During the dealloying process, one of the superficial metal atoms in the alloyed particles is eliminated, leaving the surface rich in other catalytically active metal atoms to benefit their electrocatalytic performance. A notable biosynthesis method was developed by Liu et al. (2016) to obtain the 3D porous heteroatom-doped bio-PdAu/rGO (DPARH) electrocatalyst. Their research team claimed that the amount of GO added plays a vital role: A small amount of GO makes it difficult to build the 3D

University of Malaya

porous structure, whereas an excessive amount of GO would enclose the metal catalysts, preventing the interaction between the small organic molecules and the PdAu active site.

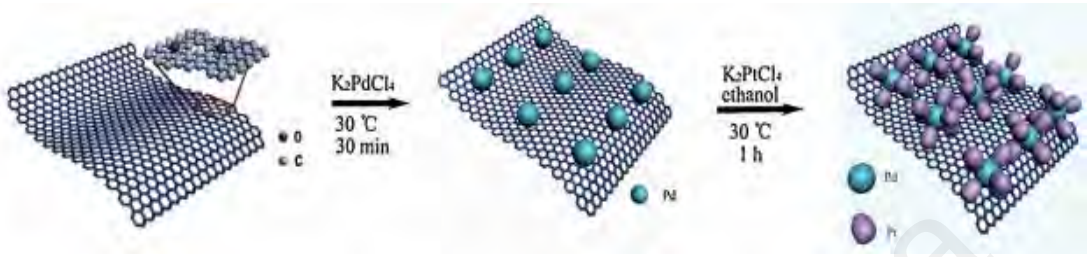

Figure 2.4: Synthesis procedure for RGO-supported Pt-on-Pd nanodendrites.

(Cai et al., 2014)

Small and uniform size electrocatalysts are highly desirable. Ultrafine size, particularly at the atomic level, corresponds to an increased specific surface area (SSA) per mass and a large number of corner and edge atoms (Hayden, 2013; Shen et al., 2014b). Nevertheless, ultrafine particles tend to grow into large particles to reduce the surface energy. Generally, the NPs grow by two mechanisms, that is, (i) dissolution and redeposition (Ostwald ripening) and (ii) migration and coalescence. Despite the drawbacks, various stabilizers as mentioned previously have been commonly used to suppress the NPs from agglomerating together (Yuan et al., 2014). Yang et al. (2011) proposed an effective separated step chemical reduction method to tailor the size and dispersion of catalyst NPs supported on graphene without any stabilizers. The reducing agent was initially partially added to reduce the catalyst ions to NPs, but was insufficient to reduce GO fully. The oxygen-containing groups anchor and stabilize the catalyst NPs. In the second step, the remaining reducing agent was added to reduce the previous incompletely reduced GO fully. Compared with the electrocatalysts obtained by synchronous chemical reduction, such a new mechanism managed to obtain a small size (3 vs. 10 nm) with better dispersion. Table 2.1 demonstrates the catalytic performance of precious metals of different morphologies.

University of Malaya

Table 2.1: Electrochemical performances of precious metals of different morphologies.

Electrocatalysts	Electrode Reaction	Electrolyte	Peak Current Density	ECSA ($m^2 g^{-1}$)	Stability	References
Branched Pt-rGO	MOR	0.50 M H_2SO_4 + 0.25 M CH_3OH	178.10 μA cm^{-2}	-	-	(Sahu et al., 2013)
Pt NSs/ rGO	MOR	0.50 M H_2SO_4 + 0.5 M CH_3OH	0.73 mA cm^{-2}	-	-	(Shengchun Yang et al., 2014)
PtPd NW/rGO	MOR	0.10 M $HclO_4$ + 1.00 M CH_3OH	0.51 A mg^{-1}	19.07	Degraded 17.20% after 1000 potential sweep cycles.	(Du et al., 2014)
RGO-supported Pt-on-Pd NDs	MOR	0.50 M H_2SO_4 + 1.00 M CH_3OH	1.61 mA cm^{-2}	-	-	(Cai et al., 2014)
Co_{core}-Pt_{shell} NPs/PDDA-graphene	MOR	0.50 M H_2SO_4 + 1.00 M CH_3OH	49.30 mA cm^{-2}	105.60	-	(Zhang et al., 2015)
Ag@Pt NRs/ L-ERGO	MOR; Ethanol Oxidation Reaction (EOR)	0.50 M NaOH + 0.50 M CH_3OH/ C_2H_5OH	MOR: 145.00 mA mg^{-1} & 1.48 mA cm^{-2}; EOR: 190.00 mA mg^{-1}; 2.00 mA cm^{-2}	53.50	-	(Jeena et al., 2016)
Dog-bone shaped Au NR_{core}-Pt/Pd_{shell} decorated on rGO	EOR	1.00 M KOH + 1.00 M C_2H_5OH	2.58 mA cm^{-2}; 3120.25 mA mg^{-1}	121.40	Retained 86.30% after 1000 accelerated cycles.	(Dutta et al., 2016)
AuPt NCs/RGO	EGOR	1.00 M KOH + 0.50 M EG	1763.50 A g^{-1}; 51.03 A m^{-2}	34.60	Retained 16.70% after 1,000 s	(Ju et al., 2016)
Pd Nanobar/rGO	ORR	O_2-saturated 0.50 M H_2SO_4	~ 1.85 mA cm^{-2}	-	-	(Carrera-Cerritos et al., 2014)
Pt-Pd nanoflowers/ rGO	ORR	O_2-saturated 0.50 M H_2SO_4	35.30 mA mg^{-1}	15.80	Retained 67% after 500 cycles	(Lv et al., 2014)

University of Malaya

2.2.1.2 Alloying

Single metal catalysts may not be sufficiently effective to completely oxidize or reduce the reactant fuels to final products, particularly cleavage of C–C bonds during the oxidation of ethanol to CO_2 for direct ethanol fuel cells (Shen et al., 2014a). Alloying is recognized as an effective method to reduce the dosage of expensive metal, particularly precious metal, to reduce the cost and enhance the performance of electrocatalytic activity (Lv et al., 2016). Upon alloying with foreign metals, the mobility of catalyst NPs can be hindered, restricting them from agglomerating together (Zhao et al., 2016). The improved performance can be attributed to the (i) bifunctional effects, (ii) ligand effects (also called intrinsic or electronic effects), and/or (iii) strain effects (Reddy et al., 2017; Sharma et al., 2010).

Through the bifunctional mechanism model, the second metal dissociates the water to generate the adsorbed OH species at a low potential as demonstrated by Equation 1 and 2. The adsorbed OH species expedites the oxidation of the poisoning intermediate species (CO) adsorbed onto the metal catalysts, reexposing the covered active sites of the catalysts (Sun et al., 2017; Xu et al., 2016; Zhao et al., 2014).

$$Ru^0 + H_2O \rightarrow Ru\text{-}OH + e^- + H^+, \quad (1)$$

$$Pt\text{-}CO + Ru\text{-}OH \rightarrow CO_2 + e^- + H^+ + Pt^0 + Ru^0. \quad (2)$$

In the meantime, through the ligand mechanism, the difference in ionization energies (Ni = 7.63 eV; Pt = 9.02 eV; Au = 9.22 eV) causes intra-atomic or interatomic charge transfer between metal catalysts, as depicted in Figure 2.5 (Dutta & Ouyang, 2015; Liu et al., 2016). Such a charge transfer reconstructs the electronic structure of neighboring metal atoms, shifting the d-band center (ε_d). Apart from that, the d-band center can also be affected by the changes in the catalyst surface bond energy and the type of reactants

University of Malaya

adsorbed onto the surface (Seo et al., 2015). A high ε_d signifies strong interactions with adsorbates, promoting the O–O bond breaking, but unfavorable for the formation of OH bond. Therefore, the elimination of poisoning intermediate species is difficult. Conversely, a low ε_d has a large vacancy of the d-band, indicating weakened binding of intermediate species through the formation of the OH bond (Chen et al., 2014; Feng et al., 2014; Seo et al., 2015). The electron transfer among the metals enhances the surface tension toward the catalytic reactions (Dutta & Ouyang, 2015). From Figure 2.5, the electrons are transferred from Ni and Pt atoms to Au atoms, reducing the *d* state of Au near the Fermi level (Shen et al., 2014a). Such negatively charged Au promotes the adsorption of oxygen, facilitating the complete reaction of reactants (such as oxidation of ethanol) and prohibiting the accumulation of intermediate species on the catalyst surface.

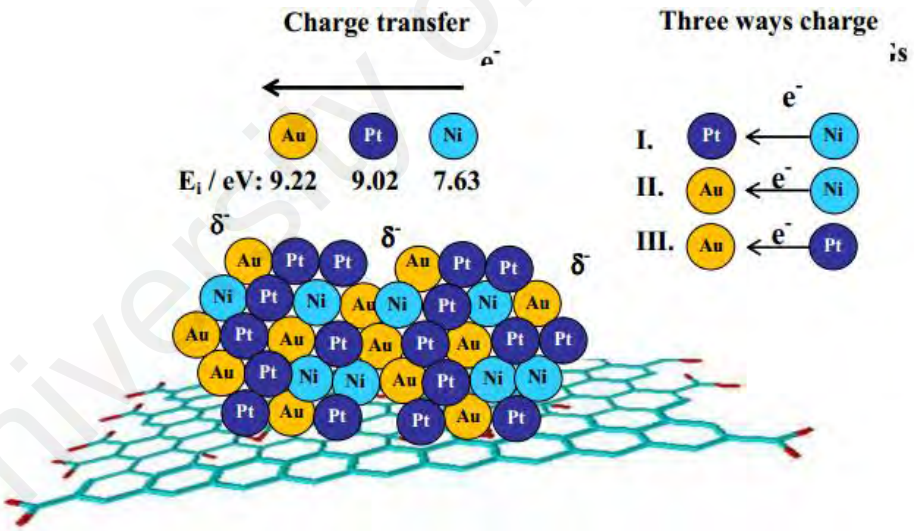

Figure 2.5: Charge distribution in rGO supported $Ni_{40}Au_{33}Pt_{27}$-NGs catalysts.

(Dutta & Ouyang, 2015)

In terms of strain effects (also called geometric effects), the incorporated heterogeneous atoms of different lattice constants alter the interatomic distance (alloying with small and large atoms will result in the decrease and increase in the lattice constant, respectively), inducing strain and shifting the d-band centers with

respect to the Fermi levels (Shen et al., 2014a). For instance, Ni and Rh have lattice constants of 1.49 and 1.73Å, respectively. When Ni and Rh are alloyed together, the resulting lattice constants become small, generating strain in the alloy NPs. This effect can also be well exemplified by graphene supported transition metal core precious metal shell electrocatalysts. The precious metal shell becomes compressive in atom arrangement which downshifts the d-band centers with respect to the Fermi levels (Zhang et al., 2015). The change in the d-band center energy of a catalyst affects the adsorption and activation energies of molecules on the catalyst surface.

Notably, upon alloying of various metal catalysts, the amount of the second or even third metal added needs to be properly controlled. For instance, in the case of NiPd alloys loaded onto graphene nanosheets, a high Ni content tends to decrease the Pd active sites on the surface, leading to poor reactivity (Gopalsamy et al., 2017).

Current works usually involve alloying between precious metals or between precious metals and 3*d* transition metals. With regard to alloying between precious metals, PtPd/rGO is one of the most prominent alloyed electrocatalysts. According to Dutta et al. (2016), the presence of Pd and rGO decreases the CO poisoning of Pt and restricts the agglomeration of NPs during the cyclic voltammetry (CV) cycles. The electrons accepted from the less electronegative Pd partially fill up the Pt 5*d* bands and weaken the carbonaceous intermediates adsorbed onto its surface, consequently improving its anti-poisoning activity. Another remarkable example is PtRu/rGO. Ru adsorbs oxygenated species $(OH)_{ads}$ at relatively more negative potentials than Pt. The high electronegative Ru withdraws more electron density from Pt, positively modifying the electronic structure of Pt by inhibiting back-donation of electrons to the CO antibonding molecular orbitals, leading to a weak Pt-CO bond. Although the reactivity of PtRu/rGO is promising, its commercialization is limited by (i) the high cost of Pt and Ru and (ii)

University of Malaya

the dissolution of Ru into the electrolyte during the operation (Dutta & Ouyang, 2015). As a consequence, other efforts, such as introducing a third or fourth component, were investigated (Shen et al., 2015). Nevertheless, upon involving a third or fourth metal, things become complicated when the binary metals form alloy NPs but the ternary metals do not because different compositions of the metals result in the variation in the phase of metal mixtures (Dutta & Ouyang, 2015).

Other studies reported that the addition of 3*d* transition metals (e.g., Cu, Co, Ni, Mn, Sn, Fe, etc.) is favorable for the reduction of the adsorption of poisoning intermediate species or reaction products, re-exposing the active sites (Ahmed et al., 2016; Stamenkovic et al., 2006; Stamenkovic et al., 2007). Cu added is inert in MOR and only helps in CO oxidation. Therefore, excess Cu can result in poor catalytic activity (Li et al., 2013). A transition metal in the alloy may undergo dissolution into metal ions during operation. Then, the ions diffusing through the membrane to the cathode may undergo reduction, and thus, degrade the fuel cell performance (Kumar et al., 2015). In this case, metal oxide (MO) is proposed to overcome this problem (Kumar et al., 2015; Niu et al., 2015). Kumar et al. (2015) determined that the amount of MO (e.g., titanium dioxide (TiO_2) and manganese oxide (MnO_x), etc.) added determines the percent utilization of precious metal catalysts. In the study of Sun et al. (2014), the incorporation of cobalt oxide (CoO_x) NPs into the CoO_x-Ag/rGO nanocomposites tailors the nucleation and growth of Ag NPs. Owing to its small size, strong interactions can be formed between CoO_x NPs with rGO and Ag NPs. These intimate interactions render a few advantages, including (i) better dispersion of Ag NPs, (ii) modifying the chemical environment of Ag location (ligand effect), and (iii) accelerating the rapid disproportionation of hydroperoxide (HO_2^-) to O_2 at low overpotential. The hydrous MnO_2 was also added, playing the roles of catalyst and catalyst support, which makes the graphene surface hydrophilic, facilitates the diffusion of precious metal ions, and

University of Malaya

restrains the metal NPs from agglomeration (Vilian et al., 2014). A significant finding was reported on the NiPd alloy deposited on graphene (Gopalsamy et al., 2017). With the addition of Ni, a small size was observed compared with the monometallic Pd NPs, indicating that Ni changes the growth of monometallic NPs under similar experimental conditions. Given the nickel (II) hydroxide ($Ni(OH)_2$) passivated surface, Ni does not dissolute during operation (Datta et al., 2011; Deivaraj et al., 2003; Loukrakpam et al., 2011; Na et al., 2015; Park et al., 2002; Paulus et al., 2002). The Ni atoms present in nickel oxide and nickel hydroxide promote the transportation of protons as well as electrons and generates OH^- groups (Equation 3) that can prevent the adsorption of intermediate species via the Langmuir–Hinshelwood mechanism (Dutta & Ouyang, 2015; Huang et al., 2015; Niu et al., 2015). $Ni(OH)_2$ is even superior to MO in dissociating water in alkaline electrolytes. Low-temperature synthesized $Ni(OH)_2$ has proliferating defects. These defects are particularly active in dissociating the adsorbed water molecules to form OH adspecies because of its appropriate bonding strength with OH. The interaction between $Ni(OH)_2$ and OH adspecies is neither too strong nor too weak, which according to the Sabatier principle, makes it particularly reactive (Huang et al., 2015; Na et al., 2015).

$$Ni(OH)_2 \rightarrow NiO + H_2O \quad \text{or} \quad Ni(OH)_2 \rightarrow NiOOH + H^+ + \bar{e} \leftrightarrow NiO + OH^- + H^+ \tag{3}$$

In addition to the combination with metals, either with precious or transition metals, several nonmetals, such as phosphorus (P) and nitrogen (N), have also been doped into precious metals, such as Pd-P, Pd-Ni-P, and Pt-Ni-P (Liu et al., 2016). Table 2.2 summarizes the catalytic performances of various graphene-supported precious metal alloys.

University of Malaya

Table 2.2: Electrochemical performances of various graphene-supported precious metal alloys.

Electrocatalysts	Electrode Reaction	Electrolyte	Peak Current Density	ECSA ($m^2 g^{-1}$)	Stability	References
Pd-Co/rGO	MOR; EOR	1.00 M KOH + 1.00 M CH_3OH/ C_2H_5OH	MOR: 320.80 mA mg^{-1} EOR: 542.80 mA mg^{-1}	56.27	-	(Wang et al., 2014)
Pd-Ag/rGO	MOR	1.00 M KOH + 1.00 M CH_3OH	630.00 mA mg^{-1}	-	-	(Li et al., 2014)
Pd-Cu/rGO	MOR; EOR	1.00 M KOH + 1.00 M CH_3OH/ C_2H_5OH	MOR: 1153.40 mA mg^{-1}; EOR: 2105.40 mA mg^{-1}	-	-	(Na et al., 2015)
Pt-Cu/rGO	MOR	0.50 M H_2SO_4 + 0.50 M CH_3OH	1.35 mA cm^{-2}; 2208.72 mA mg^{-1}	154.72	-	(Li et al., 2013)
PtRu/rGO	MOR	0.50 M H_2SO_4 + 1.00 M CH_3OH	1231.70 mA mg^{-1}	625.17	-	(Zhao et al., 2014)
Pt-MnO_2 decorated rGO	MOR	0.10 M H_2SO_4 + 1.00 M CH_3OH	-	62.80	Remained 72.5% after 200 cycles	(Vilian et al., 2014)
Pt-Pd NPs/G	MOR	1.00 M NaOH + 0.50 M CH_3OH	2.73 mA cm^{-2}	23.34	Decreased 79.44%	(Zhang et al., 2014)
PtRuNi/ few-layered graphene	MOR; EOR	1.00 M H_2SO_4 + 1.00 M CH_3OH/ C_2H_5OH	MOR: 1310.00 mA mg^{-1}; EOR: 1080.00 mA mg^{-1}	84.60	-	(Shen et al., 2015)
Pt-Ag/ graphene	MOR	0.50 M H_2SO_4 + 1.00 M CH_3OH	1842.40 mA mg^{-1}	120.30	-	(Xu et al., 2016)
PtRu/rGO	MOR	0.50 M H_2SO_4 + 1.00 M CH_3OH	570.00 mA mg^{-1}	130.46	-	(Reddy et al., 2017)
NiAuPt-NGs	EOR	0.50 M NaOH + 1.00 M C_2H_5OH	4938.00 mA mg^{-1}	80.10	Decayed 8.9% after 600 cycles	(Dutta & Ouyang, 2015)
PdNiCu/ nitrogen-doped graphene (NG)	ORR	O_2-saturated 0.1 M KOH	3.50 mA cm^{-2}	-	-	(Sun et al., 2017)
PdNiSn/ NG	ORR	O_2-saturated 0.1 M KOH	3.88 mA cm^{-2}	-	-	(Sun et al., 2017)

University of Malaya

2.2.2 Non-precious Metal Electrocatalysts

2.2.2.1 Transition metals

Apart from the transition metals that have been recognized as precious metal as mentioned in the previous section, all other transition metal elements in the periodic table are NPMs. Graphene-supported NPMs have been in the spotlight to substitute the expensive graphene-supported precious metal electrocatalysts because NPMs are abundant, environmentally benign, and low cost (Byon et al., 2011; Mohanraju et al., 2015). Of the NPMs, Mn is a prospective catalyst for ORR in fuel cells because of its availability, less toxicity, cost efficiency, excellent stability, and high tolerance to methanol (Ying Su et al., 2016). Cu is another propitious catalyst that has rich redox chemistry. Cu can be reduced to Cu(0) and Cu(I) as well as oxidized to Cu(III) or even Cu(IV). Different Cu complexes and oxides can catalyze different oxidative reactions. Multicopper oxidase has been reported to be able to catalyze the four-electron reduction of oxygen to water at overpotential lower than those of precious metals. Notably, Co-based materials exhibit single and double functional catalytic activities, making them excellent cathodic catalysts (Liu et al., 2017). The synergistic effect of various Co species can significantly improve its catalytic capability. Nonetheless, the ORR activity and stability of most NPMs are still far from being commercially applied in fuel cell technology (Ania et al., 2015; Arunchander et al., 2017). Upon long-term operation or accelerated degradation under high over-potential and strong electrolytes, the NPMs show inferior durability (Lee et al., 2017). For instance, Cu tends to be easily corroded under certain electrolytes and Co-based composites are hampered by their low conductivity as well as tendency to agglomerate (Ania et al., 2015; Liu et al., 2017).

Incorporating the NPMs on the carbon surface such as graphene, can facilitate the electron transfer from carbon to oxygen, enhancing the ORR activity (Lee et al., 2017). Lee et al. (2017) embedded Fe nanofragment into nitrogen-doped graphene-shelled

University of Malaya

nanocages (Fe@N-G), yielding a special aciniform nanostructures which provide many active sites for ORR. The inner Fe nanofragments play the role of active centers to catalyze the ORR, whereas the outer permeable thin NG shells create the nanoreactors around the Fe catalysts and prevent them from deactivating. Such unique Fe@N-G reported comparable four-electron ORR but superior catalytic stability than the commercial Pt catalyst. Barakat et al. (2014) fabricated graphene-supported CoNi alloys. Given its unique surface oxidation properties, Ni is an auspicious electrocatalyst. Co is located next to Ni in the periodic table; thus, they likely form solid solution alloys. Similar to the observations on the precious metal-based electrocatalysts where the alloyed structure always resulted in better performance than its individual counterparts, graphene supported CoNi alloys exhibited improved stability in alkaline media.

2.2.2.2 Transition MO/hydroxide/carbide/nitride/phosphide

Transition MOs have been proposed as alternative cathodic electrocatalysts of noble metals because of its good cycling stability, distinct propensity to adsorb oxygen (thus better ORR), environmental friendliness, widespread availability, low cost, and high tolerance to contaminants (Cao et al., 2017; Sun et al., 2014; Yan et al., 2015). The MOs act as donor–acceptor chemisorption sites for the reversible adsorption of oxygen (Zhao et al., 2015). Zinc oxide (ZnO), a II–IV semiconductor material, is a good example of transition MO for various applications (Sun et al., 2017). Nonetheless, few transition MOs are comparable to that of noble metals (Sun et al., 2014). Mixed valence oxides with spinel structure, also called spinel oxides (AB_2O_4), are particularly active and durable in ORR (Yan et al., 2015). Spinel manganese cobalt oxide loaded onto nitrogen-doped reduced graphene oxide ($MnCo_2O_4$/N-rmGO) was demonstrated by Liang et al. (2012), and the hybrid outperformed carbon supported Pt (Pt/C) in ORR current density as well as durability. Compared with the sample without the integration of Mn denoted as Co_3O_4/N-rmGO, $MnCo_2O_4$/N-rmGO performs well. The Mn^{3+} ions

University of Malaya

substitute Co^{3+} sites, mediating the phase and NP size. Generally, transition MOs and spinel oxides are semiconductor and exhibit poor electrical conductivity; therefore, the charge transfer between the active catalysts and the current collectors is limited (Wang et al., 2016).

Perovskite (with general chemical formula ABX_3, where A and B are two cations with A atoms larger than B atoms, whereas X is an anion that bonds to A and B) also exhibits a high catalytic activity and has a low cost. Perovskite is capable of incorporating a wide variety of cations (differing species and doping levels), allowing a wide range of doping possibilities (Hancock et al., 2014). Hu et al. (2014) obtained enhanced $La_{1-x}Ca_xMnO_3$ perovskite-graphene composite. The improvement of performance may be attributed to the doping of calcium (Ca) ions which is one of the approaches to enhance performance. Doping of other transition metal benefits the overall performance because it enriches MO species and serves as additional electrocatalysts (Sun et al., 2017). A similar technique was also utilized by Sun et al. (2017) where Co^{2+} ions were doped into ZnO/rGO and attained notable ORR activity. The added Co^{2+} ions (act as catalytic active sites) transfer electrons to the absorbed O_2 molecules. The synergistic effect of Zn^{2+} and Co^{2+} ions can also be another contributing factor.

Replacing the core poor conductive transition MO by pure metal is proven to be able to promote the electrical conductivity and transportation of electron to and from the catalysts (Wang et al., 2016). Liu et al. (2017) explored the feasibility of shell-core structural CoO@Co coupled with nitrogen-doped rGO (N-rGO), denoted as $CoO_{shell}Co_{core}$/N-rGO. The factors leading to the positive result can be attributed to the (i) existence of double catalytic active ingredients, which are N dopants and Co-related active species, with Co-O species exposing Co^{3+} or Co^{2+} ions for chemisorption of O_2

University of Malaya

(Sun et al., 2017); (ii) synergistic effect of N dopants and Co atoms; and (iii) formation of Co-N sites that are another active sites for ORR. Despite the fact that Co-O species effectively catalyze ORR, its presence can in fact cause a slight decrease in ORR activity as it reduces the effective ingredient of Co/N-rGO (Jiang et al., 2017; Liu et al., 2017). Upon the synthesis process of graphene–transition metal oxide, the concentration of the transition MO precursor needs to be considered carefully. Over concentrated precursors tend to yield large particles with irreversible agglomeration and poor distribution (Hong et al., 2017). Compared with the 0D MO NPs, the 2D MO nanosheets are exceptional in promoting the transportation of ions as well as hydrated O_2 and increasing the catalytic active surface area. Furthermore, in the study of Jin et al. (2017) who synthesized N-rGO supported MO (CoO_2/$Ti_{1-x}O_2$/ruthenium (IV) oxide (RuO_2)) nanosheets, they determined that the incorporation of 2D MO nanosheets into rGO nanosheets exposes more edge planes of graphene, which can help increase the pyridinic-N content of N-rGO (the role of pyridinic-N in the ORR activity will be discussed in the subsequent section). Owing to the high restacking tendency of rGO nanosheets and its morphological difference to MO NPs, homogeneous mixing between both can be challenging (Jin et al., 2017). In this aspect, the 2D exfoliated MO nanosheets, which have a negative surface charge similar to the rGO nanosheet, appear to be an ideal solution (Lee et al., 2016). Being sandwiched between rGO nanosheets, a few merits can be achieved, including (i) alleviating self-stacking of rGO; (ii) enabling the scalable formation of stable colloidal mixture with GO; (iii) inducing more structural defects in N-rGO, which have been recognized beneficial for the ORR activity; (iv) optimizing the pore and structure of the composites (a large number of pores allow surface expansion, thereby generating more catalytically active sites for the adsorption of oxygen); and (v) increasing the hydrophilicity of N-rGO (due to the hydrophilic nature of MO nanosheets), facilitating the transport of hydrated O_2 to the

University of Malaya

active sites in electrolyte solution. Layered double hydroxide (LDH), a class of lamellar compounds with a generic chemical formula of $[M_{1-x}^{II}M_x^{III}(OH)_2]^{x+}[(A^{n-})_{x/n}\cdot mH_2O]$, is another ideal solution. The LDH is constructed from positively charged brucite-like layers and charge-balancing interlayer anions. The water molecules and layered structure render its bulk redox and intrinsic catalytic activities. However, the LDH has poor electrical conductivity. Thus, Zhan et al. (2017) incorporated rGO into the mesoporous nitrogen-doped NiFe LDH designated as NiFe-LDH/N-rGO. 3D hierarchical structured MOs were fabricated by Ghosh et al. (2017) via the self-assembly of small Mn_2O_3 NPs with the assistance of a chelating agent. Different chelating agents, even with subtle variation, can lead to considerable variance in morphology of Mn_2O_3. PVA and *n*-Tri-octylphosphine oxide (TOPO) were used separately and acquired flower-like and rose-like Mn_2O_3, respectively. As a nonionic surfactant or structure-directing agent, PVA physically adsorbs onto the Mn_2O_3 subunits, controlling the grain growth and connecting the subunits to form a more stable morphology during the reaction process. Meanwhile, TOPO limits the growth of NPs by lowering the intermolecular interaction. Theoretically, the synthesis of crystals has two steps. The first step is the initial nucleation stage where the Mn^{2+} cations react with the O anions to form the Mn_2O_3 nuclei. These newly formed nuclei act as the seeds to direct the intrinsic shapes of the crystals. The second step is the crystal growth process that determines the ultimate architecture of the crystals. At this stage, the nanocrystals self-assemble to minimize the surface energy. Similar to graphene-supported noble metal electrocatalysts, porous transition metal-based electrocatalysts are highly favored. Bikkarolla et al. (2014) prepared a porous architecture by interconnecting Mn_3O_4 nanoflakes. The formation of the nanoflakes is initiated by strong electrostatic interactions between the oxygen functional groups of N-rGO and the Mn cations. In addition to morphology and particle size, the phase of Mn oxide has a significant effect

University of Malaya

on ORR activity in the following order: MnOOH> Mn_2O_3> Mn_3O_4> Mn_5O_8 (Bikkarolla et al., 2014). Mn oxides with high valence electrons tend to exhibit better ORR, and the Mn valence is dependent on the electrochemical cycling or heat treatment.

On account of the metal–nitrogen synergistic effect, transition metal nitrogen-containing moieties (M-N_x, M = Fe, Co, etc., x = 2 or 4) on graphene are another active site rendering them the capability to perform close to the Pt catalyst in acidic medium and even supersede the commercial Pt/C in alkaline medium (Fu et al., 2013). Among all NPMs, transition metals coordinated to heterocyclic nitrogen were reported to be the most promising (Byon et al., 2011). Co has the drawbacks of high cost, whereas Fe compounds as well as Fe-N_x are readily available and exhibit good properties (Wang et al., 2017). Thus, more attention has been focused on the Fe compounds and Fe-N_x (Videla et al., 2014). Initially, Fe-macrocycles (e.g., Fe-porphyrin and Fe-phthalocyanine) that have a Fe-N_4 moiety were applied in the synthesis process, such that the Fe-macrocycle precursor is actually unnecessary. Fe-N moieties can be directly obtained from the reaction between ammonia (NH_3) gas with Fe salts, such as Fe(III) chloride ($FeCl_3$) and Fe(II) acetate. The introduction of graphene into Fe-N moieties via the pyrolysis of Fe salt, rGO, and graphitic carbon nitride (g-C_3N_4) has been reported with fairly favorable stability (Byon et al., 2011). However, Fe atoms are more likely to alloy with carbon atoms to form FeC_x instead of alloying with nitrogen atoms because the Fe atoms are mostly surrounded by carbon atoms and the Fe ions are reduced to metallic Fe by carbon atoms (Wang et al., 2017). Nevertheless, a small amount of nitrogen atoms can substitute for the carbon atoms, producing Fe-N_x (Wang et al., 2017). Annealing of the mixture of transition metal, graphene, and nitrogen-related polymer is also a common synthesis method. Upon annealing with N-containing polymer, various kinds of nitrogen, including pyrrolic-N, pyridinic-N, and quaternary-N, are formed in the graphene sheets (Lai et al., 2012). The pyridinic-N forms defect

University of Malaya

complexes with carbon vacancies in graphene (Zhang & Northrup, 1991). The defect complexes may serve to anchor divalent metal (metal (II)) to form M-N_x moieties at the edge and within the graphene sheets (Byon et al., 2011; Choi et al., 2010; Fu et al., 2013). Thus, the more the pyridinic-N, the more the M-N_x moieties formed (Lai et al., 2012). Given the even distribution of nitrogen atoms in polyaniline (PANI), PANI is selected to form increased and uniform nitrogen sites in the catalyst (Wu et al., 2011). Instead of using single transition metal, Fu et al. (2013) synthesized FeCo-N-rGO with FeCo-N_x moieties being the active sites. In addition to N-doping, Fe and sulfur (S) are added to rGO, forming Fe-N-S/rGO by one-pot direct pyrolysis of GO, melamine, $FeCl_3$, and S in nitrogen gas (N_2) flow (Qiao et al., 2014). During the synthesis process, the reduction of GO to rGO simultaneously occurred with the multielement doping. In this electrocatalyst, three types of active centers, that is, Fe-N_x, S-C, and N-C active sites, contribute to the ORR activity. Fe catalyzes the thermal expansion process, selectively facilitating the formation of specific N-C sites. The ORR performance can also be attributed to the Fe (III)/(II) formal potential of the catalyst, where a high activity can be achieved at a positive potential. Another extraordinary electrocatalyst, that is, boron (B)-N-Fe triple-doped porous carbon and graphene nanohybrids (BNFe-C-G), was fabricated by an easy, one-pot carbonization method using the low-cost metal–polymer network (MPN), graphene, and B, as shown in Figure 2.6 (Cao et al., 2017). Carbonization leads to the formation of B-N, BC_3, Fe-N_x-C, and Fe_3O_4/Fe_3C alloys. Fe-N_x-C exhibits good durability and ORR activity. Meanwhile, the iron oxide/carbide NPs favor the adsorption of oxygen molecule via sharing the electronic cloud with single oxygen atom and weakening the interatomic forces of O_2, thus lowering the activation energy of ORR. Moreover, the iron oxide/carbide NPs can boost the catalytic activity of Fe-N_x-C, further improving the ORR activity. Therefore, electrocatalysts with a high amount of Fe-N_x-C is more active. By contrast, BC_3, B-N and heteroatom-doped

University of Malaya

molecule enhance the conductivity and electrocatalytic activity because of the synergistic effect. Notably, the application of MPN in the synthesis process has the following advantages: (i) Owing to the uniform distribution of Fe ions in MPN and the controlled immobilization of nitrogen atoms by metal ions, the MPN provides sufficient potential active sites for ORR. (ii) Assisted by special spontaneous bubble template, the MPN can facilitate the construction of foam-like porous morphology, exposing more potential reactive sites and promoting mass transfer within the electrocatalysts.

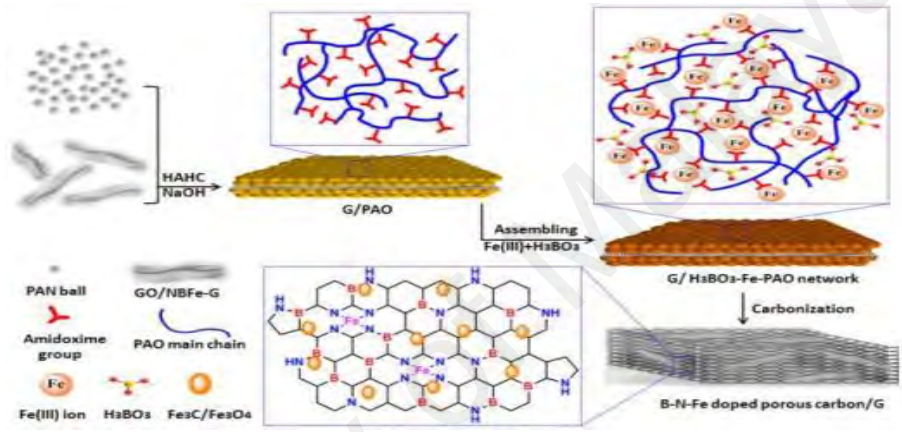

Figure 2.6: The synthetic route of B-N-Fe triple-doped porous carbon and graphene nanohybrids (BNFe-C-G).

(Cao et al., 2017)

Cobalt phosphide (Co_xP) is another transition metal-based catalyst worth mentioning. The Co_2P particles were successfully integrated into Co, nitrogen, and phosphorus codoped graphene nanosheets (Co_2P@CoNPG). Results showed that this method is effective in inhibiting the agglomeration of metallic Co as well as Co_2P particles, ensuring a high ORR performance (Jiang et al., 2017).

2.2.2.3 Transition macromolecules

Transition metal phthalocyanine (MPc)-based materials were determined to exhibit ORR activity (Jasinski, 1964). Nevertheless, their application is restricted by (i) relatively poor electrochemical stability; (ii) agglomeration; (iii) poor electrical

conductivity; and (iv) expensive synthesis due to the complex macrocyclic structure, which make it inadvisable to substitute precious metal-based catalysts (Li et al., 2014; Zhou et al., 2014). The unique properties of graphene make it an ideal support for MPc to address the previously mentioned limitations (Li et al., 2014). Polyphthalocyanines (PPcs), obtained by the polymerization of phthalocyanines, emerge as another excellent material with macrocyclic hollow channel, high SSA, and outstanding electromagnetic properties as well as conductivity. The conjugated π-electron system of transition metal polyphthalocyanine (MPPc) allows non-covalent π–π interaction with graphene that further boosts the electrocatalytic activity. The validity and novelty of this kind of material can be well represented by the work of Lin et al. (2014) where FePPc was loaded onto poly(sodium-*p*-styrenesulfonate)-modified graphene (FePPc/PSS-Gr) and was reported to supersede the commercial Pt/C.

2.2.2.4 Transition metal chalcogenides

Transition metal chalcogenides-based materials (M_xX_y, where M = molybdenum (Mo), Co, Fe, etc. and X = S, selenium (Se), and tellurium (Te)) are superior to transition MO in terms of electrical conductivity (Arunchander et al., 2017). Co-based chalcogenides (e.g., CoS_2, Co_3S_4, $Co_{1-x}S$) are particularly active in ORR activity and rather suitable as cathodic electrocatalyst of DMFC as they have high tolerance to CO poisoning (Arunchander et al., 2017). Transition metal sulfides possess noble metal-like catalytic properties. According to Wang et al. (2013), the ORR activity varies with the size of molybdenum sulfide (MoS_2). MoS_2 with the size of 2 nm performed the best as it exposes abundant Mo edges at this size. Nevertheless, scalable production of approximately 2 nm MoS_2 is difficult. Thus, a large-sized MoS_2 is more practical but anchored on NG to compensate for its poor catalytic performance (Zhao et al., 2015). Table 2.3 demonstrates the catalytic performances of graphene-supported transition metal-ralated electrocatalysts.

University of Malaya

Table 2.3: Electrochemical performances of graphene-supported transition metal-related electrocatalysts.

Electrocatalysts	Electrode Reaction	Onset Potential	Limiting Current Density	Tafel Slope (mV dec^{-1})	Number of Electron Transferred	References
FePPc/PSS-Gr	ORR	−0.08 V vs. SCE	5.90 mA cm^{-2}	-	3.93	(Lin et al., 2014)
Co_3O_4/Nitrogen-doped graphene	ORR	-	~5.00 mA cm^{-2}	42.00	~3.90	(Liang et al., 2011)
3D Mn_3O_4/N-rGO	ORR	-	4.40 mA cm^{-2}	62.00	3.70	(Bikkarolla et al., 2014)
Mn_3O_4/rGO	ORR	−0.12 V vs. SCE	4.00 mA cm^{-2}	-	3.81	(Ying Su et al., 2016)
Mn_2O_3/PVA/ rGO	ORR	−0.08 V vs. Ag/AgCl	7.11 mA cm^{-2}	-	3.75	(Ghosh et al., 2017)
Mn_2O_3/TOPO/ rGO	ORR	−0.09 V vs. Ag/AgCl	9.18 mA cm^{-2}	-	3.99	(Ghosh et al., 2017)
2D TiO_2/rGO	ORR	-	~5.80 mA cm^{-2}	60.00	4.04	(Jin et al., 2017)
$MnCo_2O_4$/graphene	ORR	0.95 V vs. RHE	~3.90 mA cm^{-2}	36.00	~3.90	(Liang et al., 2012)
$CoFe_2O_4$/PANI/rGO	ORR	−32.40 mV vs. Ag/AgCl	~4.50 mA cm^{-2}	147.00	3.90	(Mohanraju et al., 2015)
$ZnFe_2O_4$/rGO	ORR	−0.08 V vs. Hg/HgO	~4.80 mA cm^{-2}	-	3.89	(Hong et al., 2017)
Co-doped ZnO NPs@rGO	ORR	0.90 V vs. RHE	3.94 mA cm^{-2}	-	3.82	(Sun et al., 2017)
$CoO_{shell}Co_{core}$/ N-rGO	ORR	0.95 V vs. RHE	~4.70 mA cm^{-2}	88.00	-	(Liu et al., 2017)
FePc/rGO	ORR	0.89 V vs. RHE	−1.71 mA cm^{-2}	53.65	~3.88	(Li et al., 2014)
Fe-Nx/rGO	ORR	-	~3.50 mA cm^{-2}	-	3.98	(Videla et al., 2014)
Co-S/G	ORR	−0.013 V vs. Ag/AgCl	5.50 mA cm^{-2}	52.00	~3.90	(Arunchander et al., 2017)
Fe-N-rGO	ORR	-	1.50 mA mg^{-1}	-	~3.70	(Byon et al., 2011)
Fe-N-S/rGO	ORR	-	4.78 mA cm^{-2}	-	~3.90	(Qiao et al., 2014)
Fe@N-G	ORR	0.93 V vs. RHE	4.80 mA cm^{-2}	41.90	>3.90	(Lee et al., 2017)
FeCo-N-rGO	ORR	0.95 V vs. RHE	4.78 mA cm^{-2}	70.00	~3.90	(Lee et al., 2017)
2D MoS_2/ NG	ORR	−0.12 V vs. SCE	~4.10 mA cm^{-2}	-	3.90	(Zhao et al., 2015)
Co_2P@CoNPG	ORR	0.90 V vs. RHE	6.68 mA cm^{-2}	69.00	3.96	(Jiang et al., 2017)
NiFe-LDH/N-rGO	ORR	0.91 V vs. RHE	~4.90 mA cm^{-2}	63.00	3.90	(Zhan et al., 2017)

University of Malaya

2.2.3 Metal-free Electrocatalysts

Relative to metal catalysts, metal-free electrocatalysts, in general, exhibit better durability, particularly in alkaline medium (Zhou et al., 2014). Heteroatoms-doped (e.g., N, P, B, S, Se, etc.) graphene sheets, either mono or multiatom doping, are potential metal-free catalysts and catalyst supports (to be illustrated in the subsequent section). Such metal-free electrocatalysts are mainly applied as cathodic catalysts to boost the ORR activity. Compared with the graphene-supported metal catalysts generated by physical attachment, the covalent bonds between heteroatoms with the neighboring carbon atoms endow it with stronger stability (Razmjooei et al., 2014). Doping heteroatoms of different bond lengths and electronegativity (i.e., C = 2.55, B = 2.04, N = 3.04, and P = 2.19) make the graphitic plane energetically unstable, disrupting the surface charge and spin asymmetry of graphene (Liu et al., 2015). Under such a condition, the graphene plane naturally squeezes itself to achieve a more energetically stable configuration (Razmjooei et al., 2014). For the atoms with almost negligible difference in electronegativity to carbon (i.e., S = 2.58, Se = 2.55), disruption in "electron spin" dominates. The significant difference in the atomic radius of S (110 pm) and C (70 pm) relative to N (65 pm) induce strain and defects in graphene that acts as active site for oxygen adsorption. Such significantly larger atomic size polarizes S atoms, donating electrons easily and enhancing the ORR activity (Bag et al., 2015). The synthesis methods to dope heteroatoms to graphene can be categorized into high-temperature or low-temperature synthesis methods (Qu et al., 2016; Soo et al., 2017; Yuezeng Su et al., 2013). High-temperature synthesis methods are (i) chemical vapor deposition (CVD) that involves a vacuum-based system (expensive and complicated for large-scale production); (ii) thermal treatment of graphene-based derivatives in the heteroatom-containing gas atmosphere (e.g., NH_3, hydrogen sulfide (H_2S), hydrogen cyanide (HCN), sulfur dioxide (SO_2), and thiophene); and (iii) high-temperature

University of Malaya

pyrolysis of heteroatom-containing precursors together with graphene or GO. The last synthesis method has been widely used for the preparation of NG, but may not be practically applicable for the fabrication of multiatom-doped graphene, such as N,S-codoped, because of the high cost and rarity of N,S-containing precursors (Qu et al., 2016). Compared with CVD, thermal annealing is relatively simpler and cheaper with higher graphene yield. By controlling the annealing temperature, various heteroatom configurations can be obtained. Meanwhile, low-temperature synthesis methods involve hydrothermal synthesis, as demonstrated by Yuezeng Su et al. (2013). The precursors, that is, water-soluble ammonium thiocyanate (NH_4SCN; source of N and S atoms), were mixed with GO to form a stable aqueous dispersion. Upon hydrothermal treatment at 170 °C, NH_4SCN was isomerized to thiourea and decomposed into highly reactive N/S-rich species, such as H_2S, NH_3, carbon disulfide (CS_2), and residual guanidine thiocyanate. These species are particularly reactive at the defective sites and oxygen-containing groups of GO upon which GO is simultaneously reduced to rGO and assembled into 3D structure.

Hitherto, NG is the most widely investigated nonmetal electrocatalysts (Yuezeng Su et al., 2013). Upon nitrogen doping, the nitrogen atoms not only substitute several carbon atoms that are located at the edge but also decrease the oxygen functional groups on the surface of graphene (Geng et al., 2011). With a valence electron more than carbon, the energy levels in the lower part of the conduction band of graphitic, sp^2-bonded rGO were introduced to a new level (Kakaei & Marzang, 2016). Nitrogen is more electronegative than carbon. Nitrogen attracts electrons from nearby carbon atoms (intramolecular charge transfer), and thus, creates net positive charges that readily attract electrons from the anode, facilitating the oxygen (O_2) adsorption and the ORR activity (Shuangyin Wang et al., 2011). Owing to the high hydrophilicity of NG, the

University of Malaya

complex process for surface activation, which is imperative for pristine graphene, can be skipped (Liu et al., 2017). NG exhibited notably better stability and tolerance to intermediate species than noble metal electrocatalysts and commercial Pt/C (Pan et al., 2013; Qazzazie et al., 2015; Qu et al., 2010; Y. Shao et al., 2010). The electrocatalytic activity strongly depends on the N atom content. N-doped graphene with limited N content (2% to 5%) exhibited a poorer performance than Pt-based catalysts (Xia et al., 2014). The presence of oxygen-containing groups on the defective graphene is crucial to increase the level of doping (Razmjooei et al., 2014). Various nitrogen configurations within the graphene matrix have a strong effect on the catalytic activity of NG. The configurations include (i) graphitic-N (also called quaternary-N), the most important for ORR activity. The high electronegativity of graphitic-N withdraws electrons from adjacent C atoms, reducing the electron densities of adjacent C nuclei, facilitating the back-donation of electrons from N atoms to adjacent C_{Pz} orbitals. The donation and back-donation processes contribute to the rapid O_2 dissociation on adjacent C atoms to form C–O chemical bonds (Deng et al., 2011). (ii) Pyridinic-N is recognized by several researchers as a major contributor to ORR activity (Chen et al., 2009; Rao et al., 2010; Sheng et al., 2011). However, several researchers claimed that pyridinic-N is equally important as graphitic-N (Borghei et al., 2014; Lai et al., 2012; Ying Li et al., 2012; Lin et al., 2012). Located at the edge or vacancy defects of graphene, pyridinic-N contributes one p-electron to form a p-conjugated system (Lee et al., 2017). Pyridinic-N possesses an electron pair in the plane of the carbon matrix, which increases the electron donor property of the catalyst, weakening the O–O bond through the bonding between oxygen and nitrogen and/or an adjacent carbon atom and facilitating the ORR (Chen et al., 2009; Liu et al., 2015; Rao et al., 2010). According to Lai et al. (2012), graphitic-N significantly increases the limiting current density of NG samples, whereas pyridinic-N converts the ORR reaction mechanism from a two-electron mechanism to a four-

University of Malaya

electron mechanism. (iii) Pyrrolic-N contributes a pair of p-electrons to the aromatic p-system (Liu et al., 2016). The band gap of pyrrolic-N (1.20 eV) is smaller than that of pyridinic-N (1.40 eV) and graphitic-N (1.39 eV), indicating its smaller highest occupied molecular orbital- lowest unoccupied molecular orbital (HOMO–LUMO) gap, leading to low kinetic stability and high chemical reactivity (Razmjooei et al., 2014).

The commonly used nitrogen precursors include the following: (i) PDA is a soluble and nontoxic polymer with simple preparation (Zhang et al., 2015). PDA has a high carbon yield, excellent structural tenability, and strong chelation capability to metal ions, enabling the fabrication of different nanostructures (Qu et al., 2016). (ii) PDDA is a positively charged polyelectrolyte. Physical adsorption of PDDA on the surface of graphene induces a positive charge on carbon atoms in graphene via the intermolecular charge transfer. The mutual positive charge among individual graphene sheets generates electrostatic repulsion, allowing uniform dispersion and less severe agglomeration of nanosheets (Wang et al., 2011). In the presence of PDDA, enhancement of graphene conductivity can also be observed. (iii) melamine is a low-cost chemical that decomposes at high temperature into g-C_3N_4 and NH_3, accompanying surface diffusion of N atoms into graphene, and finally assembling into the N-doped graphene (Lee et al., 2017). Instead of using melamine, several researchers directly used g-C_3N_4 to dope the N atoms into graphene (Byon et al., 2011; Zhan et al., 2017). (iv) PANI has aromatic structures, and the N atoms within the structure resemble graphene and quaternary N, which results in the high tendency to form quaternary-N-dominated graphene sheet-like structure (Ma et al., 2015). (v) Polypyrrole (PPy), (vi) ammonium hydroxide (NH_4OH) (Liang et al., 2011), (vii) urea, and (viii) cyanamide (Qazzazie et al., 2015).

Multiatom-doped graphene has also been in the spotlight as it is catalytically more active than monoatom-doped graphene (Qu et al., 2016). Heteroatoms, with different

University of Malaya

numbers of valence electrons, when added to graphene, can result in electron donor or acceptor states, which can activate ORR (Ye et al., 2011). By altering the doping types, levels, and sites, catalytic capabilities can be tuned for various electrocatalytic reactions. For ternary (N, S, and P)-doped rGO, the addition of P atoms induces more pyrrolic-N and pyridinic-N in N and S-doped rGO (Razmjooei et al., 2014). Furthermore, the addition of P atoms generates active P-N species, enhancing the graphitic order and increasing the surface area as well as mesopore volume, which benefits the ORR activity.

Owing to the effects of halogen atoms ((i) electron-withdrawing capability due to the high electronegativity of halogen (i.e., fluorine (F) = 4.0, chlorine (Cl) = 3.16, bromine (Br) = 2.96, iodine (I) = 2.66) and (ii) resonance-donating capability due to its lone pair of electrons), halogen-doping is anticipated to enhance the active sites of graphene, making it active in ORR (Kakaei & Balavandi, 2016; Liu et al., 2015). Halogenation can open up the zero band gap of graphene (chlorinated graphene (0.9 eV); brominated graphene (approximately 0 eV); fluorinated graphene (0–3 eV by tuning degree of fluorination)). Chlorine-fluorine codoped graphene (ClFG) showed almost similar onset potential but better resistance to methanol crossover than the commercial Pt/C catalysts (Liu et al., 2015). Compared with the single-atom-doped graphene (chlorine-doped graphene (ClG) and fluorine-doped graphene (F–G)), ClFG exhibited more promising results, which can be ascribed to the more inhomogeneous charge distribution on the graphene layer created by codoping with different halogen atoms.

Other outstanding works reported the combination of rGO and N-doped carbon nanowires (rGO–CN). rGO–CN exhibited a high nitrogen content and a high surface area, enhancing the electron transfer efficiency and electrocatalytic activity (Babu et al., 2015). Nitrogen-doped carbon dots (N–Cdots) are well known for its exceptional

University of Malaya

electrocatalytic activity, durability, environmental friendliness, and low cost, but limited by its low electrical conductivity. Upon decoration with N-rich GO hybrid (N-Cdots/GO), outstanding ORR was obtained (Niu et al., 2016). The electrochemical performances of a few remarkable graphene-based metal free electrocatalysts are given in Table 2.4.

University of Malaya

Table 2.4: Electrochemical performances of graphene-based metal free electrocatalysts.

Electrocatalysts	Electrode Reaction	Onset Potential	Limiting Current Density (mA cm^{-2})	Tafel Slope (mV dec^{-1})	Number of Electron Transferred	References
Modified nitrogen-doped graphene	ORR	−175.00 mV vs. Ag/AgCl	~2.90	-	3.10	(Qazzazie et al., 2015)
NG	ORR	−0.12 V vs. Ag/AgCl	3.36	-	3.60	(Soo et al., 2017)
3D N/S-graphene frameworks	ORR	-	3.90	-	3.90	(Yuezeng Su et al., 2013)
N/S codoped graphene	ORR	-	~3.80	-	3.36	(Zhang et al., 2015)
SN-rGO	ORR	−15.00 mV vs. Hg/HgO	5.64	67.00	3.50	(Bag et al., 2015)
ClFG	ORR	-	~4.60	-	3.64	(Liu et al., 2015)
rGO/CN	ORR	0.23 V vs. SCE	~3.10	-	3.08	(Babu et al., 2015)
N-Cdots/GO	ORR	0.13 V vs. Ag/AgCl	3.42	114.50	3.91	(Niu et al., 2016)
Halogenated RGO	ORR	-	~7.50	52.00	4.10	(Babu et al., 2015)
PDDA-graphene	ORR	−0.12 V vs. SCE	~2.80	-	4.00	(Wang et al., 2011)

University of Malaya

2.3 Graphene as Catalyst Supports

Catalysts serve to lower down the activation energy, catalyzing the methanol oxidation reaction. However, catalysts NPs tend to agglomerate, resulting in reduced surface area for the reaction. To restrain the agglomeration, catalyst supports are actively used. The presence of catalyst supports can tailor the shape of the catalyst particles, increase the number of active sites and the activity, influence the electronic and geometric properties of the electrocatalysts, and prevent leaching of metal NPs into the electrolyte (Faraji et al., 2016; Yujing Li et al., 2012). An ideal catalyst support exhibits the following properties (Liu & Ma, 2005; Tiwari et al., 2013; Zhao et al., 2015): (i) high electrical conductivity, (ii) enhanced reactant gas contact with the electrocatalyst, (iii) adequate water-handling capability at the cathode, (iv) good corrosion resistance even in extreme condition, (v) high SSA, and (vi) improved dispersion and utilization of catalysts. Carbon has received considerable attention because of its high abundancy, low cost, excellent electronic conductivity, high surface area, relatively inert surface, and wide availability in different forms with different properties (Bailón-García et al., 2013). The common carbon supports are CB (Vulcan XC-72 is the most common commercial CB), mesoporous carbon, carbon nanofiber, single-walled carbon nanotubes, multi-walled carbon nanotubes, carbon nanocoils, and carbon aerogel. Nevertheless, these carbon supports all share common shortcomings, such as poor interaction with the catalysts, expensive, and easily corroded during long-term operation (Hong et al., 2017; Shao et al., 2007). Corrosion of the carbon supports results in three serious consequences: (i) the increased mobility of the catalyst NPs, leading to migration or agglomeration, dissolution of metal NPs from the carbon supports, and their isolation from the Nafion ionomer (Liu et al., 2010; Mayrhofer et al., 2008); (ii) decreased pore volume of the catalyst layer (Liu et al., 2010); and (iii) increased hydrophilicity of the carbon supports, resulting in “flooding” of the pores, and

University of Malaya

hence, decreased O_2 permeability (Avasarala et al., 2009; Kangasniemi et al., 2004). Thus, corrosion-resistant catalyst supports are in high demand to achieve long-term stability FCs.

Graphene, the thinnest and strongest 2D material ever reported, emerges as an attractive alternative heterogeneous catalyst support in dealing with the corrosion issue and other drawbacks (Yongjie Li et al., 2013). The honeycomb net structure formed from abundant symmetric carbon–carbon bonds renders it impressive electrical conductivity. As a consequence, electrons move through graphene as if zero mass (Barakat et al., 2014). Barakat et al. (2014) observed 10 times of enhancement in electrochemical performance after loading the metal NPs onto graphene compared with the stand-alone catalyst NPs. Anchoring metal NPs onto graphene layers downshifts the Fermi level in graphene, which accelerates the charge transfer across the graphene–metal interface (Arunchander et al., 2017). Pure graphene consists of a hexagonal sp^2-hybridized monolayer of carbon atoms with strong in-plane bonding (Song & Kim, 2015). Nonetheless, pristine graphene has weak out-of-plane interactions and its hydrophobic nature results in difficulty in homogeneous dispersion in polar solvents. Such hydrophobic nature also makes the Nafion ionomer particles in a catalyst ink unable to wet the catalyst surface, resulting in a poor catalyst/ionomer interface (Song & Kim, 2015; Zhu et al., 2010). Directly and uniformly depositing metal NPs on pristine graphene has been a considerable challenge because its surface is inactive due to high graphitization (Huang & Wang, 2014). However, a high degree of graphitization is always required for the high stability of graphene-based metal composites (Byon et al., 2011). Further information on pristine graphene will be discussed in the subsequent section. rGO or chemically converted graphene prepared by the chemical reduction method has received considerable attention because this method is scalable, has a low

University of Malaya

production cost, and is established and highly flexible for the chemical modification of graphene materials (Barakat et al., 2014). Through the chemical reduction method, graphite was first oxidized to graphite oxide, followed by sonication to exfoliate it into single-layered or few-layered GO. GO is highly soluble in water and can be easily fabricated into various architectures (Pinithchaisakula et al., 2017). The large number of oxygen-containing groups in GO increases the interlayer distance, allowing the intercalation of metal precursors into the interlayer space of GO and keeping the lamellar structure of GO (Zhang et al., 2015; Zhao et al., 2014). In the study of (Yang et al., 2011), GO was even used as a surfactant, tailoring the size and dispersion of metal NPs on graphene. Subsequently, the GO sheets are reduced to rGO by removing the oxygen functional groups on graphene. The oxygen-containing groups in rGO not only increase the hydrophilicity of graphene and act as anchoring site for the nucleation of metal catalyst NPs but also provide additional sites for the adsorption of oxygenated species (such as OH) to promote the oxidation of poisoning intermediate species (Fampiou & Ramasubramaniam, 2012; Reddy et al., 2017; Vedala et al., 2014). The precious metal ions are attracted to GO via ionic or covalent bond but converted into van der Waals forces after the reduction process (Xin et al., 2016). Covalent bonding facilitated an efficient transport path, which was formed between transition MO and the oxygen groups in hollow rGOs (HrGOs) in the study of Yan et al. (2015). Such covalent bond prevents the transition metal NPs from agglomerating and detaching from HrGOs. Nevertheless, GO or rGO are not without its drawbacks. The complete liberation of oxygen groups, even under the strongest reducing condition, is almost impossible, as demonstrated by experimental and theoretical studies (Bagri et al., 2010; Pei & Cheng, 2012). The oxidation of graphene transforms the planar sp^2 to the distorted sp^3 hybridization, whereas the reduction process for rGO synthesis generates a high level of structural defects and vacancies, destroying the unique electronic properties of graphene

University of Malaya

and decreasing the composite purity due to the fragments (Barinov et al., 2009; Choi et al., 2011; Hernandez et al., 2008; Jeon et al., 2013; Nethravathi et al., 2011; Stankovich et al., 2007; Varela-Rizo et al., 2012). The superficial defects act as Nucleation Centers for Clustering (NCC) where the catalyst NPs migrate over rGO, coalescing in its vicinity and agglomerating (Martins et al., 2014). Imperfections are highly susceptible to corrosion of graphene support during the harsh fuel cell operation, resulting in poor stability (Li et al., 2016). Moreover, the residual oxygen-containing groups result in poorer electrical conductivity than the defect-free graphene and limit its further applications (Jo et al., 2016).

In spite of the merits, pure graphene and rGO are facing a few similar daunting limitations: (i) Irreversible restacking into graphite via van der Waals forces, which covers the metal NPs, inhibiting the reactants from effectively reaching the metal catalysts and subsequently decreasing the overall catalytic activity (Lee et al., 2017). Nevertheless, several experiments proved that increasing the number of layers causes the overlapping of the conduction and valence bands. Thus, the conductivity and electronic transfer improved (Allen et al., 2010; Craciun et al., 2009; Liu et al., 2015). (ii) The lack of bonding sites (particularly for pristine graphene) and poor interaction between catalysts and graphene cause the migration/agglomeration of catalyst NPs during the fuel cell operation. Despite the fact that the existence of oxygen groups improves the interaction of rGO and metal NPs, it is still below the satisfactory level (Fan et al., 2015). The interaction between catalysts and catalyst supports is an imperative factor manipulating the catalytic activity. Such an interaction was reported to be able to modify the electronic structure of catalysts and the local work function of graphene (Deng et al., 2013; Deng et al., 2015; Yoo et al., 2009). Robust interaction

University of Malaya

facilitates the electron transfer between metal catalysts and graphene (Gopalsamy et al., 2017).

Four strategies have been recognized feasible to overcome the limitations of graphene, as follows (Bo et al., 2013; Yu et al., 2017): (i) functionalization or chemical modification of graphene (heteroatom doping, the use of capping/surfactant agents or conductive polymers, and grafting and deposition of NPs), the most extensively studied method, by either covalent or non-covalent interaction (Ensafi et al., 2014) (the chemical modification method modifies the hydrophobic nature of graphene, improving its solubility and controlling the size as well as the morphology of metal catalysts) (Eda et al., 2008; Na et al., 2015; Saminathan et al., 2009; Schniepp et al., 2006; Xin et al., 2016); (ii) incorporation of a variety of transition metal-based compounds into NG, graphene aerogels (Gas), nitrogen-doped graphene aerogels (N-Gas), or graphene sheets; (iii) geometric control where the 2D graphene sheets were assembled into a 3D architecture; and (iv) combination of graphene with foreign catalyst supports.

2.3.1 Functionalization of Graphene

2.3.1.1 Heteroatom doping

Similar to nonmetal heteroatoms (e.g., N, S, B, P, F, etc.), the introduction of active additives (e.g., Fe, Co, Ni, etc.) into graphene can change the crystal structure, vary the spin density as well as charge distribution around carbon atoms, forming an activated region on the surface of graphene, and significantly boost the catalytic activity, tolerance to contaminants as well as cycling stability of graphene (Bikkarolla et al., 2014; Sun et al., 2014; Sun et al., 2017; Wei et al., 2017). Table 2.5 compares the electrochemical performances of different promising electrocatalysts that are supported by heteroatom-doped graphene. The use of doped graphene as catalyst support for metal NPs can be considered mutually beneficial. Heteroatom doping can (i) mitigate the

University of Malaya

corrosion of metal NPs; (ii) generate more defect sites that affect the nucleation and growth kinetics of metal catalysts, resulting in a small particle size and a good distribution (a higher proportion of defective sites enhances the rate of electron transfer); (iii) change the electronic structure of Pt; and (iv) improve the affinity of metal NPs or MO (e.g., iron oxide (Fe_3O_4), tin oxide (SnO_2), Co_3O_4, TiO_2, etc.) through chemical bonding. Meanwhile, metal ions promote the incorporation of the heteroatoms into the graphene lattice (Bo et al., 2013; Liu et al., 2017; Liu et al., 2015; Sun et al., 2015; Wu et al., 2012). Among various functionalities, nitrogen-based and sulfur-based functional groups are widely investigated because they can incur soft acid–soft base interactions that contribute to their strong affinity toward noble metals (Ensafi et al., 2014). Liang et al. (2011) suggested that the active sites may not directly involve N species in the hybrids but are enhanced by N doping. As mentioned in the previous section, when the heteroatom-modified graphene sheets are used alone as catalysts, graphitic-N and pyridinic-N are essential. Nevertheless, when used as catalyst support, pyridinic-N and pyrrolic-N play the role instead, owing to the lone-pair electrons (Zhong et al., 2017). Pyridinic-N improves the onset potential for ORR, whereas pyrrolic-N enhances the limiting current density (Zhong et al., 2017). A previous study claimed that pyridinic-N can form a stronger interaction with MO than graphitic-N and pyrrolic-N because of its higher amount of accessible and reactive sp^2 lobe of lone-pair electrons (Jin et al., 2017). The angle of (C–N–C) of pyridinic-N is 60°, whereas that of pyrrolic-N is 72°. Therefore, pyridinic-N possesses a large neighboring electron lone-pair bond angle, signaling a weak *p* character. Graphitic-N with sp^2 hybrid has no lone-pair electron, but the extra electron density is in the *p* orbital, signaling a strong *p* character than pyridinic-N. Such strong *p* character of graphitic-N and pyrrolic-N results in their weak interaction with MO. The higher number of folded and wrinkled surface of NG than that of rGO results in a larger SSA, favoring the deposition of NPs (Sun et al.,

University of Malaya

2017; Vinayan et al., 2012; Xiong et al., 2013). The substitution of carbon by nitrogen disturbs the delocalized double bond in the graphene system, shifting the Pt-C bond from *5d/2p* orbitals to *6s/2s* orbitals, which results in a higher binding energy (approximately two times higher) between Pt and carbon atoms, indicating a stronger interaction that can inhibit the migration and agglomeration of metal NPs (Groves et al., 2009). The strong metal–support interaction also modulates the electronic property of the metal catalysts (Sun et al., 2017). Therefore, binding metal catalysts to NG can improve the catalytic activity and durability. Nonetheless, extra care should be taken on the amount of NG added because the excessive addition can cause the π–π stacking effect, whereas an insufficient amount will lead to poor electron transport property (Liu et al., 2016). Boron atoms have also been applied to modify graphene (BGR). With one valance electron lesser than carbon atoms, BGR exhibits a p-type transport behavior with considerably high carrier mobility at room temperature (Wang et al., 2013). Boron oxide (B_xO_y) was also incorporated into the holey graphene sheets, serving as a support for Pd (Pd/BG), and showed promising oxidation of formic acid (Xie et al., 2017). Multielement codoping that involves nonmetal and metal elements, such as Fe, N, and S-codoped rGO (Fe-N-S/rGO) (Qiao et al., 2014), Co_2P particles supported on Co, N and P-codoped graphene (Co_2P@CoNPG) (Jiang et al., 2017), has attracted increasing attention in recent years and is superior to commercial Pt/C. Through the synergistic coupling effect between the two heteroatoms, the neighboring carbon atoms are activated, distinctly increasing the catalytically active surface area (Cao et al., 2017; Lee et al., 2017). Such potential active sites may be proportionally related to the contents of heteroatoms. The types and atomic bonding states of heteroatoms are also essential to the ORR activity of the electrocatalysts. For example, the B, N, and Fe ternary-doped carbonized GO (BNFe-C-G) has B-N, BC_3, and oxidized-B moieties that can facilitate the ORR activity (Cao et al., 2017). BC_3 promotes the rate of electronic conduction rate,

University of Malaya

whereas B-N serves as the active site. With regard to Co_2P@CoNPG, the insertion of P atoms forms P–O and P–C bonds that enhance the electron-deficient property of carbon atoms (Jiang et al., 2017). The Co atoms together with the N atoms also form Co-N_x that serves as the active site for ORR (Jiang et al., 2017).

University of Malaya

Table 2.5: Electrochemical performances of heteroatom-doped graphene-supported electrocatalysts.

Electrocatalysts	Electrode Reaction	Electrolyte	Peak Current Density	ECSA ($m^2\ g^{-1}$)	Stability	References
Pt/BGR	MOR	0.50 M H_2SO_4 + 0.50 M CH_3OH	122.00 mA mg^{-1}	49.50	-	(Bo et al., 2013)
Pt/N-rGO	MOR	1.00 M H_2SO_4 + 2.00 M CH_3OH	9.40 mA cm^{-2}	71.90	-	(Sun et al., 2015)
Pt/N-rGO	MOR	0.50 M H_2SO_4 + 0.50 M CH_3OH	160.80 A g^{-1}	45.20	-	(Ma et al., 2015)
Pt/N-rGO	MOR	0.50 M H_2SO_4 + 0.50 M CH_3OH	25.90 mA cm^{-2}	-	-	(Liu et al., 2017)
Ag/N-rGO	ORR	O_2-saturated 0.10 M KOH	4.38 mA cm^{-2}	135.00	18.00% current loss after 12,000 s	(Soo et al., 2016)
Pt/sulfonated-rGO	ORR	0.5 M H_2SO_4	~5.35 mA cm^{-2}	82.60	Retained 59.60% after 4000 cycles	(He et al., 2014)
$CoWO_4$/ nitrogen-doped graphene	ORR	O_2-saturated 1.00 M KOH	4.55 mA cm^{-2}	-	Retained 89% after 1000 cycles	(Kumari & Singh, 2016)

University of Malaya

2.3.1.2 Non-heteroatom functionalization

Graphene functionalized by polymer, polyelectrolyte, and polycation have been rapidly investigated as catalyst supports at the anode and cathode. Such functionalization has a few advantages, as follows: (i) prevent the restacking of graphene nanosheets to enable easy intercalation of metal ions and conduce the transportation of reactants and products; (ii) excellent solubility that allows uniform dispersion of graphene solution; and (iii) ensure better adhesion of metal NPs because of increased binding sites and surface anchoring groups, leading to improved stability (Bo et al., 2013; Faraji et al., 2016; Jo et al., 2011; Tiido et al., 2013; Wong et al., 2013). The polyelectrolytes that have been used include PDDA, BPEI, polyacrylic acid, etc. (Fan et al., 2015). Organic additives, such as octadecylamine or PVP, have also been used as linker between graphene and metal NPs. Combining the capping role of PVP and $[C_{16}MMIm]Br$, metal NPs are uniformly distributed on the rGO surfaces (Lv et al., 2014). Xin et al. (2016) developed graphene grafted by *p*-phenyl SO_3H or *p*-phenyl NH_2 groups. These functional groups covalently bonded to graphene, strengthening the electronic interaction between graphene and catalyst NPs. Such phenomenon can be explained by (i) the modification of the chemical environment at the interface between the supporting carbons and the bottom layers of the catalyst atoms or (ii) the interaction of S and N in the functional groups with the top layers of the catalyst atoms. Functioning as anchoring sites, the functional groups enable uniform landing of catalyst NPs over the graphene surface with strong interaction, leading to the shift of electron density from catalyst atoms to SO_3H-graphene and NH_2-graphene. For the case of PDDA-grafted graphene, functionalization of PDDA on graphene incurs the charge transfer between PDDA and graphene, creating a net positive charge in the graphene plane, which favors the anchoring of metal NPs (Fan et al., 2015). Furthermore, functionalization of PDDA on graphene can also maintain the electronic

University of Malaya

property and enhance the conductivity of graphene (He et al., 2012). Zhang et al. (2015) compared the performance of Co@Pt NPs loaded onto graphene functionalized with and without PDDA. A large number of uniform Co@Pt NPs with narrow size distribution were observed on the PDDA-functionalized graphene sheets. Obviously, the strong interaction between catalyst and catalyst support has a role. The strong interaction limits the agglomeration and growth of NPs and stabilizes the metal catalysts from corrosion (He et al., 2012; Zhang et al., 2015). BPEI was reported to be useful as reducing agent and stabilizer to functionalize graphene nanosheets (Lv et al., 2013). BPEI contains abundant primary, secondary, and tertiary amino groups, which form strong interactions with oxygen functional groups of GO. During the reduction process with BPEI, the majority of oxygen-containing groups are reduced accompanying the creation of new covalent bonds such as amide bond and –Ar–NH–C bond, constituting BPEI-functionalized graphene nanosheets (BGNs). Electrostatic repulsive forces were generated between BGNs, keeping them exfoliated. Given that BPEI is a polycation, it generates positive charges on the surface of BGNs, serving as effective and controllable templates to attract the negatively charged metal NPs electrostatically. Ensafi et al. (2014) reported another notable electrocatalyst, that is, 4-aminothiophenol-modified rGO anchored 3D-Pt nanostructures ($Pt^{@}SC_6H_4$-rGO), as depicted in Figure 2.7, and its catalytic activity is available in Table 2.6. Such functionalization disrupted the π networks of graphene, forming isolated polyaromatic structures or passivated surface defects and generating a finite electronic band gap. 4-aminothiophenol produces protonated thiol groups, empowering proton transfer on the catalyst surface. The covalent bonding between S and Pt significantly depletes the *5d* population of Pt, significantly reducing the density of Pt states around the Fermi level. The adsorbed S (S_{ads}) onto Pt is repulsive to the adsorbates (e.g., CO, ethylene (C_2H_4), H_2, etc.), weakening the adsorption strength and rate of diffusion of CO on the Pt surface. Such

University of Malaya

repulsive S_{ads} ↔ CO interactions also compress local S coverage, leading to the formation of polysulfur species. The presence of sulfur was reported to promote the rate of electron transfer.

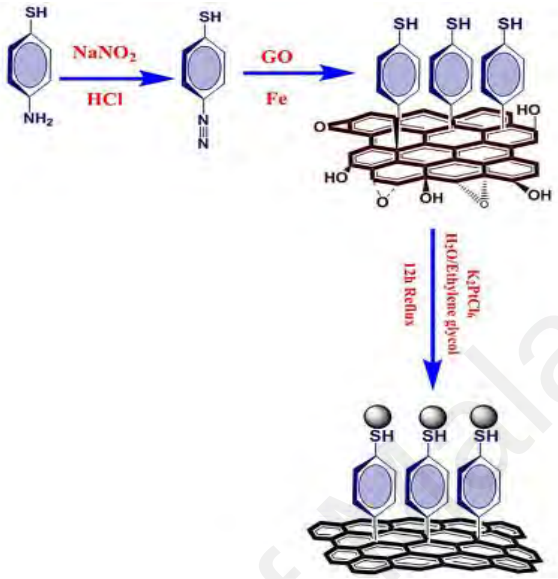

Figure 2.7: Functionalization of exfoliated graphene oxide and the decoration of Pt nanoparticles.

(Ensafi et al., 2014)

The functionalization of graphene by polymeric dispersing agent may be undesired for some applications (Lu et al., 2016). Lu et al. (2016) proposed that 2-aminoethanesulfonic acid (taurine) functionalizes GO, and the obtained sulfonic acid-grafted rGO (S-rGO) was used to enable landing of Pt NPs via the self-assembly method. The amine groups in taurine easily reacted with the epoxy groups on the basal planes of GO by ring-opening reaction. Then, the positively charged polycation, PDDA, was electrostatically self-assembled to the negatively charged S-rGO. Charge inversion occurred between PDDA monolayer and S-rGO that favored the homogeneous loading of negatively charged Pt precursors or ligands. Introducing the highly conductive sulfonic acid groups has the following advantages: (i) Donating electrons to Pt, downshifting the d-band center, which would help dissociate water molecules to form

University of Malaya

hydroxyl groups and weaken the oxophilicity of Pt/S-rGO. This occurrence promotes the removal of poisoning intermediate species. (ii) Increasing the hydrophilicity of graphene, where water absorbed S-rGO via the hydrogen bond. The water cluster at the surface enables proton transportation, and hence, extends the triple-phase boundary (TPB). Such improved hydrophilicity is also reported to be beneficial for the dispersion of Pt NPs (He et al., 2014). (iii) Facilitating the transportation of reactants, electrons, protons, and products, leading to increased TPB.

Noncovalent functionalization of graphene with conducting polymer (CP) dispersant is of particular interest as it not only exhibits the previously mentioned merits but can also maintain the electronic structure and mitigate the corrosion of graphene (Qi et al., 2010; Wang et al., 2008). CPs are well recognized by its ample reachable surface, low resistance, high stability, and excellent conductivity in 3D structure (Antolini, 2009a; Inzelt et al., 2000; Liu et al., 2014; Tsakova, 2008). Incorporating CPs between metal and graphene contributes to a simple as well as a low resistant transfer of electronic charges between metal catalysts and graphene because of the magnified specific area of the active surface (Antolini, 2010; Moghaddam & Pickup, 2013; Napporn et al., 1996). Yezhen Zhang et al. (2012) noncovalently functionalized the negatively charged water-soluble aromatic macromolecule, that is, tetrasulfophthalocyanine (FeTsPc), onto the graphene nanosheets and successfully inhibit the restacking of graphene sheets via the coulomb repulsion. Improved solubility was also verified upon functionalizing graphene with 3-aminopropyltriethoxysilane (Yang et al., 2009). Dopamine (DA) is another organic chemical that is reportedly environmentally friendly and possesses strong affinity to various substrates on account of the repetitive catecholamine structure of Orthodihydroxyphenyl and 3,4-dihydroxy-$_{L}$-phenylalanine compounds (Faraji et al., 2016). Owing to the propensity of the catechol groups to be oxidized to quinine form,

University of Malaya

DA can be used as reducing agent (Lee et al., 2013). Furthermore, the remaining amine groups after the oxidation of DA can react with the epoxy group, inhibiting the agglomeration of graphene. Xu et al. (2010) successfully employed DA derivatives to reduce and non-covalently functionalize GO. In weak alkaline solution, DA can be self-polymerized to conducting PDA (Lee et al., 2007). Owing to the roles of mild reducing capability and surface linker, PDA has been widely used to control the reduction rate and manipulate the morphology of metal NPs (Faraji et al., 2016). The aromatic structure with abundant amine and catechol groups allows one-step surface functionalization and contributes to the strong interaction as well as electric connection between metal NPs and graphene that not only benefits in terms of the corrosion protection but also thermodynamically favors metal loading (Faraji et al., 2016; Lee et al., 2007; Pinithchaisakula et al., 2017; Ye et al., 2011; Ye et al., 2014; Ye et al., 2010). The unique 2D morphology of PDA-rGO alleviates the dissolution of metal NPs into the electrolyte. Chen et al. (2014) modified rGO by using inclusion complexes between *p*-aminothiophenol (pATP) and β-cyclodextrin polymer (β-CDP) via the noncovalent bond (pATP-β-CDP/rGO). The amino and thiol groups of pATP act as anchoring sites for the self-assembly of Pt nanoworms (PtNWs) onto the surface of pATP-β-CDP/rGO, forming the PtNWs/pATP-β-CDP/rGO nanocomposite. The thiol groups of pATP strongly interact with Pt atoms, weakening CO adsorption, thus ensuring enhanced CO tolerance and less current decay during the fuel cell operation. The loading amount of PtNWs can be manipulated by the weight ratio of pATP-β-CDP:rGO ($\gamma_{IC/G}$). When the ratio is increased, a high density of PtNWs on pATP-β-CDP/rGO can be observed. Another work was conducted by Li et al. (2013) where GNs were noncovalently functionalized by 1-pyrenamine (PA) (PA-GNs) and used as catalyst support for Pt. The PA together with solvent were penetrated and intercalated into the interlayer of graphite by supercritical (SC) CO_2. SC CO_2 was selected in the study because they are less

University of Malaya

viscous and thus highly diffusive, which can ease the penetration and intercalation process. Through the synergistic effect of SC CO_2 and PA, the expanded graphite was exfoliated into few-layered graphene nanosheets. The phenyl groups of PA strongly adsorbed onto the GNs surface through π–π interaction, whereas the amine ($–NH_2$) groups serve additional roles: (i) the active sites for nucleating and restraining the growth of Pt NPs and (ii) enhance the wettability and accessibility of the reactant to the catalyst surface. Tiwari et al. (2013) successfully loaded Pt nanoclusters onto genomic DNA-graphene oxide (Pt_n/gDNA-GO) via a three-step synthesis (depicted in Figure 2.8). gDNA, a cost-effective as well as environmentally friendly template, strongly binds to GO sheets via multiple noncovalent interactions: (i) the π–π stacking between the graphitic domains of GO sheets and the base of gDNA and (ii) the hydrogen bonding between the oxygen functional groups of GO sheets and the amines of gDNA. The strong binding between gDNA and GO contributes to the better electronic conductivity and corrosion resistance.

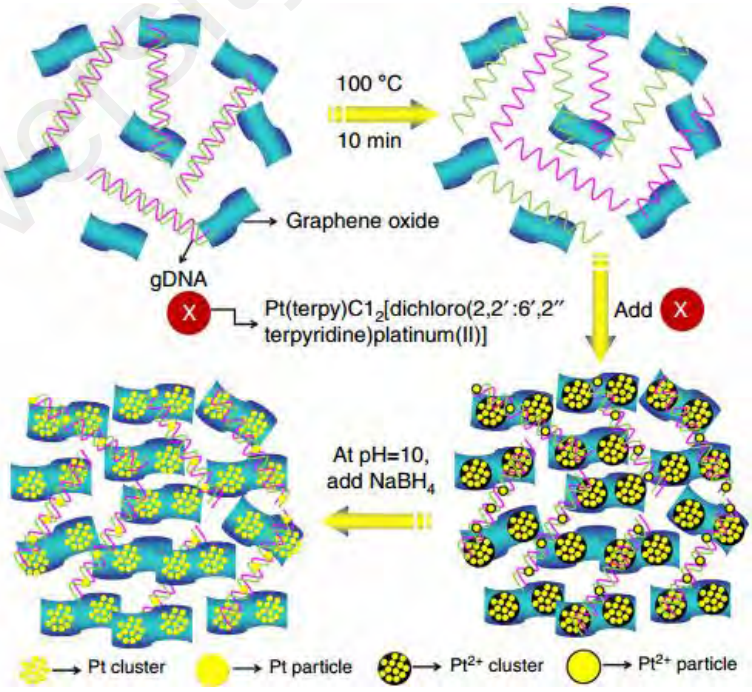

Figure 2.8: Synthetic strategy for preparing Pt_n/gDNA-GO composites.

(Tiwari et al., 2013)

University of Malaya

Table 2.6: Electrochemical performances of non-heteroatom-functionalized graphene-based electrocatalysts.

Electrocatalysts	Electrode Reaction	Electrolyte	Peak Current Density	ECSA ($m^2\ g^{-1}$)	Stability	References
PA-GNS/Pt	MOR	0.50 M H_2SO_4 + 1.00 M CH_3OH	365.60 mA mg^{-1}	82.90	-	(Li et al., 2013)
Pt NWs/pATP-β-CDP/rGO	MOR	0.50 M H_2SO_4 + 1.00 M CH_3OH	590.00 mA mg^{-1}	64.50	-	(Chen et al., 2014)
Pt@SC_6H_4-rGO	MOR	0.50 M H_2SO_4 + 1.00 M CH_3OH	~31.00 A g^{-1}	12.80	-	(Ensafi et al., 2014)
Flowerlike Pt-PDA/rGO	MOR	0.50 M H_2SO_4 + 2.00 M CH_3OH	6.24 mA	89.64	-	(Ye et al., 2014)
Pt/S-rGO	MOR	0.50 M H_2SO_4 + 1.00 M CH_3OH	465.00 mA mg^{-1}	39.42	-	(Lu et al., 2016)
PtPd/PDA-GO	MOR & EOR	0.50 M H_2SO_4 + 0.50 M CH_3OH/ C_2H_5OH	MOR: 5.58 mA cm^{-2} EOR: 6.52 mA cm^{-2}	34.50	-	(Pinithchaisakula et al., 2017)
Pt_n/gDNA-GO	ORR	O_2-saturated 0.10 M $HClO_4$	~4.40 mA cm^{-2}	149.80	Decayed ~6% after 10,000 cycles	(Tiwari et al., 2013)
Pt/p-phenyl NH_2-graphene	ORR	O_2-saturated 0.10 M $HClO_4$	0.29 mA cm^{-2}	59.30	Retained 89.40% after 20,000 cycles	(Xin et al., 2016)
Pt/p-phenyl SO_3H-graphene	ORR	O_2-saturated 0.10 M $HClO_4$	0.29 mA cm^{-2}	55.10	Retained 91.30% after 20,000 cycles	(Xin et al., 2016)
Pt@PDA-rGO	ORR	O_2-saqturated 0.50 M H_2SO_4	3.20 mA cm^{-2}	91.61	Decayed <10% after 1,400 cycles	(Faraji et al., 2016)

University of Malaya

2.3.1.3 Transition metal-related compounds functionalization

Substantial efforts have been devoted to the oxide–carbon composite materials to replace the use of CBs (Tiido et al., 2013). Table 2.7 provides a few examples of electrocatalysts using the transition metal-related compounds functionalized-graphene as catalyst support. The introduction of semiconductor oxides (e.g., TiO_2, SnO_2, copper oxide (CuO), strontium titanate ($SrTiO_3$), or tungsten trioxide (WO_3)) with high oxidation properties can improve the stability of metal–carbon electrocatalysts as well as modify the metal–support interaction, making them outstanding corrosion-resistant supports (Bauer et al., 2010; de Tacconi et al., 2008; Ioroi et al., 2008; Kim et al., 2010; Tian et al., 2008). Tiido et al. (2013) obtained nano-sized Pt catalyst supported onto TiO_2 functionalized graphene nanosheets (Pt/TiO_2-FGSs). The chemical interaction of Pt centers with TiO_2 NPs changes the electronic structure of Pt and brings excellent kinetics and self-refreshment functional behavior (Bauer et al., 2010; Lee et al., 2008; Ruiz Camacho et al., 2013; Tian et al., 2012).

Compared with MO, transition metal carbide (TMC)-based and transition metal nitride (TMN)-based catalyst supports exhibit better performance in terms of anti-corrosion, onset potential, catalytic activity, and stability (Huang et al., 2015). TMC-based electrocatalysts are promising anodic catalysts, whereas TMN-based electrocatalysts are suitable as cathodic catalysts (Cohen et al., 2007). TMNs, particularly titanium nitride (TiN) and chromium nitride (CrN), are recognized as ideal candidates for catalyst supports with improved durability because of its outstanding conductivity, superior thermal stability, high melting point, excellent corrosion resistance, and good catalyst–support interaction (Cui et al., 2014; Kuttiyiel et al., 2015; Pan et al., 2014; Tian et al., 2015; Tian et al., 2016; Wang et al., 2011; Xiao et al., 2014). The introduction of small hollow TiN spheres with a large amount of mesopores

University of Malaya

was proposed and was determined to be ideal for electrocatalytic application (Moon et al., 2014). Nevertheless, the small size and abundant mesopores of TiN NPs may exhibit many grain boundaries and defects and are discontinuous. Therefore, conductivity and electron transport efficiency are reduced (Li et al., 2010; Lu et al., 2012; Xiao et al., 2014). Realizing the advantages of TMN-based and TMC-based electrocatalysts, metal carbonitrides was investigated. Through the integration of carbon and nitrogen anions, synergistic effects with the catalyst can be induced. Furthermore, defects can be generated in greater amount, leading to increased active sites. Graphene-supported vanadium carbonitride (G-V(C,N)) hybrid was found as a novel support for Pt catalyst and obtained outstanding MOR (Huang et al., 2015). Carbide and nitride anions play a critical role in catalyzing methanol oxidation. Carbon and nitrogen anions induced defects that can act as additional active sites on the surfaces of rGO and V(C,N). Metal sulfide is another potential semiconductor added to graphene to form nanocomposite. Cadmium sulfide (CdS) has a rather narrow band gap (2.52 eV) at room temperature. When coupled to GO with a wide band gap, the obtained CdS-graphene nanocomposites were reported to exhibit improved catalytic activity (Arabzadeh et al., 2016). $Ni(OH)_2$ has also attracted attention because it exhibits better dissociative adsorption of water molecules to form OH_{ad} in alkaline electrolytes relative to MOs (Subbaraman et al., 2012; Subbaraman et al., 2011). The appropriate interaction, neither too strong nor too weak, of $Ni(OH)_2$ and OH_{ad} renders it highly reactive in electrocatalytic reaction according to the Sabatier principle. Moreover, the appropriate interaction of $Ni(OH)_2$ and OH_{ad} favors CO oxidation through the Langmuir–Hinshelwood pathway, significantly reducing the onset overpotentials (Subbaraman et al., 2012). Huang et al. (2015) synthesized a Pt-$Ni(OH)_2$-graphene ternary hybrid. Each component of the hybrid plays a specific role: the metal serves as the active site for methanol oxidation; hydroxide facilitates the oxidative removal of the poisoning carbonaceous intermediates

University of Malaya

on adjacent metal sites; and graphene provides a high electrical conductivity for rapid electrocatalysis.

Table 2.7: Electrochemical performances of transition metal-related compounds functionalized graphene-supported electrocatalysts.

Electrocatalysts	Electrode Reaction	Electrolyte	Peak Current Density	ECSA ($m^2\ g^{-1}$)	Stability	References
Pt/$MnCo_2O_4$/ graphene nanosheets	MOR	0.50 M H_2SO_4 + 1.00 M CH_3OH	675.20 mA mg^{-1}	3791.00	-	(Kumar et al., 2015)
Pt–$Ni(OH)_2$–graphene	MOR	1.00 M KOH + 1.00 M CH_3OH	1236.00 mA mg^{-1}	64.10	Retained 74.00% after 50,000 s	(Huang et al., 2015)
Pt/G-V(C,N)	MOR	1.00 M KOH + 0.50 M CH_3OH	48.00 mA cm^{-2}	-	-	(Huang et al., 2015)
Pt/TiO_2–FGS	ORR	O_2-saturated 0.50 M H_2SO_4/ 0.10 M KOH	Acidic: ~5.00 mA cm^{-2}; Alkaline: ~5.50 mA cm^{-2}	-	-	(Tiido et al., 2013)

2.3.2 Morphology

Similar to catalysts, the texture, configuration, and structure of catalyst supports have a profound effect on the fuel cell performance (Jung et al., 2014; Li et al., 2015). Ordered mesoporous and microporous CBs are widely applied as support because of its porous structure and chemical inertness (Debe, 2012; Wan et al., 2006; Wang et al., 2011). Nonetheless, mesoporous carbon containing amorphous pore walls possesses low graphitic degree and electron conductivity, whereas microporous CBs are chemically less durable during the fuel cell operation (Guo et al., 2015; Jing Tang et al., 2013). Graphene emerges to be a potential alternative since its discovery in the year 2004.

University of Malaya

Nevertheless, the 2D structure of graphene tends to lie flat on the substrate, which will cover the metal NPs between the rGO layers, obstructing the accessibility of the reactants and products to the surface of the catalyst NPs. Therefore, the catalyst NPs are not fully utilized. Vertically oriented graphene (VG) was proposed to overcome this problem. However, the feasibility of VG has been limited by its synthesis process, where CVD, which has been known to be complicated and expensive, is usually required. With regard to this issue, a high amount of metal NPs were loaded onto rGO to obtain a nearly standing structure electrode surface (Liu et al., 2014; Yang et al., 2014). Yang et al. (2015) managed to construct vertically oriented rGO by the electrodeposition method with the aid of higher contents of Pd precursor than PdCu/flat-lying rGO and achieved improved catalytic activity. Their work solved the dilemma of CVD as electrodeposition is one of the simple, rapid, and green techniques to obtain "clean" binder-free electrode materials. Recently, 3D Gas have been extensively applied in catalysis and energy storage applications because of their abundant macroporosity and multidimensional electron and mass transportation pathways (Wang et al., 2016; Wu et al., 2012; Yin et al., 2014). The interpenetrating porous structure confines metal NPs within the 3D framework and decreases the diffusion resistance of reactants as well as products to and from the metal NPs, improving the stability and catalytic activity of the nanocatalysts (Yan Zhang et al., 2016; Zhao et al., 2016). Stemming from the benefits of Gas, Zhao et al. (2016) reported an easy and green hydrothermal process to synthesize Pt/C/Gas. The graphene sheets partially overlap or coalesce, forming continuous interconnected macropores in the micrometer size range. Some scientific communities also reported the use of surfactant to obtain a 3D nanostructure despite the fact that the surfactants are known to be non-conductive and can cover the active sites (Wei et al., 2017). The graphene nanopores allow the catalyst NPs to be robustly embedded into it, increasing the stability, promoting the diffusion of reactants as well as

University of Malaya

products, and modulating the electronic properties of catalyst NPs (Wu et al., 2012; Zhong et al., 2017). Meanwhile, mesopores are conducive for the uptake as well as diffusion of reactants or ions in the electrolyte and exposure of more active sites (Qu et al., 2016; Razmjooei et al., 2014). An interesting observation was observed in the study of (Geng et al., 2011) during the synthesis of N-graphene using ammonia. Upon the reaction of ammonia and graphene, hydrogen cyanide and hydrogen were formed ($C + NH_3 \rightarrow HCN + H_2$). According to the equation, carbon was consumed, making graphene more porous without affecting the graphene layers (Geng et al., 2011). Another approach to obtain a 3D support material was achieved by growing g-C_3N_4 polymer on rGO (g-C_3N_4@rGO). sp^2 bonding of carbon–nitrogen structures (CNs) in g-C_3N_4 serves as active sites and uniformly distributes the metal NPs (Song & Kim, 2015). The amines in g-C_3N_4 are hydrophobic, but the oxygen-containing groups on rGO are hydrophilic. Therefore, the resulting g-C_3N_4@rGO is amphiphilic. A novel dual templating approach in obtaining 3D porous graphene "nanostack" morphology was also proposed (Gokhale et al., 2017). The two templates were sodium salt (hard template) and small organic molecule benzimidazole carboxylic acid (soft template). Sodium salt templates and silica (SiO_2) sacrificial support method were used. Upon pyrolysis, the sodium ions (Na^+) react with COO^- to yield Na_2CO_3, which is subsequently etched by acid removal, resulting in microporosity and mesoporosity. By contrast, SiO_2 NPs are etched by hydrogen fluoride (HF), resulting in mesoporosity and macroporosity. A significant finding was also observed on the sample synthesized by the annealing approach where the calcination temperature can influence the morphology of the samples (Zhong et al., 2017). Zhong et al. (2017) embedded the Pt_2Pd alloy into nitrogen-rich graphene nanopores (Pt_2Pd/NPG) calcined at different temperatures (i.e., 650 °C, 700 °C, 750 °C, and 800 °C). No mesopores were formed on the sample calcined at 650 °C. Meanwhile, nanopores were formed on the latter three samples but

University of Malaya

severe agglomeration occurred at temperatures of 750 °C and 800 °C. They proved that the nanopores have a decent effect on the stability of catalyst NPs.

Apart from the 3D structure, 0D graphene nanospheres are also expected to be able to increase the exposure area of graphene layers, making it an ideal catalyst support (Lin et al., 2013). With this understanding, Lin et al. (2013) loaded Pt NPs onto 0D rGO-encapsulated amine-functionalized Fe_3O_4 magnetic nanospheres (rGO-AMs) and proved its validity in improving the utilization of Pt NPs for MOR. Yan et al. (2015) further explored the possibility to combine the 0D and 3D structure catalyst supports, where $FeCo_2O_4$ spinel NPs were covalently coupled to hollow rGO spheres denoted as (FCO/HrGOS) as depicted in Figure 2.9. Such a unique nanostructure provides a large ECSA (as shown in Table 2.8) and efficient triple-phase (solid–liquid–gas) region for efficient mass transportation. Liu et al. (2016) obtained another remarkable hollow mesoporous TiN/N-G/Pt hybrid, as depicted in Figure 2.10. Their work combines the advantages that can be brought about by (i) nitrogen doping, (ii) modification by TMN, and (iii) porous structure. Notably, the size of graphene is also a crucial factor. Nanographene can effectively shorten the length of channels and pores for the transportation of the reactants and products of the catalytic reaction (Xin et al., 2016).

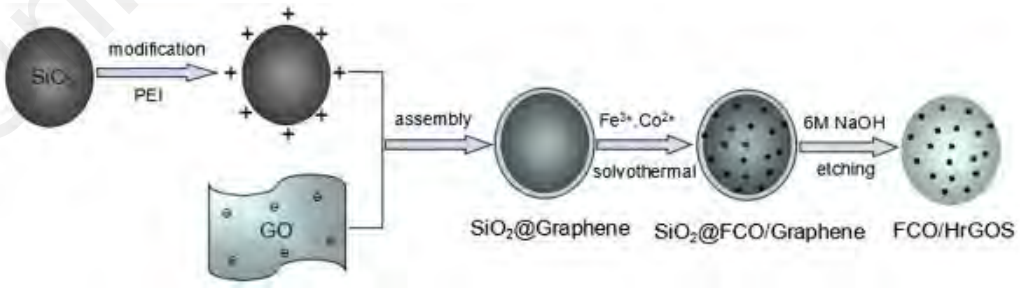

Figure 2.9: Synthesis of FCO/HrGOs.

(Yan et al., 2015)

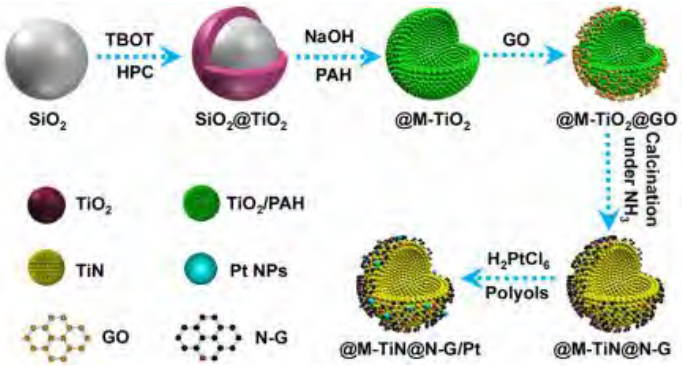

Figure 2.10: Synthesis of hollow mesoporous-shelled @M-TiN/N-G/Pt catalyst.

(Liu et al., 2016)

Table 2.8: Electrochemical performances of electrocatalysts synthesized with graphene of different morphologies.

Electrocatalysts	Electrode Reaction	Electrolyte	Peak Current Density	ECSA ($m^2\ g^{-1}$)	Stability	Reference s
PdCu/ vertically oriented rGO	MOR	1.00 M KOH + 1.00 M CH_3OH	762.80 A g^{-1}	0.19	-	(Yang et al., 2015)
@M–TiN/N–G/Pt	MOR	0.50 M H_2SO_4 + 1.00 M CH_3OH	739.00 mA mg^{-1}	60.20	-	(Liu et al., 2016)
Pt/g-C_3N_4@rGO	MOR	1.00 M H_2SO_4 + 2.00 M CH_3OH	13.70 mA cm^{-2}	81.50	-	(Song & Kim, 2015)
Pt/porous graphene	ORR	O_2-saturated 0.10 M KOH	4.00 mA cm^{-2}	-	Almost shows no change after 500 cycles.	(Yan Zhang et al., 2016)
Pt_2Pd/NPG	ORR	O_2-saturated 0.10 M KOH	4.10 mA cm^{-2}	103.10	Decayed 1.9% after 3000 cycles	(Zhong et al., 2017)
FCO/HrGOs	ORR	O_2-saturated 0.10 M KOH	~5.80 mA cm^{-2}	145.42	Decayed ~7.9% over 86,400 s	(Yan et al., 2015)
Co_3O_4/ N-Gas	ORR	O_2-saturated 0.10 M KOH	5.20 mA cm^{-2}	-	Retained 83.30% after 10,000 s	(Yu et al., 2017)

University of Malaya

2.3.3 Composite Support

The combination of graphene with other catalyst supports has been extensively investigated and a few examples are given in Table 2.9. (Jing Tang et al., 2013) presented a remarkable synthesis of reduced graphene oxide-ordered mesoporous carbon (RGO-OMC) composite materials. Functioning as a "spacer", OMC prevents rGO from restacking and agglomerating. In fact, the surface OMC is rather inert, which is unfavorable for the deposition of metal NPs. As a consequence, Pt NPs seriously agglomerate on the rGO sheets upon limited supply of rGO. Increasing the content of rGO, the electron conductivity can be improved and rGO can be fully coated onto most OMC. Thus, catalyst NPs can deposit onto the entire carbon material. The rGO-AMs mentioned in the previous section is another excellent support composite for the deposition of Pt NPs (Lin et al., 2013). The addition of highly conductive AMs offers two significant benefits, that is, (i) improving the electronic conductivity and (ii) enhancing the utilization of catalyst NPs by exposing them on the surface of the support. Without the assistance of a surfactant, Na et al. (2015) inserted a carbon sphere in between the graphene sheets and obtained a sandwich-like structure. The carbon particles expand the distance between graphene sheets, thereby altering the array of graphene sheets and exposing the catalyst NPs within the graphene layers (Park et al., 2011). Xin et al. (2016) further enhanced the work by prefunctionalizing the graphitic CB by *p*-phenyl sulfonic acid, denoted as SO_3H-GCB. The incorporation of SO_3H-GCB resulted in short channel lengths and pores that are beneficial for the O_2 mass transport within the catalyst layers. Du et al. (2012) developed a stand-up structured graphene nanosheet–CNT (GNS-CNT) hybrid (as shown in Figure 2.11) via the two-step growth method. First, the CNTs were directly grown on a carbon cloth. Then, the GNS was fabricated on the CNT surface. Such extraordinary structure contains abundant edge planes, affording high electrochemical activity and low energy loss. Wei et al. (2017)

University of Malaya

similarly constructed a hybrid composed of 1D CNTs and 2D graphene, resulting in a 3D morphology. Different from the common surfactant-assisted method, the CNTs were in situ grown from the 2D graphene surface, as illustrated in Figure 2.12.

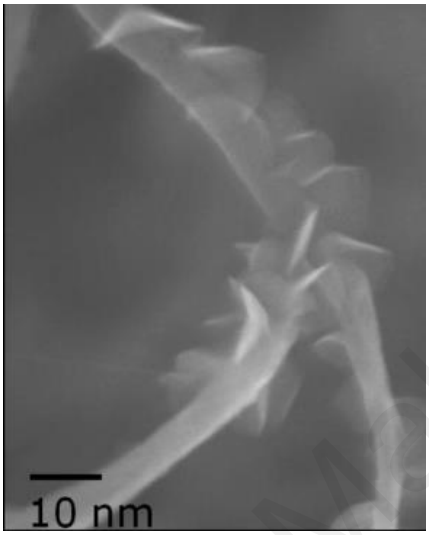

Figure 2.11: HRSEM image of standup GNS-CNT structure.

(Du et al., 2012)

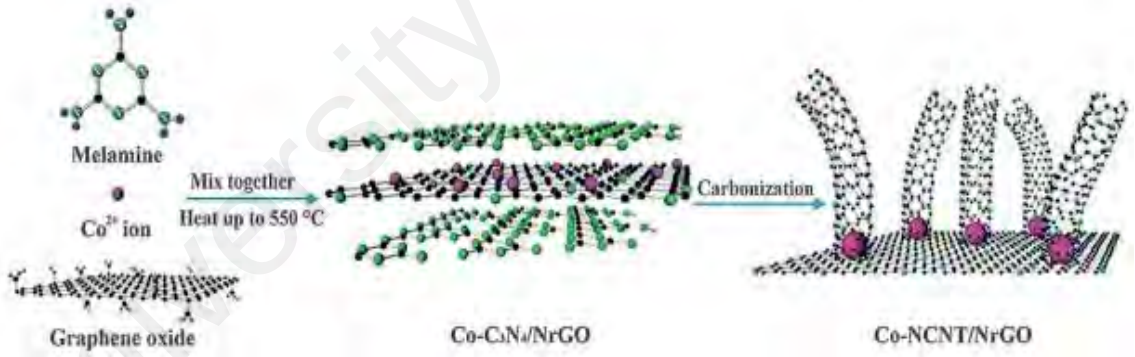

Figure 2.12: The preparation process for typical cobalt-embedded nitrogen-doped carbon nanotubes and nitrogen-doped reduced graphene oxide (Co-NCNT/NrGO).

(Wei et al., 2017)

A thin layered N-rich carbon (CN_x) has also been reported as an efficient 2D crosslinker between rGO and catalyst NPs without compromising the intrinsic properties of rGO (Liu et al., 2015). The CN_x with extremely high N content (approximately 59 wt%) may donate the lone-pair electrons of N heteroatoms to anchor the metal NPs, allowing homogeneous nucleation and growth of metal NPs on the

University of Malaya

surface of rGO. The combination and synergy of the metal organic framework (MOF) with GO (MOF/GO) has also achieved a remarkable ORR activity (Ania et al., 2015). The MOF itself is in fact a poor electron conductor and has limited charge transfer capability. Thus, GO was added to form specific chemical linkages with the MOF units, improving the electrical conductivity. Nevertheless, under a moisture environment, the long-term stability of MOF/GO becomes a challenge.

Table 2.9: Electrochemical performances of graphene composite-supported electrocatalysts.

Electrocatalysts	Electrode Reaction	Electrolyte	Peak Current Density	ECSA ($m^2\ g^{-1}$)	Stability	References
Pt/rGO–OMC	MOR	1.00 M H_2SO_4 + 2.00 M CH_3OH	112.74 mA cm^{-2}	80.40	-	(Jing Tang et al., 2013)
Pt/carbon/ graphene aerogel	MOR	0.50 M H_2SO_4 + 0.50 M CH_3OH	405.30 mA mg^{-1}	70.40	-	(Zhao et al., 2016)
Graphene/ carbon nanospheres/ graphene sandwich supported Pt_3Ni	MOR	0.10 M $HClO_4$ + 1.00 M CH_3OH	360.40 mA mg^{-1}	52.70	-	(Niu et al., 2015)
Ag/GO/Carbon black	ORR	O_2-saturated 0.10 M NaOH	5.10 mA cm^{-2}	92.65	-	(Yuan et al., 2014)
Pt/GNS–CNT	ORR	0.50 M H_2SO_4	0.25 A mg^{-1}	116.20	-	(Du et al., 2012)
Fe_3O_4/CN_x/rGO	ORR	O_2-saturated 0.10 M KOH	5.60 mA cm^{-2}	-	Retained 95% after 20,000 s	(Liu et al., 2015)
Co–NCNT/NrGO	ORR	O_2-saturated 0.10 M KOH	4.38 mA cm^{-2}	-	-	(Wei et al., 2017)

University of Malaya

2.3.4 Pristine Graphene

Despite the fact that rGO obtained by the wet chemical oxidation and reduction processes has been extensively used as catalyst support because of its cost-effective, large-scale, and easy operation, the oxygen-containing groups and rough graphene surface can result in the conglomeration of metal NPs. Moreover, the high defects in rGO serve as source of the instability during the fuel cell operation. In this regard, a few studies (as exemplified in Table 2.10) have been focusing on the metal NP-pristine graphene to address these problems (Shen et al., 2015; Shen et al., 2014a; Shen et al., 2014; Shen et al., 2014b; Zhao et al., 2015; Zhao et al., 2015). The exceptional conductivity of pristine graphene promotes electron transfer from the support to the metal catalysts. Shen et al. (2014a) loaded Pt subnano/nanoclusters onto pristine GNs, which were obtained by the CVD method at high temperature. In view of the fact that Pt subnanoclusters have numerous edges and corners, it has a low coordination number, activating its "cationic" behavior (Shen et al., 2014b). The carbon p^* empty orbitals hybridize with the Pt-filled *d* orbitals, shifting the d-band center of Pt NPs away from the Fermi level, which weaken the adsorption of CO molecules on the Pt surface. Apart from CVD, direct ultrasound-assisted exfoliation of graphite powder in organic solvents, such as *N*-methyl-2-pyrrolidone (NMP) has also been explored (Zhao et al., 2015; Zhao et al., 2015). To be used as a competent catalyst support, pristine graphene is still limited by a few drawbacks, as follows: (i) synthesis using CVD is relatively complex, which requires a high temperature, whereas NMP is a high boiling point and non-innocuous solvent that encumbers further processing of the exfoliated graphene flakes (in this regard, production/processing in water would be clearly preferable); (ii) uniform deposition of metal NPs with strong interaction on pristine graphene is rather challenging because of the absence or low content of chemical groups and defects in pristine graphene (Ayán-Varela et al., 2017); and (iii) the use of surfactants or

University of Malaya

stabilizers, which act to stabilize NPs on the graphene surface and promote the compatibility of graphene in solvents, tend to cover the active sites of catalysts. A few extraordinary works have recently been reported to resolve the previously mentioned limitations to a great extent (but not to the full extent). The utilization of certain amphiphilic molecules emerged as a good solution. The amphiphilic molecules strongly adsorbed onto graphene, acting as colloidal stabilizers in the processing of pristine graphene flakes in aqueous medium and anchoring sites for the high-density uniform decoration of metal NPs on the graphene flakes (Ayán-Varela et al., 2017). In this respect, Ayán-Varela et al. (2017) proposed the use of FMN, a nontoxic and benign derivative of vitamin B_2, as an efficient dispersant of pristine graphene flakes in water (Ayán-Varela et al., 2015). FMN is capable to colloidally stabilize concentrated graphene (up to approximately 50 mg mL^{-1}) even in low fractions (FMN/graphene mass ratios down to 0.04). Moreover, the π–π interactions between FMN and graphene do not significantly alter the structure of the carbon lattice, ensuring that the FMN-based graphene films have a high electrical conductivity (Ayán-Varela et al., 2015). Other appealing works where metal NPs were directly deposited on pristine graphene sheets by a simple yet effective supercritical CO_2 route without using any surfactant or stabilizer were also proposed (Zhao et al., 2015; Zhao et al., 2015). Given the unique properties of supercritical fluid, such as gas-like diffusion rate, near-zero surface tension, and low viscosity, metal NPs can uniformly disperse on pristine graphene. The excellent wettability between carbon surface and supercritical CO_2 enables the strong interaction of ultrafine metal NPs and pristine graphene. Furthermore, supercritical CO_2 is highly penetrative and can effectively unbundle (by intercalation and exfoliation) and distribute the metal NPs, inhibiting restacking of the graphene sheets. The commonly used H_2 was substituted with dimethyl amine borane (DMAB) as reductant to simplify the experimental procedure further. Such substitution appreciably lowered the synthesis

University of Malaya

temperature to only 50 °C for metal reduction (Kim et al., 2010; Stankovich et al., 2007).

Table 2.10: Electrochemical performances of pristine graphene-supported electrocatalysts.

Electrocatalysts	Electrode Reaction	Electrolyte	Peak Current Density ($A\ g^{-1}$)	ECSA ($m^2\ g^{-1}$)	Stability	References
Pd/pristine graphene	MOR	0.50 M NaOH + 1.00 M CH_3OH	823.40	115.00	-	(Zhao et al., 2015)
Pt subnano/ nanoclusters stabilized by pristine graphene nanosheets	MOR	1.00 M H_2SO_4 + 1.00 M CH_3OH	316.00	112.00	-	(Shen et al., 2014b)
Pt/FMN-exfoliated pristine graphene	MOR	0.50 M CH_3OH + 0.50 M H_2SO_4/ 0.10 M KOH	Acidic: 1140.00; Alkaline: 1180.00	49.20	Retained 23% after 30 min in alkaline medium	(Ayán-Varela et al., 2017)
PtRuNi/ pristine graphene	MOR	0.50 M H_2SO_4 + 1.00 M CH_3OH	1271.40	-	-	(Zhao et al., 2015)

In summary, graphene is actively used as catalyst support for precious metal and non-precious metal catalysts. Graphene-supported metal catalysts (both precious and non-precious metal catalysts) generally obtained smaller size with improved distribution compared to the standalone catalyst NPs, endowing better electrochemical performance. In fact, graphene can itself be catalyst. Nevertheless, its catalytic effect is too weak and requires (i) heteroatom doping, (ii) controlling of graphene morphology, and (iii) combination with other metal-free compound. These graphene-related electrocatalysts without the presence of metal catalysts are referred as metal-free catalysts. Worth mentioning, graphene-related/supported precious metal catalysts achieved the best catalytic activity and metal-free electrocatalysts exhibited the best stability.

University of Malaya

CHAPTER 3: METHODOLOGY

3.1 Introduction

This chapter illustrates details of chemicals used and their respective sources, experimental procedures, characterizations, and electrochemical measurements involved throughout the entire study. Figure 3.1 shows the research work flow chart. It first started with the synthesis of GO. The GO nanosheets were subsequently applied in preliminary studies. With the optimized sample, indepth studies were conducted and followed by structural and chemical characterization and electrochemical measurements. The structural and chemical characterizations enable thorough understanding and explanation for the outcomes, whereas the electrochemical measurements verify the feasibility of the synthesized electrocatalysts.

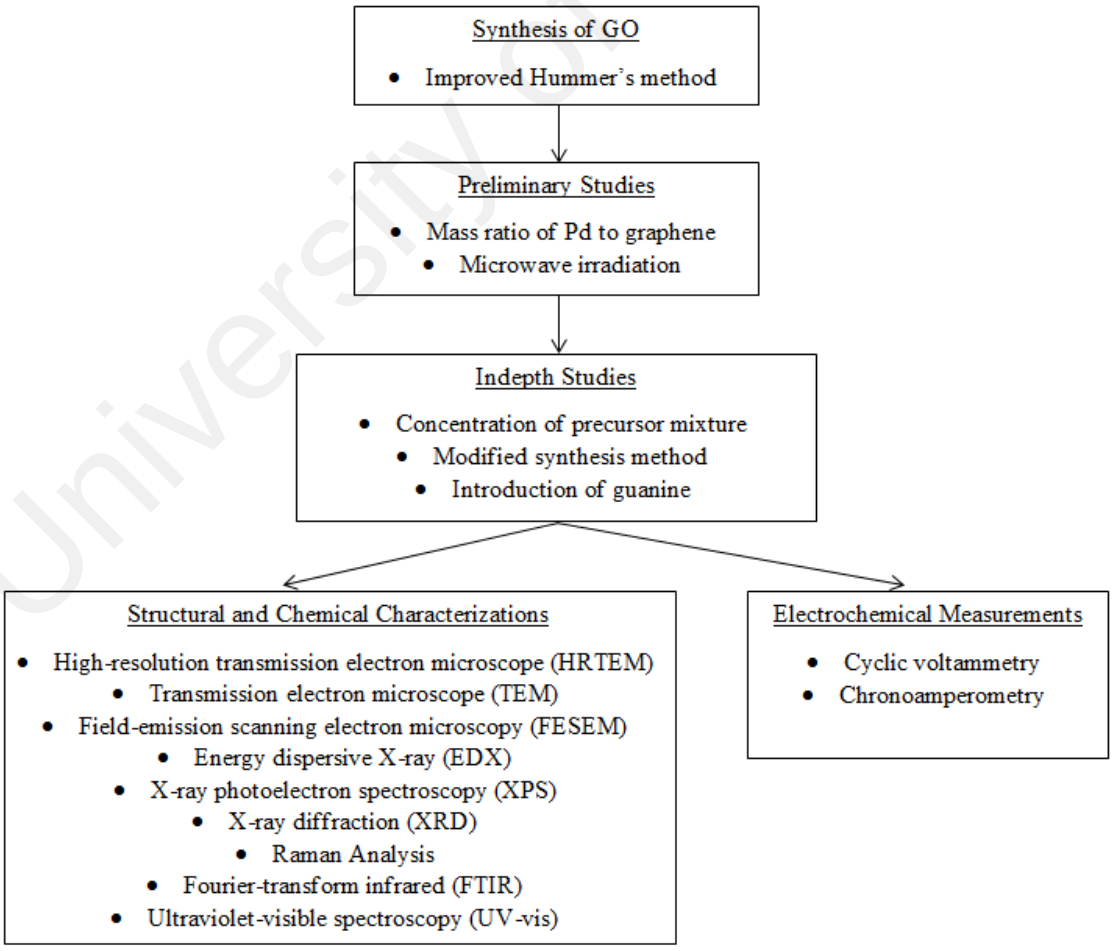

Figure 3.1: Research work flow chart.

University of Malaya

3.2 Chemicals

A graphite flake (50 mesh) was purchased from Asbury Carbons, America. Concentrated phosphoric acid (H_3PO_4), potassium permanganate ($KMnO_4$), and Na_2CO_3 were obtained from Wako Pure Chemical Industries, Ltd. Concentrated sulfuric acid (H_2SO_4), H_2O_2, fuming hydrochloric acid (HCl, 37%), $PdCl_2$, EG, nafion, guanine, sodium hydroxide (NaOH), and potassium hydroxide (KOH) were from Sigma Aldrich. All chemicals were analytically pure and used as received without further purification. The deionized (DI) water for solution preparation was produced from Advantec Aquarius RFD230NA, Japan (conductivity= 0.06 μS).

3.3 Electrocatalysts Synthesis

3.3.1 Graphite Oxide preparation

The graphite flakes are used as starting material to obtain graphene nanosheets. The synthesis began with the oxidation of graphite flakes to graphite oxide by improved Hummer's method (Chen et al., 2013). H_2SO_4 was mixed with H_3PO_4 at ratio of 360:40 mL followed by the addition of 3 g of graphite flake. Then, 18 g of $KMnO_4$ was added into the above mixture and stirred. After three days of stirring, by immersing in ice bath, 500 mL of DI water was added to the above mixture, and 17 mL of H_2O_2 was added dropwise to halt the oxidation process. The mixture was then sequentially washed with 1 M of HCl thrice at 6,000 rpm for 30 min by centrifuging. This process was followed up by using DI water for seven times at 10,000 rpm for 1 h. The synthesized graphite oxide was dried overnight at 60 °C in an oven.

University of Malaya

3.3.2 Pd/rGO Nanocomposites Preparation

3.3.2.1 Effect of mass ratio of Pd to graphene

The dried graphite oxide (120 mg) was dispersed in 80 mL of DI water, and ultrasonicated for 2 h to obtain GO. To synthesize Pd/rGO with ratio of Pd to graphene equal to 2:1, 1:1, and 0.5:1 (designated as Pd/rGO(2:1), Pd/rGO(1:1), and Pd/rGO(0.5:1), respectively), 400 mg, 200 mg, and 100 mg of $PdCl_2$ were added separately. The mixtures were sonicated for 30 min, and followed by stirring for 1 h at room temperature. Upon stirring, 80 mL of EG was added dropwise. The pH of the mixtures were then adjusted to 10 by 1 M of NaOH. Subsequently, the mixtures were reduced by microwave irradiation at 700 W for 700 s. Finally, the resulting black solid powders were washed by DI water via centrifugation at 6000 rpm for 30 min. The samples were dried overnight in an oven at 60 °C.

3.3.2.2 Effect of reduction duration

The dried graphite oxide (120 mg) was dispersed in 80 mL of DI water and ultrasonicated for 2 h to exfoliate it to GO. 200 mg of $PdCl_2$ were added to the GO solution and sonicated for 30 min, followed by 1 h stirring at room temperature. 80 mL of EG was added dropwise during the stirring process. The pH of the mixture was then adjusted to 10 by 1 M of NaOH. Subsequently, the mixture was irradiated by microwave at 700 W for 500 s, 700 s, and 900 s, designated as Pd/rGO_{500}, Pd/rGO_{700}, and Pd/rGO_{900}, respectively. Eventually, the resulting black solid powders were sequentially washed by DI water via centrifugation and dried overnight in an oven at 60 °C.

3.3.2.3 Effect of concentration of the precursor mixture solution ($PdCl_2$ + GO)

For the synthesis of Pd/rGO at concentration 0.5 mg mL^{-1}, denoted as Pd/rGO (0.5), the dried graphite oxide (30 mg) was dispersed in 80 mL of DI water, and ultrasonicated

University of Malaya

for 2 h to obtain GO. Subsequently, 50 mg of $PdCl_2$ was added and sonicated for 30 min. Then, the above mixture was stirred for 1 h at room temperature, during which 80 mL of EG was added dropwise. The pH of the mixture was then adjusted to 10 by 1 M of NaOH. Subsequently, the mixture was reduced by microwave irradiation at 700 W for 700 s. Finally, the resulting black solid powders were washed by DI water thrice via centrifugation at 6,000 rpm for 30 min and dried overnight in oven at 60 °C. Samples at concentrations of 1.0, 2.0, 3.0, and 4.0 mg mL^{-1} (denoted as Pd/rGO (1.0), Pd/rGO (2.0), Pd/rGO (3.0), and Pd/rGO (4.0), respectively) were synthesized by repeating the above procedures with 60, 120, 180, and 240 mg of GO, and 100, 200, 300, and 400 mg of $PdCl_2$, respectively.

3.3.2.4 A modified synthesis method (Pd/rGO_M)

The dried graphite oxide (120 mg) was dispersed in 80 mL of DI water by 2 h of ultrasonicated to obtain GO. $PdCl_2$ (200 mg) was then added and sonicated for 30 min. The process was followed by 1 h of stirring at room temperature. On the other side, 200 mg of Na_2CO_3 was added to 80 mL of EG, and microwave-irradiated for 100 s at 700 W. Then, the room temperature mixture that had been stirred was added to the pre-irradiated EG and Na_2CO_3 and microwave-irradiated for another 600 s. Finally, the resulting black solid powders were washed by DI water thrice via centrifugation at 6,000 rpm for 30 min and dried overnight in oven at 60 °C.

3.3.2.5 Palladium nanoparticles on guanine functionalized reduced graphene oxide (Pd/rGO_G)

The dried graphite oxide (120 mg) was dispersed in 80 mL of DI water and ultrasonicated for 2 h to obtain GO. Guanine (200 mg) was added and stirred for another 30 min. Then, $PdCl_2$ (200 mg) was added and sonicated for 30 min followed by 1 h stirring at room temperature. Upon stirring, 80 mL of EG was added dropwise. The pH

University of Malaya

of the mixture was then adjusted to 10 by 1 M of NaOH. Subsequently, the mixture was microwave reduced by microwave oven at 700 W for 700 s. Finally, the resulting black solid powders were washed by DI water thrice via centrifugation at 6,000 rpm for 30 min and dried overnight in oven at 60 °C.

3.4 Structural and Chemical Characterization

The characterization techniques discussed below involve FESEM, EDX, TEM, HRTEM, XRD, Raman analysis, UV-vis, FTIR, and XPS.

3.4.1 Field-emission Scanning Electron Microscopy/Energy Dispersive X-Ray

Field-emission scanning electron microscopy (FESEM)(HITACHI S-4800) was used to characterize the morphology of the electrocatalysts and verify the successful loading of Pd NPs on rGO. FESEM was also used to examine the chemical composition of specimen by equipping with energy-dispersive X-ray (EDX). FESEM is an advanced scanning electron microscopy (SEM) that uses a field emission type gun. This kind of gun emits electron beam with high beam brightness (Leng, 2009, p. 127). FESEM captures images by scanning over the surface of the specimen by a focused electron beam. The high-energy electrons hit on the sample, producing either inelastic or elastic scattering. The inelastic scattering ejects electrons from atoms of the sample and this kind of electron signal is known as secondary electrons. Meanwhile, another electron signal, namely, backscattered electrons (the incident electrons scattered by atoms of the sample) are produced in the case of elastic scattering (Leng, 2009, p. 130). The secondary electrons and backscattered electrons are the signal source to form FESEM images, where the formal is used for surface topographic images and the latter is for the purpose of compositional images. To prepare the specimen for FESEM analysis, the

University of Malaya

sample was dispersed by sonication in DI water for 10 min. A drop of the solution was subsequently deposited onto the silicon wafer. Notably, surface contaminants should always be avoided. Thus, the silicon wafers need to be cleaned by acetone or methanol in an ultrasonic cleaner before the deposition of sample solution. Touching with bare hands on the cleaned silicon wafer is also prohibited because our fingerprints contain volatile hydrocarbon compounds. The electron beam can decompose the hydrocarbon compounds, leaving a deposit of carbon on the surface.

3.4.2 Transmission Electron Microscopy/High-resolution Transmission Electron Microscopy

Similar to FESEM, transmission electron microscopy (TEM) and high-resolution transmission electron microscopy (HRTEM) (FEI Tecnai F20) are applied to study the surface morphology of the samples, but in much higher resolution and magnification due to the short de Broglie wavelength of electrons. The wavelength of electrons is approximately 10,000 times shorter than that of visible light (Leng, 2009, p. 83). The high resolution allows the measurement of particle size. Measurement of lattice spacing of Pd NPs is even possible by using HRTEM. The specimen for both TEM and HRTEM is the same. First, the sample was sonicated in DI water for 10 min. Next, copper grid was dipped into the specimen solution and let dry at room temperature.

3.4.3 X-ray Diffraction

X-ray diffraction is an effective approach to characterize the particle size and crystalline structure of materials. Based on the crystalline structure, the identity of chemical compound can be defined. X-ray, high-energy beam of electromagnetic radiation with short wavelength, incident on the sample is diffracted. The interaction of the incident wave and the deflected wave gives information on the interplanar spacing from the Bragg's Law (Equation 4):

University of Malaya

$$n\lambda = 2d \sin\theta \quad (4)$$

Where n is an integer, λ is wavelength of X-rays, d is the interplanar spacing, and θ is the diffraction angle. From the XRD data, mean Pd particle size can also be calculated from Scherrer's equation (Equation 5):

$$d = K\lambda/(B \cos\theta) \quad (5)$$

Where *d* is the particle diameter (nm), K is the shape factor, B is the full width at half-maximum (FWHM) of the peak of the interest, and θ is the Bragg angle of the peak.

The XRD analysis was performed by using an Ultima IV X-ray Diffractometer (Rigaku, America) with a Cu X-ray source (λ = 0.1541 nm) operating at 40 kV and 40 mA over a 2θ = 5° to 90°, with a step size of 0.05°.

3.4.4 Raman Analysis

Raman spectroscopy operates on the theory of Raman scattering phenomenon of electromagnetic radiation by molecules (Leng, 2009, p. 287). It is a common technique to study the defect levels, crystallinity, and structure of both organic and inorganic materials. Notably, metallic materials cannot be examined because they will strongly reflect electromagnetic waves. The electromagnetic radiation with single frequency irradiated on materials is elastically and inelastically scattered by the molecules. The elastic scattering is known as Rayleigh scattering. Meanwhile inelastic scattering is named as Raman scattering. The Rayleigh and Raman scattered light exhibit the same and different frequency as that of the incident radiation, respectively. The frequency change of the incident radiation and scattered light is called the Raman shift, providing information about the molecular vibrational behaviour. Each chemical bond of

University of Malaya

molecules has specific vibrational frequency, enabling the identification of the molecule and chemical bonding. The Raman shift is typically plotted over a range of wavenumbers (800–3500 cm^{-1}) with the unit of inverse length. For the Raman measurement, the sample preparation is similar to that of FESEM preparation. The procedure was performed by a JASCO NRS-3100 equipped with a charge-coupled-device (CCD) detector by using Argon ion at a wavelength of 532 nm.

3.4.5 Ultraviolet-visible Spectroscopy

Ultraviolet-visible spectroscopy (UV-vis) examines absorbance or transmittance from the UV range (200-400 nm) to the visible wavelength range (400-700 nm) to explore the interaction between guanine and rGO. The reduction of Pd ions to NPs can also be determined by UV-vis (PerkinElmer Spectrum 400). The wavelengths of absorbance/transmittance peaks can be associated with the functional groups and types of bonds in a given molecule. The sample for measurement was in liquid form. A small amount of sample was dispersed in DI water by sonication for 30 min and placed in a transparent rectangular quartz glass cuvette with 1 cm internal width.

3.4.6 Fourier-transform Infrared Spectroscopy

Fourier-transform infrared spectroscopy (FTIR) was performed to verify the successful reduction of GO and investigate the interaction between guanine and rGO. FTIR is an infrared spectroscopy applying the Fourier transform method to get infrared spectrum in the wavenumber range of 500 cm^{-1} to 4000 cm^{-1} (Leng, 2009, p. 297). For the FTIR measurement, pellet sample is required. The pellet sample was prepared by transferring approximately 2 mg of sample and approximately 300 mg of potassium bromide (KBr) powder into an agate mortar. Notably, the KBr powder needs to be spectroscopically dry and be spectroscopic grade purity. The mixture powders were then ground to well dispersion and transferred to the die. Subsequently, the die was placed

University of Malaya

into a hydraulic press and pressed to 15 tons. The pressure was slowly released after approximately 1 min. Finally, the translucent sample pellet was removed from the die.

3.4.7 X-ray Photoelectron Spectroscopy

X-ray photoelectron spectroscopy (ULVAC-PHI Quantera II; Software: Multipak Smartsoft) is a technique for surface chemical analysis, revealing the elemental composition, electronic states, and chemical states of the sample (Leng, 2009, p. 221). The chemical elements are determined from the binding energy spectra of X-ray photoelectrons. Each binding energy peak carries the information of element symbol and a shell symbol. The X-ray photoelectron is an electron ejected from an electron shell of an atom when the atom absorbs an X-ray photon (Leng, 2009, p. 221). Notably, only materials with atomic numbers equal to or greater than 3 can be analyzed by XPS. The orbital number of helium or hydrogen is too small for the measurement.

3.5 Electrochemical Measurement

The electrocatalytic activities of the synthesized samples were examined by electrochemical test. All the electrochemical experiments were examined with a conventional three-electrode electrochemical cell (Solartron 1280C with computerized control by ZPlot software) at room temperature. A Pt sheet with a size of 1 cm^2, Ag/AgCl (3 M potassium chloride (KCl)) electrode, and glassy carbon electrode (GCE, 3.0 mm diameter) were used as counter, reference, and working electrodes, respectively.

To prepare the working electrode, 2 mg as-prepared catalysts were first dispersed in 1 mL of DI water and ultrasonicated for 30 min. Then, 10 μL of the suspension was casted onto the surface of the polished GCE and dried in an oven at 60 °C. Subsequently, 5 μL of Nafion (0.05 wt%) was dropped onto the electrode surface and dried at 60 °C in the oven.

University of Malaya

The ECSA of each electrocatalyst was studied via CV measurement in a solution of 1 M KOH from −1.0 V to 0.6 V vs. Ag/AgCl. Meanwhile, the methanol oxidation activity was investigated via CV measurements in 1 M KOH + 1 M methanol at a similar potential range. All electrochemical tests were carried out at a scan rate of 50 mV s^{-1} for 10 runs. CA measurements were studied in the same methanol-contained KOH solution at an applied voltage of −0.2 V for 1000 s. Electrolytes were all purged with N_2 gas for 30 min to remove any dissolved oxygen prior to the measurements.

In summary, GO was obtained by improved Hummer's method. The Pd/rGOs were then synthesized by microwave-reduction method from five different considerations: (i) mass ratio of Pd to graphene, (ii) microwave irradiation duration, (iii) concentration of precursor mixture ($PdCl_2$ + GO), (iv) modified synthesis method, and (v) introduction of guanine that acts as interlinker between graphene and Pd. The obtained samples were then send for different structural and chemical characterization, involving XPS, HRTEM, TEM, FESEM, EDX, XRD, UV-vis, FTIR, and raman analysis. Electrochemical measurements were also conducted to study the electrochemical performance.

University of Malaya

CHAPTER 4: RESULTS AND DISCUSSION

4.1 Effect of Mass Ratio of Pd to Graphene

4.1.1 Structural and Chemical Characterizations

Figure 4.1 demonstrates XRD data of GO and Pd/rGOs prepared at various ratios. The peak at 10.3° was the typical peak of GO. The GO peak disappeared and new weak broad peak located at 24° appeared upon reduction, signaling the successful reduction of Pd/rGO of all ratios. The deposition of Pd NPs can be proven by the peaks at approximately 40.1°, 46.5°, 68.2°, 82.1°, and 86.7° that were attributed to the (111), (200), (220), (311), and (422) lattice planes of the Pd with fcc crystalline structure (JCPDS No. 46-1043), respectively. By using Scherrer's formula based on Pd(220) peak, the crystallite sizes of Pd/rGO(0.5:1), Pd/rGO(1:1), and Pd/rGO(2:1) were calculated to be 12.19, 7.57, and 13.62 nm, respectively. Noteworthily, the Pd(220) peak was selected for the calculation of crystallite size because this peak is not affected by the presence of graphene.

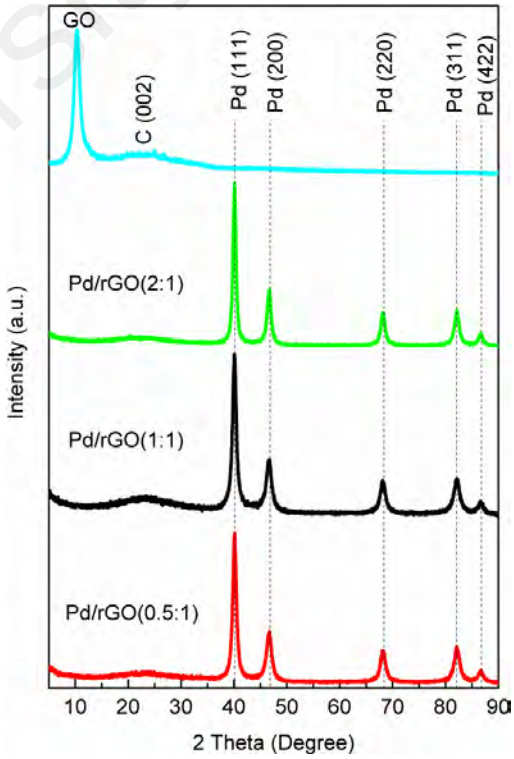

Figure 4.1: XRD images of Pd/rGO(0.5:1), Pd/rGO(1:1), Pd/rGO(2:1), and GO.

University of Malaya

Wrinkles and ripples induced by the removal of the oxygenated groups of GO can be observed on all the Pd/rGOs of various ratios (Figures 4.2A–4.2C)). The density of Pd NPs deposited on the surface of rGO increased by increasing the mass ratio. The agglomeration of Pd NPs also became significant with the increased mass ratio and thus agglomeration of Pd/rGO(2:1) was the most severe.

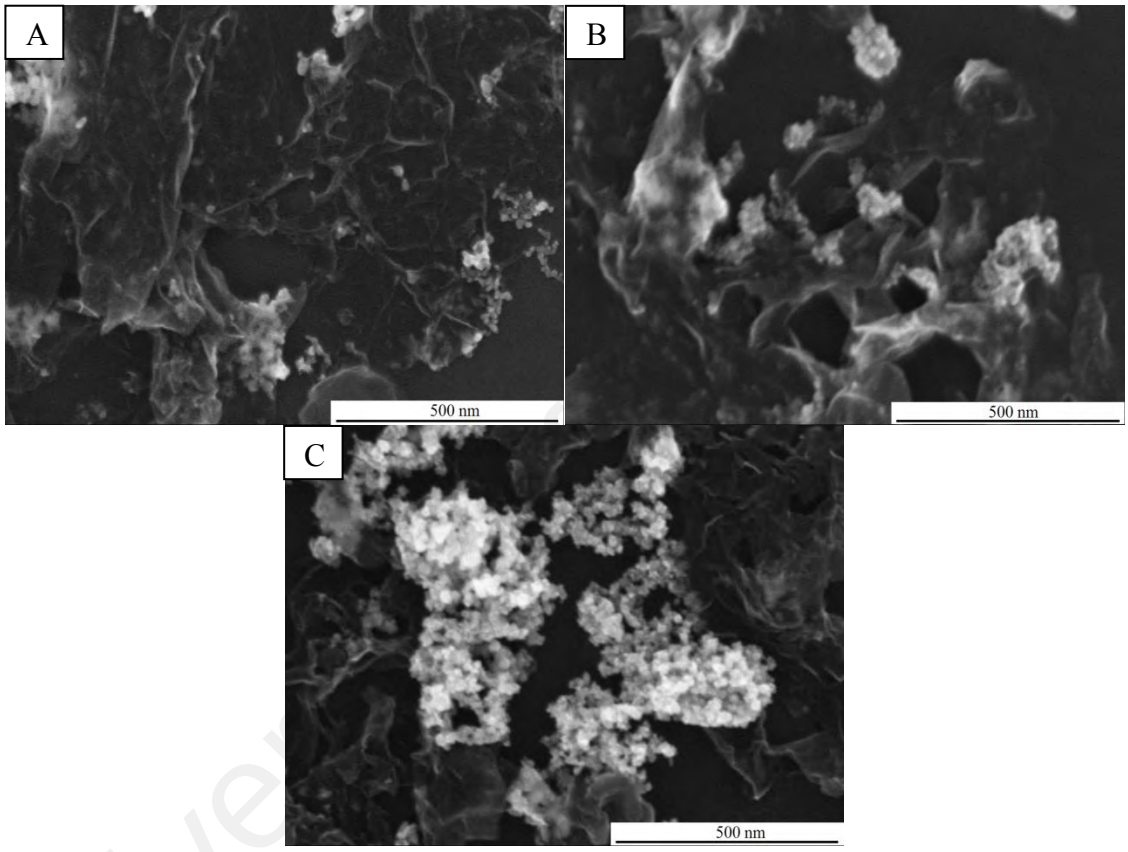

Figure 4.2: FESEM images of (A) Pd/rGO(0.5:1), (B) Pd/rGO(1:1), and (C) Pd/rGO(2:1).

Raman analysis was characterized to study the quality and defect level of rGO. Two sharp peaks corresponding to D band and G band that located at 1330–1350 cm^{-1} and approximately 1590 cm^{-1}, respectively, can be observed in Figure 4.3. The D band conveyed the information of the structural disorder or intrinsic defects due to an A_{1g} vibrational mode. Meanwhile, the G band correlated to the first-order scattering of the E_{2g} mode of graphite that was associated to the coplanar vibration of sp^2-hybridized

carbon atoms in a two-dimensional hexagonal lattice (Zhao et al., 2015). Two weak broad peaks associated to 2D and D+G bands that implied the local disorder and defects in the sp^2 phase of the rGO-based nanocomposite also exist (Zhao et al., 2011). The 2D peaks located below 2700 cm^{-1} signified the obtained samples were in few-layered structure (Videla et al., 2014). The smaller wavenumber of 2D peak (Pd/rGO(2:1) = 2629.46 cm^{-1}; Pd/rGO(1:1) = 2665.12 cm^{-1}; Pd/rGO(0.5:1) = 2667.59 cm^{-1}) with increased mass ratio proved that the graphene sheets were less restacked. The intensity ratio of D band to G band ($\frac{I_D}{I_G}$) delivers the message of defect density of graphene. The increased ratio (Pd/rGO(2:1) = 1.204, Pd/rGO(1:1) = 1.05, and Pd/rGO(0.5:1) = 1.02) compared with GO (1.00) confirmed the successful reduction of GO, and deposition of Pd NPs on rGO (Chen et al., 2015; Ji et al., 2014). It has been claimed that the defects on rGO act as NCC for the coalescence of Pd NPs at its vicinity (Martins et al., 2014). These findings well explained the observations in the FESEM images.

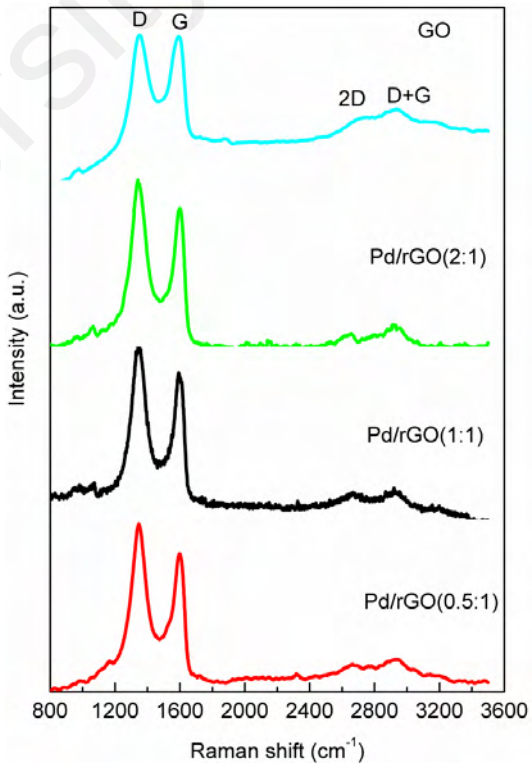

Figure 4.3: Raman image of Pd/rGO(0.5:1), Pd/rGO(1:1), Pd/rGO(2:1), and GO.

University of Malaya

4.1.2 Electrochemical Measurements

The ECSA of the electrocatalysts accounts for the number of catalytic sites that are active for electrochemical reaction and provides information on the conductive path accessible for electron transfer to and from the electrode surface (Hsieh et al., 2013; Zheng et al., 2014). The value of ECSA was calculated from the area of reduction peak of palladium oxide (PdO) in the potential region of −0.7 to −0.2 V vs. Ag/AgCl on the CV in Figure 4.4A according to Equation 6 (Qi et al., 2016):

$$\text{ECSA} = \frac{Q}{Sl} \tag{6}$$

where "Q" is the coulombic charge (mC) for the PdO reduction, "S" is a conversion factor corresponding to 0.424 mC cm^{-2}, and "l" is the mass of catalyst (mg) loaded on the GCE (Qi et al., 2016). The ECSA values were calculated to be 19.81, 63.80, and 59.57 $m^2 g^{-1}$ for Pd/rGO(2:1), Pd/rGO(1:1), and Pd/rGO(0.5:1), respectively. Therefore, the low density of Pd NPs of Pd/rGO(0.5:1) did not provide sufficient active sites and agglomeration of Pd/rGO(2:1) has greatly reduced the active surface area for electro-oxidation of methanol.

University of Malaya

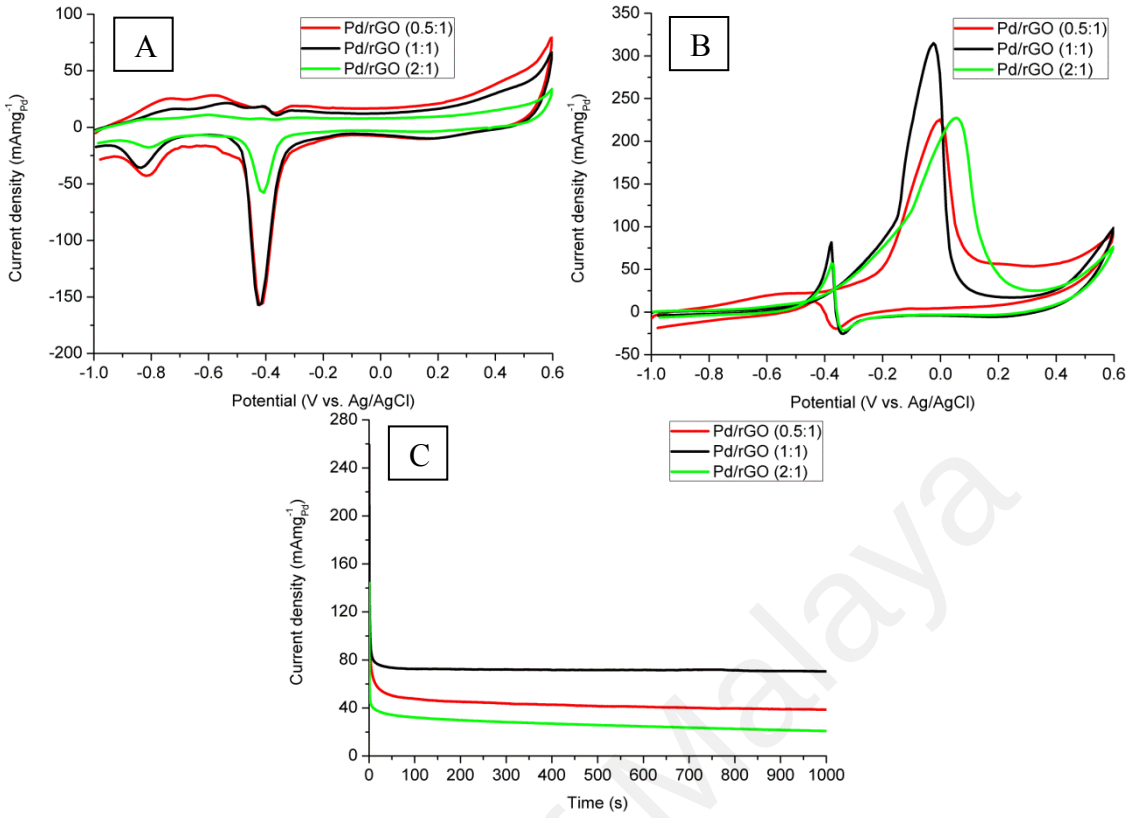

Figure 4.4: Cyclic voltammograms of Pd/rGO(0.5:1), Pd/rGO(1:1), and Pd/rGO(2:1) in nitrogen saturated solutions of (A) 1 M KOH and (B) 1 M KOH/ 1 M CH_3OH with scan rate of 50 mV s^{-1}. (C) Chronoamperogram of Pd/rGO(0.5:1), Pd/rGO(1:1), and Pd/rGO(2:1) in nitrogen saturated solutions of 1 M KOH/ 1 M CH_3OH with scan rate of 50 mV s^{-1} at an applied potential of −0.2 V.

As shown in Figure 4.4B, Pd/rGO(1:1) attained the best MOR activity, which is 314.94 mA mg^{-1} compared with Pd/rGO(2:1) and Pd/rGO(0.5:1) with 227.93 and 226.42 mA mg^{-1}, respectively. The Pd/rGO (1:1) also reported the most negative onset potential (E_{onset}) (−0.43 V) and peak potential (E_{peak}) (−0.07 V), whereas Pd/rGO (2:1) (E_{onset} = −0.21 V; E_{peak} = 0.05 V) and Pd/rGO(0.5:1) (E_{onset} = −0.40 V; E_{peak} = −0.0023 V) were slightly more positive. The undesired great positive-shift in onset potential and peak potential of Pd/rGO(0.5:1) can be explained by the insufficient number of Pd NPs to catalyse the reaction.

CA (Figure 4.4C) was conducted to evaluate the stability of the as-synthesized electrocatalysts. At the first 50 s, the current dropped rapidly due to the coverage of active sites by the poisoning intermediate species during the methanol oxidation (Ma et

University of Malaya

al., 2013). Further operation oxidized the intermediate species, releasing the active sites (Kakaei & Dorraji, 2014). Thus, the current density decreased steadily. The small size, moderate defect level, and well catalyst particles distribution rendered Pd/rGO(1:1) the best durability. Owing to the fact that the defects served as the sites where corrosion occurred easily during the electrochemical operation, the Pd/rGO (2:1) with high defect level retained the lowest current density (Zhao et al., 2015).

4.2 Effect of Reduction Duration

4.2.1 Structural and Chemical Characterizations

Figure 4.5 shows the XRD conducted on Pd/rGO_{500}, Pd/rGO_{700}, Pd/rGO_{900}, and GO to investigate their size and crystalline phase structures. It can clearly be observed that the representative peak of GO at 10.3° disappeared and a weak broad C(002) peak emerged at 24° for Pd/rGO_{700}, and Pd/rGO_{900}. Such phenomenon marked the GO was successfully reduced to rGO (Videla et al., 2014). Viewing the peak of Pd/rGO_{500}, the GO peak was still discernible despite the intensity was greatly reduced. Therefore, 500 s is too short for the complete reduction process. Peaks at approximately 40.1°, 46.5°, 68.2°, 82.1°, and 86.7° were attributed to the (111), (200), (220), (311), and (422) lattice planes of the fcc of Pd (JCPDS No. 46-1043), respectively. The 700 s seemed to be the optimum reduction duration as its particles size is smaller than the Pd/rGO_{900} (7.57 vs. 12.75 nm) based on the calculation from the Pd (220) peak by using Scherrer's formula. Prolonged synthesis time caused the individual particles to combine together into large structures to decrease the overall surface energy and thus the obtained larger particle size of Pd/rGO_{900}.

University of Malaya

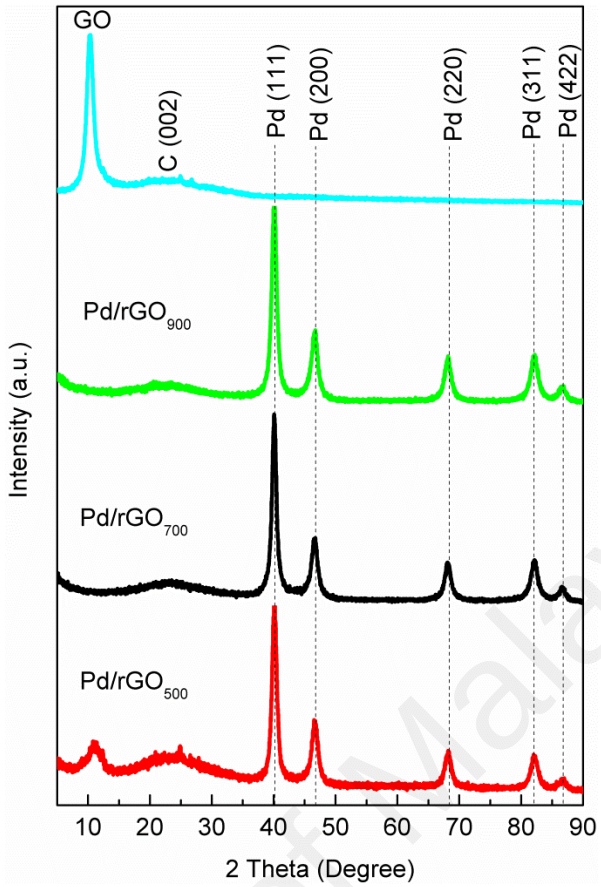

Figure 4.5: XRD images of Pd/rGO_{500}, Pd/rGO_{700}, Pd/rGO_{900}, and GO.

Figures 4.6A–4.6C are the FESEM images of Pd/rGO_{500}, Pd/rGO_{700}, and Pd/rGO_{900}, respectively. Wrinkles and ripples can clearly be observed on the rGO sheets. A small number of Pd NPs were anchored on rGO because of the incomplete reduction at 500 s. By contrast, slight agglomeration was observed on the Pd/rGO_{700}. As for Pd/rGO_{900}, serious conglomeration occurred.

University of Malaya

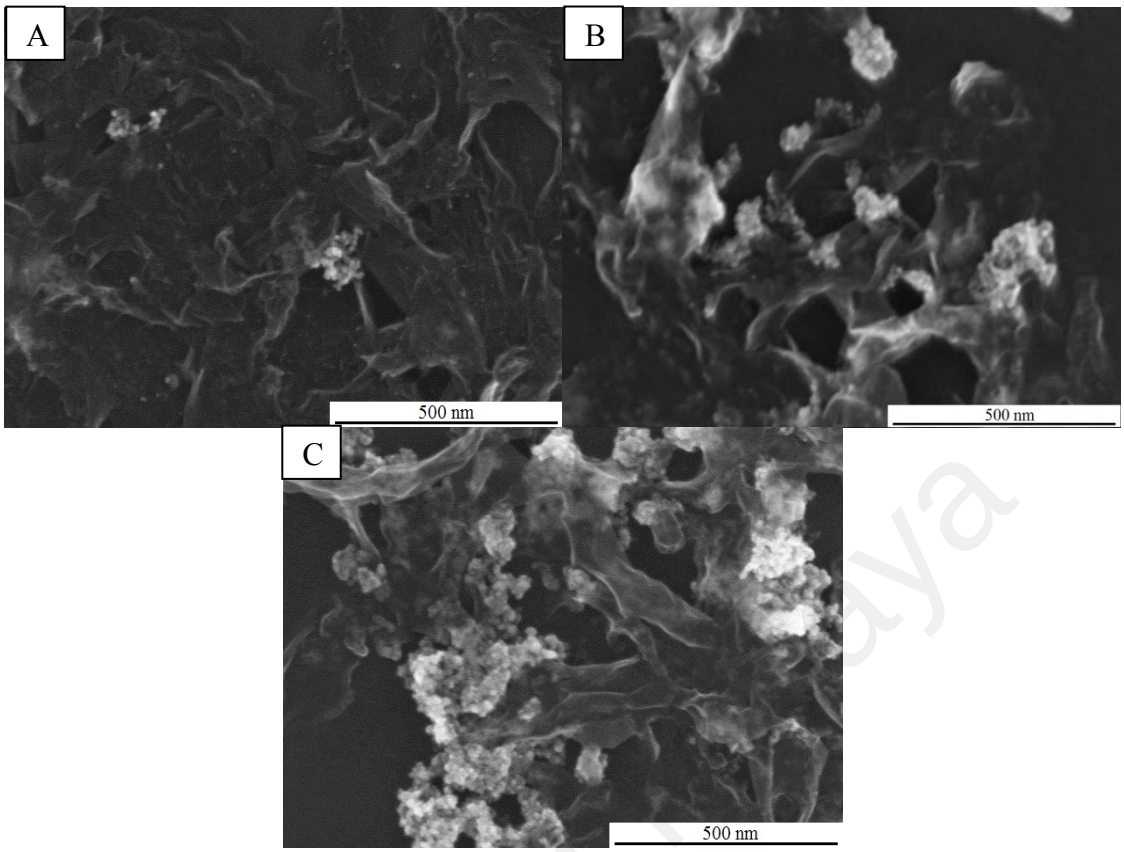

Figure 4.6: FESEM images of (A) Pd/rGO$_{500}$, (B) Pd/rGO$_{700}$, and (C) Pd/rGO$_{900}$.

Similar to previous Raman spectrum, four peaks of D band, G band, 2D band, and (D+G) band located at 1330-1350 cm^{-1}, ~1590 cm^{-1}, ~2650 cm^{-1}, and ~2926 cm^{-1}, respectively, can be noticed in Figure 4.7. The existence of 2D band below 2700 cm^{-1} signified the as-obtained rGO nanosheets were in few-layered structure. Findings discorvered that the longer the reduction duration led to larger $\frac{I_D}{I_G}$. The recorded $\frac{I_D}{I_G}$ of Pd/rGO$_{500}$, Pd/rGO$_{700}$, and Pd/rGO$_{900}$ were 1.04, 1.05, and 1.12, respectively. The increased ratios of the nanocomposites relative to the GO verified that the GO was reduced concurrently with the deposition of Pd NPs on its surface. As mentioned in the previous section, the defects are the NCC where agglomeration occurs, illustrating the severe agglomeration of Pd/rGO$_{900}$.

University of Malaya

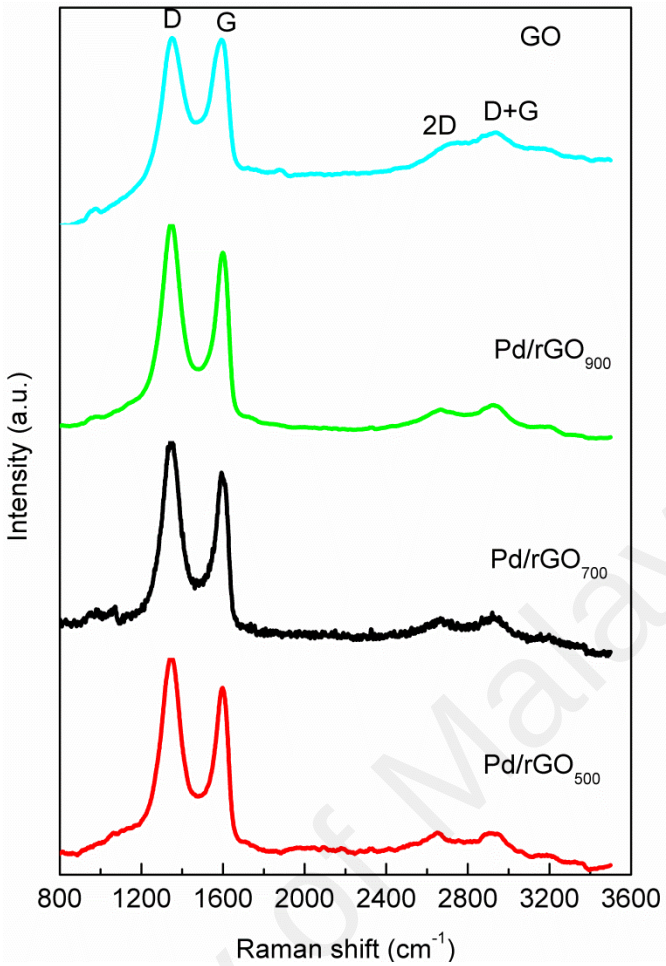

Figure 4.7: Raman image of Pd/rGO_{500}, Pd/rGO_{700}, Pd/rGO_{900}, and GO.

4.2.2 Electrochemical Measurements

In the context of ECSA (Figure 4.8A), Pd/rGO_{500}, Pd/rGO_{700}, and Pd/rGO_{900} amounted to 11.31, 63.80, and 61.55 $m^2\ g^{-1}$ as recorded in Table 4.1. As known, GO is an insulator and reduction is required to recover the unique properties of graphene. The incomplete recovery of the graphene properties and low density of Pd NPs explained the low ECSA of Pd/rGO_{500}. At the satisfactory degree of GO reduction, the even distribution of Pd NPs with slight agglomeration served as the major governing factor to the high ECSA of Pd/rGO_{700}.

University of Malaya

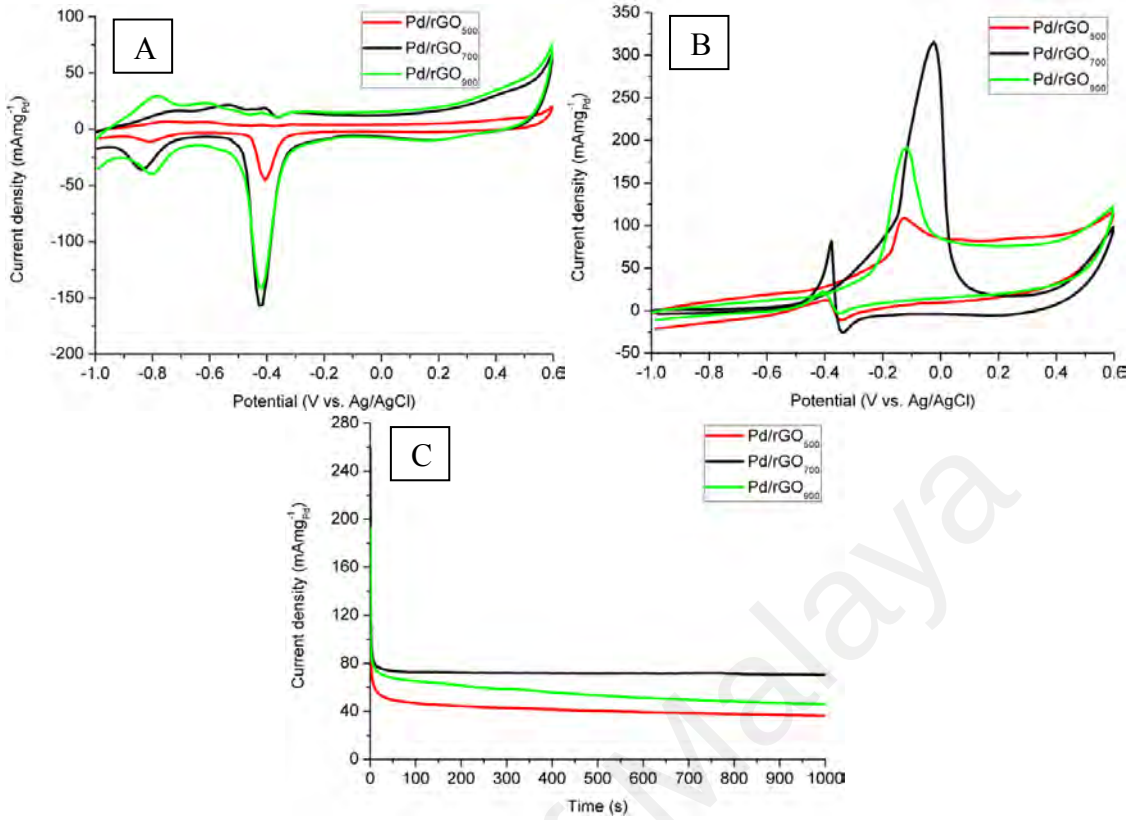

Figure 4.8: Cyclic voltammograms of Pd/rGO_{500}, Pd/rGO_{700}, and Pd/rGO_{900} in nitrogen saturated solutions of (A) 1 M KOH and (B) 1 M KOH/ 1 M CH_3OH with scan rate of 50 mV s^{-1}. (C) Chronoamperogram of Pd/rGO_{500}, Pd/rGO_{700}, and Pd/rGO_{900} in nitrogen saturated solutions of 1 M KOH/ 1 M CH_3OH with scan rate of 50 mV s^{-1} at an applied potential of −0.2V.

Table 4.1: The ECSA, peak current density (I_{peak}), and E_{onset} of Pd/rGO_{500}, Pd/rGO_{700}, and Pd/rGO_{900}.

Electrocatalysts	ECSA, ($m^2\ g^{-1}$)	I_{peak}, (mA mg^{-1})	E_{onset}, (V vs. Ag/AgCl)
Pd/rGO_{500}	11.31	108.75	−0.36
Pd/rGO_{700}	63.80	314.94	−0.43
Pd/rGO_{900}	61.55	191.37	−0.39

In Figure 4.8B, Pd/rGO_{700} attained the best MOR with highest I_{peak} and most negative E_{onset}. The Pd/rGO_{700} also marked victory in the aspect of stability as illustrated in Figure 4.8C. It can be concluded that complete reduction was essential and agglomeration was highly unintended for enhanced electrocatalysts. In brief, 700 s is the optimum synthesis duration.

University of Malaya

4.3 Effect of Concentration of the Precursor Mixture Solution ($PdCl_2$ + GO)

4.3.1 Structural and Chemical Characterizations

Figure 4.9 shows the XRD of GO, rGO, and Pd/rGOs at different concentrations. All samples were successfully reduced by microwave irradiation as reflected by the disappearance of the peak of GO at 10.3°, and emergence of weak broad C(002) peak of rGO at 24^o (Videla et al., 2014). Meanwhile, the peaks at approximately 40.1°, 46.5°, 68.2°, 82.1°, and 86.7° can be indexed to the (111), (200), (220), (311), and (422) lattice planes of the fcc crystalline structure of Pd (JCPDS No. 46-1043), respectively. By using Scherrer's formula based on the Pd (220) peak, the Pd particle sizes were calculated to be 8.69, 8.08, 7.57, 8.32, and 8.64 nm for Pd/rGO (0.5), Pd/rGO (1.0), Pd/rGO (2.0), Pd/rGO (3.0), and Pd/rGO (4.0), respectively. Increasing the concentration to 1.0 mg mL^{-1}, the particle size became smaller. Such phenomenon can be rationalized by Figure 4.10. The nucleus formed is stable only when it overcomes the critical energy (ΔG*) and exceeds the critical size (r*). Equations 7–11 are the related formulas (Cao, 2004):

$$\Delta G^* = \frac{16\pi\gamma}{(3\Delta G_v)^2} \quad (7)$$

$$\Delta G_v = -\frac{kT}{\Omega} \ln\left(\frac{C}{C_o}\right) \quad (8)$$

$$\Delta G_v = -\frac{kT}{\Omega} \ln(1+\dot{O}) \quad (9)$$

$$\dot{O} = C\text{-}C_o/C_o \quad (10)$$

$$r^* = \frac{-2\gamma}{\Delta G_v} \quad (11)$$

University of Malaya

where γ is the surface energy per unit area of the formed nucleus, ΔG_v is the change of Gibbs free energy per unit volume of the nucleus, C is the concentration of the solute, C_o is the equilibrium concentration or solubility, k is the Boltzmann constant, T is the temperature, and $\dot{O}$ is the supersaturation. From equations 7–11, the critical size and critical energy can be reduced with increased supersaturation that relates to concentration. High initial concentration favoured the formation of a large number of nuclei, signifying smaller sized nuclei (Cao, 2004). Nevertheless, further increment of concentration beyond 1.0 mg mL^{-1} resulted to big Pd NPs. At concentration beyond 1.0 mg mL^{-1}, the newly formed small nuclei have high surface energy, causing it to be unstable. Thus, the small nuclei tend to grow bigger by Ostwald ripening and agglomerate to reduce the surface energy (Cao, 2004). At concentration beyond 1.0 mg mL^{-1}, nuclei are in close proximity and collide with each other all the time, resulting in large agglomeration and high growth rate (Cao, 2004).

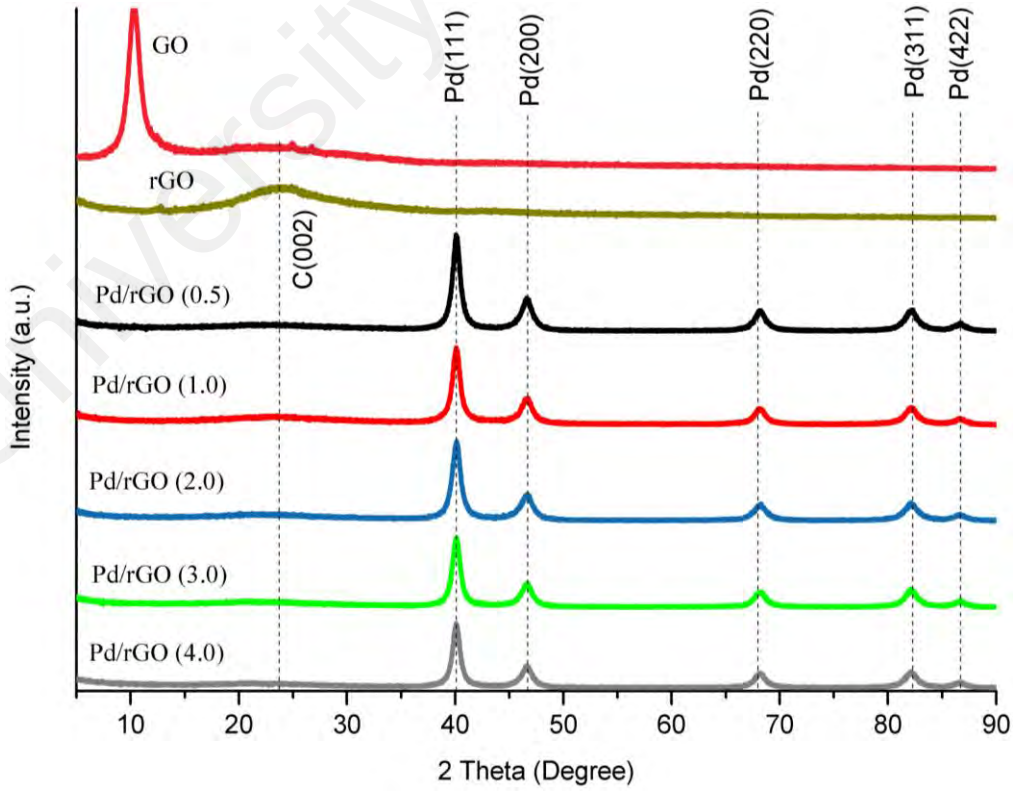

Figure 4.9: XRD images of Pd/rGO (0.5), Pd/rGO (1.0), Pd/rGO (2.0), Pd/rGO (3.0), Pd/rGO (4.0), rGO, and GO.

University of Malaya

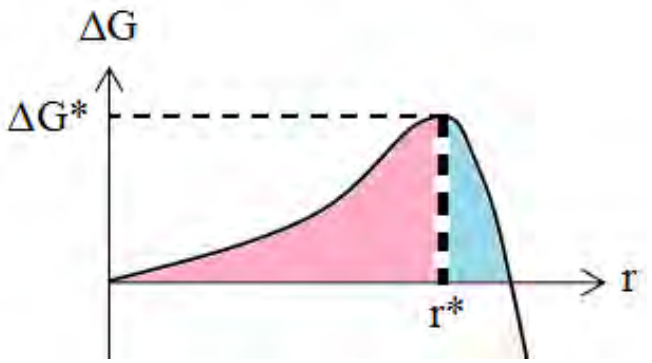

Figure 4.10: Figure illustrating the change of total free energy, ΔG, as a function of the nucleus' radius, r.

Figures 4.11A–4.11E and Figures 4.11F–4.11J show FESEM and TEM images, respectively, of the Pd/rGOs at different concentrations. Mean particle size as well as size distribution were calculated from randomly selected 50 NPs and are shown in Figures 4.11K–4.11O. Pd NPs and agglomerates are shown by red arrows and red circles/ovals, respectively. Pd NPs can be observed on the surface of wrinkled and wavy rGO for all samples. Pd NPs appeared as white particles and black dots on the transparent rGO sheets in the FESEM and TEM images, respectively. Serious agglomeration with wide size distribution occurred at Pd/rGO (0.5) because the low concentration of GO was unable to stabilize the Pd NPs. At concentration 1.0 mg mL^{-1}, the agglomeration was alleviated. The GO is at appropriate concentration to stabilize the Pd NPs, uniformly distributing the Pd NPs on rGO surface and contributing to narrow size distribution. Further increment in concentration beyond 1.0 mg mL^{-1} resulted to wide particle size range and serious agglomeration because of the close proximity between neighboring particles. The particles agglomerated together to reduce surface energy, causing adverse effect. The tendency of agglomeration of NPs exceeded the stabilizing effect of GO for concentrated precursor mixture with concentration beyond 1.0 mg mL^{-1}.

University of Malaya

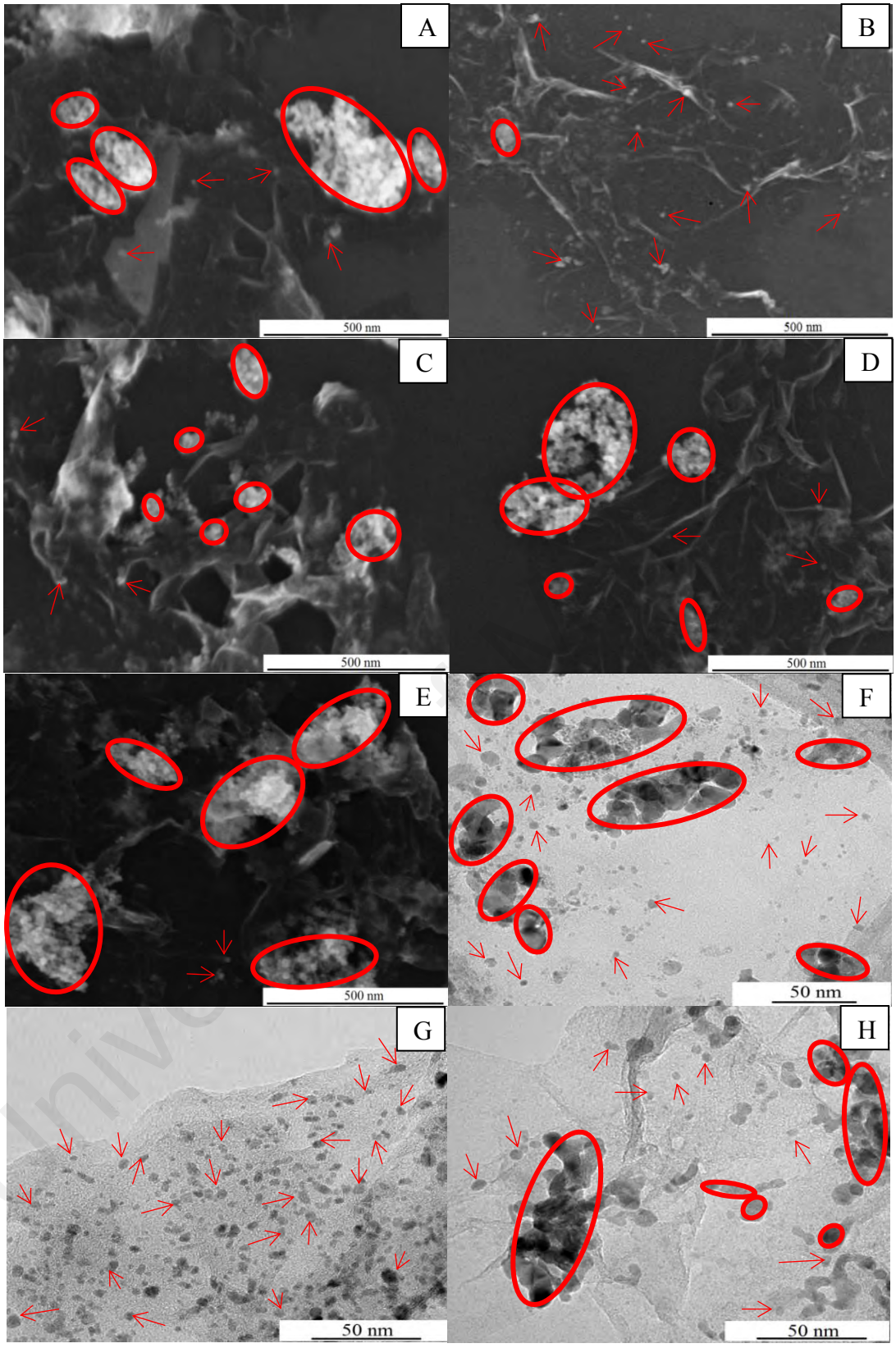

Figure 4.11: FESEM images of (A) Pd/rGO (0.5), (B) Pd/rGO (1.0), (C) Pd/rGO (2.0), (D) Pd/rGO (3.0), and (E) Pd/rGO (4.0). TEM images of (F) Pd/rGO (0.5), (G) Pd/rGO (1.0), (H) Pd/rGO (2.0), (I) Pd/rGO (3.0), and (J) Pd/rGO (4.0). NP size distributions of (K) Pd/rGO (0.5), (L) Pd/rGO (1.0), (M) Pd/rGO (2.0), (N) Pd/rGO (3.0), and (O) Pd/rGO (4.0).

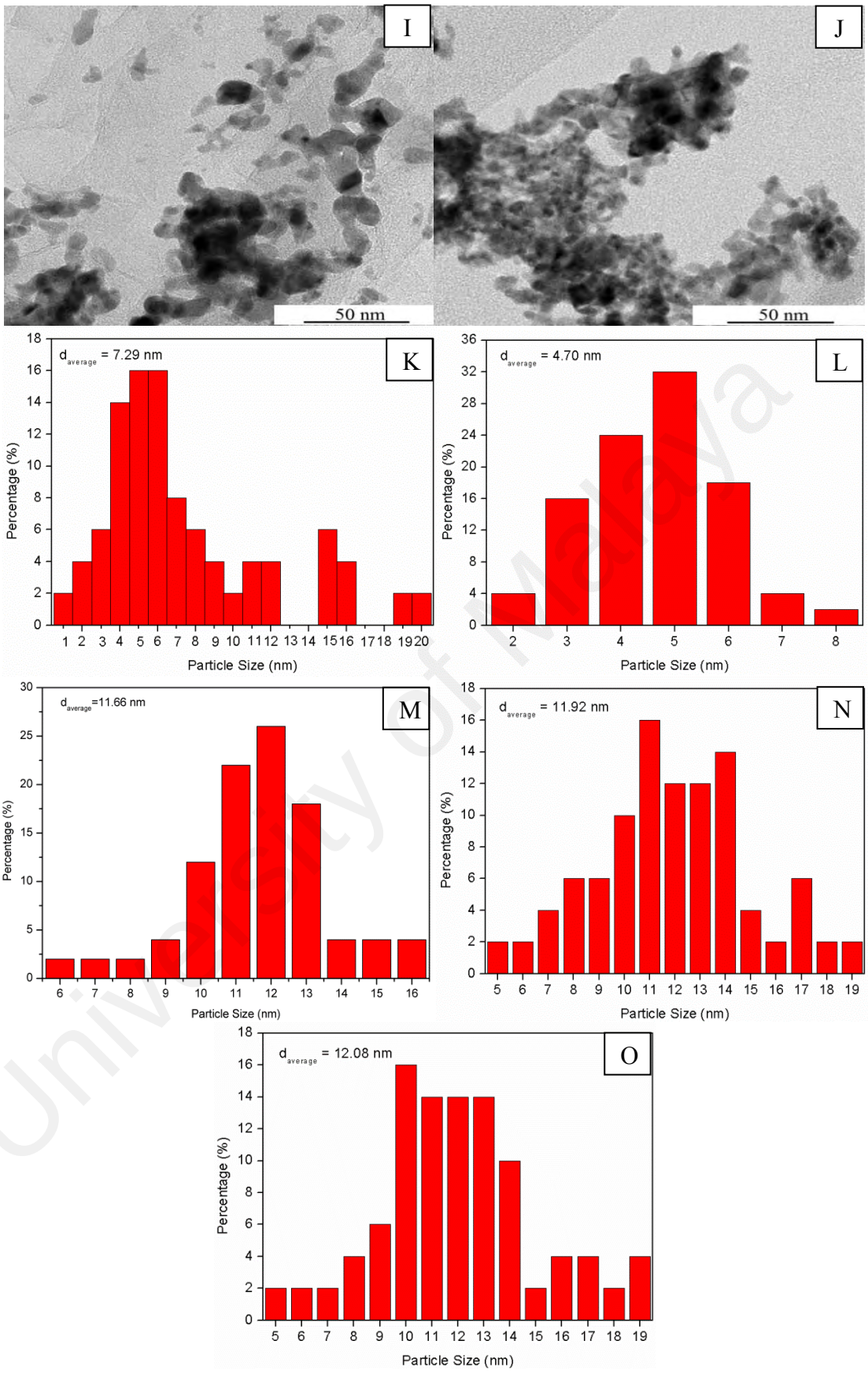

'Figure 4.11, continued'

University of Malaya

EDX (Table 4.2) showed higher mass loading of Pd for concentrated samples, and the Pd/rGO (2.0) having the highest amount of Pd deposition. Correlating to the FESEM images, it is suggested that the high mass loading led to agglomeration. The unexpected lower mass of Pd/rGO (3.0) and Pd/rGO (4.0) can be explained by the possible severe agglomeration that detached from rGO surface during centrifugation.

Table 4.2: The EDX of Pd/rGO (0.5), Pd/rGO (1.0), Pd/rGO (2.0), Pd/rGO (3.0), and Pd/rGO (4.0).

Electrocatalysts	Weight percentage, wt%		
	Pd	C	O
Pd/rGO (0.5)	53.42	32.01	14.57
Pd/rGO (1.0)	53.37	31.95	12.68
Pd/rGO (2.0)	73.29	20.00	6.72
Pd/rGO (3.0)	69.03	23.39	7.58
Pd/rGO (4.0)	69.27	24.22	6.51

As shown in Figure 4.12, all samples presented two intense Raman peaks at 1330-1350 cm^{-1} and approximately 1590 cm^{-1} that correspond to D band and G band, respectively. Increased $\frac{I_D}{I_G}$ ratio of samples relative to GO ($\frac{I_D}{I_G}$ = 1.00) signified that rGO nanosheets were formed, and Pd NPs were loaded on rGO (Chen et al., 2015; Ji et al., 2014). Higher intensity of D band suggested the generation of larger number of sp^2 domains with smaller size upon the reduction of GO (Zhao et al., 2015). The chemical reduction induced defects, such as edges and ripples, to the graphitic plane (Antony et al., 2015). Interaction of metal NPs with rGO also created superficial defects to the rGO. Thereby Pd/rGO (2.0), Pd/rGO (3.0), and Pd/rGO (4.0) with high Pd mass loading reported high value of $\frac{I_D}{I_G}$ (Martins et al., 2014). As previously mentioned, the Pd NPs would migrate over the rGO and coalesce at the vicinity of defects (Martins et al., 2014). Thus, agglomeration was particularly obvious in the Pd/rGO (2.0), Pd/rGO (3.0),

University of Malaya

and Pd/rGO (4.0). Appropriate level of defects has been reported to promote Pd dispersion with high uniformity (Du et al., 2012). This explains for the better distribution of Pd/rGO (1.0). Notably, the unique properties of graphene will be destructed when the defects are high (Ensafi et al., 2014; Zhao et al., 2015).

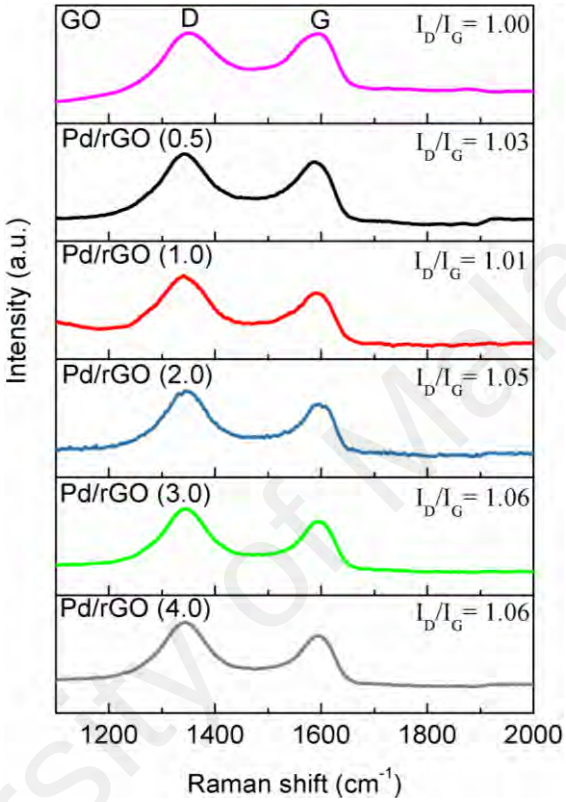

Figure 4.12: Raman images of Pd/rGO (0.5), Pd/rGO (1.0), Pd/rGO (2.0), Pd/rGO (3.0), Pd/rGO (4.0), and GO.

Figure 4.13 shows FTIR spectra of the GO and samples at different concentrations. All samples exhibited rather similar spectra. Peaks of GO can clearly be observed at 1126, 1637, and 3431 cm^{-1}, corresponding to C–O stretching vibration, sp^2-hybridized C=C stretching vibrations, and OH stretching vibration, respectively (Zhang et al., 2015). Most of the associated oxygen-containing peaks were removed or greatly decreased after the reduction process, verifying the successful reduction of the samples despite some weak residual O–H peaks can be observed at approximately 1048 and 1173 cm^{-1} (Andrijanto et al., 2016). Some new peaks also appeared at approximately 2923 and 2852 cm^{-1} attributing to the CH_2 stretching vibration and CH stretching

University of Malaya

vibrations, respectively (Basirun et al., 2013). The appearance of these new peaks can be ascribed to the reduction of the carboxylic acids in GO to CH_2OH. The strong peak at 1575 cm^{-1}, associating to skeletal vibration of sp^2 hybridized carbon ring in graphene, suggested the recovery of sp^2 lattice (Andrijanto et al., 2016).

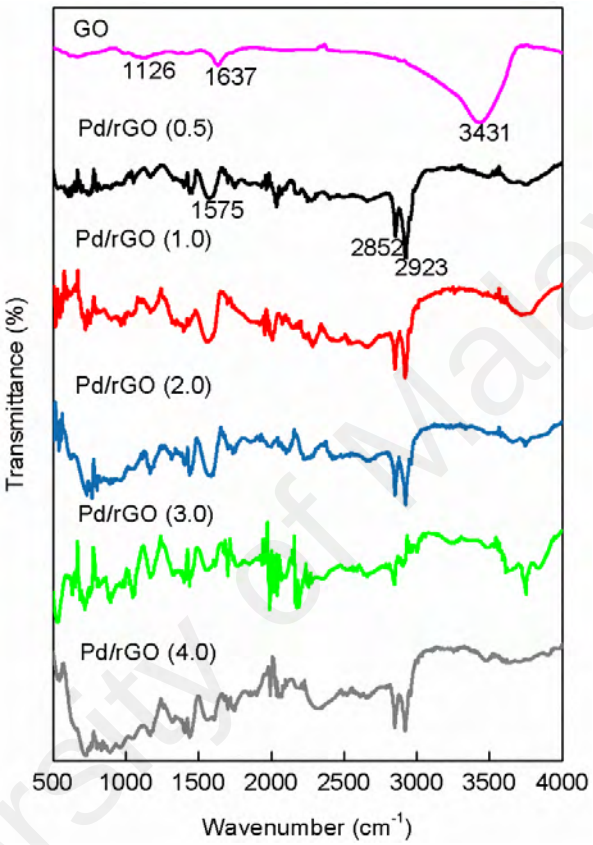

Figure 4.13: FTIR spectra of GO, Pd/rGO (0.5), Pd/rGO (1.0), Pd/rGO (2.0), Pd/rGO (3.0), and Pd/rGO (4.0).

4.3.2 Electrochemical Measurements

Figure 4.14A is the CV to calculate the ECSA of electrocatalysts. The ECSA values of various electrocatalysts were recorded in Table 4.3, ranging from 30.68 to 83.57 m^2 g^{-1}. Evidently, well distribution of Pd NPs on the surface of rGO, small particle size (8.08 nm), and less defects of rGO (as reflected by $\frac{I_D}{I_G}$ = 1.01) render Pd/rGO (1.0) highest ECSA.

University of Malaya

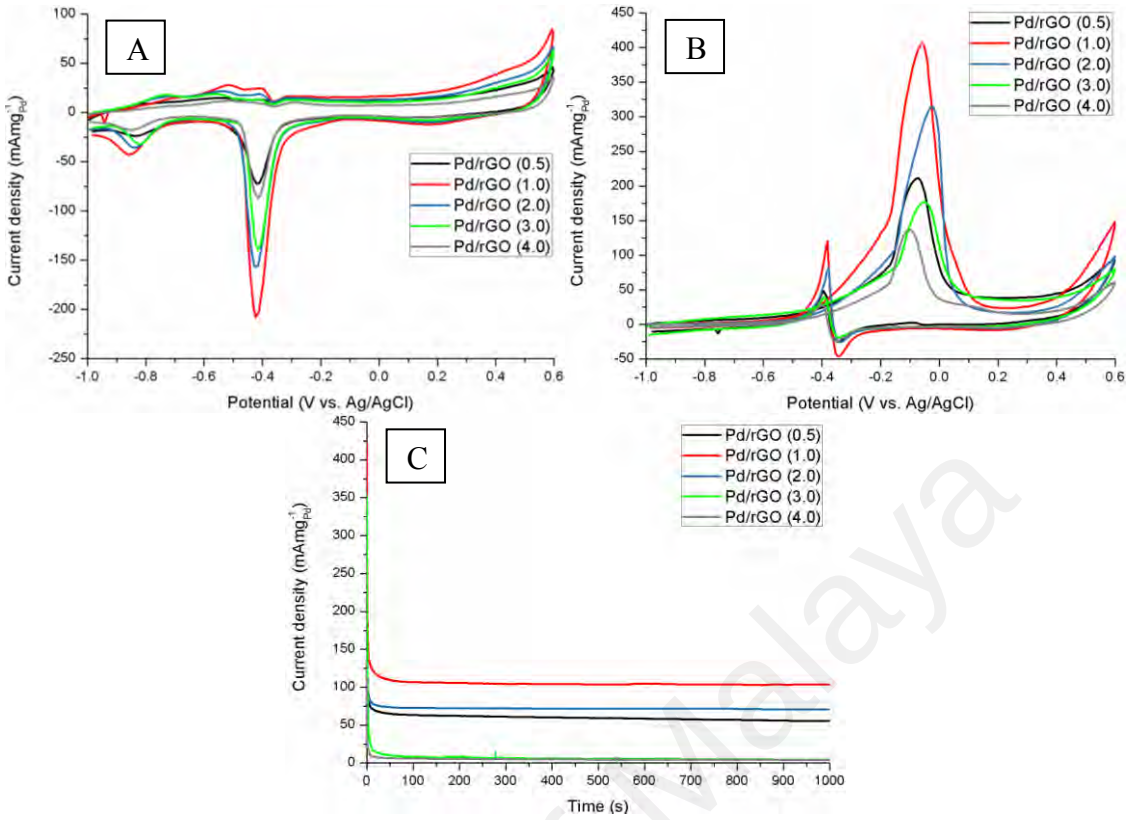

Figure 4.14: Cyclic voltammograms of Pd/rGO (0.5), Pd/rGO (1.0), Pd/rGO (2.0), Pd/rGO (3.0), and Pd/rGO (4.0) in nitrogen saturated solutions of (A) 1 M KOH and (B) 1 M KOH/ 1 M CH_3OH with scan rate of 50 mV s^{-1}. (C) Chronoamperogram of Pd/rGO (0.5), Pd/rGO (1.0), Pd/rGO (2.0), Pd/rGO (3.0), and Pd/rGO (4.0) in nitrogen saturated solution of 1 M KOH/ 1 M CH_3OH with scan rate of 50 mV s^{-1} at an applied potential of −0.2 V.

Table 4.3: ECSA, E_{peak}, I_{peak}, and percentage of current drop over time of various Pd/rGOs.

Electrocatalysts	ECSA ($m^2\ g^{-1}$)	E_{peak} (V vs. Ag/AgCl)	I_{peak} (mA mg^{-1}_{Pd})	Percentage of current drop over time (%)
Pd/rGO (0.5)	30.68	−0.074	212.22	9.89
Pd/rGO (1.0)	83.57	−0.062	405.37	1.22
Pd/rGO (2.0)	63.80	−0.026	314.36	2.21
Pd/rGO (3.0)	45.78	−0.053	177.25	32.74
Pd/rGO (4.0)	33.37	−0.104	137.59	22.22

The electro-oxidation of methanol of as-prepared electrocatalysts is shown in Figure 4.14B. All results were normalized by the mass of Pd loaded on electrode. Peak current density and peak potential of electrocatalysts are recorded in Table 4.3. The highest current density of Pd/rGO (1.0) can be attributed to the small size, uniform distribution, and large ECSA of Pd catalysts. CA in Figure 4.14C revealed that Pd/rGO (1.0) retained

highest current density and smallest current drop (Table 4.3). The better stability could be attributed to the lower defects because defects can cause the as-synthesized electrocatalysts to corrode easily under electrochemical operation (Zhao et al., 2015). Owing to the attachment of intermediate species which generated during methanol electro-oxidation to the surface of electrocatalysts, the initial current density dropped rapidly (Ma et al., 2013). As the poisoning species released over time, approximately 100s, the current dropped steadily (Kakaei & Dorraji, 2014).

4.4 A Modified Synthesis Method (Pd/rGO_M)

4.4.1 Structural and Chemical Characterizations

To certify the occurrence of multi-stages reduction, a few samples were prepared involving the mixture of GO and $PdCl_2$ before ultrasonication ($(PdCl_2\text{-}GO)_{BU}$), after ultrasonication ($(PdCl_2\text{-}GO)_{AU}$), after addition of EG ($(PdCl_2\text{-}GO)_{EG}$), and after pH adjustment ($(PdCl_2\text{-}GO)_{pH}$). Colour change of the precursor mixtures was observed and further examined via UV-vis spectroscopy. As shown in Figure 4.15, the GO was in yellow-brown colour. The addition of $PdCl_2$ to the GO slightly darkened the mixture solution because of the original "rusty" colour of $PdCl_2$. After ultrasonication of the mixture precursor, the colour of $(PdCl_2\text{-}GO)_{AU}$ slightly changed to brown, indicating the first mild reduction. Upon the addition of EG where the second mild reduction stage occurred, the colour turned dark brown. The mixture solution eventually turned black when the NaOH was added, signalling the third reduction stage.

University of Malaya

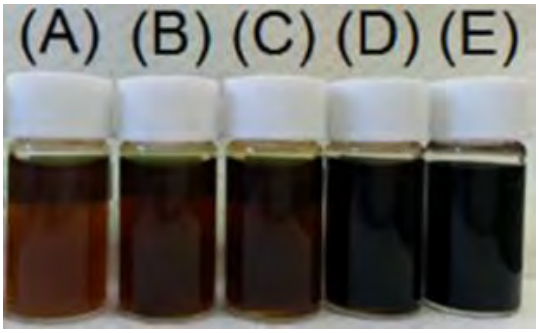

Figure 4.15: Solutions of (A) GO, (B) $(PdCl_2\text{-}GO)_{BU}$, (C) $(PdCl_2\text{-}GO)_{AU}$, (D) $(PdCl_2\text{-}GO)_{EG}$, and (E) $(PdCl_2\text{-}GO)_{pH}$.

The UV-vis spectra in shown Figure 4.16 further consolidated the above statements. The peak at 410 nm was a typical absorbance band of Pd(II) ions of $PdCl_2$ (Khan et al., 2014). Before being subjected to ultrasonication, the peak of $(PdCl_2\text{-}GO)_{BU}$ can be observed clearly. The consecutive ultrasonication of the mixture solution ($(PdCl_2\text{-}GO)_{AU}$) reduced the intensity and broadened the peak, signalling that the Pd(II) ions were fractionally reduced to Pd(0) NPs. When the EG was added, the peak became even broader and almost disappeared, further validating the second mild reduction stage. Meanwhile, the third mild reduction stage was proven as this peak completely disappeared after the addition of NaOH.

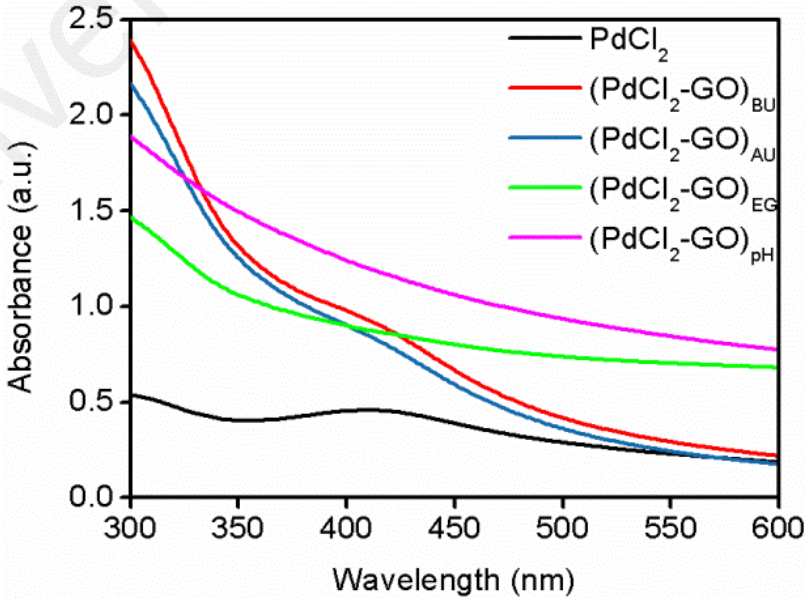

Figure 4.16: UV-vis spectra of $PdCl_2$, $(PdCl_2\text{-}GO)_{BU}$, $(PdCl_2\text{-}GO)_{AU}$, $(PdCl_2\text{-}GO)_{EG}$, and $(PdCl_2\text{-}GO)_{pH}$.

University of Malaya

The multi-stages nucleation before the final microwave-irradiation can be elaborated as follows:

First mild reduction: Ultrasonication induced free radicals. The free radicals were highly reactive and reduced the Pd precursors to zero-valent Pd (Bang & Suslick, 2010).

$$H_2O \rightarrow H\bullet + OH\bullet \quad (12)$$

$$H\bullet + H\bullet \rightarrow H_2 \quad (13)$$

$$H\bullet + OH\bullet \rightarrow H_2O \quad (14)$$

$$OH\bullet + OH\bullet \rightarrow H_2O_2 \quad (15)$$

$$Pd(II) + H\bullet \rightarrow Pd(0) + H^+ \quad (16)$$

Second mild reduction: Addition of EG at stirring stage. EG is a reducing agent, and thus, a slow reduction reaction at room temperature. In addition, there may be some free radicals might have remained and they induced free radicals of EG.

$$H\bullet + C_2H_6O_2 \rightarrow C_2H_5O_2\bullet + H_2 \quad (17)$$

$$OH\bullet + C_2H_6O_2 \rightarrow C_2H_5O_2\bullet + H_2O \quad (18)$$

$$Pd(II) + C_2H_5O_2\bullet \rightarrow Pd(0) + C_2H_4O_2\bullet + H^+ \quad (19)$$

$$GO + C_2H_5O_2\bullet \rightarrow rGO + C_2H_4O_2\bullet + H^+ \quad (20)$$

$$Pd(II) + C_2H_6O_2 \rightarrow Pd(0) + C_2H_4O_2 + 2H^+ \quad (21)$$

Third mild reduction: pH adjustment. The addition of NaOH favoured the rightward chemical reaction. In other words, it enhanced the reduction rate (Cao, 2004).

University of Malaya

$$Pd(II) + C_2H_6O_2 + 2OH^- \rightarrow Pd(0) + C_2H_2O_4 + 3H_2 \quad (22)$$

$$GO + C_2H_6O_2 + OH^- \rightarrow rGO + C_2H_3O_2^- + H_2O + H_2 \quad (23)$$

In the current work, Pd/rGO_M was conducted to (i) reduce the multi-stages gradual nucleation by not adding in EG during the stirring of the mixture and by eliminating the pH adjustment step, (ii) incur rapid nucleation through prior microwave-irradiation of EG and Na_2CO_3 to induce large amounts of free radicals, and (iii) increase the supersaturation via the subsequent addition of the room temperature mixture. As described in Equation 24, the Na_2CO_3 provided an alkaline condition, which was reported to have considerable influence to the final performance of electrocatalysts (Cao, 2004; Hsieh et al., 2013). Furthermore, Na_2CO_3 acted the role as second reducing agent. The rapid nucleation and high supersaturation favoured the formation of large number of nuclei, resulting in small-sized nuclei for a given concentration of solute (Cao, 2004).

$$Na_2CO_3 + 2H_2O <=> 2Na^+ + 2OH^- + H_2CO_3 \quad (24)$$

Figure 4.10 illustrates the critical energy, ΔG^*, and critical size, r^*, related to the formation of nuclei. The nuclei formed at the pink region are unstable and will dissolve back to the solution (Cao, 2004). Meanwhile, the nuclei at blue shaded region are stable. With increased supersaturation, $\dot{O}$, can reduce the ΔG^* and r^* as given by Equations 7–11 (Cao, 2004). Upon the synthesis of nanoparticles, the reduced critical size indicates a lower limit on how small NPs can be formed (Cao, 2004). A low critical energy also facilitated the formation of a large number of nuclei, implying smaller sized nuclei (Cao, 2004).

University of Malaya

Figure 4.17 shows the XRD of GO, Pd/rGO$_O$, and Pd/rGO$_M$. The disappearance of the GO peak at 10.3° and the appearance of weak and broad C (002) peak at 24° suggested that GO was successfully reduced after microwave irradiation (Videla et al., 2014). Peaks at about 40.1°, 46.5°, 68.2°, 82.1°, and 86.7° can be indexed to the (111), (200), (220), (311), and (422) lattice planes of the fcc crystalline structure of Pd (JCPDS No. 46-1043), respectively. The crystallite size of Pd was calculated by using Scherrer's formula based on the Pd (220) peak. The calculated crystallite size of Pd/rGO$_O$ and Pd/rGO$_M$ were 7.74 and 7.57 nm, respectively. The smaller size of Pd/rGO$_M$ vouched that the rapid nucleation and high supersaturation were conducive to fabricate fine NPs.

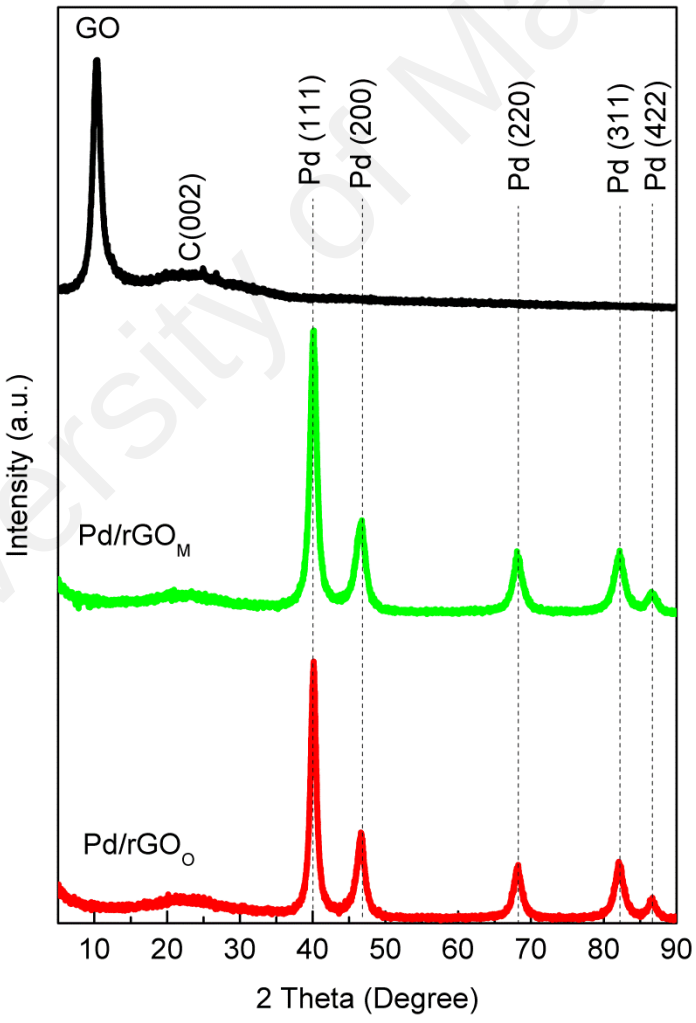

Figure 4.17: XRD images of Pd/rGO$_O$, Pd/rGO$_M$, and GO.

University of Malaya

Wrinkles and ripples can be observed clearly from the TEM images of Pd/rGO_O (Figures 4.18A and 4.18C) and Pd/rGO_M (Figures 4.18B and 4.18D). Pd NPs were successfully loaded and immobilized on the surface of the rGO for both methods. Pd/rGO_O exhibited some agglomeration of NPs, while uniform distribution can be observed for Pd/rGO_M. An average particle size was measured from 50 NPs, and was found to be 11.66 and 6.23 nm for Pd/rGO_O and Pd/rGO_M, respectively. Figures 4.18E and 4.18F demonstrate that the size distribution of the electrocatalysts synthesized by modified synthesis method was narrower. This finding manifested the feasibility of current proposed method.

University of Malaya

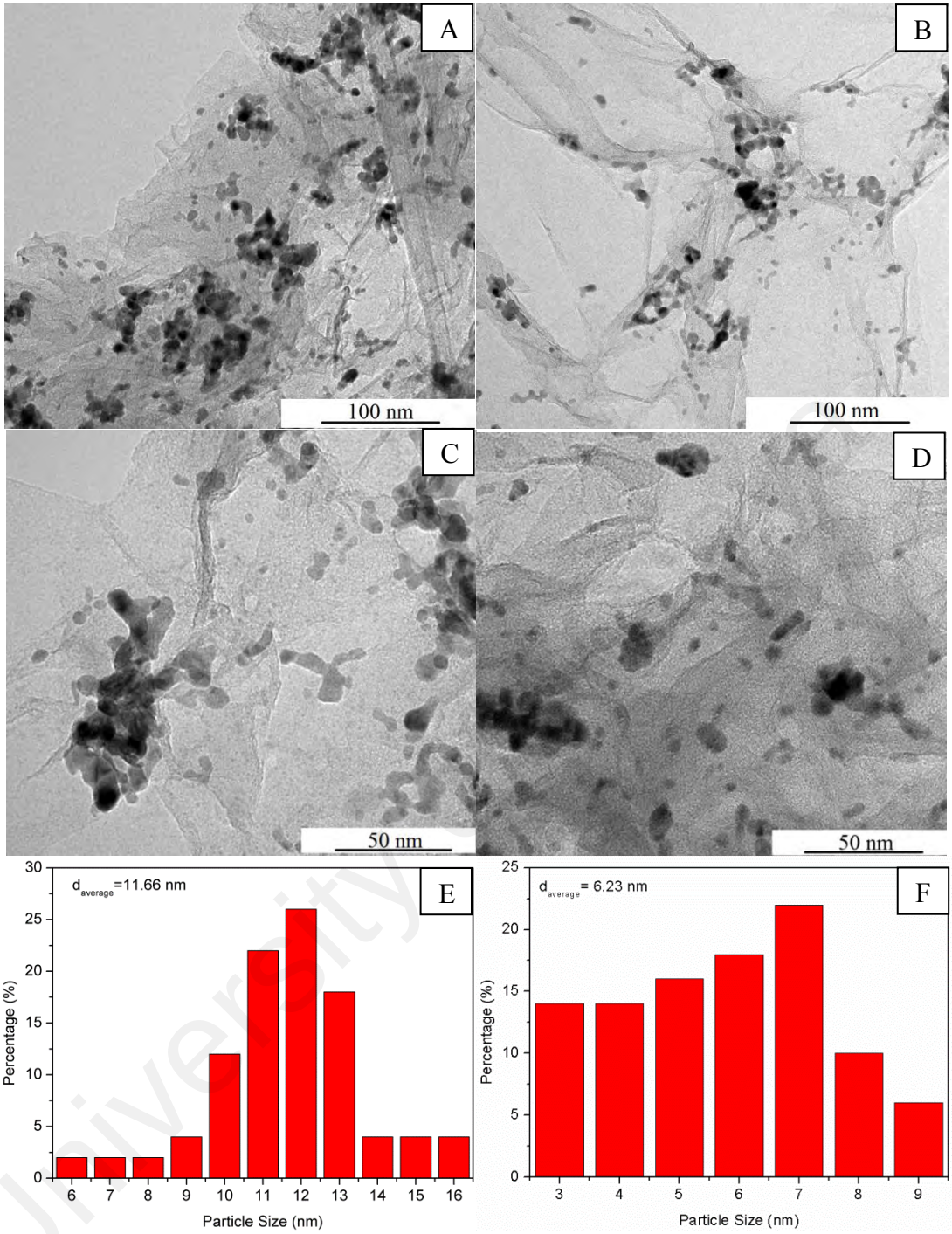

Figure 4.18: TEM images of (A, C) Pd/rGO$_O$ and (B, D) Pd/rGO$_M$. NP size distribution of (E) Pd/rGO$_O$, and (F) Pd/rGO$_M$.

EDX (Table 4.4) shows that Pd/rGO$_O$ has a higher Pd loading than Pd/rGO$_M$. When more Pd NPs attached onto the surface of rGO, the distance between each other was shortened, increasing the mutual attractive force of the NPs. The Pd NPs migrated over the support and agglomerated to reduce surface energy. Our finding corresponded to the observation of Nagaraju et al. (2014) that agglomeration of electrocatalysts increased

for the sample with high Pd NPs density. The lower mass loading and well distribution of Pd/rGO_M can have resulted from the shorter microwave reduction duration. The higher $\frac{C}{O}$ ratio of the modified method indicated a better reduction efficiency, which can be attributed to the free radicals induced from prior microwave irradiation and the addition of second reducing agent.

Table 4.4: EDX of Pd/rGO_O and Pd/rGO_M.

Electrocatalysts	Weight Percentage, (wt%)			$\frac{C\ (wt\%)}{O\ (wt\%)}$
	Pd	C	O	
Pd/rGO_O	73.29	20.00	6.72	2.98
Pd/rGO_M	68.76	23.53	7.72	3.05

Two intense Raman peaks at 1330-1350 cm^{-1} and approximately 1590 cm^{-1} in Figure 4.19 corresponded to D and G bands, respectively. The presence of weak broad 2D peaks of both electrocatalysts at ~2650 cm^{-1} corresponded to few-layered graphene (Videla et al., 2014). The intensity ratio D band to G band, $\frac{I_D}{I_G}$, of GO is 1.00. The intensity ratio of both electrocatalysts increased after reduction, signifying successful reduction of GO and the loading of Pd NPs on rGO (D.-J. Chen et al., 2015; Ji et al., 2014). The higher intensity ratio of Pd/rGO_O (1.05) than to the Pd/rGO_M (1.04) implied a slightly higher defect density of graphene. This explained for the agglomeration of Pd NPs because the defects on rGO act as a NCC where the Pd NPs coalesced at its vicinity (Martins et al., 2014).

University of Malaya

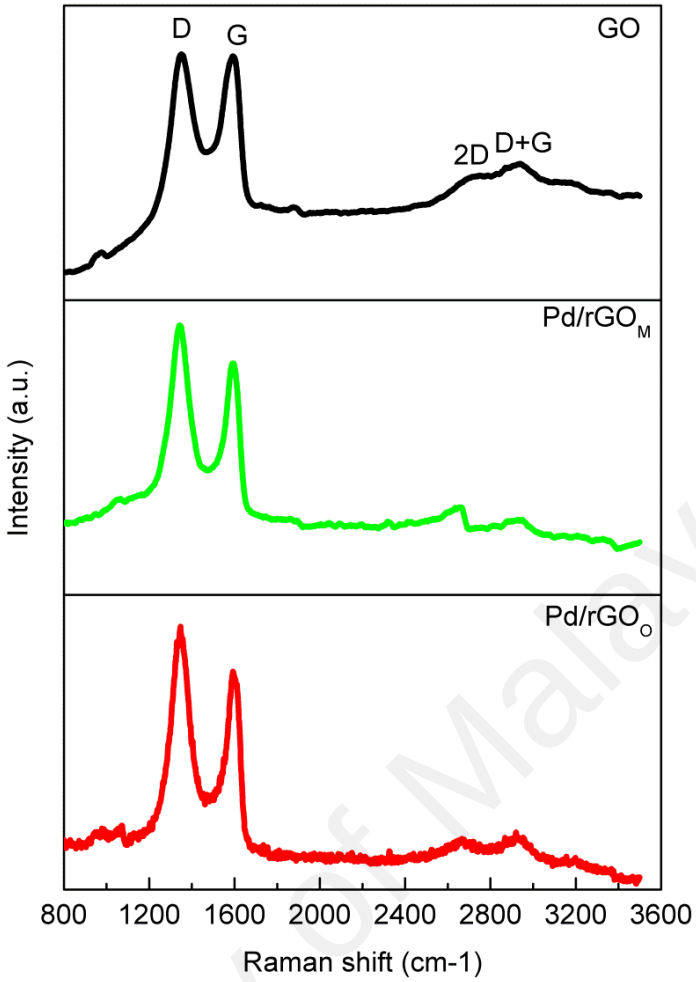

Figure 4.19: Raman images of Pd/rGO$_O$, Pd/rGO$_M$, and GO.

4.4.2 Electrochemical Measurements

From Figure 4.20A, the ECSA values of Pd/rGO$_O$ and Pd/rGO$_M$ were calculated to be 63.80 and 78.97 $m^2\ g^{-1}$, respectively. The uniform distribution, small size of Pd NPs, and appropriate level of defects on graphene, contributed to the larger ECSA of the latter electrocatalyst.

University of Malaya

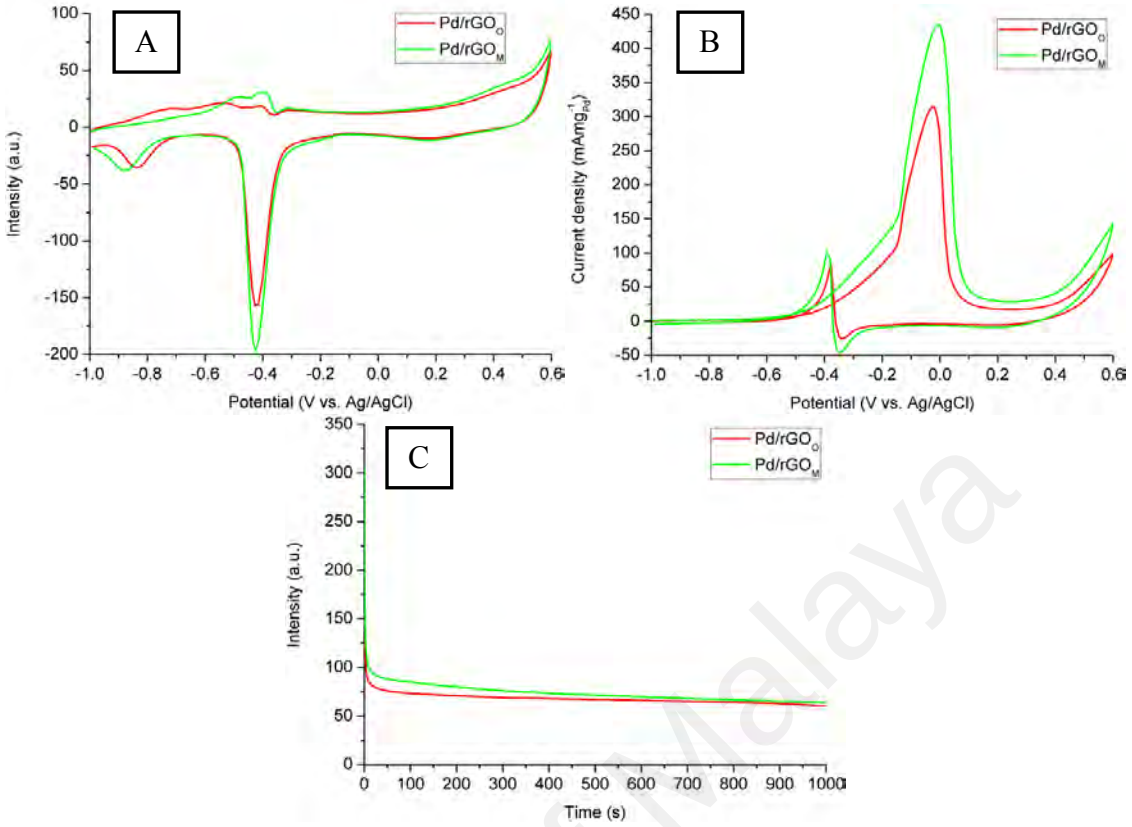

Figure 4.19: Cyclic voltammograms of of Pd/rGO$_O$ and Pd/rGO$_M$ in nitrogen saturated solutions of (A) 1 M KOH and (B) 1 M KOH/ 1 M CH_3OH with scan rate of 50 mV s^{-1}. (C) Chronoamperogram of Pd/rGO$_O$ and Pd/rGO$_M$ in nitrogen saturated solution of 1 M KOH/ 1 M CH_3OH with scan rate of 50 mV s^{-1} at an applied potential of −0.2V.

The MOR of the as-synthesized electrocatalysts was displayed in Figure 4.20B. All results were normalized by the mass of Pd loaded on electrode. Peak current density and onset potential were 314.94 mA mg^{-1} and −0.43 V as well as 434.49 mA mg^{-1} and −0.45 V for Pd/rGO$_O$ and Pd/rGO$_M$, respectively. The slightly more negative onset potential of the latter sample demonstrated its better ability in initiating the electrooxidation of methanol. The result achieved in this work showed better performance than similar graphene-based electrocatalysts, such as Pd NPs supported on polypyrrole-functionalized graphene (Pd/Ppy-graphene) (359.8 mA mg^{-1}_{Pd}) synthesized by Zhao et al. (2011), and pristine graphene supported Pd NPs stabilized by FMN prepared by Ayán-Varela et al. (2017). The ratio of forward to backward peak current density ($\frac{I_f}{I_b}$) is a measure of the capability of the electrocatalyst to resist CO-poisoning

which is an intermediate species of MOR (Antony et al., 2015). A higher $\frac{I_f}{I_b}$ signifies better oxidation of methanol to carbon dioxide and better elimination of intermediate species that formed during the forward scan (Kakaei, 2015). Therefore, Pd/rGO$_M$ ($\frac{I_f}{I_b}$ = 4.23) tolerated CO-poisoning better than Pd/rGO$_O$ ($\frac{I_f}{I_b}$ = 3.98). These findings were reasonable because the former electrocatalyst has a larger ECSA, signifying more catalytic sites and enhanced electron transfer for complete methanol oxidation. The more efficient reduction of Pd/rGO$_M$ as proven by a higher $\frac{C}{O}$ in EDX implied that the unique properties of rGO were recovered to a greater extent, which improved the MOR.

Stability of electrocatalysts was assessed via CA as depicted in Figure 4.20C. Pd/rGO$_M$ retained a higher current density (63.74 mA mg^{-1} vs. 60.14 mA mg^{-1}). The better stability can be ascribed to the lower defects because defects can cause the as-synthesized electrocatalysts to corrode easily under electrochemical operation (Zhao et al., 2015). Nevertheless, the improvement in stability is insignificant because the defect level of both electrocatalysts was very close, as demonstrated in the Raman analysis.

4.5 Palladium Nanoparticles on Guanine Functionalized Reduced Graphene Oxide (Pd/rGO$_G$)

4.5.1 Structural and Chemical Characterizations

Guanine adsorption on rGO was examined by UV–vis spectroscopy. As observed in Figure 4.21, two UV–vis absorption peak of GO occurred at 220 and 247 nm corresponding to the π–π* transition of the aromatic ring C=C. A shoulder peak can also be observed at 310 nm caused by the n–π* transition of C=O bonds. Upon the formation of the nanocomposite Pd/rGO$_O$, the peaks red-shifted to 223, 258, and 322 nm. This

University of Malaya

phenomenon signified the successful reduction of GO and the restoration of the electronic conjugation of graphene. The further shift of Pd/rGO_G peaks to 245, 273, and 327 nm provided persuasive evidence on the coordination of guanine with rGO via π–π interactions as the guanine was characterized by the peaks at 248, 275, and 322 nm (Chandraboss et al., 2015).

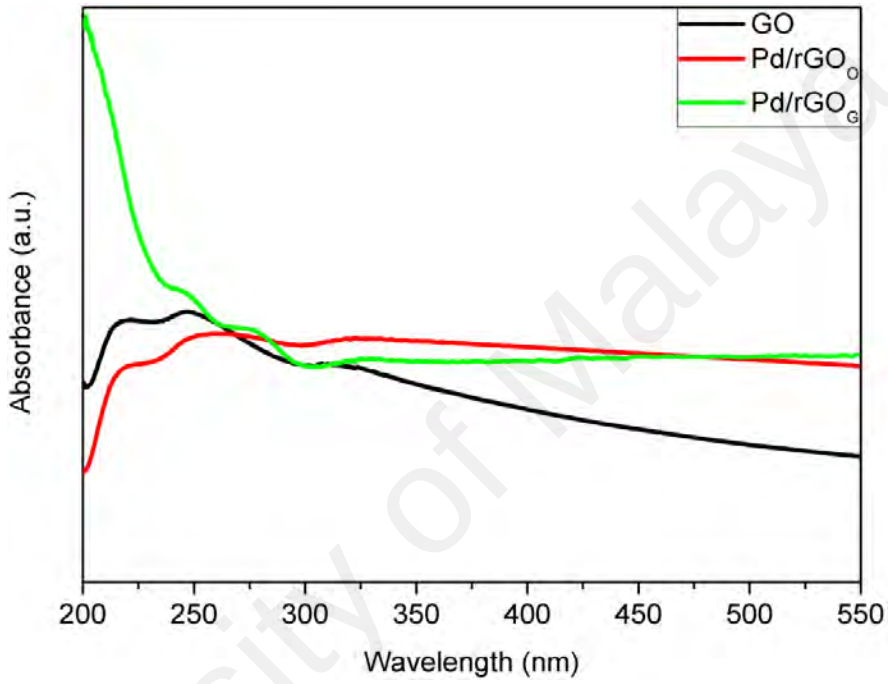

Figure 4.20: UV-vis absorption spectra of GO, Pd/rGO_O, and Pd/rGO_G.

The nanocomposites were further characterized by FTIR analysis. FTIR spectrometry of GO, Pd/rGO_O, and Pd/rGO_G is demonstrated in Figures 4.22A–4.22C, respectively. The peaks of GO at 676, 1119, 1631, and 3425 cm^{-1} were attributed to the C=C bending vibration, C–O stretching vibration of alkoxy groups, C=C stretching vibration, and O–H group stretching vibration of phenols, respectively. Meanwhile, the peaks at 1358 and 1417 cm^{-1} can be ascribed to the O–H bending vibrations of phenols. For the sample Pd/rGO_O, peaks related to oxygen functional groups, such as C–O stretching vibration (1172 cm^{-1}), O–H bending vibration (1406 cm^{-1}), and O–H stretching vibration (3687 cm^{-1}), exhibited reduced intensities, indicating rGO formation. The low intensity peaks ranging from 580–780 cm^{-1} and at approximately

University of Malaya

800 cm^{-1} belong to the vibrations of the C–H bonds of the benzene rings and C–H out of plane bending vibration, respectively. As for Pd/rGO_G, a much decreased intensity of O–H stretching vibration occurred at 3107 cm^{-1}. New peaks of N–H stretching vibration were obtained at 3317, 2907, and 2852 cm^{-1}. C=N stretching vibration was noticed at 1671 cm^{-1}. Furthermore, peaks of C–N stretching vibration of amine were found at 1259, 1214, 1173, and 1118 cm^{-1}. The existence of peaks of both N–H and C–N stretching vibration affirmed the presence of the amide functional group. Meanwhile, peaks of C–N and C=N verified the functionalization of guanine in Pd/rGO_G.

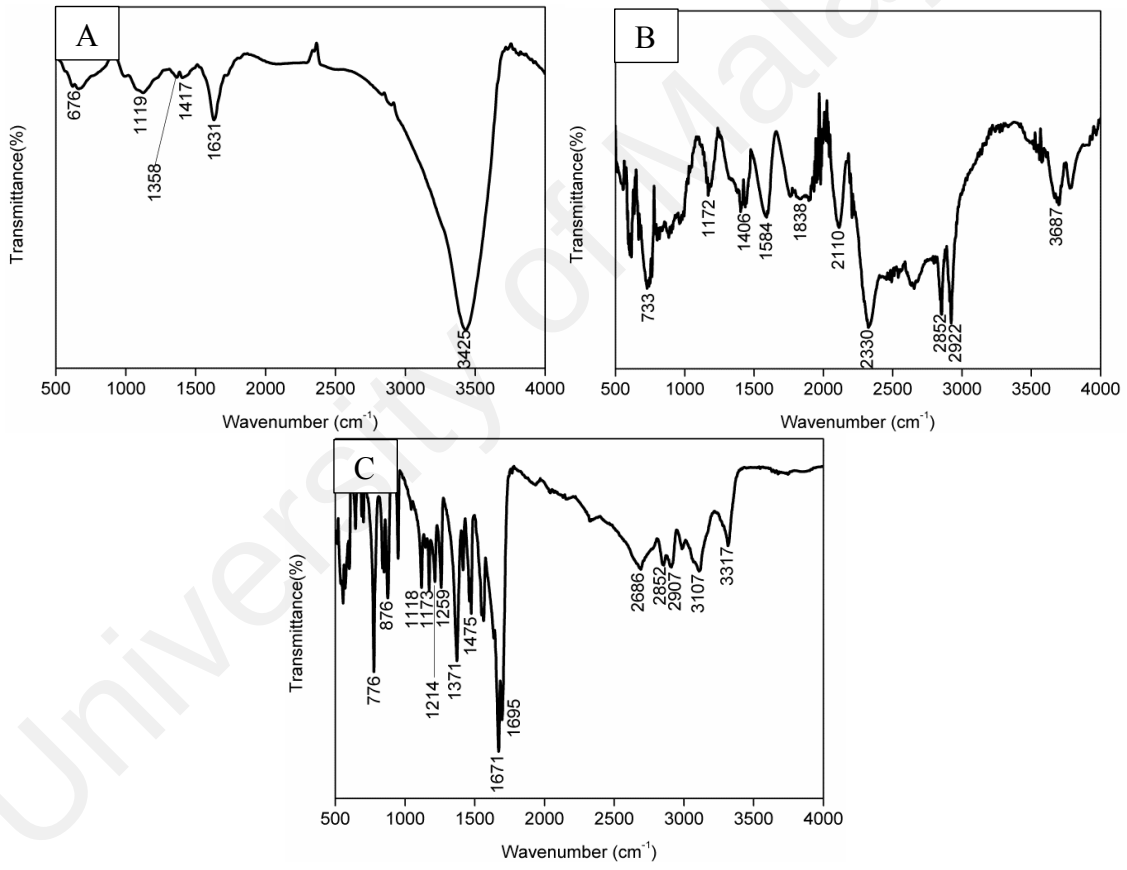

Figure 4.21: FTIR spectra of (A) GO, (B) Pd/rGO_O, and (C) Pd/rGO_G.

Figure 4.23 shows that the XRD peak of GO at 10.3° disappeared, and a weak and broad C (002) peak at 24° occurred, suggesting the feasibility of microwave-assisted reduction method in reducing the GO (Videla et al., 2014). Three representative peaks of guanine at 14.0°, 26.1°, and 27.9° can clearly be observed in the XRD spectrum of

University of Malaya

Pd/rGO_G, manifesting the adsorption of guanine on the surface of rGO. Peaks at approximately 40.1°, 46.5°, 68.2°, 82.1°, and 86.7° corresponded to the (111), (200), (220), (311), and (422) lattice planes of the fcc crystalline structure of Pd (JCPDS No. 46-1043), respectively. Therefore, Pd NPs were loaded on rGO, forming the nanocomposites. Notably, the (111) peak shows the highest intensities, indicating that the Pd NPs were mainly growing in the (111) directions. Crystallite size of Pd was calculated by Scherrer's formula based on the Pd (220) peak and recorded 7.57 and 2.66 nm for Pd/rGO_O and Pd/rGO_G, respectively.

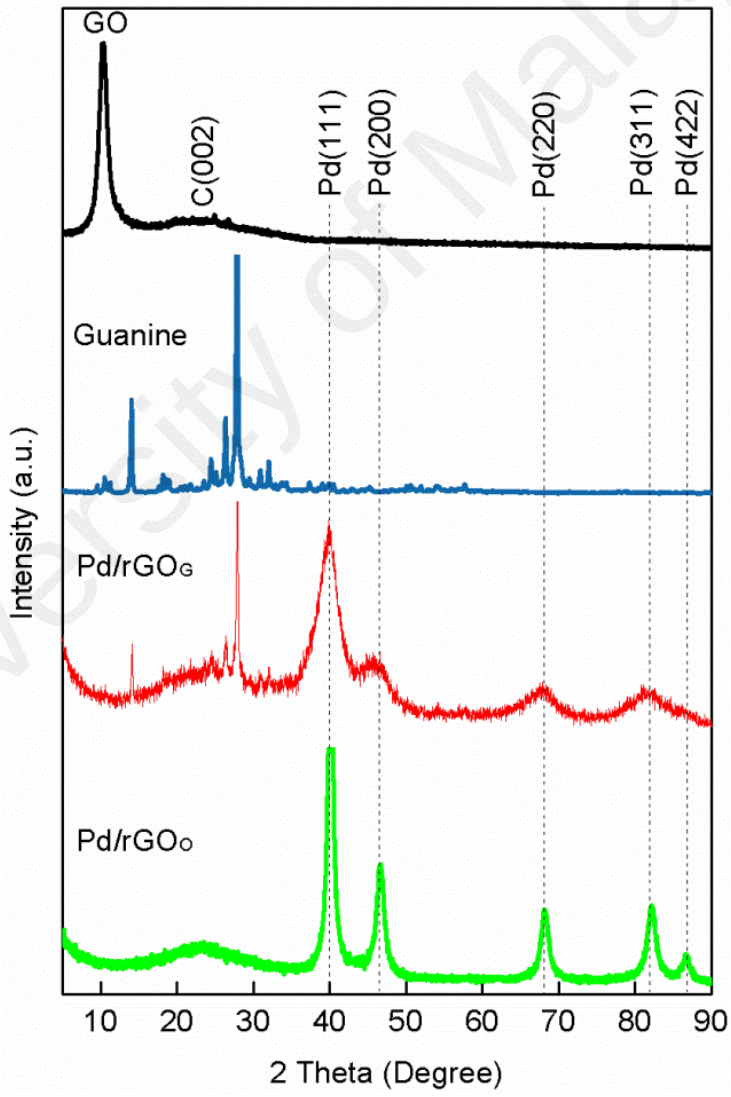

Figure 4.22: XRD image of Pd/rGO_O, Pd/rGO_G, and GO.

University of Malaya

Wrinkles and ripples induced from the GO deoxygenation were obvious for the Pd/rGO_O in Figure 4.24A (Antony et al., 2015). By contrast, Pd/rGO_G (Figure 4.24B) appeared slightly thickened in graphene sheets, further validating the attachment of guanine on its surface. Pd NPs with average size of 7.51 and 11.66 nm were deposited on the surface of both the functionalized and non-functionalized rGO, respectively. Pd NPs agglomerated in Pd/rGO_O but was uniformly dispersed with slight agglomeration for Pd/rGO_G. This observation suggested that the introduction of guanine was effective in restraining the agglomeration of Pd NPs. In contrast to the circular nanoparticles of Pd/rGO_O (Figure 4.24C), various shapes, such as triangular, square, circular, and diamond shapes, were observed for Pd/rGO_G (Figure 4.24D). These shapes revealed the capability of the amino, amide, and imino groups of guanine to control the synthesis of Pd NPs. HRTEM shows the lattice spacing of both samples was approximately 0.22 nm (Figures 4.24E and 4.24F), conforming to the (111) planes of the fcc of Pd.

University of Malaya

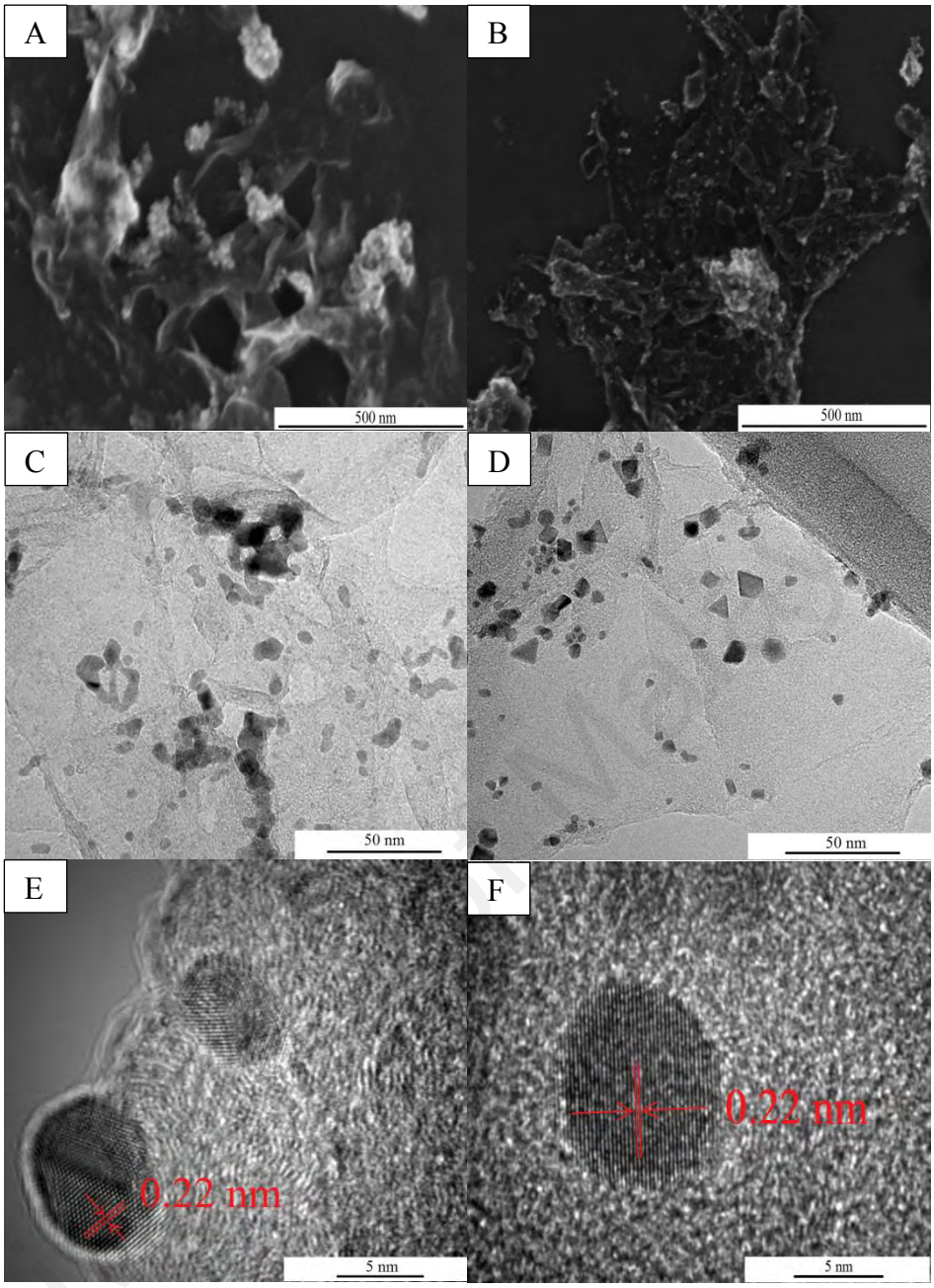

Figure 4.23: FESEM images of (A) Pd/rGO$_O$ and (B) Pd/rGO$_G$. TEM images of (C) Pd/rGO$_O$ and (D) Pd/rGO$_G$. HRTEM images of (E) Pd/rGO$_O$ and (F) Pd/rGO$_G$.

As shown in Figure 4.25, two representative Raman bands of graphene, D band and G band, occur at 1330–1350 cm^{-1} and approximately 1590 cm^{-1}, respectively. The G band of Pd/rGO$_O$ and Pd/rGO$_G$ red-shifted from 1589 cm^{-1} of GO to 1592 cm^{-1} and 1598 cm^{-1}, respectively. Therefore, the GO was partially reduced and the graphitic structure was restored. Relative to GO, $\frac{I_D}{I_G}$ increased from 1.00 to 1.05 and 1.01 for Pd/rGO$_O$ and Pd/rGO$_G$, respectively. Such increase in ratio can be ascribed to the

creation of defects during the reduction of GO and deposition of Pd NPs on rGO (Chen et al., 2015; Ji et al., 2014). The low ratio of Pd/rGO_G implied that it has high degree of graphitization and low defect density. The introduction of guanine was signified to preferably preserve the electronic structure and integrity of rGO and offers more active sites on the surface of rGO for the loading of Pd NPs. As defects on rGO served as NCC for the coalescence of Pd NPs at its vicinity, agglomeration was serious in Pd/rGO_O (Martins et al., 2014).

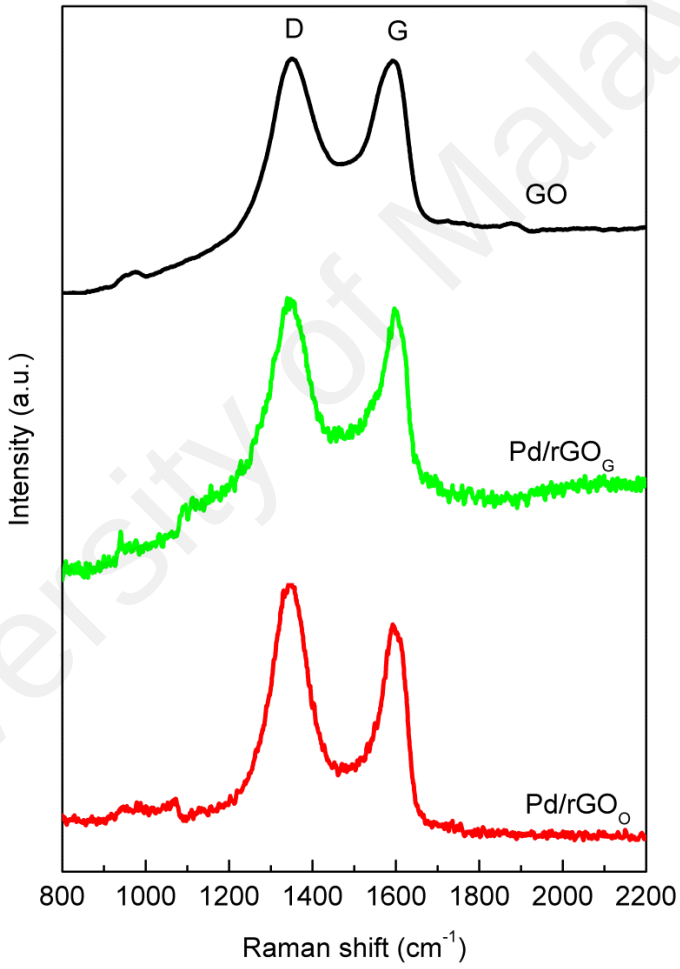

Figure 4.24: Raman image of Pd/rGO_O, Pd/rGO_G, and GO.

XPS analysis was conducted to probe the chemical composition and content of Pd/rGO_G and to verify the attachment of guanine to the rGO. Figure 4.26A demonstrates the XPS spectra of Pd/rGO_G. N1s peak can clearly be observed at 398 eV, signaling the functionalization of guanine on rGO. The peaks at approximately 285 eV,

University of Malaya

340 eV, and 530 eV are the peaks of C1s, Pd3d, and O1s, respectively. The presence of Pd peak confirmed the successful deposition of Pd NPs. Deconvolution of C1s XPS spectrum (Figure 4.26B) shows a dominant C–N bonds (285.8 eV), C–C/C=C bonds (284.7 eV), C–O bonds (286.7 eV), NH_2/N–C=O bonds (287.5 eV), and C=O bonds (288.1 eV). The C–O bonds involved hydroxyl (–OH) and epoxide (–O–); C=O bonds comprise carboxyl (–COOH), carbonyl (–C=O), and carboxylate (–COOR) (L. Zhao et al., 2016). The low intensity of C–O and C=O peak signified successful reduction of GO, where a large number of oxygen-containing species of GO were removed. The existence of C–N and NH_2/N–C=O bonds indicated guanine has been adsorbed onto the surface of rGO. Noteworthily, shift correction referring to the C–C (284.8 eV) was done prior to the deconvolution of XPS spectra. The shift correction is essential so that surface charge and linear background will be corrected. In Figure 4.26C, the N1s peak was deconvoluted into the peak of –N= groups (N1) at 398.54 eV and peak of $–NH_2$ bond (N2) at 399.94 eV. The former peak was resulted from the pyridinic nitrogen of guanine, whereas the latter was attributed to the amine groups. The observation in Figure 4.26D where the Pd^0 peaks dominated in the deconvolution of the Pd3d peak further verified the high degree reduction of the synthesis. In brief, the findings are in accordance with the UV-vis, FTIR, XRD, and Raman results.

University of Malaya

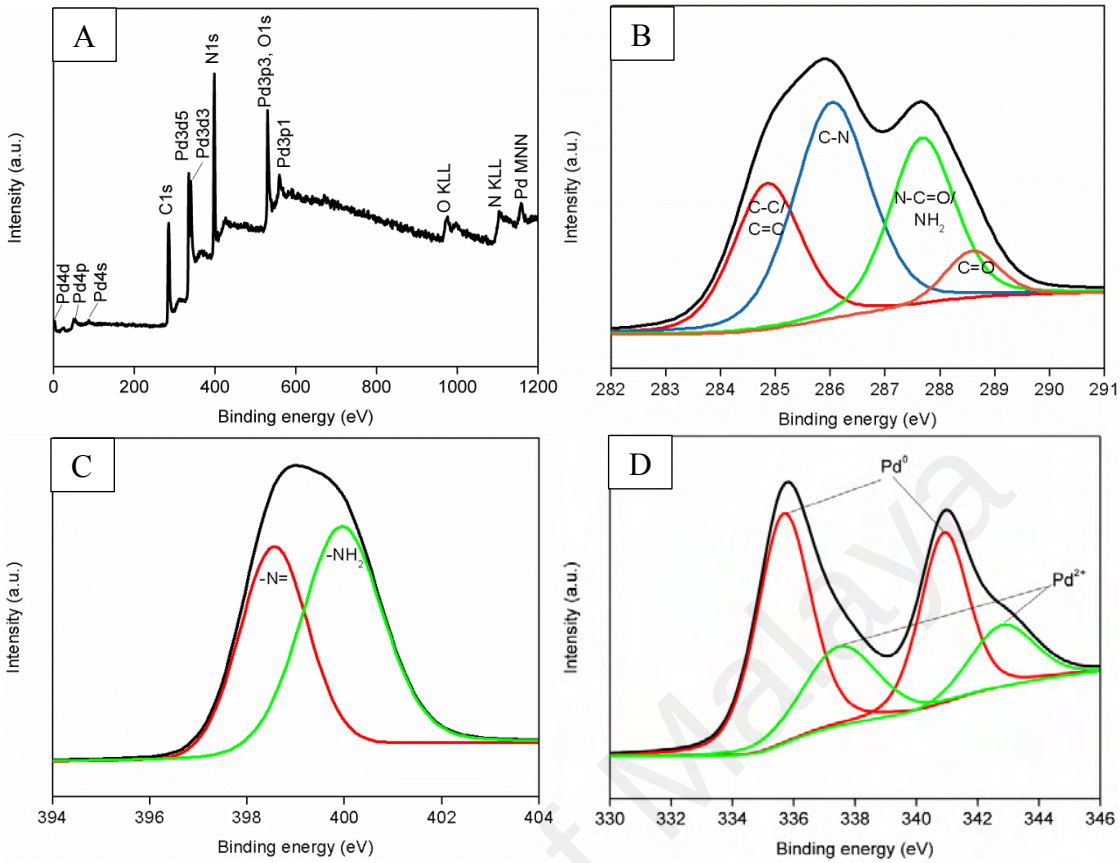

Figure 4.25: XPS spectrum of (A) Pd/rGO$_G$. Deconvolution of the high resolution XPS spectra of (B) C1s, (C) N1s, and (D) Pd3d in Pd/rGO$_G$.

4.5.2 Electrochemical Measurements

Figures 4.27A and 4.27B show the electrochemical tests to provide insight to the effect of introduction of guanine to the catalytic activity. The inset in Figure 4.27A clearly reveals that the rGO and guanine can be a catalyst with the former slightly stronger than the latter. Both rGO and guanine catalysed the MOR, achieving peak at −0.17 and −0.15 V vs. Ag/AgCl, respectively. Nevertheless, the standalone guanine was weak in the electrooxidation of methanol. Upon functionalization of guanine on rGO, the electrooxidation of methanol was enhanced significantly. The electrochemical performance was further boosted as high as 164% at the presence of Pd NPs. It was hypothesized that the addition of guanine to rGO led to larger ECSA and thus the extraordinary methanol oxidation activity of rGO+guanine. However, Figure 4.27B

University of Malaya

declined the hypothesis because the introduction of guanine to rGO did not have any impact to the ECSA. Such an observation complies with the FESEM image in Figure 4.24B, where the rGO became thicker at the presence of guanine. Thus, such improvement can be credited to the unique properties of graphene that facilitated the electron transfer of guanine, leading to the increase in current densities (Juan Tang et al., 2012).

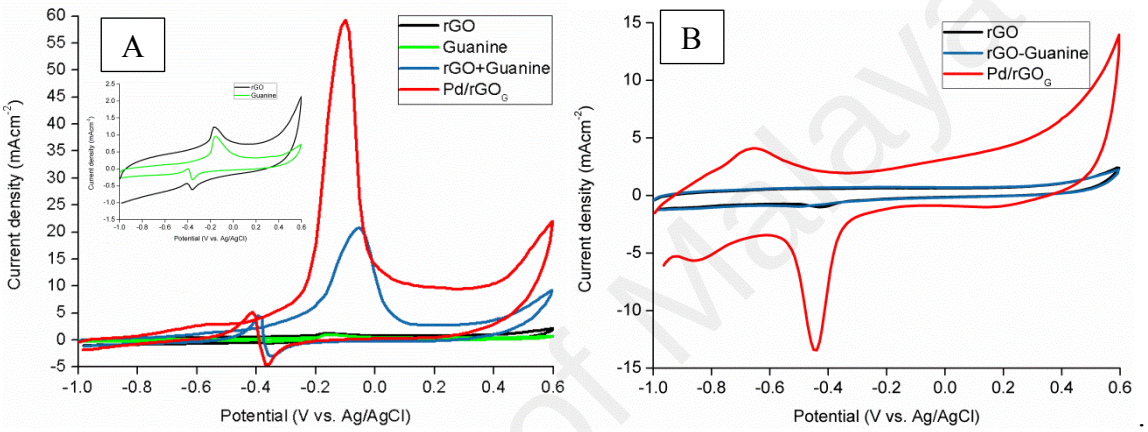

Figure 4.26: (A) Cyclic voltammogram of rGO, rGO + guanine, and Pd/rGO$_G$ in nitrogen saturated solutions of 1 M KOH. (Inset of (A) is magnified cyclic voltammogram of rGO and guanine). (B) Cyclic voltammogram of rGO, guanine, rGO + guanine, and Pd/rGO$_G$ in nitrogen saturated solutions of 1 M KOH/ 1 M CH_3OH with scan rate of 50 mV s^{-1}.

The ECSA values of Pd/rGO$_O$ and Pd/rGO$_G$ were compared based on Figure 4.28A. The ECSA values of Pd/rGO$_O$ and Pd/rGO$_G$ were calculated to be 63.80 and 111.98 m^2 g^{-1}, respectively. In the discussion above, the introduction of guanine did not contribute to the ECSA of rGO. Therefore, the increased ECSA was mainly from the Pd NPs. Evidently, the small size and uniform dispersion of Pd NPs were the governing factors to the great ECSA of the Pd/rGO$_G$.

University of Malaya

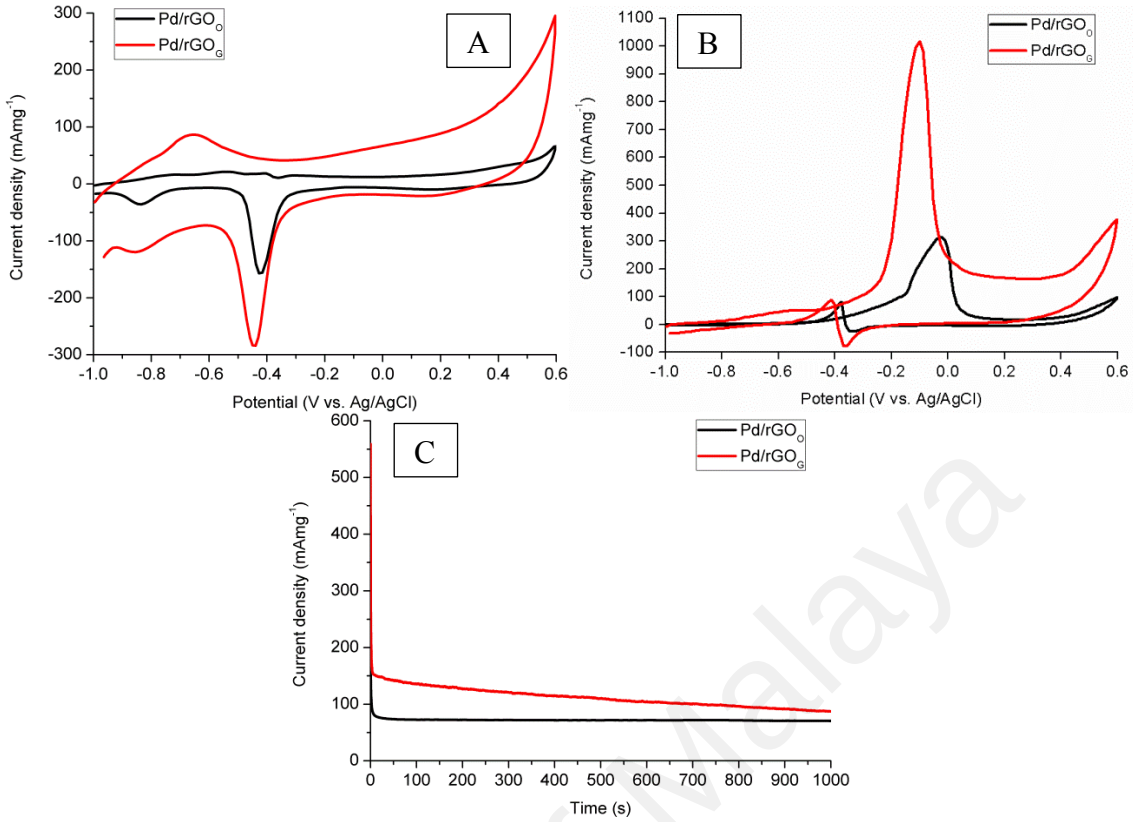

Figure 4.27: Cyclic voltammogram of Pd/rGO_O and Pd/rGO_G in nitrogen saturated solutions of (A) 1 M KOH and (B) 1 M KOH/ 1 M CH_3OH with scan rate of 50 mV s^{-1}. (C) Chronoamperogram of Pd/rGO_O and Pd/rGO_G in nitrogen saturated solutions of 1 M KOH/ 1 M CH_3OH with scan rate of 50 mV s^{-1} at an applied potential of −0.2 V vs. Ag/AgCl.

As shown in Figure 4.28B, Pd/rGO_G reported 183% improvement in MOR (1017.42 vs. 359.80 mA mg^{-1}). Despite the almost similar E_{onset} (−0.44 vs. −0.43 V vs. Ag/AgCl), the incorporation of guanine favoured negative half-wave potential ($E_{1/2}$; −0.18 vs. −0.12 V vs. Ag/AgCl) and E_{peak} (−0.10 vs. −0.07 V vs. Ag/AgCl). Such an outcome can be attributed to the combination of the catalytic capabilities of Pd NPs, guanine, and rGO. Certainly, the evenly dispersed small Pd NPs and great ECSA also play a part. A promising electrocatalyst can also be defined by its ability to resist poisoning of intermediate species particularly CO that can be embodied by the $\frac{I_f}{I_b}$. In this context, Pd/rGO_G recorded much higher ratio (11.38) compared to Pd/rGO_O (3.98). Therefore, Pd/rGO_G has better capability to facilitate the oxidation of CO to CO_2, re-exposing the active sites.

University of Malaya

In term of the stability of electrocatalysts (Figure 4.28C), Pd/rGO$_G$ retained high current density (87.36 mA mg^{-1} vs. 70.56 mA mg^{-1}). Both electrocatalysts underwent rapid degradation in MOR performance during the first 50 s due to the formation of intermediate species. Further continuous operation oxidized the intermediate species, liberating the active sites and thus the subsequent steady drop in current density. The good stability of Pd/rGO$_G$ can be reasoned by its high graphitization level and low defect density. Defects can promote the corrosion of electrocatalysts under electrochemical operation. Small particle size, uniform distribution, and large ECSA were other contributing factors.

In summary, particle size and distribution of Pd NPs on graphene can significantly impact the catalytic activity. The particle size and distribution can be manipulated by the mass ratio of Pd to graphene, microwave irradiation duration, concentration of precursor mixture, synthesis method, and introduction of interlinker. The above mentioned considerations also have influencial effect to the quality of graphene which directly define the stability of the final product. The results obtained showed that 1:1, 700 s, and 1.0 mg mL^{-1} are the optimum mass ratio of Pd to graphene, microwave-irradiation duration, and precursor mixture concentration, respectively. The proposed modified method and introduction of guanine were also proved to be feasible and successfully obtained improvement.

University of Malaya

CHAPTER 5: CONCLUSIONS

5.1 Conclusions

Fuel cell is an energy conversion device whose potential still need to be explored to the maximum so that it can be commercialized. In this research work, Pd and rGO were chosen as the catalysts and catalyst support, respectively. The rGO was derived from the oxidation of graphite followed by exfoliation to GO. The GO was subsequently reduced to rGO by microwave reduction method. The reduction method recovered the superb properties of graphene to a great extent. With this rGO supported Pd, denoted as Pd/rGO, as the ground electrocatalyst, a few preliminary studies in the aspects of mass ratio of palladium to graphene and reduction duration were done. At low mass ratio (Pd:rGO = 0.5:1), the density of Pd NPs on rGO tend to be low, leading to slightly more restacking of graphene sheets. Nonetheless, high ratio (Pd:rGO = 2:1) lead to serious agglomeration of Pd NPs, greatly reducing the ECSA and thus inferior MOR activity. Regarding the reduction duration, 500 s was too short to satisfactorily recover the properties of graphene, therefore unfit to support the Pd NPs. Meanwhile, agglomeration of NPs tends to occur to sample with prolonged microwave reduction (900 s). The optimized Pd/rGO fabricated at mass ratio of 1:1 and 700 s was then further improved from the perspectives of catalyst and catalyst support (graphene).

This research work aims to synthesize Pd/rGOs that are active toward MOR via microwave-assisted reduction approach. The performance of catalysts was investigated by controlling the particle size and dispersion of Pd NPs. The particle size and dispersion of Pd NPs were manipulated by altering the concentration of precursor mixture and modifying the conventional synthesis method. With respect to catalyst support, guanine was introduced on the surface of rGO. The imino, amino, and amide

University of Malaya

groups of guanine act as anchoring sites to immobilize the Pd NPs, preventing agglomeration.

Based on the outcomes obtained, conclusions can be drawn as below:

Regarding the first objectives:

(i) Pd NPs were successfully loaded on rGO based on the FESEM and TEM images. Pd NPs agglomerated on the surface of rGO but uniformly dispersed on rGO for samples synthesized at concentration 0.5 and 1.0 mg mL^{-1}, respectively. The agglomeration became more severe with the increment of concentration beyond 1.0 mg mL^{-1}.

(ii) Increasing the concentration from 0.5 to 1.0 mg mL^{-1}, the average size of Pd NPs decreased from 7.29 to 4.70 nm. However, particle size was increased when the concentration was further increased beyond 1.0 mg mL^{-1}.

(iii) Altering the concentration of precursor mixture, the rate of nucleation and growth of Pd NPs as well as stabilizing effect of GO change.

(iv) Small particle size and well distribution of Pd NPs rendered the sample obtained at concentration 1.0 mg mL^{-1} the largest ECSA (83.57 m^2 g^{-1}), peak current density (405.37 mA mg^{-1}), and best stability. Performance difference as high as 195 % was observed by varying the concentration of precursor mixture.

Regarding the second objective:

(i) GO nanosheets were successfully reduced to rGO as reflected by the data of XRD and Raman measurements.

(ii) The modified synthesis method was proved more efficient in reducing the GO as indicated by the higher ratio of $\frac{C}{O}$ (3.05 vs. 2.98) in EDX.

University of Malaya

(iii) The rGO reduced by modified method possessed less defects, endowing better stability of the sample because defects can cause the as-synthesized electrocatalysts to corrode easily under electrochemical operation.

(iv) Pd NPs could clearly be observed on the surface of rGO. Pd NPs in the range of 6-16 nm with average particle size of 11.66 nm was obtained by conventional synthesis method. The proposed modified method reduced the average particle size to 6.23 nm and narrowed the size distribution to 3-9 nm. The rapid nucleation and high supersaturation of modified method contributed to the small size and narrow size distribution.

(v) The modified method facilitated even distribution of Pd NPs on the surface of rGO.

(vi) The modified method increased the ECSA and MOR from 63.80 to 78.97 $m^2\ g^{-1}$ and 314.94 to 434.49 mA mg^{-1}, respectively.

(vii) Sample synthesized by the modified method exhibited better resistance to CO-poisoning as shown by the higher ratio of $\frac{I_f}{I_b}$ (4.23 vs. 3.98) than that of conventional sample.

(viii) The modified sample also retained higher current density (63.74 mA mg^{-1} vs. 60.14 mA mg^{-1}) after 1000 s, signifying enhanced stability.

Regarding the third objectives:

(i) Guanine was successfully functionalized on the surface of rGO via π–π interaction.

(ii) The amino, imino, and amide groups of guanine immobilized the Pd NPs, restricting their agglomeration.

University of Malaya

(iii) Guanine was capable to direct the structure of Pd NPs, attaining triangular, rectangular, circular, and diamond shapes.

(iv) Similar to rGO, the standalone guanine was revealed to have catalytic effect. The catalytic activities of individual rGO and guanine were weak with the former slightly stronger than the latter. Upon functionalization of guanine to rGO, a surprising significant enhancement in MOR was attained. The electrooxidation of methanol as high as 164 % was further boosted at the existence of Pd NPs. Compared to the sample without guanine, 183 % higher current density (1017.42 mA mg^{-1} vs. 359.80 mA mg^{-1}), larger ECSA (111.98 $m^2 g^{-1}$ vs. 63.80 $m^2 g^{-1}$), and more negative half-wave and peak potential were achieved with the introduction of guanine.

(v) The guanine functionalized sample also better resisted CO-poisoning as represented by higher ratio of $\frac{I_f}{I_b}$ (11.38 vs. 3.98).

(vi) With respect to stability, the guanine functionalized sample showed slight improvement, retaining high current density (87.36 mA mg^{-1} vs 70.56 mA mg^{-1}) at the end of the stability test.

5.2 Future Work Recommendation

The catalytic activity of electrocatalysts can be further enhanced in the direction of: (i) morphology of catalysts loaded on graphene, (ii) restacking issue of graphene, and (iii) amount of Pd loaded on the surface of graphene. To achieve these, concern can be paid on fabricating porous Pd/rGO. Electrocatalysts of different dimensions display distinct properties. Thus, Pd/rGO with mixed multi-dimensional (0D, 1D, 2D, and 3D) could be a potential electrocatalyst. Carbon nanoscrolls (CNSs) can also be added into the Pd/rGO to inhibit the agglomeration of graphene.

University of Malaya

REFERENCES

Ahmed, M. S., Park, D., & Jeon, S. (2016). Ultrasmall Pd m Mn 1− m O x binary alloyed nanoparticles on graphene catalysts for ethanol oxidation in alkaline media. *Journal of Power Sources, 308*, 180-188.

Allen, M. J., Tung, V. C., & Kaner, R. B. (2010). Honeycomb Carbon: A Review of Graphene. *Chemical Reviews, 110*(1), 132-145. doi: 10.1021/cr900070d

Andrijanto, E., Shoelarta, S., Subiyanto, G., & Rifki, S. (2016). *Facile synthesis of graphene from graphite using ascorbic acid as reducing agent.* Paper presented at the AIP Conference Proceedings.

Ania, C. O., Seredych, M., Rodriguez-Castellon, E., & Bandosz, T. J. (2015). New copper/GO based material as an efficient oxygen reduction catalyst in an alkaline medium: The role of unique Cu/rGO architecture. *Applied Catalysis B: Environmental, 163*, 424-435.

Antolini, E. (2009a). Carbon supports for low-temperature fuel cell catalysts. *Applied Catalysis B: Environmental, 88*(1), 1-24. doi: http://dx.doi.org/10.1016/j.apcatb.2008.09.030

Antolini, E. (2009b). Palladium in fuel cell catalysis. *Energy & Environmental Science, 2*(9), 915-931. doi: 10.1039/B820837A

Antolini, E. (2010). Composite materials: An emerging class of fuel cell catalyst supports. *Applied Catalysis B: Environmental, 100*(3), 413-426. doi: http://dx.doi.org/10.1016/j.apcatb.2010.08.025

Antony, R. P., Preethi, L. K., Gupta, B., Mathews, T., Dash, S., & Tyagi, A. K. (2015). Efficient electrocatalytic performance of thermally exfoliated reduced graphene oxide-Pt hybrid. *Materials Research Bulletin, 70*(Supplement C), 60-67. doi: https://doi.org/10.1016/j.materresbull.2015.04.015

Arabzadeh, A., Salimi, A., Ashrafi, M., Soltanian, S., & Servati, P. (2016). Enhanced visible light driven photoelectrocatalytic oxidation of ethanol at reduced graphene oxide/CdS nanowires decorated with Pt nanoparticles. *Catalysis Science & Technology, 6*(10), 3485-3496.

Aristatil, G., Karthikeyan, S., Mani, N., & Ingersoll, J. (2015). Direct Electrodeposition of Graphene and Platinum Based Alloys-Analysis by SEM/EDX. *Asian Journal of Scientific Research, 8*(3), 245.

Arunchander, A., Peera, S. G., Giridhar, V., & Sahu, A. (2017). Synthesis of cobalt sulfide-graphene as an efficient oxygen reduction catalyst in alkaline medium and its application in anion exchange membrane fuel cells. *Journal of The Electrochemical Society, 164*(2), F71-F80.

University of Malaya

Avasarala, B., Moore, R., & Haldar, P. (2010). Surface oxidation of carbon supports due to potential cycling under PEM fuel cell conditions. *Electrochimica Acta, 55*(16), 4765-4771. doi: http://dx.doi.org/10.1016/j.electacta.2010.03.056

Ayán-Varela, M., Paredes, J. I., Guardia, L., Villar-Rodil, S., Munuera, J. M., Díaz-González, M., Fernández-Sánchez, C., Martínez-Alonso, A., & Tascón, J. M. D. (2015). Achieving Extremely Concentrated Aqueous Dispersions of Graphene Flakes and Catalytically Efficient Graphene-Metal Nanoparticle Hybrids with Flavin Mononucleotide as a High-Performance Stabilizer. *ACS applied materials & interfaces, 7*(19), 10293-10307. doi: 10.1021/acsami.5b00910

Ayán-Varela, M., Ruiz-Rosas, R., Villar-Rodil, S., Paredes, J. I., Cazorla-Amorós, D., Morallón, E., Martínez-Alonso, A., & Tascón, J. M. D. (2017). Efficient Pt electrocatalysts supported onto flavin mononucleotide–exfoliated pristine graphene for the methanol oxidation reaction. *Electrochimica Acta, 231*, 386-395. doi: http://dx.doi.org/10.1016/j.electacta.2016.12.177

Babu, K. F., Rajagopalan, B., Chung, J. S., & Choi, W. M. (2015). Facile synthesis of graphene/N-doped carbon nanowire composites as an effective electrocatalyst for the oxygen reduction reaction. *International Journal of Hydrogen Energy, 40*(21), 6827-6834.

Bag, S., Mondal, B., Das, A. K., & Raj, C. R. (2015). Nitrogen and sulfur dual-doped reduced graphene oxide: synergistic effect of dopants towards oxygen reduction reaction. *Electrochimica Acta, 163*, 16-23.

Bagri, A., Mattevi, C., Acik, M., Chabal, Y. J., Chhowalla, M., & Shenoy, V. B. (2010). Structural evolution during the reduction of chemically derived graphene oxide. *Nat Chem, 2*(7), 581-587. doi: http://www.nature.com/nchem/journal/v2/n7/suppinfo/nchem.686_S1.html

Bailón-García, E., Maldonado-Hódar, F., Pérez-Cadenas, A., & Carrasco-Marín, F. (2013). Catalysts Supported on Carbon Materials for the Selective Hydrogenation of Citral. *Catalysts, 3*(4), 853.

Bang, J. H., & Suslick, K. S. (2010). Applications of Ultrasound to the Synthesis of Nanostructured Materials. *Advanced Materials, 22*(10), 1039-1059. doi: 10.1002/adma.200904093

Barakat, N. A., Motlak, M., Lim, B. H., El-Newehy, M. H., & Al-Deyab, S. S. (2014). Effective and stable CoNi alloy-loaded graphene for ethanol oxidation in alkaline medium. *Journal of The Electrochemical Society, 161*(12), F1194-F1201.

Barinov, A., Malcioğlu, O. B., Fabris, S., Sun, T., Gregoratti, L., Dalmiglio, M., & Kiskinova, M. (2009). Initial Stages of Oxidation on Graphitic Surfaces: Photoemission Study and Density Functional Theory Calculations. *The Journal of Physical Chemistry C, 113*(21), 9009-9013. doi: 10.1021/jp902051d

University of Malaya

Basirun, W. J., Sookhakian, M., Baradaran, S., Mahmoudian, M. R., & Ebadi, M. (2013). Solid-phase electrochemical reduction of graphene oxide films in alkaline solution. *Nanoscale Research Letters, 8*(1), 397.

Bauer, A., Lee, K., Song, C., Xie, Y., Zhang, J., & Hui, R. (2010). Pt nanoparticles deposited on TiO2 based nanofibers: Electrochemical stability and oxygen reduction activity. *Journal of Power Sources, 195*(10), 3105-3110. doi: http://dx.doi.org/10.1016/j.jpowsour.2009.11.107

Bauer, A., Song, C., Ignaszak, A., Hui, R., Zhang, J., Chevallier, L., Jones, D. & Rozière, J. (2010). Improved stability of mesoporous carbon fuel cell catalyst support through incorporation of TiO2. *Electrochimica Acta, 55*(28), 8365-8370. doi: http://dx.doi.org/10.1016/j.electacta.2010.07.025

Bikkarolla, S. K., Yu, F., Zhou, W., Joseph, P., Cumpson, P., & Papakonstantinou, P. (2014). A three-dimensional Mn 3 O 4 network supported on a nitrogenated graphene electrocatalyst for efficient oxygen reduction reaction in alkaline media. *Journal of Materials Chemistry A, 2*(35), 14493-14501.

Bo, X., Li, M., Han, C., & Guo, L. (2013). The influence of boron dopant on the electrochemical properties of graphene as an electrode material and a support for Pt catalysts. *Electrochimica Acta, 114*, 582-589. doi: http://dx.doi.org/10.1016/j.electacta.2013.10.088

Borghei, M., Azcune, I., Carrasco, P. M., Sainio, J., Kauppinen, E., & Ruiz, V. (2014). Nitrogen-doped graphene with enhanced oxygen reduction activity produced by pyrolysis of graphene functionalized with imidazole derivatives. *International Journal of Hydrogen Energy, 39*(24), 12749-12756. doi: http://dx.doi.org/10.1016/j.ijhydene.2014.06.105

Byon, H. R., Suntivich, J., & Shao-Horn, Y. (2011). Graphene-based non-noble-metal catalysts for oxygen reduction reaction in acid. *Chemistry of materials, 23*(15), 3421-3428.

Cai, Z.-x., Liu, C.-c., Wu, G.-h., Chen, X.-m., & Chen, X. (2014). Green synthesis of Pt-on-Pd bimetallic nanodendrites on graphene via in situ reduction, and their enhanced electrocatalytic activity for methanol oxidation. *Electrochimica Acta, 127*, 377-383. doi: http://dx.doi.org/10.1016/j.electacta.2014.02.055

Cao, C., Wei, L., Wang, G., & Shen, J. (2017). Superiority of boron, nitrogen and iron ternary doped carbonized graphene oxide-based catalysts for oxygen reduction in microbial fuel cells. *Nanoscale, 9*(10), 3537-3546.

Cao, G. (2004). *Nanostructures and Nanomaterials: Synthesis, Properties and Applications* (1 edition ed.). London: Imperial College Press.

Carrera-Cerritos, R., Baglio, V., Aricò, A. S., Ledesma-García, J., Sgroi, M. F., Pullini, D., Pruna, A. J., Mataix, D. B., Fuentes-Ramírez, R. & Arriaga, L. G. (2014). Improved Pd electro-catalysis for oxygen reduction reaction in direct methanol fuel cell by reduced graphene oxide. *Applied Catalysis B: Environmental, 144*, 554-560. doi: http://dx.doi.org/10.1016/j.apcatb.2013.07.057

University of Malaya

Chandraboss, V. L., Karthikeyan, B., & Senthilvelan, S. (2015). Experimental and first-principles investigation of the adsorption and entrapping of guanine with SiO2 clusters of sol-gel silicate material for understanding DNA photodamage. *Physical Chemistry Chemical Physics, 17*(18), 12100-12114. doi: 10.1039/C5CP00451A

Chen, B., Cheng, D., & Zhu, J. (2014). Synthesis of PtCu nanowires in nonaqueous solvent with enhanced activity and stability for oxygen reduction reaction. *Journal of Power Sources, 267*, 380-387. doi: http://dx.doi.org/10.1016/j.jpowsour.2014.05.104

Chen, D.-J., Zhang, Q.-L., Feng, J.-X., Ju, K.-J., Wang, A.-J., Wei, J., & Feng, J.-J. (2015). One-pot wet-chemical co-reduction synthesis of bimetallic gold–platinum nanochains supported on reduced graphene oxide with enhanced electrocatalytic activity. *Journal of Power Sources, 287*(Supplement C), 363-369. doi: https://doi.org/10.1016/j.jpowsour.2015.04.080

Chen, J., Yao, B., Li, C., & Shi, G. (2013). An improved Hummers method for eco-friendly synthesis of graphene oxide. *Carbon, 64*, 225-229. doi: http://dx.doi.org/10.1016/j.carbon.2013.07.055

Chen, M., Meng, Y., Zhou, J., & Diao, G. (2014). Platinum nanoworms self-assemble on β-cyclodextrin polymer inclusion complexes functionalized reduced graphene oxide as enhanced catalyst for direct methanol fuel cells. *Journal of Power Sources, 265*, 110-117. doi: http://dx.doi.org/10.1016/j.jpowsour.2014.04.031

Chen, Z., Higgins, D., Tao, H., Hsu, R. S., & Chen, Z. (2009). Highly Active Nitrogen-Doped Carbon Nanotubes for Oxygen Reduction Reaction in Fuel Cell Applications. *The Journal of Physical Chemistry C, 113*(49), 21008-21013. doi: 10.1021/jp908067v

Choi, H.-J., Jung, S.-M., Seo, J.-M., Chang, D. W., Dai, L., & Baek, J.-B. (2012). Graphene for energy conversion and storage in fuel cells and supercapacitors. *Nano Energy, 1*(4), 534-551. doi: http://dx.doi.org/10.1016/j.nanoen.2012.05.001

Choi, S. M., Seo, M. H., Kim, H. J., & Kim, W. B. (2011). Synthesis of surface-functionalized graphene nanosheets with high Pt-loadings and their applications to methanol electrooxidation. *Carbon, 49*(3), 904-909. doi: http://dx.doi.org/10.1016/j.carbon.2010.10.055

Choi, W. I., Jhi, S.-H., Kim, K., & Kim, Y.-H. (2010). Divacancy-nitrogen-assisted transition metal dispersion and hydrogen adsorption in defective graphene: a first-principles study. *Physical Review B, 81*(8), 085441.

Cohen, J. L., Volpe, D. J., & Abruna, H. D. (2007). Electrochemical determination of activation energies for methanol oxidation on polycrystalline platinum in acidic and alkaline electrolytes. *Physical Chemistry Chemical Physics, 9*(1), 49-77. doi: 10.1039/B612040G

University of Malaya

Craciun, M. F., RussoS, YamamotoM, Oostinga, J. B., Morpurgo, A. F., & TaruchaS. (2009). Trilayer graphene is a semimetal with a gate-tunable band overlap. *Nat Nano, 4*(6), 383-388. doi: http://www.nature.com/nnano/journal/v4/n6/suppinfo/nnano.2009.89_S1.html

Cui, Z., Yang, M., & DiSalvo, F. J. (2014). Mesoporous Ti0.5Cr0.5N Supported PdAg Nanoalloy as Highly Active and Stable Catalysts for the Electro-oxidation of Formic Acid and Methanol. *ACS Nano, 8*(6), 6106-6113. doi: 10.1021/nn5014337

Datta, J., Dutta, A., & Mukherjee, S. (2011). The Beneficial Role of the Cometals Pd and Au in the Carbon-Supported PtPdAu Catalyst Toward Promoting Ethanol Oxidation Kinetics in Alkaline Fuel Cells: Temperature Effect and Reaction Mechanism. *The Journal of Physical Chemistry C, 115*(31), 15324-15334. doi: 10.1021/jp200318m

de Tacconi, N. R., Chenthamarakshan, C. R., Rajeshwar, K., Lin, W.-Y., Carlson, T. F., Nikiel, L., Wampler, W. A., Sambandam, S., & Ramani, V. (2008). Photocatalytically Generated Pt / C – TiO2 Electrocatalysts with Enhanced Catalyst Dispersion for Improved Membrane Durability in Polymer Electrolyte Fuel Cells. *Journal of The Electrochemical Society, 155*(11), B1102-B1109. doi: 10.1149/1.2969418

Debe, M. K. (2012). Electrocatalyst approaches and challenges for automotive fuel cells. *Nature, 486*(7401), 43-51.

Deivaraj, T. C., Chen, W., & Lee, J. Y. (2003). Preparation of PtNi nanoparticles for the electrocatalytic oxidation of methanol. *Journal of Materials Chemistry, 13*(10), 2555-2560. doi: 10.1039/B307040A

Deng, D., Pan, X., Yu, L., Cui, Y., Jiang, Y., Qi, J., Li, W.-X., Fu, Q., Ma, X., Xue, Q., Sun, G. & Bao, X. (2011). Toward N-Doped Graphene via Solvothermal Synthesis. *Chemistry of materials, 23*(5), 1188-1193. doi: 10.1021/cm102666r

Deng, D., Yu, L., Chen, X., Wang, G., Jin, L., Pan, X., Deng, J., Sun, G., & Bao, X. (2013). Iron Encapsulated within Pod-like Carbon Nanotubes for Oxygen Reduction Reaction. *Angewandte Chemie International Edition, 52*(1), 371-375. doi: 10.1002/anie.201204958

Deng, J., Ren, P., Deng, D., & Bao, X. (2015). Enhanced Electron Penetration through an Ultrathin Graphene Layer for Highly Efficient Catalysis of the Hydrogen Evolution Reaction. *Angewandte Chemie International Edition, 54*(7), 2100-2104. doi: 10.1002/anie.201409524

Du, H.-Y., Wang, C.-H., Hsu, H.-C., Chang, S.-T., Huang, H.-C., Chen, L.-C., & Chen, K.-H. (2012). Graphene nanosheet–CNT hybrid nanostructure electrode for a proton exchange membrane fuel cell. *International Journal of Hydrogen Energy, 37*(24), 18989-18995. doi: http://dx.doi.org/10.1016/j.ijhydene.2012.09.130

University of Malaya

Du, S., Lu, Y., & Steinberger-Wilckens, R. (2014). PtPd nanowire arrays supported on reduced graphene oxide as advanced electrocatalysts for methanol oxidation. *Carbon, 79*, 346-353.

Du, X., Skachko, I., Barker, A., & Andrei, E. Y. (2008). Approaching ballistic transport in suspended graphene. *Nature nanotechnology, 3*(8), 491.

Dutta, A., & Ouyang, J. (2015). Ternary NiAuPt Nanoparticles on Reduced Graphene Oxide as Catalysts toward the Electrochemical Oxidation Reaction of Ethanol. *ACS Catalysis, 5*(2), 1371-1380. doi: 10.1021/cs501365y

Dutta, S., Ray, C., Sasmal, A. K., Negishi, Y., & Pal, T. (2016). Fabrication of dog-bone shaped Au NRcore-Pt/Pdshell trimetallic nanoparticle-decorated reduced graphene oxide nanosheets for excellent electrocatalysis. *Journal of Materials Chemistry A, 4*(10), 3765-3776. doi: 10.1039/C6TA00379F

Eda, G., Fanchini, G., & Chhowalla, M. (2008). Large-area ultrathin films of reduced graphene oxide as a transparent and flexible electronic material. *Nat Nano, 3*(5), 270-274. doi: http://www.nature.com/nnano/journal/v3/n5/suppinfo/nnano.2008.83_S1.html

Ensafi, A. A., Jafari-Asl, M., & Rezaei, B. (2014). A new strategy for the synthesis of 3-D Pt nanoparticles on reduced graphene oxide through surface functionalization, Application for methanol oxidation and oxygen reduction. *Electrochimica Acta, 130*, 397-405. doi: http://dx.doi.org/10.1016/j.electacta.2014.03.057

Fampiou, I., & Ramasubramaniam, A. (2012). Binding of Pt Nanoclusters to Point Defects in Graphene: Adsorption, Morphology, and Electronic Structure. *The Journal of Physical Chemistry C, 116*(11), 6543-6555. doi: 10.1021/jp2110117

Fan, Y., Zhao, Y., Chen, D., Wang, X., Peng, X., & Tian, J. (2015). Synthesis of Pd nanoparticles supported on PDDA functionalized graphene for ethanol electro-oxidation. *International Journal of Hydrogen Energy, 40*(1), 322-329. doi: http://dx.doi.org/10.1016/j.ijhydene.2014.10.115

Faraji, M., Gharibi, H., & Javaheri, M. (2016). High Pt Loading on Polydopamine Functionalized Graphene as a High Performance Cathode Electrocatalyst for Proton Exchange Membrane Fuel Cells. *Journal of Nanostructures, 6*(2), 156-166.

Feng, Y., Liu, H., & Yang, J. (2014). Bimetallic nanodendrites via selective overgrowth of noble metals on multiply twinned Au seeds. *Journal of Materials Chemistry A, 2*(17), 6130-6137. doi: 10.1039/C3TA14121G

Fu, X., Liu, Y., Cao, X., Jin, J., Liu, Q., & Zhang, J. (2013). FeCo–N x embedded graphene as high performance catalysts for oxygen reduction reaction. *Applied Catalysis B: Environmental, 130*, 143-151.

Geng, D., Yang, S., Zhang, Y., Yang, J., Liu, J., Li, R., Sham, T.-K., Sun, X., Ye, S., & Knights, S. (2011). Nitrogen doping effects on the structure of graphene. *Applied Surface Science, 257*(21), 9193-9198.

University of Malaya

Ghosh, S., Kar, P., Bhandary, N., Basu, S., Maiyalagan, T., Sardar, S., & Pal, S. K. (2017). Reduced graphene oxide supported hierarchical flower like manganese oxide as efficient electrocatalysts toward reduction and evolution of oxygen. *International Journal of Hydrogen Energy, 42*(7), 4111-4122.

Gokhale, R., Chen, Y., Serov, A., Artyushkova, K., & Atanassov, P. (2017). Novel dual templating approach for preparation of highly active Fe-NC electrocatalyst for oxygen reduction. *Electrochimica Acta, 224*, 49-55.

Gong, M.-X., Jiang, X., Xue, T.-Y., Shen, T.-Y., Xu, L., Sun, D.-M., & Tang, Y.-W. (2015). PtCu nanodendrite-assisted synthesis of PtPdCu concave nanooctahedra for efficient electrocatalytic methanol oxidation. *Catalysis Science & Technology, 5*(12), 5105-5109. doi: 10.1039/C5CY01603G

Gopalsamy, K., Balamurugan, J., Thanh, T. D., Kim, N. H., Hui, D., & Lee, J. H. (2017). Surfactant-free synthesis of NiPd nanoalloy/graphene bifunctional nanocomposite for fuel cell. *Composites Part B: Engineering, 114*, 319-327.

Groves, M. N., Chan, A. S. W., Malardier-Jugroot, C., & Jugroot, M. (2009). Improving platinum catalyst binding energy to graphene through nitrogen doping. *Chemical Physics Letters, 481*(4), 214-219. doi: http://dx.doi.org/10.1016/j.cplett.2009.09.074

Guo, L., Jiang, W.-J., Zhang, Y., Hu, J.-S., Wei, Z.-D., & Wan, L.-J. (2015). Embedding Pt Nanocrystals in N-Doped Porous Carbon/Carbon Nanotubes toward Highly Stable Electrocatalysts for the Oxygen Reduction Reaction. *ACS Catalysis, 5*(5), 2903-2909. doi: 10.1021/acscatal.5b00117

Hancock, C. A., Ong, A. L., Slater, P. R., & Varcoe, J. R. (2014). Development of CaMn1-xRuxO3-y (x = 0 and 0.15) oxygen reduction catalysts for use in low temperature electrochemical devices containing alkaline electrolytes: ex situ testing using the rotating ring-disk electrode voltammetry method. *Journal of Materials Chemistry A, 2*(9), 3047-3056. doi: 10.1039/C3TA14383J

Hayden, B. E. (2013). Particle Size and Support Effects in Electrocatalysis. *Accounts of Chemical Research, 46*(8), 1858-1866. doi: 10.1021/ar400001n

He, D., Kou, Z., Xiong, Y., Cheng, K., Chen, X., Pan, M., & Mu, S. (2014). Simultaneous sulfonation and reduction of graphene oxide as highly efficient supports for metal nanocatalysts. *Carbon, 66*, 312-319.

He, W., Jiang, H., Zhou, Y., Yang, S., Xue, X., Zou, Z., Zhang, X., Akins, D. L., & Yang, H. (2012). An efficient reduction route for the production of Pd–Pt nanoparticles anchored on graphene nanosheets for use as durable oxygen reduction electrocatalysts. *Carbon, 50*(1), 265-274. doi: http://dx.doi.org/10.1016/j.carbon.2011.08.044

Hernandez, Y., Nicolosi, V., Lotya, M., Blighe, F. M., Sun, Z., De, S., McGovern, I. T., Holland, B., Byrne, M., Gun'Ko, Y. K., Boland, J. J., Niraj, P., Duesberg, G., Krishnamurthy, S., Goodhue, R., Hutchison, J., Scardaci, V., Ferrari, A. C., & Coleman, J. N. (2008). High-yield production of graphene by liquid-phase

University of Malaya

exfoliation of graphite. *Nat Nano, 3*(9), 563-568. doi: http://www.nature.com/nnano/journal/v3/n9/suppinfo/nnano.2008.215_S1.html

Hong, W., Li, L., Xue, R., Xu, X., Wang, H., Zhou, J., Zhao, H., Song, Y., Liu, Y., & Gao, J. (2017). One-pot hydrothermal synthesis of Zinc ferrite/reduced graphene oxide as an efficient electrocatalyst for oxygen reduction reaction. *Journal of Colloid and Interface Science, 485*, 175-182.

Hsieh, C.-T., Gu, J.-L., Chen, Y.-C., & Tzou, D.-Y. (2013). Pulse microwave synthesis of palladium catalysts on graphene electrodes for proton exchange membrane fuel cells. *Electrochimica Acta, 98*, 39-47. doi: http://dx.doi.org/10.1016/j.electacta.2013.03.039

Hu, J., Wang, L., Shi, L., & Huang, H. (2014). Preparation of La 1− x Ca x MnO 3 perovskite–graphene composites as oxygen reduction reaction electrocatalyst in alkaline medium. *Journal of Power Sources, 269*, 144-151.

Hu, X., Yu, J. C., Gong, J., Li, Q., & Li, G. (2007). α‐Fe2O3 nanorings prepared by a microwave‐assisted hydrothermal process and their sensing properties. *Advanced Materials, 19*(17), 2324-2329.

Huang, H., & Wang, X. (2014). Recent progress on carbon-based support materials for electrocatalysts of direct methanol fuel cells. *Journal of Materials Chemistry A, 2*(18), 6266-6291. doi: 10.1039/C3TA14754A

Huang, T., Mao, S., Zhou, G., Zhang, Z., Wen, Z., Huang, X., Ci, S., & Chen, J. (2015). A high-performance catalyst support for methanol oxidation with graphene and vanadium carbonitride. *Nanoscale, 7*(4), 1301-1307. doi: 10.1039/C4NR05244G

Huang, W., Wang, H., Zhou, J., Wang, J., Duchesne, P. N., Muir, D., Zhang, P., Han, N., Zhao, F., Zeng, M., Zhong, J., Jin, C., Li, Y., Lee, S.-T., & Dai, H. (2015). Highly active and durable methanol oxidation electrocatalyst based on the synergy of platinum–nickel hydroxide–graphene. *6*, 10035. doi: 10.1038/ncomms10035

Inzelt, G., Pineri, M., Schultze, J. W., & Vorotyntsev, M. A. (2000). Electron and proton conducting polymers: recent developments and prospects. *Electrochimica Acta, 45*(15), 2403-2421. doi: http://dx.doi.org/10.1016/S0013-4686(00)00329-7

Ioroi, T., Senoh, H., Yamazaki, S.-i., Siroma, Z., Fujiwara, N., & Yasuda, K. (2008). Stability of Corrosion-Resistant Magnéli-Phase Ti4O7-Supported PEMFC Catalysts at High Potentials. *Journal of The Electrochemical Society, 155*(4), B321-B326. doi: 10.1149/1.2833310

James, L., & Andrew, D. (2003). *Fuel cell systems explained* (2nd ed.). England: John Wiley & Sons Ltd.

Jasinski, R. (1964). A New Fuel Cell Cathode Catalyst. *Nature, 201*(4925), 1212-1213.

Jeena, S. E., Gnanaprakasam, P., & Selvaraju, T. (2016). Unusual attempt to direct the growth of bimetallic Ag@Pt nanorods on electrochemically reduced graphene

University of Malaya

oxide nanosheets by electroless exchange of Cu by Pt for an efficient alcohol oxidation. *Journal of Nanoparticle Research, 19*(1), 1. doi: 10.1007/s11051-016-3643-3

Jeon, I.-Y., Choi, H.-J., Jung, S.-M., Seo, J.-M., Kim, M.-J., Dai, L., & Baek, J.-B. (2013). Large-Scale Production of Edge-Selectively Functionalized Graphene Nanoplatelets via Ball Milling and Their Use as Metal-Free Electrocatalysts for Oxygen Reduction Reaction. *Journal of the American Chemical Society, 135*(4), 1386-1393. doi: 10.1021/ja3091643

Ji, Z., Shen, X., Xu, Y., Zhu, G., & Chen, K. (2014). Anchoring noble metal nanoparticles on CeO2 modified reduced graphene oxide nanosheets and their enhanced catalytic properties. *Journal of Colloid and Interface Science, 432*(Supplement C), 57-64. doi: https://doi.org/10.1016/j.jcis.2014.06.045

Jiang, H., Li, C., Shen, H., Liu, Y., Li, W., & Li, J. (2017). Supramolecular gel-assisted synthesis Co 2 P particles anchored in multielement co-doped graphene as efficient bifunctional electrocatalysts for oxygen reduction and evolution. *Electrochimica Acta, 231*, 344-353.

Jiang, Z., Jiang, Z.-j., Tian, X., & Chen, W. (2014). Amine-functionalized holey graphene as a highly active metal-free catalyst for the oxygen reduction reaction. *Journal of Materials Chemistry A, 2*(2), 441-450. doi: 10.1039/C3TA13832A

Jin, X., Lim, J., Lee, N.-S., & Hwang, S.-J. (2017). A powerful role of exfoliated metal oxide 2D nanosheets as additives for improving electrocatalyst functionality of graphene. *Electrochimica Acta, 235*, 720-729.

Jo, E. H., Chang, H., Kim, S. K., Choi, J.-H., Park, S.-R., Lee, C. M., & Jang, H. D. (2016). One-Step Synthesis of Pt/Graphene Composites from Pt Acid Dissolved Ethanol via Microwave Plasma Spray Pyrolysis. *6*, 33236. doi: 10.1038/srep33236

Jo, K., Lee, T., Choi, H. J., Park, J. H., Lee, D. J., Lee, D. W., & Kim, B.-S. (2011). Stable Aqueous Dispersion of Reduced Graphene Nanosheets via Non-Covalent Functionalization with Conducting Polymers and Application in Transparent Electrodes. *Langmuir, 27*(5), 2014-2018. doi: 10.1021/la104420p

Ju, K.-J., Feng, J.-J., Zhang, Q.-L., Wei, J., & Wang, A.-J. (2016). 5-Aminoorotic acid directed synthesis of graphene-supported AuPt nanocrystals with enhanced electrocatalytic properties. *Electrochimica Acta, 190*, 1159-1166. doi: http://dx.doi.org/10.1016/j.electacta.2015.12.149

Jung, N., Chung, D. Y., Ryu, J., Yoo, S. J., & Sung, Y.-E. (2014). Pt-based nanoarchitecture and catalyst design for fuel cell applications. *Nano Today, 9*(4), 433-456. doi: http://dx.doi.org/10.1016/j.nantod.2014.06.006

Kakaei, K. (2015). Decoration of graphene oxide with Platinum Tin nanoparticles for ethanol oxidation. *Electrochimica Acta, 165*(Supplement C), 330-337. doi: https://doi.org/10.1016/j.electacta.2015.02.068

University of Malaya

Kakaei, K., & Balavandi, A. (2016). Synthesis of halogen-doped reduced graphene oxide nanosheets as highly efficient metal-free electrocatalyst for oxygen reduction reaction. *Journal of Colloid and Interface Science, 463*, 46-54.

Kakaei, K., & Dorraji, M. (2014). One-pot synthesis of Palladium Silver nanoparticles decorated reduced graphene oxide and their application for ethanol oxidation in alkaline media. *Electrochimica Acta, 143*, 207-215. doi: http://dx.doi.org/10.1016/j.electacta.2014.07.134

Kakaei, K., & Marzang, K. (2016). One–Step synthesis of nitrogen doped reduced graphene oxide with NiCo nanoparticles for ethanol oxidation in alkaline media. *Journal of Colloid and Interface Science, 462*, 148-153.

Kakaei, K., & Zhiani, M. (2013). A new method for manufacturing graphene and electrochemical characteristic of graphene-supported Pt nanoparticles in methanol oxidation. *Journal of Power Sources, 225*(Supplement C), 356-363. doi: https://doi.org/10.1016/j.jpowsour.2012.10.003

Kang, Y. S., Jung, N., Choi, K.-H., Lee, M. J., Ahn, M., Cho, Y.-H., & Sung, Y.-E. (2014). Anode electrode with carbon buffer layer for improving methanol oxidation reaction in direct methanol fuel cell. *Applied Surface Science, 290*, 246-251. doi: http://dx.doi.org/10.1016/j.apsusc.2013.11.059

Kangasniemi, K. H., Condit, D. A., & Jarvi, T. D. (2004). Characterization of Vulcan Electrochemically Oxidized under Simulated PEM Fuel Cell Conditions. *Journal of The Electrochemical Society, 151*(4), E125-E132. doi: 10.1149/1.1649756

Khan, M., Khan, M., Kuniyil, M., Adil, S. F., Al-Warthan, A., Alkhathlan, H. Z., Tremel, W., Tahir, M. N., & Siddiqui, M. R. (2014). Biogenic synthesis of palladium nanoparticles using Pulicaria glutinosa extract and their catalytic activity towards the Suzuki coupling reaction. *Dalton Trans, 43*(24), 9026-9031. doi: 10.1039/c3dt53554a

Kim, D.-S., Zeid, E. F. A., & Kim, Y.-T. (2010). Additive treatment effect of TiO2 as supports for Pt-based electrocatalysts on oxygen reduction reaction activity. *Electrochimica Acta, 55*(11), 3628-3633. doi: http://dx.doi.org/10.1016/j.electacta.2010.01.055

Kim, Y. T., Lee, H., Kim, H. J., & Lim, T. H. (2010). PtRu nano-dandelions on thiolated carbon nanotubes: a new synthetic strategy for supported bimetallic core-shell clusters on the atomic scale. *Chem Commun (Camb), 46*(12), 2085-2087. doi: 10.1039/b920149a

Koenigsmann, C., & Wong, S. S. (2011). One-dimensional noble metal electrocatalysts: a promising structural paradigm for direct methanol fuel cells. *Energy & Environmental Science, 4*(4), 1161-1176.

Kowal, A., Li, M., Shao, M., Sasaki, K., Vukmirovic, M. B., Zhang, J., Marinkovic, N. S., Liu, P., Frenkel, A. I., & Adzic, R. R. (2009). Ternary Pt/Rh/SnO2

University of Malaya

electrocatalysts for oxidizing ethanol to CO2. *Nat Mater, 8*(4), 325-330. doi: http://www.nature.com/nmat/journal/v8/n4/suppinfo/nmat2359_S1.html

Ksar, F., Ramos, L., Keita, B., Nadjo, L., Beaunier, P., & Remita, H. (2009). Bimetallic Palladium−Gold Nanostructures: Application in Ethanol Oxidation. *Chemistry of materials, 21*(15), 3677-3683. doi: 10.1021/cm901364w

Kumar, A., Srirapu, V. K. V. P., Sharma, C. S., & Singh, R. N. (2015). Platinum - Manganese Cobaltite- Graphene Ternary Nanocomposites as Efficient Electrocatalysts for Methanol Electrooxidation in 0.5 M H2SO4. *International Journal of Innovative Research in Science, Engineering and Technology., 4*(7), 6289-6297. doi: 10.15680/IJIRSET.2015.0407137

Kumari, N., & Singh, R. N. (2016). Nanocomposites of nitrogen-doped graphene and cobalt tungsten oxide as efficient electrode materials for application in electrochemical devices. *AIMS MATERIALS SCIENCE, 3*(4), 1456-1473.

Kuttiyiel, K. A., Choi, Y., Hwang, S.-M., Park, G.-G., Yang, T.-H., Su, D., Sasaki, K., Liu, P., & Adzic, R. R. (2015). Enhancement of the oxygen reduction on nitride stabilized pt-M (M=Fe, Co, and Ni) core–shell nanoparticle electrocatalysts. *Nano Energy, 13*, 442-449. doi: http://dx.doi.org/10.1016/j.nanoen.2015.03.007

Lai, L., Potts, J. R., Zhan, D., Wang, L., Poh, C. K., Tang, C., Gong, H., Shen, Z., Lin, J., & Ruoff, R. S. (2012). Exploration of the active center structure of nitrogen-doped graphene-based catalysts for oxygen reduction reaction. *Energy & Environmental Science, 5*(7), 7936-7942. doi: 10.1039/C2EE21802J

Lee, H., Dellatore, S. M., Miller, W. M., & Messersmith, P. B. (2007). Mussel-Inspired Surface Chemistry for Multifunctional Coatings. *Science, 318*(5849), 426-430. doi: 10.1126/science.1147241

Lee, J. Y., Kim, N. Y., Shin, D. Y., Park, H.-Y., Lee, S.-S., Kwon, S. J., Lim, D.-H., Bong, K. W., Son, J. G., & Kim, J. Y. (2017). Nitrogen-doped graphene-wrapped iron nanofragments for high-performance oxygen reduction electrocatalysts. *Journal of Nanoparticle Research, 19*(3), 98.

Lee, S., Jin, X., Kim, I. Y., Gu, T.-H., Choi, J.-W., Nahm, S., & Hwang, S.-J. (2016). Superior Additive of Exfoliated RuO2 Nanosheet for Optimizing the Electrode Performance of Metal Oxide over Graphene. *The Journal of Physical Chemistry C, 120*(22), 11786-11796. doi: 10.1021/acs.jpcc.6b02257

Lee, W.-J., Alhosan, M., Yohe, S. L., Macy, N. L., & Smyrl, W. H. (2008). Synthesis of Pt / TiO2 Nanotube Catalysts for Cathodic Oxygen Reduction. *Journal of The Electrochemical Society, 155*(9), B915-B920. doi: 10.1149/1.2946726

Lee, W., Lee, J. U., Jung, B. M., Byun, J.-H., Yi, J.-W., Lee, S.-B., & Kim, B.-S. (2013). Simultaneous enhancement of mechanical, electrical and thermal properties of graphene oxide paper by embedding dopamine. *Carbon, 65*, 296-304.

University of Malaya

Lee, Y. H., Lee, G., Shim, J. H., Hwang, S., Kwak, J., Lee, K., Song, H., & Park, J. T. (2006). Monodisperse PtRu nanoalloy on carbon as a high-performance DMFC catalyst. *Chemistry of materials, 18*(18), 4209-4211.

Leng, Y. (2009). *Materials characterization: introduction to microscopic and spectroscopic methods* (Second ed.): John Wiley & Sons.

Levitan, O., Dinamarca, J., Hochman, G., & Falkowski, P. G. (2014). Diatoms: a fossil fuel of the future. *Trends in Biotechnology, 32*(3), 117-124. doi: http://dx.doi.org/10.1016/j.tibtech.2014.01.004

Li, F., Guo, Y., Liu, Y., Qiu, H., Sun, X., Wang, W., Liu, Y., & Gao, J. (2013). Fabrication of Pt–Cu/RGO hybrids and their electrochemical performance for the oxidation of methanol and formic acid in acid media. *Carbon, 64*, 11-19. doi: http://dx.doi.org/10.1016/j.carbon.2013.05.056

Li, G.-r., Wang, F., Jiang, Q.-w., Gao, X.-p., & Shen, P.-w. (2010). Carbon Nanotubes with Titanium Nitride as a Low-Cost Counter-Electrode Material for Dye-Sensitized Solar Cells. *Angewandte Chemie International Edition, 49*(21), 3653-3656. doi: 10.1002/anie.201000659

Li, J., Cai, W., Ma, L., Zhang, Y., Chen, Z., & Cheng, H. (2015). Towards neat methanol operation of direct methanol fuel cells: a novel self-assembled proton exchange membrane. *Chemical Communications, 51*(30), 6556-6559. doi: 10.1039/C4CC09420D

Li, J., Fu, X., Mao, Z., Yang, Y., Qiu, T., & Wu, Q. (2016). Synthesis of PtM (M=Co, Ni)/Reduced Graphene Oxide Nanocomposites as Electrocatalysts for the Oxygen Reduction Reaction. *Nanoscale Research Letters, 11*(1), 3. doi: 10.1186/s11671-015-1208-5

Li, L., Chen, M., Huang, G., Yang, N., Zhang, L., Wang, H., Liu, Y., Wang, W., & Gao, J. (2014). A green method to prepare Pd–Ag nanoparticles supported on reduced graphene oxide and their electrochemical catalysis of methanol and ethanol oxidation. *Journal of Power Sources, 263*, 13-21. doi: http://dx.doi.org/10.1016/j.jpowsour.2014.04.021

Li, L., Hu, L., Li, J., & Wei, Z. (2015). Enhanced stability of Pt nanoparticle electrocatalysts for fuel cells. *Nano Research, 8*(2), 418-440. doi: 10.1007/s12274-014-0695-5

Li, L., Zhang, J., Liu, Y., Zhang, W., Yang, H., Chen, J., & Xu, Q. (2013). Facile Fabrication of Pt Nanoparticles on 1-Pyrenamine Functionalized Graphene Nanosheets for Methanol Electrooxidation. *ACS Sustainable Chemistry & Engineering, 1*(5), 527-533. doi: 10.1021/sc4000016

Li, M., Bo, X., Zhang, Y., Han, C., & Guo, L. (2014). Comparative study on the oxygen reduction reaction electrocatalytic activities of iron phthalocyanines supported on reduced graphene oxide, mesoporous carbon vesicle, and ordered mesoporous carbon. *Journal of Power Sources, 264*, 114-122.

University of Malaya

Li, N., Cao, M., & Hu, C. (2012). Review on the latest design of graphene-based inorganic materials. *Nanoscale, 4*(20), 6205-6218. doi: 10.1039/C2NR31750H

Li, Y., Gao, W., Ci, L., Wang, C., & Ajayan, P. M. (2010). Catalytic performance of Pt nanoparticles on reduced graphene oxide for methanol electro-oxidation. *Carbon, 48*(4), 1124-1130. doi: http://dx.doi.org/10.1016/j.carbon.2009.11.034

Li, Y., Li, T., Yao, M., & Liu, S. (2012). Metal-free nitrogen-doped hollow carbon spheres synthesized by thermal treatment of poly (o-phenylenediamine) for oxygen reduction reaction in direct methanol fuel cell applications. *Journal of Materials Chemistry, 22*(21), 10911-10917.

Li, Y., Li, Y., Zhu, E., McLouth, T., Chiu, C.-Y., Huang, X., & Huang, Y. (2012). Stabilization of High-Performance Oxygen Reduction Reaction Pt Electrocatalyst Supported on Reduced Graphene Oxide/Carbon Black Composite. *Journal of the American Chemical Society, 134*(30), 12326-12329. doi: 10.1021/ja3031449

Liang, Y., Li, Y., Wang, H., Zhou, J., Wang, J., Regier, T., & Dai, H. (2011). Co3O4 nanocrystals on graphene as a synergistic catalyst for oxygen reduction reaction. *Nat Mater, 10*(10), 780-786. doi: http://www.nature.com/nmat/journal/v10/n10/abs/nmat3087.html#supplementary-information

Liang, Y., Wang, H., Zhou, J., Li, Y., Wang, J., Regier, T., & Dai, H. (2012). Covalent Hybrid of Spinel Manganese–Cobalt Oxide and Graphene as Advanced Oxygen Reduction Electrocatalysts. *Journal of the American Chemical Society, 134*(7), 3517-3523. doi: 10.1021/ja210924t

Lim, B., Jiang, M., Camargo, P. H. C., Cho, E. C., Tao, J., Lu, X., Zhu, Y., & Xia, Y. (2009). Pd-Pt Bimetallic Nanodendrites with High Activity for Oxygen Reduction. *Science, 324*(5932), 1302-1305. doi: 10.1126/science.1170377

Lin, L., Li, M., Jiang, L., Li, Y., Liu, D., He, X., & Cui, L. (2014). A novel iron (Ⅱ) polyphthalocyanine catalyst assembled on graphene with significantly enhanced performance for oxygen reduction reaction in alkaline medium. *Journal of Power Sources, 268*, 269-278. doi: http://dx.doi.org/10.1016/j.jpowsour.2014.06.062

Lin, S., Shen, C., Lu, D., Wang, C., & Gao, H.-J. (2013). Synthesis of Pt nanoparticles anchored on graphene-encapsulated Fe3O4 magnetic nanospheres and their use as catalysts for methanol oxidation. *Carbon, 53*, 112-119. doi: http://dx.doi.org/10.1016/j.carbon.2012.10.037

Lin, Z., Song, M.-k., Ding, Y., Liu, Y., Liu, M., & Wong, C.-p. (2012). Facile preparation of nitrogen-doped graphene as a metal-free catalyst for oxygen reduction reaction. *Physical Chemistry Chemical Physics, 14*(10), 3381-3387. doi: 10.1039/C2CP00032F

University of Malaya

Liu, A., Li, W., Jin, H., Yu, X., Bu, Y., He, Y., Huang, H., Wang, S., & Wang, J. (2015). The enhanced electrocatalytic activity of graphene co-doped with chlorine and fluorine atoms. *Electrochimica Acta, 177*, 36-42.

Liu, B., Huo, L., Zhang, G., & Zhang, J. (2016). Ternary Hollow Mesoporous TiN/N-Graphene/Pt Hybrid Results in Enhanced Electrocatalytic Performance for Methanol Oxidation and Oxygen Reduction Reaction. *Electrochimica Acta, 213*, 771-782. doi: http://dx.doi.org/10.1016/j.electacta.2016.07.098

Liu, C., Zhang, H., Tang, Y., & Luo, S. (2014). Controllable growth of graphene/Cu composite and its nanoarchitecture-dependent electrocatalytic activity to hydrazine oxidation. *Journal of Materials Chemistry A, 2*(13), 4580-4587. doi: 10.1039/C3TA14137C

Liu, D., Li, L., & You, T. (2017). Superior catalytic performances of platinum nanoparticles loaded nitrogen-doped graphene toward methanol oxidation and hydrogen evolution reaction. *Journal of Colloid and Interface Science, 487*, 330-335.

Liu, H. P., & Ma, R. Q. (2005). Littlewood–Paley g–function on the Heisenberg Group. *Acta Mathematica Sinica, 22*(1), 95. doi: 10.1007/s10114-004-0469-1

Liu, J., Zheng, Y., Hong, Z., Cai, K., Zhao, F., & Han, H. (2016). Microbial synthesis of highly dispersed PdAu alloy for enhanced electrocatalysis. *Science Advances, 2*(9). doi: 10.1126/sciadv.1600858

Liu, S., Dong, Y., Zhao, C., Zhao, Z., Yu, C., Wang, Z., & Qiu, J. (2015). Nitrogen-rich carbon coupled multifunctional metal oxide/graphene nanohybrids for long-life lithium storage and efficient oxygen reduction. *Nano Energy, 12*, 578-587.

Liu, X. X., Zang, J. B., Chen, L., Chen, L. B., Chen, X., Wu, P., Zhou, S. Y., & Wang, Y. H. (2017). A microwave-assisted synthesis of CoO@Co core-shell structures coupled with N-doped reduced graphene oxide used as a superior multi-functional electrocatalyst for hydrogen evolution, oxygen reduction and oxygen evolution reactions. *Journal of Materials Chemistry A, 5*(12), 5865-5872. doi: 10.1039/C6TA10591B

Liu, Y., Ai, K., & Lu, L. (2014). Polydopamine and Its Derivative Materials: Synthesis and Promising Applications in Energy, Environmental, and Biomedical Fields. *Chemical Reviews, 114*(9), 5057-5115. doi: 10.1021/cr400407a

Liu, Z. Y., Zhang, J. L., Yu, P. T., Zhang, J. X., Makharia, R., More, K. L., & Stach, E. A. (2010). Transmission Electron Microscopy Observation of Corrosion Behaviors of Platinized Carbon Blacks under Thermal and Electrochemical Conditions. *Journal of The Electrochemical Society, 157*(6), B906-B913. doi: 10.1149/1.3391737

Loukrakpam, R., Luo, J., He, T., Chen, Y., Xu, Z., Njoki, P. N., Wanjala, B. N., Fang, B., Mott, D., Yin, J., Klar, J., Powell, B., & Zhong, C.-J. (2011). Nanoengineered PtCo and PtNi Catalysts for Oxygen Reduction Reaction: An

University of Malaya

Assessment of the Structural and Electrocatalytic Properties. *The Journal of Physical Chemistry C, 115*(5), 1682-1694. doi: 10.1021/jp109630n

Lu, J., Li, Y., Li, S., & Jiang, S. P. (2016). Self-assembled platinum nanoparticles on sulfonic acid-grafted graphene as effective electrocatalysts for methanol oxidation in direct methanol fuel cells. *6*, 21530. doi: 10.1038/srep21530

Lu, X., Wang, G., Zhai, T., Yu, M., Xie, S., Ling, Y., Liang, C., Tong, Y., & Li, Y. (2012). Stabilized TiN Nanowire Arrays for High-Performance and Flexible Supercapacitors. *Nano Letters, 12*(10), 5376-5381. doi: 10.1021/nl302761z

Lu, Y., Jiang, Y., & Chen, W. (2013). PtPd porous nanorods with enhanced electrocatalytic activity and durability for oxygen reduction reaction. *Nano Energy, 2*(5), 836-844. doi: http://dx.doi.org/10.1016/j.nanoen.2013.02.006

Lv, J.-J., Li, S.-S., Wang, A.-J., Mei, L.-P., Feng, J.-J., Chen, J.-R., & Chen, Z. (2014). One-pot synthesis of monodisperse palladium–copper nanocrystals supported on reduced graphene oxide nanosheets with improved catalytic activity and methanol tolerance for oxygen reduction reaction. *Journal of Power Sources, 269*, 104-110.

Lv, J.-J., Zheng, J.-N., Wang, Y.-Y., Wang, A.-J., Chen, L.-L., & Feng, J.-J. (2014). A simple one-pot strategy to platinum–palladium@palladium core–shell nanostructures with high electrocatalytic activity. *Journal of Power Sources, 265*, 231-238. doi: http://dx.doi.org/10.1016/j.jpowsour.2014.04.108

Lv, J.-J., Zheng, J.-N., Zhang, H.-B., Lin, M., Wang, A.-J., Chen, J.-R., & Feng, J.-J. (2014). Simple synthesis of platinum–palladium nanoflowers on reduced graphene oxide and their enhanced catalytic activity for oxygen reduction reaction. *Journal of Power Sources, 269*, 136-143. doi: http://dx.doi.org/10.1016/j.jpowsour.2014.06.149

Lv, Z., Yang, X., & Wang, E. (2013). Highly concentrated polycations-functionalized graphene nanosheets with excellent solubility and stability, and its fast, facile and controllable assembly of multiple nanoparticles. *Nanoscale, 5*(2), 663-670.

Ma, C. a., Liu, W., Shi, M., Lang, X., Chu, Y., Chen, Z., Zhao, D., Lin, W., & Hardacre, C. (2013). Low loading platinum nanoparticles on reduced graphene oxide-supported tungsten carbide crystallites as a highly active electrocatalyst for methanol oxidation. *Electrochimica Acta, 114*, 133-141. doi: http://dx.doi.org/10.1016/j.electacta.2013.10.034

Ma, J.-h., Wang, L., Mu, X., & Li, L. (2015). Nitrogen-doped graphene supported Pt nanoparticles with enhanced performance for methanol oxidation. *International Journal of Hydrogen Energy, 40*(6), 2641-2647. doi: http://dx.doi.org/10.1016/j.ijhydene.2014.12.080

Martins, C. A., Fernández, P. S., de Lima, F., Troiani, H. E., Martins, M. E., Arenillas, A., Maia, G., & Camara, G. A. (2014). Remarkable electrochemical stability of one-step synthesized Pd nanoparticles supported on graphene and multi-walled

University of Malaya

carbon nanotubes. *Nano Energy, 9*, 142-151. doi: http://dx.doi.org/10.1016/j.nanoen.2014.07.009

Mayrhofer, K. J. J., Ashton, S. J., Meier, J. C., Wiberg, G. K. H., Hanzlik, M., & Arenz, M. (2008). Non-destructive transmission electron microscopy study of catalyst degradation under electrochemical treatment. *Journal of Power Sources, 185*(2), 734-739. doi: http://dx.doi.org/10.1016/j.jpowsour.2008.08.003

Mazumder, V., Lee, Y., & Sun, S. (2010). Recent Development of Active Nanoparticle Catalysts for Fuel Cell Reactions. *Advanced Functional Materials, 20*(8), 1224-1231. doi: 10.1002/adfm.200902293

Moghaddam, R. B., & Pickup, P. G. (2013). Influences of aniline, carbazole, indole, and pyrrole monomers and polymers on formic acid oxidation at Pt electrodes. *Electrochimica Acta, 107*, 225-230. doi: http://dx.doi.org/10.1016/j.electacta.2013.06.006

Mohanraju, K., Sreejith, V., Ananth, R., & Cindrella, L. (2015). Enhanced electrocatalytic activity of PANI and CoFe 2 O 4/PANI composite supported on graphene for fuel cell applications. *Journal of Power Sources, 284*, 383-391.

Moon, G. D., Joo, J. B., Dahl, M., Jung, H., & Yin, Y. (2014). Nitridation and Layered Assembly of Hollow TiO2 Shells for Electrochemical Energy Storage. *Advanced Functional Materials, 24*(6), 848-856. doi: 10.1002/adfm.201301718

Na, H., Zhang, L., Qiu, H., Wu, T., Chen, M., Yang, N., Li, L., Xing, F., & Gao, J. (2015). A two step method to synthesize palladium–copper nanoparticles on reduced graphene oxide and their extremely high electrocatalytic activity for the electrooxidation of methanol and ethanol. *Journal of Power Sources, 288*, 160-167. doi: http://dx.doi.org/10.1016/j.jpowsour.2015.04.116

Nagaraju, D. H., Devaraj, S., & Balaya, P. (2014). Palladium nanoparticles anchored on graphene nanosheets: Methanol, ethanol oxidation reactions and their kinetic studies. *Materials Research Bulletin, 60*(Supplement C), 150-157. doi: https://doi.org/10.1016/j.materresbull.2014.08.027

Napporn, W. T., Laborde, H., Léger, J. M., & Lamy, C. (1996). Electro-oxidation of C1 molecules at Pt-based catalysts highly dispersed into a polymer matrix: effect of the method of preparation. *Journal of Electroanalytical Chemistry, 404*(1), 153-159. doi: http://dx.doi.org/10.1016/0022-0728(95)04333-0

Nethravathi, C., Anumol, E. A., Rajamathi, M., & Ravishankar, N. (2011). Highly dispersed ultrafine Pt and PtRu nanoparticles on graphene: formation mechanism and electrocatalytic activity. *Nanoscale, 3*(2), 569-571. doi: 10.1039/C0NR00664E

Niu, W.-J., Zhu, R.-H., Zeng, H.-B., Cosnier, S., Zhang, X.-J., & Shan, D. (2016). One-pot synthesis of nitrogen-rich carbon dots decorated graphene oxide as metal-free electrocatalyst for oxygen reduction reaction. *Carbon, 109*, 402-410.

University of Malaya

Niu, W., Li, L., Liu, X., Zhou, W., Li, W., Lu, J., & Chen, S. (2015). One-pot synthesis of graphene/carbon nanospheres/graphene sandwich supported Pt 3 Ni nanoparticles with enhanced electrocatalytic activity in methanol oxidation. *International Journal of Hydrogen Energy, 40*(15), 5106-5114.

Novoselov, K. S., Geim, A. K., Morozov, S. V., Jiang, D., Zhang, Y., Dubonos, S. V., Grigorieva, I. V., & Firsov, A. A. (2004). Electric Field Effect in Atomically Thin Carbon Films. *Science, 306*(5696), 666-669. doi: 10.1126/science.1102896

Ojani, R., Raoof, J.-B., Goli, M., & Valiollahi, R. (2014). Pt–Co nanostructures electrodeposited on graphene nanosheets for methanol electrooxidation. *Journal of Power Sources, 264*, 76-82. doi: http://dx.doi.org/10.1016/j.jpowsour.2014.03.147

Pan, F., Jin, J., Fu, X., Liu, Q., & Zhang, J. (2013). Advanced oxygen reduction electrocatalyst based on nitrogen-doped graphene derived from edible sugar and urea. *ACS applied materials & interfaces, 5*(21), 11108-11114.

Pan, Z., Xiao, Y., Fu, Z., Zhan, G., Wu, S., Xiao, C., Hu, G., & Wei, Z. (2014). Hollow and porous titanium nitride nanotubes as high-performance catalyst supports for oxygen reduction reaction. *Journal of Materials Chemistry A, 2*(34), 13966-13975. doi: 10.1039/C4TA02402H

Park, K.-W., Choi, J.-H., Kwon, B.-K., Lee, S.-A., Sung, Y.-E., Ha, H.-Y., Hong, S.-A., Kim, H., & Wieckowski, A. (2002). Chemical and Electronic Effects of Ni in Pt/Ni and Pt/Ru/Ni Alloy Nanoparticles in Methanol Electrooxidation. *The Journal of Physical Chemistry B, 106*(8), 1869-1877. doi: 10.1021/jp013168v

Park, S., Shao, Y., Wan, H., Rieke, P. C., Viswanathan, V. V., Towne, S. A., Saraf, L. V., Liu, J., Lin, Y., & Wang, Y. (2011). Design of graphene sheets-supported Pt catalyst layer in PEM fuel cells. *Electrochemistry Communications, 13*(3), 258-261.

Paulus, U. A., Wokaun, A., Scherer, G. G., Schmidt, T. J., Stamenkovic, V., Radmilovic, V., Markovic, N. M., & Ross, P. N. (2002). Oxygen Reduction on Carbon-Supported Pt−Ni and Pt−Co Alloy Catalysts. *The Journal of Physical Chemistry B, 106*(16), 4181-4191. doi: 10.1021/jp013442l

Pei, S., & Cheng, H.-M. (2012). The reduction of graphene oxide. *Carbon, 50*(9), 3210-3228. doi: http://dx.doi.org/10.1016/j.carbon.2011.11.010

Peigney, A., Laurent, C., Flahaut, E., Bacsa, R., & Rousset, A. (2001). Specific surface area of carbon nanotubes and bundles of carbon nanotubes. *Carbon, 39*(4), 507-514.

Pinithchaisakula, A., Themsirimongkon, S., Promsawan, N., Weankeaw, P., Ounnunkad, K., & Saipanya, S. (2017). An Investigation of a Polydopamine-Graphene Oxide Composite as a Support for an Anode Fuel Cell Catalyst. *Electrocatalysis, 8*(1), 36-45. doi: 10.1007/s12678-016-0338-6

University of Malaya

Qazzazie, D., Beckert, M., Mülhaupt, R., Yurchenko, O., & Urban, G. (2015). Modified Nitrogen-Doped Graphene Electrocatalyst for Oxygen Reduction Reaction in Alkaline Fuel Cells. *Editorial Board Members*, 886.

Qi, J., Benipal, N., Liang, C., & Li, W. (2016). PdAg/CNT catalyzed alcohol oxidation reaction for high-performance anion exchange membrane direct alcohol fuel cell (alcohol=methanol, ethanol, ethylene glycol and glycerol). *Applied Catalysis B: Environmental, 199*(Supplement C), 494-503. doi: https://doi.org/10.1016/j.apcatb.2016.06.055

Qi, X., Pu, K. Y., Zhou, X., Li, H., Liu, B., Boey, F., Huang, W., & Zhang, H. (2010). Conjugated-polyelectrolyte-functionalized reduced graphene oxide with excellent solubility and stability in polar solvents. *Small, 6*(5), 663-669. doi: 10.1002/smll.200902221

Qian, H., Chen, S., Fu, Y., & Wang, X. (2015). Platinum–palladium bimetallic nanoparticles on graphitic carbon nitride modified carbon black: A highly electroactive and durable catalyst for electrooxidation of alcohols. *Journal of Power Sources, 300*, 41-48. doi: http://dx.doi.org/10.1016/j.jpowsour.2015.09.051

Qiao, X., You, C., Shu, T., Fu, Z., Zheng, R., Zeng, X., Li, X., & Liao, S. (2014). A one-pot method to synthesize high performance multielement co-doped reduced graphene oxide catalysts for oxygen reduction. *Electrochemistry Communications, 47*, 49-53.

Qu, K., Zheng, Y., Dai, S., & Qiao, S. Z. (2016). Graphene oxide-polydopamine derived N, S-codoped carbon nanosheets as superior bifunctional electrocatalysts for oxygen reduction and evolution. *Nano Energy, 19*, 373-381.

Qu, L., Liu, Y., Baek, J.-B., & Dai, L. (2010). Nitrogen-doped graphene as efficient metal-free electrocatalyst for oxygen reduction in fuel cells. *ACS Nano, 4*(3), 1321-1326.

Rao, C. V., Cabrera, C. R., & Ishikawa, Y. (2010). In Search of the Active Site in Nitrogen-Doped Carbon Nanotube Electrodes for the Oxygen Reduction Reaction. *The Journal of Physical Chemistry Letters, 1*(18), 2622-2627. doi: 10.1021/jz100971v

Razmjooei, F., Singh, K. P., Song, M. Y., & Yu, J.-S. (2014). Enhanced electrocatalytic activity due to additional phosphorous doping in nitrogen and sulfur-doped graphene: a comprehensive study. *Carbon, 78*, 257-267.

Reddy, G. V., Raghavendra, P., Ankamwar, B., Sri Chandana, P., Senthil Kumar, S. M., & Sarma, L. S. (2017). Ultrafine Pt-Ru bimetallic nanoparticles anchored on reduced graphene oxide sheets as highly active electrocatalysts for methanol oxidation. *Materials Chemistry Frontiers, 1*(4), 757-766. doi: 10.1039/C6QM00212A

Ruan, L., Zhu, E., Chen, Y., Lin, Z., Huang, X., Duan, X., & Huang, Y. (2013). Biomimetic Synthesis of an Ultrathin Platinum Nanowire Network with a High

University of Malaya

Twin Density for Enhanced Electrocatalytic Activity and Durability. *Angewandte Chemie International Edition, 52*(48), 12577-12581. doi: 10.1002/anie.201304658

Ruiz Camacho, B., Morais, C., Valenzuela, M. A., & Alonso-Vante, N. (2013). Enhancing oxygen reduction reaction activity and stability of platinum via oxide-carbon composites. *Catalysis Today, 202*, 36-43. doi: http://dx.doi.org/10.1016/j.cattod.2012.03.033

Sahu, S. C., Samantara, A. K., Satpati, B., Bhattacharjee, S., & Jena, B. K. (2013). A facile approach for in situ synthesis of graphene-branched-Pt hybrid nanostructures with excellent electrochemical performance. *Nanoscale, 5*(22), 11265-11274. doi: 10.1039/C3NR03372D

Salvi, B. L., Subramanian, K. A., & Panwar, N. L. (2013). Alternative fuels for transportation vehicles: A technical review. *Renewable and Sustainable Energy Reviews, 25*, 404-419. doi: http://dx.doi.org/10.1016/j.rser.2013.04.017

Saminathan, K., Kamavaram, V., Veedu, V., & Kannan, A. M. (2009). Preparation and evaluation of electrodeposited platinum nanoparticles on in situ carbon nanotubes grown carbon paper for proton exchange membrane fuel cells. *International Journal of Hydrogen Energy, 34*(9), 3838-3844. doi: http://dx.doi.org/10.1016/j.ijhydene.2009.03.009

Schniepp, H. C., Li, J.-L., McAllister, M. J., Sai, H., Herrera-Alonso, M., Adamson, D. H., Prud'homme, R. K., Car, R., Saville, D. A., & Aksay, I. A. (2006). Functionalized Single Graphene Sheets Derived from Splitting Graphite Oxide. *The Journal of Physical Chemistry B, 110*(17), 8535-8539. doi: 10.1021/jp060936f

Seo, M. H., Choi, S. M., Lee, D. U., Kim, W. B., & Chen, Z. (2015). Correlation between theoretical descriptor and catalytic oxygen reduction activity of graphene supported palladium and palladium alloy electrocatalysts. *Journal of Power Sources, 300*, 1-9. doi: http://dx.doi.org/10.1016/j.jpowsour.2015.08.079

Shao, M. (2013). *Electrocatalysis in fuel cells: a non-and low-platinum approach* (Vol. 9): Springer Science & Business Media.

Shao, Y., Yin, G., Wang, Z., & Gao, Y. (2007). Proton exchange membrane fuel cell from low temperature to high temperature: Material challenges. *Journal of Power Sources, 167*(2), 235-242. doi: http://dx.doi.org/10.1016/j.jpowsour.2007.02.065

Shao, Y., Zhang, S., Engelhard, M. H., Li, G., Shao, G., Wang, Y., Liu, J., Aksay, I. A., & Lin, Y. (2010). Nitrogen-doped graphene and its electrochemical applications. *Journal of Materials Chemistry, 20*(35), 7491-7496.

Sharma, S., Ganguly, A., Papakonstantinou, P., Miao, X., Li, M., Hutchison, J. L., Delichatsios, M., & Ukleja, S. (2010). Rapid Microwave Synthesis of CO Tolerant Reduced Graphene Oxide-Supported Platinum Electrocatalysts for

University of Malaya

Oxidation of Methanol. *The Journal of Physical Chemistry C, 114*(45), 19459-19466. doi: 10.1021/jp107872z

Shen, Y., Xiao, K., Xi, J., & Qiu, X. (2015). Comparison study of few-layered graphene supported platinum and platinum alloys for methanol and ethanol electro-oxidation. *Journal of Power Sources, 278*, 235-244. doi: http://dx.doi.org/10.1016/j.jpowsour.2014.12.062

Shen, Y., Zhang, M. Z., Xiao, K., & Xi, J. (2014a). Synthesis of Pt, PtRh, and PtRhNi Alloys Supported by Pristine Graphene Nanosheets for Ethanol Electrooxidation. *ChemCatChem, 6*(11), 3254-3261. doi: 10.1002/cctc.201402629

Shen, Y., Zhang, Z., Long, R., Xiao, K., & Xi, J. (2014). Synthesis of ultrafine Pt nanoparticles stabilized by pristine graphene nanosheets for electro-oxidation of methanol. *ACS applied materials & interfaces, 6*(17), 15162-15170.

Shen, Y., Zhang, Z., Xiao, K., & Xi, J. (2014b). Electrocatalytic activity of Pt subnano/nanoclusters stabilized by pristine graphene nanosheets. *Physical Chemistry Chemical Physics, 16*(39), 21609-21614. doi: 10.1039/C4CP03048F

Sheng, Z.-H., Shao, L., Chen, J.-J., Bao, W.-J., Wang, F.-B., & Xia, X.-H. (2011). Catalyst-Free Synthesis of Nitrogen-Doped Graphene via Thermal Annealing Graphite Oxide with Melamine and Its Excellent Electrocatalysis. *ACS Nano, 5*(6), 4350-4358. doi: 10.1021/nn103584t

Singh, R. N., & Sharma, C. S. (2012). Preparation of bimetallic Pd-Co nanoparticles on graphene support for use as methanol tolerant oxygen reduction electrocatalysts. *Engineering, Technology & Applied Science Research, 2*(6), pp. 295-301.

Solano, E., Perez-Mirabet, L., Martinez-Julian, F., Guzmán, R., Arbiol, J., Puig, T., Obradors, X., Yañez, R., Pomar, A., & Ricart, S. (2012). Facile and efficient one-pot solvothermal and microwave-assisted synthesis of stable colloidal solutions of MFe 2 O 4 spinel magnetic nanoparticles. *Journal of Nanoparticle Research, 14*(8), 1034.

Song, C., & Kim, S. (2015). Preparation and Electrochemical Characterization of Pt-Supported Flake-like Graphitic Carbon Nitride on Reduced Graphene Oxide as Fuel Cell Catalysts. *Journal of The Electrochemical Society, 162*(10), F1181-F1190. doi: 10.1149/2.0341510jes

Soo, L. T., Loh, K. S., Mohamad, A. B., & Daud, W. R. W. (2017). The effect of varying N/C ratios of nitrogen precursors during non-metal graphene catalyst synthesis. *International Journal of Hydrogen Energy, 42*(14), 9069-9076.

Soo, L. T., Loh, K. S., Mohamad, A. B., Daud, W. R. W., & Wong, W. Y. (2016). Synthesis of silver/nitrogen-doped reduced graphene oxide through a one-step thermal solid-state reaction for oxygen reduction in an alkaline medium. *Journal of Power Sources, 324*, 412-420. doi: http://dx.doi.org/10.1016/j.jpowsour.2016.05.106

University of Malaya

Stamenkovic, V., Mun, B. S., Mayrhofer, K. J. J., Ross, P. N., Markovic, N. M., Rossmeisl, J., Greeley, J., & Nørskov, J. K. (2006). Changing the Activity of Electrocatalysts for Oxygen Reduction by Tuning the Surface Electronic Structure. *Angewandte Chemie International Edition, 45*(18), 2897-2901. doi: 10.1002/anie.200504386

Stamenkovic, V. R., Fowler, B., Mun, B. S., Wang, G., Ross, P. N., Lucas, C. A., & Marković, N. M. (2007). Improved Oxygen Reduction Activity on Pt₃Ni(111) via Increased Surface Site Availability. *Science, 315*(5811), 493-497. doi: 10.1126/science.1135941

Stamenkovic, V. R., Mun, B. S., Arenz, M., Mayrhofer, K. J. J., Lucas, C. A., Wang, G., Ross, P. N., & Markovic, N. M. (2007). Trends in electrocatalysis on extended and nanoscale Pt-bimetallic alloy surfaces. *Nat Mater, 6*(3), 241-247. doi: http://www.nature.com/nmat/journal/v6/n3/suppinfo/nmat1840_S1.html

Stankovich, S., Dikin, D. A., Piner, R. D., Kohlhaas, K. A., Kleinhammes, A., Jia, Y., Wu, Y., Nguyen, S. T., & Ruoff, R. S. (2007). Synthesis of graphene-based nanosheets via chemical reduction of exfoliated graphite oxide. *Carbon, 45*(7), 1558-1565. doi: http://dx.doi.org/10.1016/j.carbon.2007.02.034

Su, Y., Chai, H., Sun, Z., Liu, T., Jia, D., & Zhou, W. (2016). High-Performance Manganese Nanoparticles on Reduced Graphene Oxide for Oxygen Reduction Reaction. *Catalysis Letters, 146*(6), 1019-1026.

Su, Y., Jiang, H., Zhu, Y., Zou, W., Yang, X., Chen, J., & Li, C. (2014). Hierarchical porous iron and nitrogen co-doped carbons as efficient oxygen reduction electrocatalysts in neutral media. *Journal of Power Sources, 265*, 246-253. doi: https://doi.org/10.1016/j.jpowsour.2014.04.140

Su, Y., Zhang, Y., Zhuang, X., Li, S., Wu, D., Zhang, F., & Feng, X. (2013). Low-temperature synthesis of nitrogen/sulfur co-doped three-dimensional graphene frameworks as efficient metal-free electrocatalyst for oxygen reduction reaction. *Carbon, 62*, 296-301.

Subbaraman, R., Tripkovic, D., Chang, K.-C., Strmcnik, D., Paulikas, A. P., Hirunsit, P., Chan, M., Greeley, J., Stamenkovic, V., & Markovic, N. M. (2012). Trends in activity for the water electrolyser reactions on 3d M (Ni, Co, Fe, Mn) hydr (oxy) oxide catalysts. *Nature materials, 11*(6), 550.

Subbaraman, R., Tripkovic, D., Strmcnik, D., Chang, K.-C., Uchimura, M., Paulikas, A. P., Stamenkovic, V., & Markovic, N. M. (2011). Enhancing hydrogen evolution activity in water splitting by tailoring Li+-Ni (OH) 2-Pt interfaces. *Science, 334*(6060), 1256-1260.

Sun, F., Zhang, G., Xu, Y., Chang, Z., Wan, P., Li, Y., & Sun, X. (2014). Promoted Oxygen Reduction Activity of Ag/Reduced Graphene Oxide by Incorporated CoOx. *Electrochimica Acta, 132*, 136-141. doi: http://dx.doi.org/10.1016/j.electacta.2014.03.125

University of Malaya

Sun, L., Liao, B., Ren, X., Li, Y., Zhang, P., Deng, L., & Gao, Y. (2017). Ternary PdNi-based nanocrystals supported on nitrogen-doped reduced graphene oxide as highly active electrocatalysts for the oxygen reduction reaction. *Electrochimica Acta, 235*, 543-552. doi: http://dx.doi.org/10.1016/j.electacta.2017.03.159

Sun, Q., Park, S. J., & Kim, S. (2015). Enhanced Catalytic Activity of Pt Supported on Nitrogen-Doped Reduced Graphene Oxide Electrodes for Fuel Cells. *J Nanosci Nanotechnol, 15*(11), 9088-9092.

Sun, S., Zhang, G., Geng, D., Chen, Y., Li, R., Cai, M., & Sun, X. (2011). A highly durable platinum nanocatalyst for proton exchange membrane fuel cells: multiarmed starlike nanowire single crystal. *Angewandte Chemie, 123*(2), 442-446.

Sun, Y., Shen, Z., Xin, S., Ma, L., Xiao, C., Ding, S., Li, F., & Gao, G. (2017). Ultrafine Co-doped ZnO nanoparticles on reduced graphene oxide as an efficient electrocatalyst for oxygen reduction reaction. *Electrochimica Acta, 224*, 561-570.

Tan, J. L., De Jesus, A. M., Chua, S. L., Sanetuntikul, J., Shanmugam, S., Tongol, B. J. V., & Kim, H. (2017). Preparation and characterization of palladium-nickel on graphene oxide support as anode catalyst for alkaline direct ethanol fuel cell. *Applied Catalysis A: General, 531*, 29-35. doi: http://dx.doi.org/10.1016/j.apcata.2016.11.034

Tang, J., Hou, L., Tang, D., Zhou, J., Wang, Z., Li, J., & Chen, G. (2012). Magneto-controlled electrochemical immunoassay of brevetoxin B in seafood based on guanine-functionalized graphene nanoribbons. *Biosensors and Bioelectronics, 38*(1), 86-93.

Tang, J., Wang, T., Sun, X., Hu, Y., Xie, Q., Guo, Y., Xue, H., & He, J. (2013). Novel synthesis of reduced graphene oxide-ordered mesoporous carbon composites and their application in electrocatalysis. *Electrochimica Acta, 90*, 53-62. doi: http://dx.doi.org/10.1016/j.electacta.2012.11.099

Tian, J., Sun, G., Cai, M., Mao, Q., & Xin, Q. (2008). PtTiO x / C Electrocatalysts with Improved Durability in H2 / O2 PEMFCs without External Humidification. *Journal of The Electrochemical Society, 155*(2), B187-B193. doi: 10.1149/1.2816290

Tian, M., Wu, G., & Chen, A. (2012). Unique Electrochemical Catalytic Behavior of Pt Nanoparticles Deposited on TiO2 Nanotubes. *ACS Catalysis, 2*(3), 425-432. doi: 10.1021/cs200691a

Tian, N., Zhou, Z.-Y., Sun, S.-G., Ding, Y., & Wang, Z. L. (2007). Synthesis of Tetrahexahedral Platinum Nanocrystals with High-Index Facets and High Electro-Oxidation Activity. *Science, 316*(5825), 732-735. doi: 10.1126/science.1140484

Tian, X., Luo, J., Nan, H., Fu, Z., Zeng, J., & Liao, S. (2015). Binary transition metal nitrides with enhanced activity and durability for the oxygen reduction reaction.

University of Malaya

Journal of Materials Chemistry A, 3(32), 16801-16809. doi: 10.1039/C5TA04410C

Tian, X., Luo, J., Nan, H., Zou, H., Chen, R., Shu, T., Li, X., Li, Y., Song, H., Liao, S., & Adzic, R. R. (2016). Transition Metal Nitride Coated with Atomic Layers of Pt as a Low-Cost, Highly Stable Electrocatalyst for the Oxygen Reduction Reaction. *Journal of the American Chemical Society, 138*(5), 1575-1583. doi: 10.1021/jacs.5b11364

Tiido, K., Alexeyeva, N., Couillard, M., Bock, C., MacDougall, B. R., & Tammeveski, K. (2013). Graphene–TiO2 composite supported Pt electrocatalyst for oxygen reduction reaction. *Electrochimica Acta, 107*, 509-517. doi: http://dx.doi.org/10.1016/j.electacta.2013.05.155

Tiwari, J. N., Nath, K., Kumar, S., Tiwari, R. N., Kemp, K. C., Le, N. H., Youn, D. H., Lee, J. S., & Kim, K. S. (2013). Stable platinum nanoclusters on genomic DNA–graphene oxide with a high oxygen reduction reaction activity. *Nature communications, 4*.

Tsakova, V. (2008). How to affect number, size, and location of metal particles deposited in conducting polymer layers. *Journal of Solid State Electrochemistry, 12*(11), 1421-1434. doi: 10.1007/s10008-007-0494-y

Varela-Rizo, H., Martín-Gullón, I., & Terrones, M. (2012). Hybrid Films with Graphene Oxide and Metal Nanoparticles Could Now Replace Indium Tin Oxide. *ACS Nano, 6*(6), 4565-4572. doi: 10.1021/nn302221q

Vedala, H., Sorescu, D. C., Kotchey, G. P., & Star, A. (2011). Chemical Sensitivity of Graphene Edges Decorated with Metal Nanoparticles. *Nano Letters, 11*(6), 2342-2347. doi: 10.1021/nl2006438

Videla, A. H. M., Ban, S., Specchia, S., Zhang, L., & Zhang, J. (2014). Non-noble Fe–NX electrocatalysts supported on the reduced graphene oxide for oxygen reduction reaction. *Carbon, 76*, 386-400.

Vilian, A. E., Rajkumar, M., Chen, S.-M., Hu, C.-C., Boopathi, K. M., & Chu, C.-W. (2014). High electrocatalytic performance of platinum and manganese dioxide nanoparticle decorated reduced graphene oxide sheets for methanol electro-oxidation. *RSC Advances, 4*(78), 41387-41397.

Vinayan, B. P., Nagar, R., Rajalakshmi, N., & Ramaprabhu, S. (2012). Novel Platinum–Cobalt Alloy Nanoparticles Dispersed on Nitrogen-Doped Graphene as a Cathode Electrocatalyst for PEMFC Applications. *Advanced Functional Materials, 22*(16), 3519-3526. doi: 10.1002/adfm.201102544

Wan, Y., Yang, H., & Zhao, D. (2006). "Host−Guest" Chemistry in the Synthesis of Ordered Nonsiliceous Mesoporous Materials. *Accounts of Chemical Research, 39*(7), 423-432. doi: 10.1021/ar050091a

Wang, H., Zhou, Y., Wu, D., Liao, L., Zhao, S., Peng, H., & Liu, Z. (2013). Synthesis of Boron-Doped Graphene Monolayers Using the Sole Solid Feedstock by

University of Malaya

Chemical Vapor Deposition. *Small, 9*(8), 1316-1320. doi: 10.1002/smll.201203021

Wang, K., Xiao, P., Liu, Y., Wang, T., & Zhang, M. (2017). Rational design and synthesis of sandwich-like iron nitride-graphene composites as efficient catalysts for oxygen reduction reaction. *International Journal of Hydrogen Energy, 42*(1), 202-211.

Wang, M., Hou, Y., Slade, R. C. T., Wang, J., Shi, D., Wexler, D., Liu, H., & Chen, J. (2016). Core-Shell Co/CoO Integrated on 3D Nitrogen Doped Reduced Graphene Oxide Aerogel as an Enhanced Electrocatalyst for the Oxygen Reduction Reaction. *Frontiers in Chemistry, 4*(36). doi: 10.3389/fchem.2016.00036

Wang, S., Wang, X., & Jiang, S. P. (2008). PtRu nanoparticles supported on 1-aminopyrene-functionalized multiwalled carbon nanotubes and their electrocatalytic activity for methanol oxidation. *Langmuir, 24*(18), 10505-10512. doi: 10.1021/la800925t

Wang, S., Yu, D., Dai, L., Chang, D. W., & Baek, J.-B. (2011). Polyelectrolyte-functionalized graphene as metal-free electrocatalysts for oxygen reduction. *ACS Nano, 5*(8), 6202-6209.

Wang, T., Gao, D., Zhuo, J., Zhu, Z., Papakonstantinou, P., Li, Y., & Li, M. (2013). Size-Dependent Enhancement of Electrocatalytic Oxygen-Reduction and Hydrogen-Evolution Performance of MoS2 Particles. *Chemistry – A European Journal, 19*(36), 11939-11948. doi: 10.1002/chem.201301406

Wang, T., Lin, C., Ye, F., Fang, Y., Li, J., & Wang, X. (2008). MEA with double-layered catalyst cathode to mitigate methanol crossover in DMFC. *Electrochemistry Communications, 10*(9), 1261-1263. doi: http://dx.doi.org/10.1016/j.elecom.2008.05.049

Wang, Y.-J., Wilkinson, D. P., & Zhang, J. (2011). Noncarbon Support Materials for Polymer Electrolyte Membrane Fuel Cell Electrocatalysts. *Chemical Reviews, 111*(12), 7625-7651. doi: 10.1021/cr100060r

Wang, Y., Zhao, Y., He, W., Yin, J., & Su, Y. (2013). Palladium nanoparticles supported on reduced graphene oxide: Facile synthesis and highly efficient electrocatalytic performance for methanol oxidation. *Thin Solid Films, 544*, 88-92. doi: http://dx.doi.org/10.1016/j.tsf.2013.04.119

Wang, Y., Zhao, Y., Yin, J., Liu, M., Dong, Q., & Su, Y. (2014). Synthesis and electrocatalytic alcohol oxidation performance of Pd–Co bimetallic nanoparticles supported on graphene. *International Journal of Hydrogen Energy, 39*(3), 1325-1335.

Wei, C., Wang, H., Eid, K., Kim, J., Kim, J. H., Alothman, Z. A., Yamauchi, Y., & Wang, L. (2017). A Three‐Dimensionally Structured Electrocatalyst: Cobalt‐Embedded Nitrogen‐Doped Carbon Nanotubes/Nitrogen‐Doped Reduced

University of Malaya

Graphene Oxide Hybrid for Efficient Oxygen Reduction. *Chemistry-A European Journal, 23*(3), 637-643.

Wong, W. Y., Daud, W. R. W., Mohamad, A. B., Kadhum, A. A. H., Loh, K. S., & Majlan, E. H. (2013). Recent progress in nitrogen-doped carbon and its composites as electrocatalysts for fuel cell applications. *International Journal of Hydrogen Energy, 38*(22), 9370-9386. doi: http://dx.doi.org/10.1016/j.ijhydene.2012.12.095

Wu, G., More, K. L., Johnston, C. M., & Zelenay, P. (2011). High-performance electrocatalysts for oxygen reduction derived from polyaniline, iron, and cobalt. *Science, 332*(6028), 443-447. doi: 10.1126/science.1200832

Wu, J., Qi, L., You, H., Gross, A., Li, J., & Yang, H. (2012). Icosahedral Platinum Alloy Nanocrystals with Enhanced Electrocatalytic Activities. *Journal of the American Chemical Society, 134*(29), 11880-11883. doi: 10.1021/ja303950v

Wu, J., Zhang, J., Peng, Z., Yang, S., Wagner, F. T., & Yang, H. (2010). Truncated Octahedral Pt3Ni Oxygen Reduction Reaction Electrocatalysts. *Journal of the American Chemical Society, 132*(14), 4984-4985. doi: 10.1021/ja100571h

Wu, K.-H., Wang, D.-W., & Gentle, I. R. (2014). The value of mixed conduction for oxygen electroreduction on graphene–chitosan composites. *Carbon, 73*, 234-243. doi: http://dx.doi.org/10.1016/j.carbon.2014.02.059

Wu, Z.-S., Yang, S., Sun, Y., Parvez, K., Feng, X., & Müllen, K. (2012). 3D Nitrogen-Doped Graphene Aerogel-Supported Fe3O4 Nanoparticles as Efficient Electrocatalysts for the Oxygen Reduction Reaction. *Journal of the American Chemical Society, 134*(22), 9082-9085. doi: 10.1021/ja3030565

Wu, Z., Lv, Y., Xia, Y., Webley, P. A., & Zhao, D. (2012). Ordered Mesoporous Platinum@Graphitic Carbon Embedded Nanophase as a Highly Active, Stable, and Methanol-Tolerant Oxygen Reduction Electrocatalyst. *Journal of the American Chemical Society, 134*(4), 2236-2245. doi: 10.1021/ja209753w

Xia, B., Yan, Y., Wang, X., & Lou, X. W. (2014). Recent progress on graphene-based hybrid electrocatalysts. *Materials Horizons, 1*(4), 379-399. doi: 10.1039/C4MH00040D

Xiao, Y., Zhan, G., Fu, Z., Pan, Z., Xiao, C., Wu, S., Chen, C., Hu, G., & Wei, Z. (2014). Robust non-carbon titanium nitride nanotubes supported Pt catalyst with enhanced catalytic activity and durability for methanol oxidation reaction. *Electrochimica Acta, 141*, 279-285. doi: http://dx.doi.org/10.1016/j.electacta.2014.07.070

Xie, Y., Wang, J., Huang, X., Luo, B., Yu, W., & Shao, L. (2017). Palladium nanoparticles supported on graphene sheets incorporating boron oxides (B x O y) for enhanced formic acid oxidation. *Electrochemistry Communications, 74*, 48-52.

University of Malaya

Xin, L., Yang, F., Qiu, Y., Uzunoglu, A., Rockward, T., Borup, R. L., Stanciu, L. A., Li, W., & Xie, J. (2016). Polybenzimidazole (PBI) Functionalized Nanographene as Highly Stable Catalyst Support for Polymer Electrolyte Membrane Fuel Cells (PEMFCs). *Journal of The Electrochemical Society, 163*(10), F1228-F1236. doi: 10.1149/2.0921610jes

Xin, L., Yang, F., Rasouli, S., Qiu, Y., Li, Z.-F., Uzunoglu, A., Sun, C.-J., Liu, Y., Ferreira, P., & Li, W. (2016). Understanding Pt nanoparticle anchoring on graphene supports through surface functionalization. *ACS Catalysis, 6*(4), 2642-2653.

Xiong, B., Zhou, Y., Zhao, Y., Wang, J., Chen, X., O'Hayre, R., & Shao, Z. (2013). The use of nitrogen-doped graphene supporting Pt nanoparticles as a catalyst for methanol electrocatalytic oxidation. *Carbon, 52*, 181-192. doi: http://dx.doi.org/10.1016/j.carbon.2012.09.019

Xu, L. Q., Yang, W. J., Neoh, K.-G., Kang, E.-T., & Fu, G. D. (2010). Dopamine-Induced Reduction and Functionalization of Graphene Oxide Nanosheets. *Macromolecules, 43*(20), 8336-8339. doi: 10.1021/ma101526k

Xu, S., Ye, L., Li, Z., Wang, Y., Lei, F., & Lin, S. (2016). Facile Synthesis of Bimetallic Pt-Ag/Graphene Composite and Its Electro-Photo-Synergistic Catalytic Properties for Methanol Oxidation. *Catalysts, 6*(9), 144.

Yan, J., Wei, T., Qiao, W., Shao, B., Zhao, Q., Zhang, L., & Fan, Z. (2010). Rapid microwave-assisted synthesis of graphene nanosheet/Co3O4 composite for supercapacitors. *Electrochimica Acta, 55*(23), 6973-6978.

Yan, W., Yang, Z., Bian, W., & Yang, R. (2015). FeCo2O4/hollow graphene spheres hybrid with enhanced electrocatalytic activities for oxygen reduction and oxygen evolution reaction. *Carbon, 92*, 74-83. doi: https://doi.org/10.1016/j.carbon.2015.03.021

Yang, H., Li, F., Shan, C., Han, D., Zhang, Q., Niu, L., & Ivaska, A. (2009). Covalent functionalization of chemically converted graphene sheets via silane and its reinforcement. *Journal of Materials Chemistry, 19*(26), 4632-4638. doi: 10.1039/B901421G

Yang, J., Tian, C., Wang, L., & Fu, H. (2011). An effective strategy for small-sized and highly-dispersed palladium nanoparticles supported on graphene with excellent performance for formic acid oxidation. *Journal of Materials Chemistry, 21*(10), 3384-3390.

Yang, L., Tang, Y., Luo, S., Liu, C., Song, H., & Yan, D. (2014). Palladium Nanoparticles Supported on Vertically Oriented Reduced Graphene Oxide for Methanol Electro-Oxidation. *ChemSusChem, 7*(10), 2907-2913. doi: 10.1002/cssc.201402352

Yang, L., Yan, D., Liu, C., Song, H., Tang, Y., Luo, S., & Liu, M. (2015). Vertically oriented reduced graphene oxide supported dealloyed palladium–copper

University of Malaya

nanoparticles for methanol electrooxidation. *Journal of Power Sources, 278*, 725-732. doi: http://dx.doi.org/10.1016/j.jpowsour.2014.12.141

Yang, S., Dong, J., Yao, Z., Shen, C., Shi, X., Tian, Y., Lin, S., & Zhang, X. (2014). One-pot synthesis of graphene-supported monodisperse Pd nanoparticles as catalyst for formic acid electro-oxidation. *Scientific reports, 4*.

Yang, S., Qiu, P., & Yang, G. (2014). Graphene induced formation of single crystal Pt nanosheets through 2-dimensional aggregation and sintering of nanoparticles in molten salt medium. *Carbon, 77*, 1123-1131. doi: http://dx.doi.org/10.1016/j.carbon.2014.06.030

Ye, Q., Zhou, F., & Liu, W. (2011). Bioinspired catecholic chemistry for surface modification. *Chemical Society Reviews, 40*(7), 4244-4258. doi: 10.1039/C1CS15026J

Ye, W., Chen, Y., Zhou, Y., Fu, J., Wu, W., Gao, D., Zhou, F., Wang, C., & Xue, D. (2014). Enhancing the catalytic activity of flowerike Pt nanocrystals using polydopamine functionalized graphene supports for methanol electrooxidation. *Electrochimica Acta, 142*, 18-24.

Ye, W., Wang, D., Zhang, H., Zhou, F., & Liu, W. (2010). Electrochemical growth of flowerlike gold nanoparticles on polydopamine modified ITO glass for SERS application. *Electrochimica Acta, 55*(6), 2004-2009. doi: http://dx.doi.org/10.1016/j.electacta.2009.11.022

Yin, H., Zhang, C., Liu, F., & Hou, Y. (2014). Hybrid of Iron Nitride and Nitrogen-Doped Graphene Aerogel as Synergistic Catalyst for Oxygen Reduction Reaction. *Advanced Functional Materials, 24*(20), 2930-2937. doi: 10.1002/adfm.201303902

Yoo, E., Okata, T., Akita, T., Kohyama, M., Nakamura, J., & Honma, I. (2009). Enhanced Electrocatalytic Activity of Pt Subnanoclusters on Graphene Nanosheet Surface. *Nano Letters, 9*(6), 2255-2259. doi: 10.1021/nl900397t

Yu, D., Xu, C., Su, Y., Liu, D., & He, X. (2017). Nitrogen-doped graphene aerogels-supported cobaltosic oxide nanocrystals as high-performance bi-functional electrocatalysts for oxygen reduction and evolution reactions. *Journal of Electroanalytical Chemistry, 787*, 46-54.

Yuan, L., Jiang, L., Liu, J., Xia, Z., Wang, S., & Sun, G. (2014). Facile synthesis of silver nanoparticles supported on three dimensional graphene oxide/carbon black composite and its application for oxygen reduction reaction. *Electrochimica Acta, 135*, 168-174. doi: http://dx.doi.org/10.1016/j.electacta.2014.04.137

Zhan, T., Liu, X., Lu, S., & Hou, W. (2017). Nitrogen doped NiFe layered double hydroxide/reduced graphene oxide mesoporous nanosphere as an effective bifunctional electrocatalyst for oxygen reduction and evolution reactions. *Applied Catalysis B: Environmental, 205*, 551-558.

University of Malaya

Zhang, H., Liu, X., He, G., Zhang, X., Bao, S., & Hu, W. (2015). Bioinspired synthesis of nitrogen/sulfur co-doped graphene as an efficient electrocatalyst for oxygen reduction reaction. *Journal of Power Sources, 279*, 252-258.

Zhang, J., Liu, H., Shi, P., Li, Y., Huang, L., Mai, W., Tan, S., & Cai, X. (2014). Growth of nickel (111) plane: The key role in nickel for further improving the electrochemical property of hexagonal nickel hydroxide-nickel & reduced graphene oxide composite. *Journal of Power Sources, 267*, 356-365. doi: http://dx.doi.org/10.1016/j.jpowsour.2014.05.106

Zhang, J., Tang, S., Liao, L., Yu, W., Li, J., Seland, F., & Haarberg, G. M. (2014). Improved catalytic activity of mixed platinum catalysts supported on various carbon nanomaterials. *Journal of Power Sources, 267*, 706-713. doi: http://dx.doi.org/10.1016/j.jpowsour.2014.05.137

Zhang, M., Li, Y., Yan, Z., Jing, J., Xie, J., & Chen, M. (2015). Improved catalytic activity of cobalt core–platinum shell nanoparticles supported on surface functionalized graphene for methanol electro-oxidation. *Electrochimica Acta, 158*, 81-88. doi: http://dx.doi.org/10.1016/j.electacta.2015.01.160

Zhang, S., & Northrup, J. E. (1991). Chemical potential dependence of defect formation energies in GaAs: Application to Ga self-diffusion. *Physical review letters, 67*(17), 2339.

Zhang, Y., Chang, G., Shu, H., Oyama, M., Liu, X., & He, Y. (2014). Synthesis of Pt–Pd bimetallic nanoparticles anchored on graphene for highly active methanol electro-oxidation. *Journal of Power Sources, 262*, 279-285. doi: http://dx.doi.org/10.1016/j.jpowsour.2014.03.127

Zhang, Y., Liu, H., Wu, H., Sun, Z., & Qian, L. (2016). Facile synthesis of Pt nanoparticles loaded porous graphene towards oxygen reduction reaction. *Materials & Design, 96*, 323-328.

Zhang, Y., Mo, G., Li, X., & Ye, J. (2012). Iron tetrasulfophthalocyanine functionalized graphene as a platinum-free cathodic catalyst for efficient oxygen reduction in microbial fuel cells. *Journal of Power Sources, 197*, 93-96.

Zhao, D., Shi, M. Q., Liu, W. M., Chu, Y. Q., & Ma, C. A. (2014). Special microwave-assisted one-pot synthesis of low loading Pt-Ru alloy nanoparticles on reduced graphene oxide for methanol oxidation. *IET Micro & Nano Letters, 9*(1), 50-54. doi: 10.1049/mnl.2013.0525

Zhao, J., Li, H., Liu, Z., Hu, W., Zhao, C., & Shi, D. (2015). An advanced electrocatalyst with exceptional eletrocatalytic activity via ultrafine Pt-based trimetallic nanoparticles on pristine graphene. *Carbon, 87*, 116-127. doi: http://dx.doi.org/10.1016/j.carbon.2015.01.038

Zhao, J., Liu, Z., Li, H., Hu, W., Zhao, C., Zhao, P., & Shi, D. (2015). Development of a Highly Active Electrocatalyst via Ultrafine Pd Nanoparticles Dispersed on Pristine Graphene. *Langmuir, 31*(8), 2576-2583. doi: 10.1021/la5049425

University of Malaya

Zhao, K., Gu, W., Zhao, L., Zhang, C., Peng, W., & Xian, Y. (2015). MoS 2/nitrogen-doped graphene as efficient electrocatalyst for oxygen reduction reaction. *Electrochimica Acta, 169*, 142-149.

Zhao, L., Thomas, J. P., Heinig, N. F., Abd-Ellah, M., Wang, X., & Leung, K. T. (2014). Au-Pt alloy nanocatalysts for electro-oxidation of methanol and their application for fast-response non-enzymatic alcohol sensing. *Journal of Materials Chemistry C, 2*(15), 2707-2714. doi: 10.1039/C3TC32317J

Zhao, L., Wang, Z.-B., Li, J.-L., Zhang, J.-J., Sui, X.-L., & Zhang, L.-M. (2016). Hybrid of carbon-supported Pt nanoparticles and three dimensional graphene aerogel as high stable electrocatalyst for methanol electrooxidation. *Electrochimica Acta, 189*, 175-183. doi: http://dx.doi.org/10.1016/j.electacta.2015.12.072

Zhao, Y., Zhan, L., Tian, J., Nie, S., & Ning, Z. (2011). Enhanced electrocatalytic oxidation of methanol on Pd/polypyrrole–graphene in alkaline medium. *Electrochimica Acta, 56*(5), 1967-1972. doi: http://dx.doi.org/10.1016/j.electacta.2010.12.005

Zheng, J.-N., Li, S.-S., Chen, F.-Y., Bao, N., Wang, A.-J., Chen, J.-R., & Feng, J.-J. (2014). Facile synthesis of platinum–ruthenium nanodendrites supported on reduced graphene oxide with enhanced electrocatalytic properties. *Journal of Power Sources, 266*, 259-267. doi: http://dx.doi.org/10.1016/j.jpowsour.2014.04.128

Zhong, X., Qin, Y., Chen, X., Xu, W., Zhuang, G., Li, X., & Wang, J. (2017). PtPd alloy embedded in nitrogen-rich graphene nanopores: High-performance bifunctional electrocatalysts for hydrogen evolution and oxygen reduction. *Carbon, 114*, 740-748. doi: http://dx.doi.org/10.1016/j.carbon.2016.12.004

Zhou, X., Qiao, J., Yang, L., & Zhang, J. (2014). A Review of Graphene-Based Nanostructural Materials for Both Catalyst Supports and Metal-Free Catalysts in PEM Fuel Cell Oxygen Reduction Reactions. *Advanced Energy Materials, 4*(8), 1301523-n/a. doi: 10.1002/aenm.201301523

Zhou, Z.-Y., Huang, Z.-Z., Chen, D.-J., Wang, Q., Tian, N., & Sun, S.-G. (2010). High-Index Faceted Platinum Nanocrystals Supported on Carbon Black as Highly Efficient Catalysts for Ethanol Electrooxidation. *Angewandte Chemie International Edition, 49*(2), 411-414. doi: 10.1002/anie.200905413

Zhu, Y., Murali, S., Cai, W., Li, X., Suk, J. W., Potts, J. R., & Ruoff, R. S. (2010). Graphene and Graphene Oxide: Synthesis, Properties, and Applications. *Advanced Materials, 22*(35), 3906-3924. doi: 10.1002/adma.201001068

University of Malaya

LIST OF PUBLICATIONS AND PAPERS PRESENTED

Publications:

- Jen Chao Ng, Chou Yong Tan, Boon Hoong Ong, Atsunori Matsuda, Wan Jefrey Basirun, Wai Kian Tan, Ramesh Singh, Boon Kar Yap; **Novel palladium-guanine-reduced graphene oxide nanocomposite as efficient electrocatalyst for methanol oxidation reaction,** *(2019) Materials Research Bulletin, Vol. 112, 213-220.*
- Jen Chao Ng, Chou Yong Tan, Boon Hoong Ong, Atsunori Matsuda, Wan Jefrey Basirun, Wai Kian Tan, Ramesh Singh, Boon Kar Yap; **Nucleation and growth controlled reduced graphene oxide supported palladium electrocatalysts for methanol oxidation reaction,** *(2019) Nanomaterials and Nanotechnology, Vol. 9, 1-9.*
- Jen Chao Ng, Chou Yong Tan, Boon Hoong Ong, Atsunori Matsuda, Wan Jefrey Basirun, Wai Kian Tan, Ramesh Singh, Boon Kar Yap; **Rapid nucleation of reduced graphene oxide-supported palladium electrocatalysts for methanol oxidation reaction,** *(2019) Journal of Nanoscience and Nanotechnology, Vol. 19(11), 7236-7243.*
- Jen Chao Ng, Chou Yong Tan, Boon Hoong Ong, Atsunori Matsuda; **Effect of synthesis method on methanol oxidation reaction on reduced graphene oxide supported palladium electrocatalysts,** (2017) *Procedia Engineering*, Vol. 187, 587-594.

Awards:

- **ITEX 2018 GOLD MEDAL. Graphene-doped zirconia engineered for industrial and machine applications.** *29th International Invention, Innovation & Technology Exhibition 2018 (ITEX 2018).*

University of Malaya